JAEA-Research
2018-018
DOI:10.11484/jaea-research-2018-018

JAEA-Research

DECOVALEX-2019 Task C: GREET Intermediate Report

Teruki IWATSUKI, Hironori ONOE, Masayuki ISHIBASHI, Yusuke OZAKI
Yifeng WANG, Teklu HADGU, Carlos F. JOVE-COLON, Elena KALININA
Milan HOKR, Aleš BALVÍN, Josef ZEMAN, Jiří LANDA and Jan ŠEMBERA

Geoscientific Research Department
Tono Geoscience Center
Sector of Nuclear Fuel, Decommissioning and Waste Management Technology Development

March 2019
Japan Atomic Energy Agency
日本原子力研究開発機構

国立研究開発法人日本原子力研究開発機構　研究連携成果展開部　研究成果管理課
〒319-1195 茨城県那珂郡東海村大字白方 2 番地4
電話 029-282-6387, Fax 029-282-5920, E-mail:ird-support@jaea.go.jp

Institutional Repository Section,
Intellectual Resources Management and R&D Collaboration Department,
Japan Atomic Energy Agency.
2-4 Shirakata, Tokai-mura, Naka-gun, Ibaraki-ken 319-1195 Japan
Tel +81-29-282-6387, Fax +81-29-282-5920, E-mail:ird-support@jaea.go.jp

JAEA-Research 2018-018

DECOVALEX-2019 Task C: GREET Intermediate Report

Teruki IWATSUKI, Hironori ONOE, Masayuki ISHIBASHI, Yusuke OZAKI,
Yifeng WANG*1, Teklu HADGU*1, Carlos F. JOVE-COLON*1, Elena KALININA*1,
Milan HOKR*2, Aleš BALVÍN*2, Josef ZEMAN*2, Jiří LANDA*2 and Jan ŠEMBERA*2

Geoscientific Research Department, Tono Geoscience Center
Sector of Nuclear Fuel, Decommissioning and Waste Management Technology Development
Japan Atomic Energy Agency
Akiyo-cho, Mizunami-shi, Gifu-ken

(Received December 25, 2018)

An experiment known as GREET (**G**roundwater **RE**covery **E**xperiment in **T**unnel) is being conducted at the Mizunami Underground Research Laboratory of the Japan Atomic Energy Agency (JAEA) to evaluate the environmental recovery process around underground galleries in fractured crystalline rock. The experiment has been planned to observe any environmental changes following water-filling in Closure Test Drift (CTD). The baseline hydro – mechanical – chemical (H-M-C) condition was identified prior to excavation of CTD. Then excavation of CTD and isolation by the water-tight plug, and subsequent flooding with groundwater were conducted. Environmental disturbance and recovery were observed for more than 3 years.

DECOVALEX-2019 Task C aims to develop modelling and prediction methods using numerical simulation based on the water-filling experiment to examine the post drift-closure environment recovery processes. The Task consists of following three Steps;

Step1: Modelling and prediction of environmental disturbance by CTD excavation
Step2: Modelling and prediction of environmental recovery by CTD isolation
Step3: Modelling and prediction of long-term environmental condition after CTD isolation

In this intermediate report, the results of Step 1 are summarized from each of the research teams (JAEA, SNL, TUL). Groundwater inflow rates to the tunnel during the excavation, hydraulic drawdown, and variation of chlorine concentration at monitoring boreholes in the vicinity of the tunnel were chosen as comparison metrics for Step1.

JAEA team constructed a reference model to check the viability of the original simulation code "COUPLYS", and then examined the sensitivity of the various parameters to the simulation results. The target parameters were estimated by using a DFN model and an ECPM model. SNL team developed a DFN model based on the fracture data (size distributions, orientation, volumetric intensity, the relationship between the aperture and permeability and the radius). Simulations of homogeneous and fractured system models were conducted using the coupled "DAKOTA-PFLOTRAN" codes. TUL team applied a multidimensional concept (discrete fractures + equivalent continuum) using the code "Flow123d" for modelling.

Consequently, prior to tunnel excavation in fractured granite, it is likely to be possible to foresee the scales of inflow rate and hydraulic drawdown by current simulation techniques. On the other hand, the predictions of precise drawdown location and chemical variation have large uncertainties using the current models and associated process understanding.

Keywords: Mizunami Underground Research Laboratory, DECOVALEX-2019 Project, Groundwater REcovery Experiment in Tunnel (GREET)

---

*1 Sandia National Laboratories (SNL)
*2 Technical University of Liberec (TUL)

JAEA-Research 2018-018

DECOVALEX-2019 Task C: GREET　中間報告書

岩月　輝希，尾上　博則，石橋　正祐紀，尾崎　裕介，Yifeng Wang[*1]，Teklu Hadgu[*1]，
Carlos F. Jove-colon[*1]，Elena Kalinina[*1]，Milan Hokr[*2]，Aleš Balvín[*2]，Josef Zeman[*2]，
Jiří Landa[*2]，Jan Šembera[*2]

日本原子力研究開発機構
核燃料・バックエンド研究開発部門
東濃地科学センター　地層科学研究部

（2018 年 12 月 25 日　受理）

瑞浪超深地層研究所では，花崗岩中における環境回復プロセスを理解するため GREET（**G**roundwater **RE**covery **E**xperiment in **T**unnel）プロジェクトを実施している。この実験は，坑道の埋め戻しを行う前に地下水による坑道の冠水試験を行うものである。冠水による環境変化（コンクリート吹付けによる影響も含む）を評価することを目的として，深度 500m に原位置の実規模実験坑道を建設した。坑道掘削に先立ち周辺の水理－力学－化学条件を観測した後，坑道の掘削，閉鎖，地下水による冠水を行い，環境擾乱とその回復過程を約 3 年間にわたって観測した。

DECOVALEX-2019 は，シミュレーション技術の開発に関わる国際協同プロジェクトであり，様々な国・機関の解析技術専門家が参加し複数の解析課題に取り組んでいる。上述の GREET は解析課題の一つ（Task C）として採用され，坑道掘削から閉鎖までの環境擾乱とその回復過程に関わるモデル化手法，シミュレーション手法を開発することを目的として，次の 3 つのステップに分けて進められている。

ステップ 1：坑道掘削に伴う環境擾乱のモデル化・予測
ステップ 2：坑道閉鎖に伴う環境回復のモデル化・予測
ステップ 3：坑道閉鎖後の長期的な環境変化のモデル化・予測

本中間報告書は，Task C の参加機関（日本原子力研究開発機構（JAEA），アメリカ サンディア国立研究所，チェコ リベレツ工科大学）により行われたステップ 1 の結果を取りまとめるものである。ステップ 1 では，坑道掘削時の湧水量，水圧低下，塩化物イオン濃度の変化が予測課題とされた。以下に各機関の実施概要と結果を要約する。

JAEA は，シミュレーションコード“COUPLYS”の適用性確認のため参照用水理地質構造モデルを構築し，様々な解析パラメータが解析結果に与える影響について感度解析を行った。その後，割れ目ネットワークモデル（DFN モデル），等価多孔質連続体モデル（ECPM モデル）を構築した。サンディア国立研究所は，坑道と周辺ボーリング孔の割れ目データ（坑道で観察された割れ目の大きさ，分布，方向，開口幅，割れ目半径，透水性など）に基づいて DFN モデルを構築した。その後，シミュレーションコード“DAKOTA-PFLOTRAN”により，均質媒体と割れ目媒体での予測解析を行った。リベレツ工科大学は，均質媒体と割れ目媒体を同時に取り扱うことができる多次元のシミュレーションコード“Flow123d”を用いて水理地質構造のモデル化を行った。

以上の各機関の予測解析技術を比較した結果，現行のシミュレーション技術によって，花崗岩において坑道掘削に先立って行うパイロットボーリングの調査データに基づいて，坑道掘削時の地下水湧水量および水圧低下程度を凡そ予測可能であると考えられた。一方で，正確な水圧低下位置や地下水の水質変化の予測に関しては，不確実性が高いと考えられた。

東濃地科学センター：〒509-6132　岐阜県瑞浪市明世町山野内 1-64
*1 Sandia National Laboratories　（SNL）
*2 Technical University of Liberec　（TUL）

Contents

目次

1. Overview of Mizunami Underground Research Laboratory (MIU) and GREET project

The Mizunami Underground Research Laboratory (MIU) is being operated by the Japan Atomic Energy Agency (JAEA), in the Cretaceous Toki Granite in the Tono area, Central Japan. The MIU project is a broad-based, multi-disciplinary study of the deep geological environment, providing a scientific basis for the research and development of technologies needed for geological disposal. The MIU design consists of two shafts, and several horizontal research galleries (Figure 1.1).

JAEA is performing GREET (Groundwater REcovery Experiment in Tunnel) project for an understanding of the post-closure recovery of the geological environment in and around the MIU construction site. In GREET project, a part of research tunnel at 500 m depth is being filled with in-situ groundwater prior to the backfilling test with burial materials. These drift closure tests are preliminary studies for the facility closure of the MIU in future (Figure 1.1).

1.1 Geology

Figure 1.2 shows the geological structures in and around the MIU construction site. In this site, Pliocene to Pleistocene rocks of the Seto Group (5 to 0.7 Ma) unconformably overlies Miocene sedimentary rocks of the Mizunami Group (20 to 15 Ma). The Mizunami Group in turn unconformably overlies a basement of Cretaceous granitic rocks, the Toki Granite (72.3 Ma [1), 2)]. The middle and upper parts of the Mizunami Group, the Akeyo Formation and Oidawara Formation respectively (18 to 15 Ma), are composed of alternating shallow marine siltstone-sandstone. In contrast, the lower part of the Mizunami Group, the Toki Lignite-Bearing Formation (ca. 20 Ma) consists of lignite-bearing fluvial deposits.

The vertical shafts of the MIU facility penetrate through the Mizunami Group into the Toki granite at the unconformity, which is at about 170 m below ground level (GL) (Figure 1.2). The Toki granite of the Tono district, Central Japan, is a Late Cretaceous plutonic intrusive in the Sanyo Belt. The Toki granitic rocks consist of medium- to coarse-grained biotite granite and medium-grained hornblende-biotite porphyry, and are partly intruded by quartz porphyry and aplite dikes.

Toki granite can be divided into two structural domains, an upper highly fractured domain (UHFD) and a lower sparsely fractured domain (LSFD), based on the distribution of fracture frequency. In addition, a low-angle fracture zone (LAFZ) which is a significant water conducting feature has been identified in the UHFD, which zone distributed approximately GL-200 m. GREET experiment is being conducted in a part of the deepest stage of at the GL - 500m in LAFZ. In addition, the presence of several faults has been confirmed and their geometry determined (Figure 1.2).

1.2 MIU facility

Figure 1.3 shows the layout of shafts and galleries of the MIU and several monitoring boreholes drilled from the galleries. The design of the underground facility consists of a Main Shaft and Ventilation Shaft, two Access/Research galleries at 300 m and 500 m below ground level, and sub-stages at 100 m depths between two shafts. The length of 300 m Access/Research Gallery and 500 m Access/Research Gallery (North) is about 100 m. The shafts have been excavated by two 1.3 m blasting and mucking cycles followed by emplacement of a concrete liner in every 2.6 m section of shaft [3)]. Pre-excavation grouting of a water-conducting fracture zone was carried out in both shafts and gallery. The construction of the shafts commenced in July 2003. The construction of the -500 m Stage was completed by the end of February 2014.

GREET is being conducted in the deepest part of the -500m Stage.

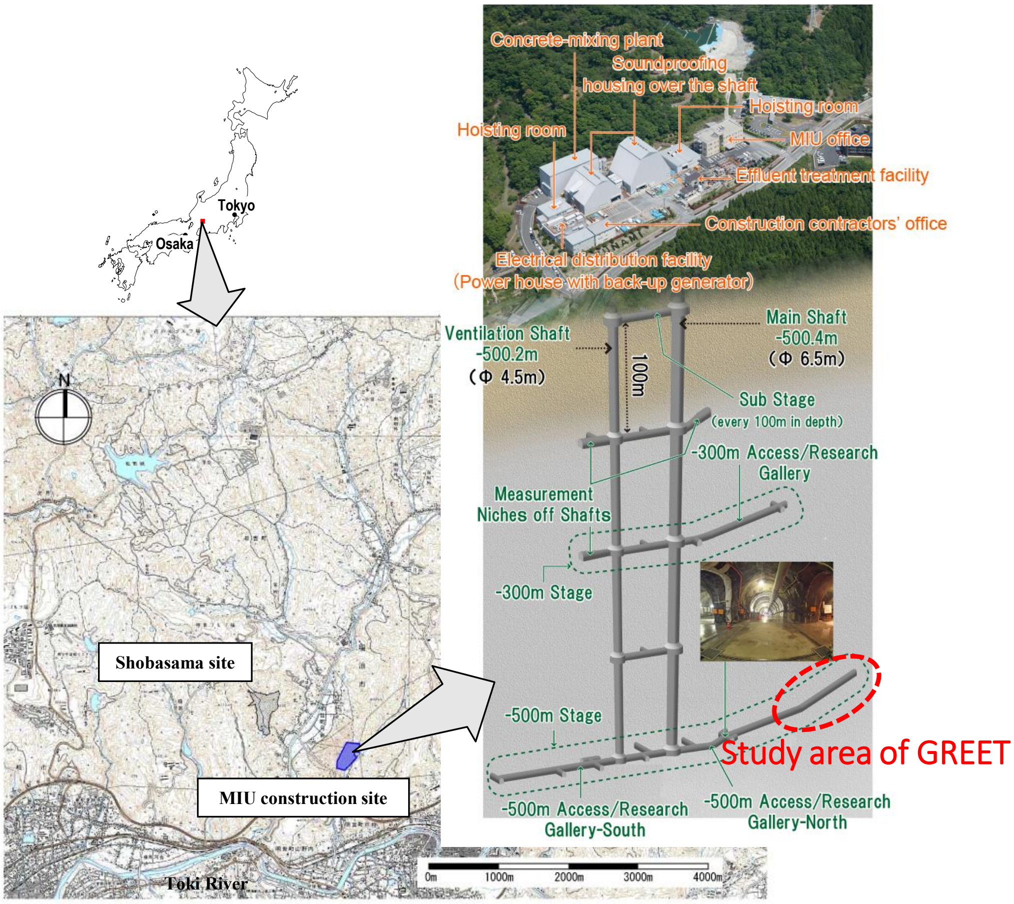

*Topographic map: 1/25,000 (Published by Geographical Survey Institute)

Figure 1.1 Location and layout of the MIU

1.3 Concept of GREET project

The geological disposal project is expected to extend over a period of around 100 years to repository closure [4]. Geological environments would likely be influenced for several decades due to the construction and operation of a large underground facility. In particular, groundwater flows into an underground facility would likely lead to significant changes in hydraulic pressure distribution and hydrochemical conditions.

Long-term hydraulic pressure and hydrochemical monitoring were conducted in the boreholes in and around the MIU construction site in Surface-based Investigations Phase to determine baseline conditions before the MIU facility was constructed (Figure 1.3). This monitoring has provided the basis on which to assess hydraulic and hydrochemical disturbances in response to the construction of the MIU.

From the results of various monitoring in the MIU, it is estimated that shallow groundwater infiltrated into deep parts of the granite, accompanying the changes in hydraulic pressure distributions during construction and operation of the facility (Figure 1.4 and Figure 1.5). Changes of hydraulic and hydrochemical conditions from the baseline conditions are influenced by hydrogeological heterogeneities such as faults. It is important to understand the recovery process of the geological environment during underground facility closure.

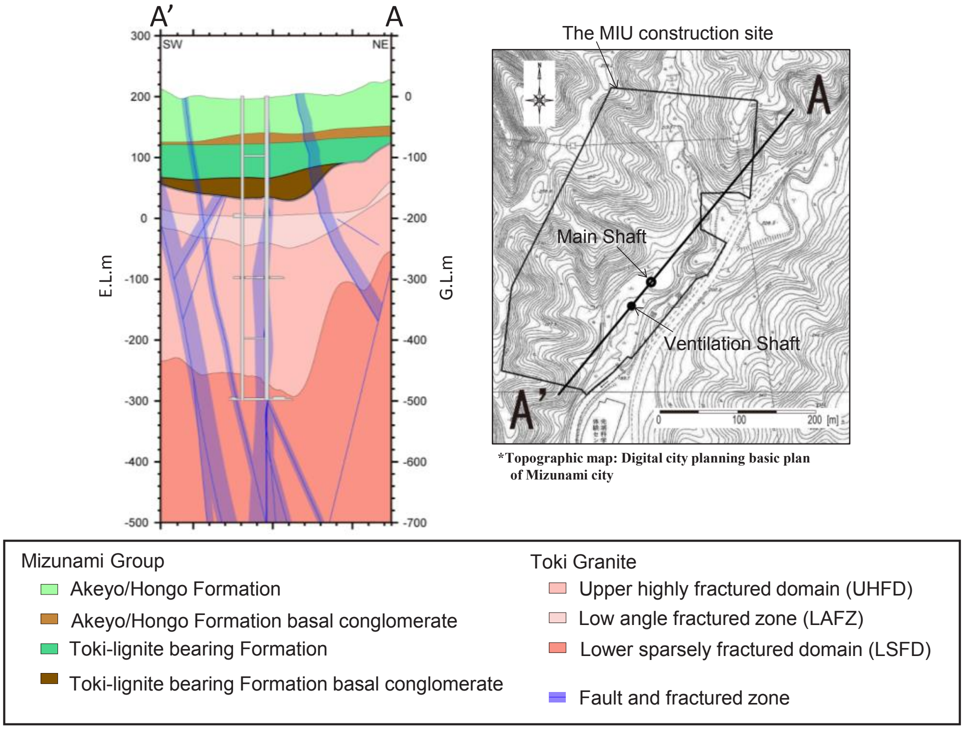

Figure 1.2 Estimated geological structures around the MIU construction site

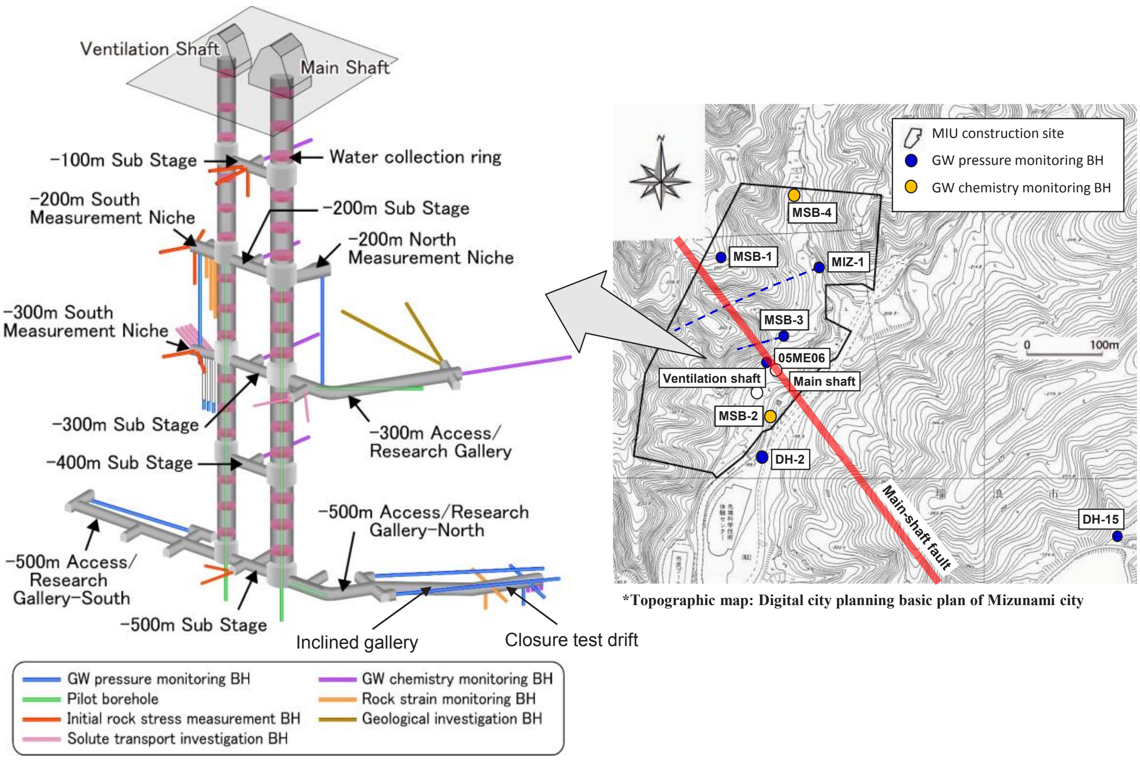

Figure 1.3 Layout of the MIU facility and monitoring boreholes

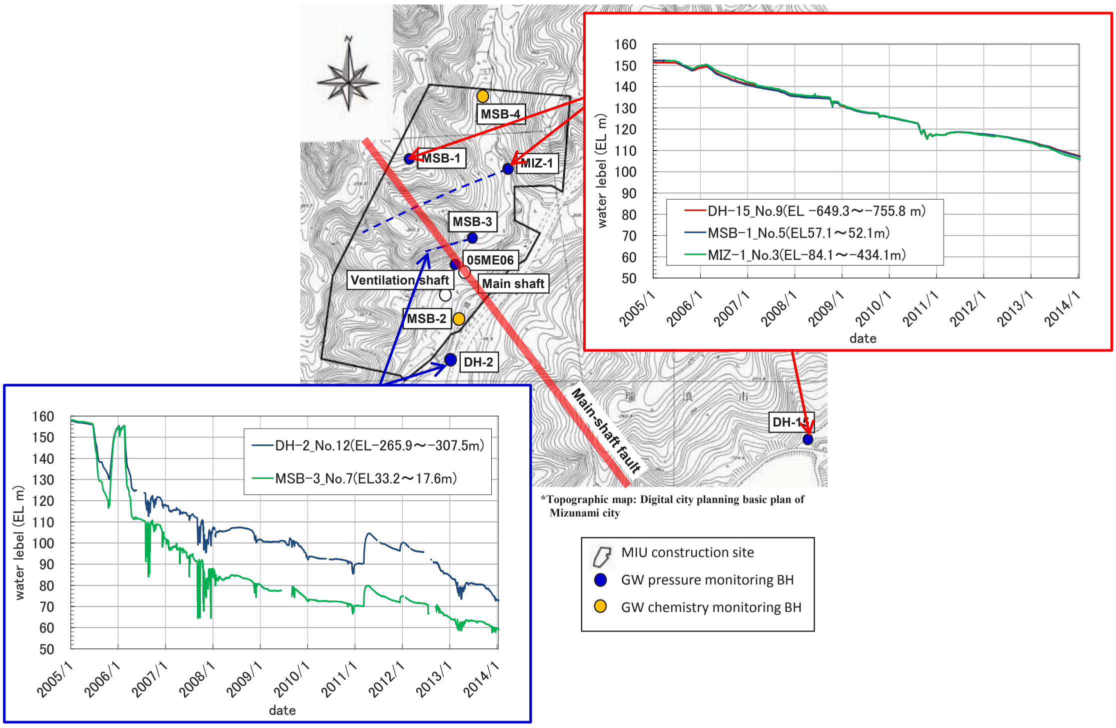

Figure 1.4 Pressure response in the granite due to construction of the MIU facility

It is planned to understand the evolution of the geological environment near the drift during and after closure to reduce uncertainties in the long-term safety of deep geological disposal. The drift closure test will provide preliminary knowledge on the recovery of geological environments prior to the facility closure; GREET is such a preliminary test (Figure 1.6). Drift closure experiments without backfilling are rare when compared with previous international studies where the focus has been on backfilled drifts. The un-backfilled condition is suitable to carry out a repetitive drift-scale hydraulic test and to understand simple hydrochemical process regarding cementing materials, amongst other processes.

The project aims to understand the relevant recovery processes operating in the geological environment during facility closure, to verify the H-M-C-(B: Biology) simulation methods for recovery processes in fractured granite and to develop monitoring techniques for the facility closure phase and appropriate closure methodologies taking recovery processes into account.

The experiment gallery is located 500 m below ground level. The length of the experiment gallery is 46.5 m, the width is 5 m and height is 4.5 m (approx. 900m^3). The fracture distribution around the test drift, hydraulic and hydrochemical baseline have been identified by monitoring boreholes (Figure 1.7).

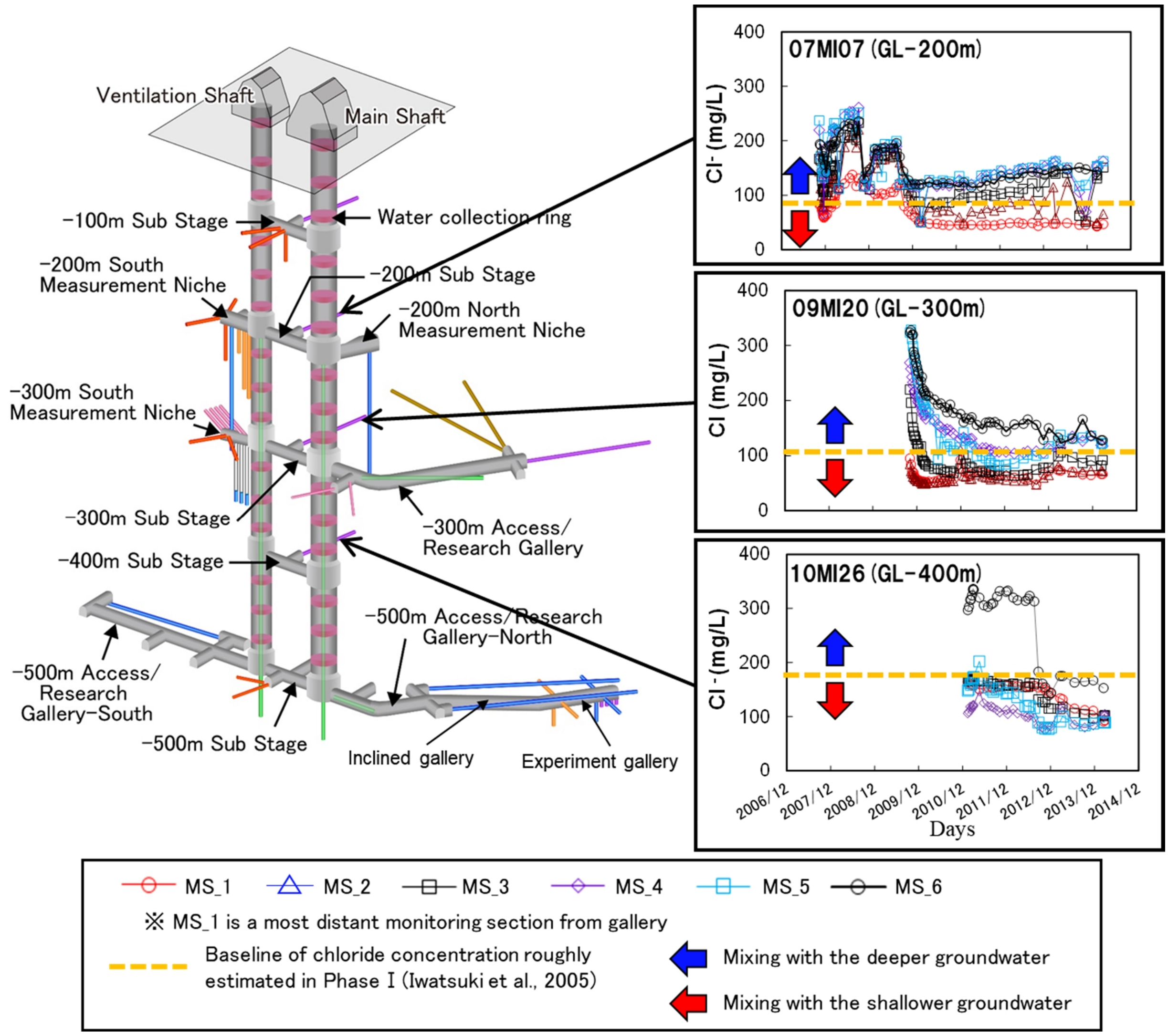

Figure 1.5 Example of changes in salinity in groundwater sampled from horizontal boreholes at several Sub-stages

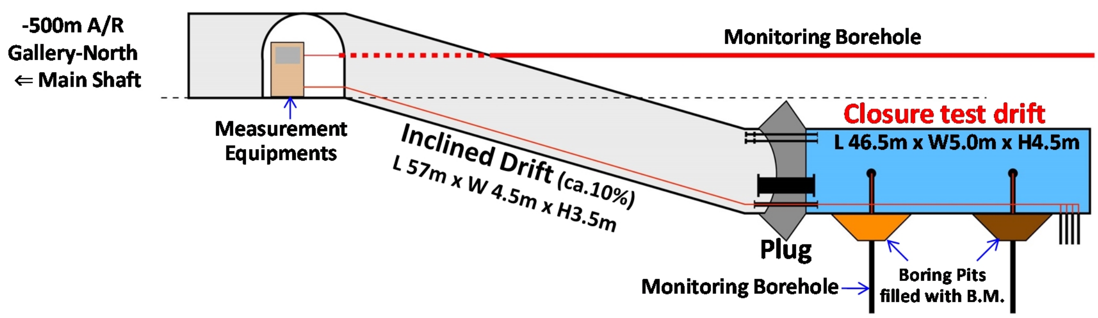

Figure 1.6 Schematic view of test drift

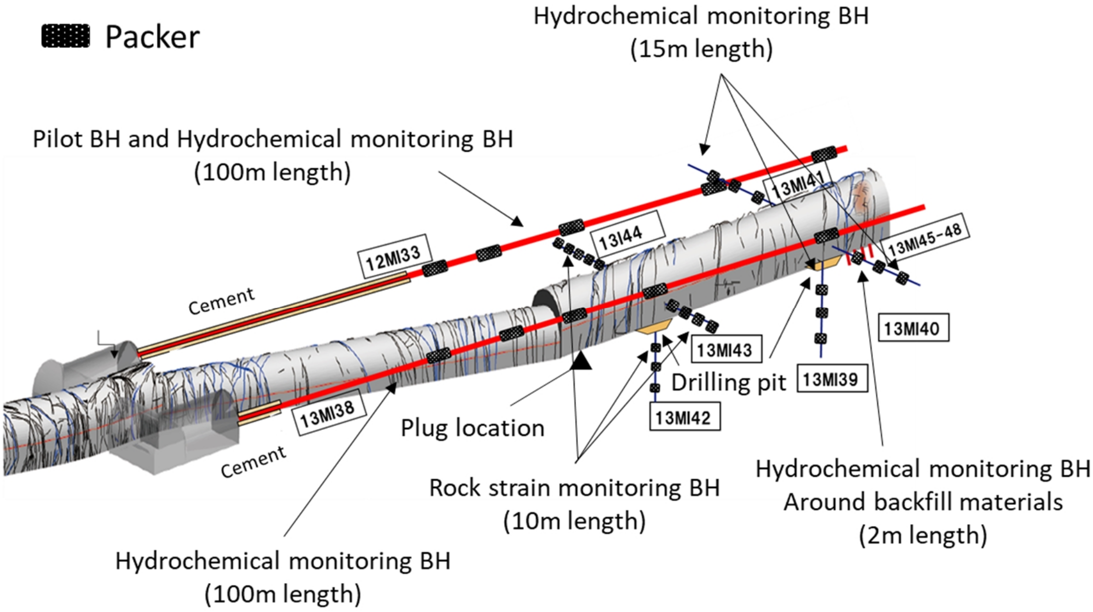

Figure 1.7 Layout of monitoring boreholes around the Closure test drift

The experimental step of the groundwater recovery experiment is shown in Figure 1.8. The overall approach is as follows; prior to construction of the experiment gallery, a pilot borehole, adjacent and parallel to the gallery, is drilled to estimate a baseline of hydraulic and hydrochemical conditions. Hydraulic and hydrochemical conditions and any changes during gallery construction are monitored in the borehole. Geological mapping of the gallery is conducted to characterize the fracture distribution. Additional monitoring boreholes are drilled and an impervious plug installed at the entrance to the experiment gallery in order to understand and assess the recovery process in terms of hydraulic pressure changes, changes in hydrochemical conditions and in rock stress distribution around the experiment gallery during water filling and draining events. A backfill material test is then carried out using pit bored into the experiment gallery floor in order to accumulate data on saturation phenomenon of the backfill material and its influence on the hydrochemical environment in the rock mass. Applicability of monitoring techniques and plug performance during a facility closure phase can be validated based on the result. Validation of the numerical analyses methodology will be carried out by comparison with the result of the experiment and prediction results.

Initial hydraulic pressures and hydrochemical distributions around the experiment gallery are determined using a multi-interval monitoring system in the 12MI33 borehole. This system also aims to monitor hydraulic response and hydrochemical disturbance during the experiment gallery construction. After the construction of the experiment gallery, additional monitoring boreholes are drilled and a multi-interval monitoring system installed for observation of hydraulic pressure, hydrochemical and rock mechanics response during the water filling and draining events.

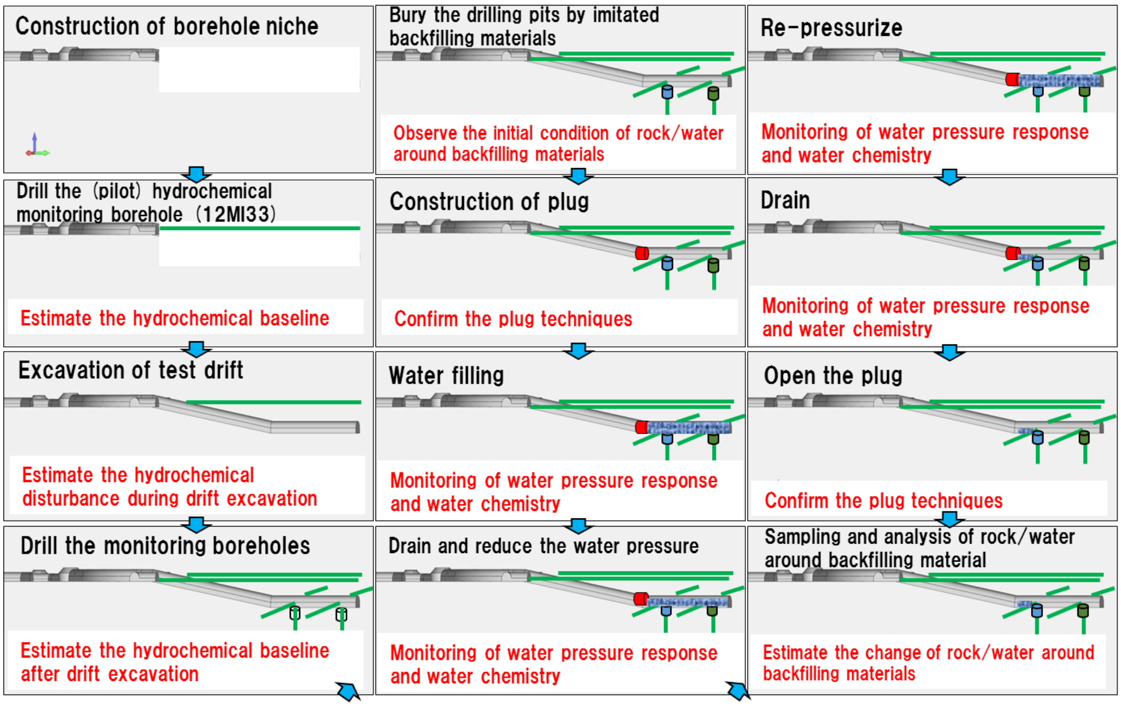

Figure 1.8 Outline of field experiments

The main purpose of groundwater pressure monitoring is to observe the hydraulic response and any heterogeneities influenced by fracture distribution in the rock mass. The main purpose of geochemical monitoring is to observe evolution of hydrochemical conditions and any heterogeneities that may be related to hydraulic response around the experiment gallery such as a change in redox conditions in the vicinity of and/or in the gallery walls, changes in mineralogy and microbial diversity in the gallery wall. The main purpose of fibre-optical rock mechanics monitoring is to determine what may be induced by hydraulic pressure disturbance rock displacement and stress changes occur during the cycling of the drift.

Seismic tomography and electrical resistivity surveys are carried out prior to and after the water filling and draining events in order to identify the excavation damaged zone (EDZ) and any changes to the EDZ. Fracture distributions around gallery wall are characterized using ground penetrating radar.

The conceptual models to estimate the long-term evolution of geological environment around gallery wall will be constructed based on the monitoring data. Then, the numerical simulation with those models will be performed to support the conceptual models quantitatively.

2. Planning for DECOVALEX2019 - Task C

2.1 Objective of simulation in Task C

The purpose of Task C through the modeling of GREET are a reproduction and quantitative evaluation of interactions between Hydro-Mechanical-Chemical (H-M-C) phenomena. In addition, the establishment of a modeling method for fractured media in H-M-C simulations is included in this task because prediction of disturbance of the geological environment through excavation to repository closure is common issue. This is also one of the reasons that Task C is run in parallel with the actual progress of the GREET experiment, so that the performance of the adopted modeling approaches can be judged.

Spatial heterogeneity of hydrogeological properties has observed in the volume of interest. Characterization of fracture distribution at drift scale using modeling tools such as Discrete Fracture Network [5] modeling is included as an objective. Moreover, several cycles of water pressurizing and depressurizing by water inflow and drainage are planned in this project. From such cycles, it is possible to carry out verification and validation of constructed model and modeling methodology.

To achieve this objective, Task C is scheduled along the actual operation of the experiment. The simulation works in Task C are divided into three steps (Figure 2.1 and Figure 2.2).

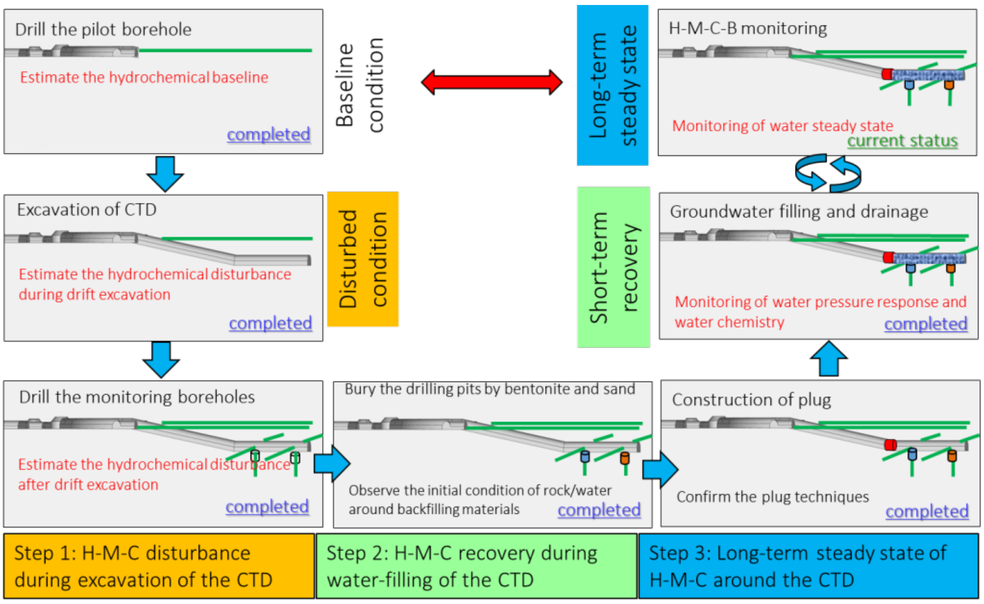

Figure 2.1 Simulation image of Task C

- In the Step 1 a blind simulation is conducted to verify the basic concept and methods of the prediction analysis of the environmental disturbance of the baseline condition during the excavation of Closure test drift (CTD) using baseline hydrogeological and hydraulic/hydrochemical data.
- In the Step 2, calibration of models is conducted based on the observation data during the CTD excavation. Furthermore, blind simulations are conducted to infer the recovery by the water-inflow.
- The Step 3 is calibration of previous models and simulations to predict the steady state condition of the wider geological environment.

2.2 Schedule of Task C

The schedule of Task C is shown in Figure 2.3. This work schedule is designed to reflect progress of the GREET project. More data will be provided as it becomes available and at suitable points in the task allowing the simulations to be developed and updated. The promotion of understanding of phenomena during GREET experiment is also expected through the step-by-step calibration of the simulation model.

Step	Simulation ⇔	Validation data
Step 1: H-M-C disturbance during excavation of the CTD	• Water pressure drawdown • Groundwater chemistry (pH-Eh condition) • Groundwater inflow rate	• Water pressure and groundwater chemistry in monitoring boreholes during the excavation • Groundwater inflow rate
Step 2: H-M-C recovery during water filling of the CTD	• Water pressure recovery • Groundwater chemistry (pH-Eh condition) • Rock displacement	• Water pressure, groundwater chemistry and rock displacement in CTD and monitoring boreholes after the water filling
Step 3: Long-term steady state of H-M-C around the CTD	• Water pressure • Groundwater chemistry (pH-Eh condition) • Rock displacement	• Water pressure, groundwater chemistry and rock displacement in CTD and monitoring boreholes during monitoring

Figure 2.2 Simulation and validation data in each Step

*CTD: Closure test drift	FY2016		FY2017		FY2018		FY2019	
	Step 1		Step 2		Step 3			Step 4
	1a	1b	2a	2b	3a	3b	3c	-
Objectives	Prediction of H-M-C disturbance during excavation		Prediction of H-M-C recovery during re-saturation around the CTD		Predicition of long-term steady state of H-M-C condition around the CTD			-
Implementation	Confirmation of dataset and modeling methodology	Modeling and prediction analysis	Validation and model calibration	Modeling and prediction analysis	Validation and model calibration	Modeling and prediction analysis	Validation (proposal of modeling for backfilling of the CTD / URL?)	Final reporting
Data kind/location	Previous investigation in facility scale and pilot boring prior to excavation of the CTD		Geological mapping of drift (the inclined drift and the CTD) and borehole investigations		Water-filling and observation in and around CTD including the impervious plug			-
	· Geological environmental model/Site scale · Pilot boring / 12MI33 near		· Monitoring in pilot boring / 12MI33	· Boreholes /13MI38-48 in and around CTD	· Monitoring/ CTD and boreholes (13MI33 - 48)	· Continuous monitoring of H-M-C-B condition		
Data	- Geology - Mineralogy - Hydrogeology - Chemistry - Rock mechanics		- Hydrogeology - Chemistry	- Geology - Mineralogy - Hydrogeology - Chemistry - Biology - Rock mechanics	- Hydrogeology - Chemistry - Biology - Rock mechanics - Stress in plug	- Hydrogeology - Chemistry - Biology - Rock mechanics - Stress in plug		-
	▲ Data set 1	▲	▲ Data set 2	▲	▲ Data set 3	▲	▲	▲
Meeting of DECOVALEX 2019	18-20 May 2016	29 Nov.-2 Dec. 2016	Apr. 2017?	Nov. 2017?	Apr. 2018?	Nov. 2018?	Apr. 2019?	Nov. 2019?

Step x a: Validation and calibration Step x b: Modeling and prediction analysis Step x c: Calibration

Figure 2.3 Schedule of Task C and detail of data for each step

2.3 General setting of numerical simulation

In Task C, the scale of modeling area, mesh size and degree of heterogeneity for numerical simulation are not standardized because this condition should depend on the method to set the boundary condition, computer resources that each group uses, etc. On the other hand, it is important to standardize the visualization area and output points for the comparison of numerical simulation results of each group and also reporting requirements.

The visualization area in 150 m × 100 m × 100 m square domain as shown in Figure 2.4, is set to the surroundings of the inclined drift and the CTD. The coordinate information of the visualization area is shown in Table 2.1.

Output points of numerical simulation for graphical comparison at specific monitoring boreholes are as shown in Figure 1.7. The number of output points will be increased with the progress of step in Task C because the number of available data for comparison will increase as the step proceeds.

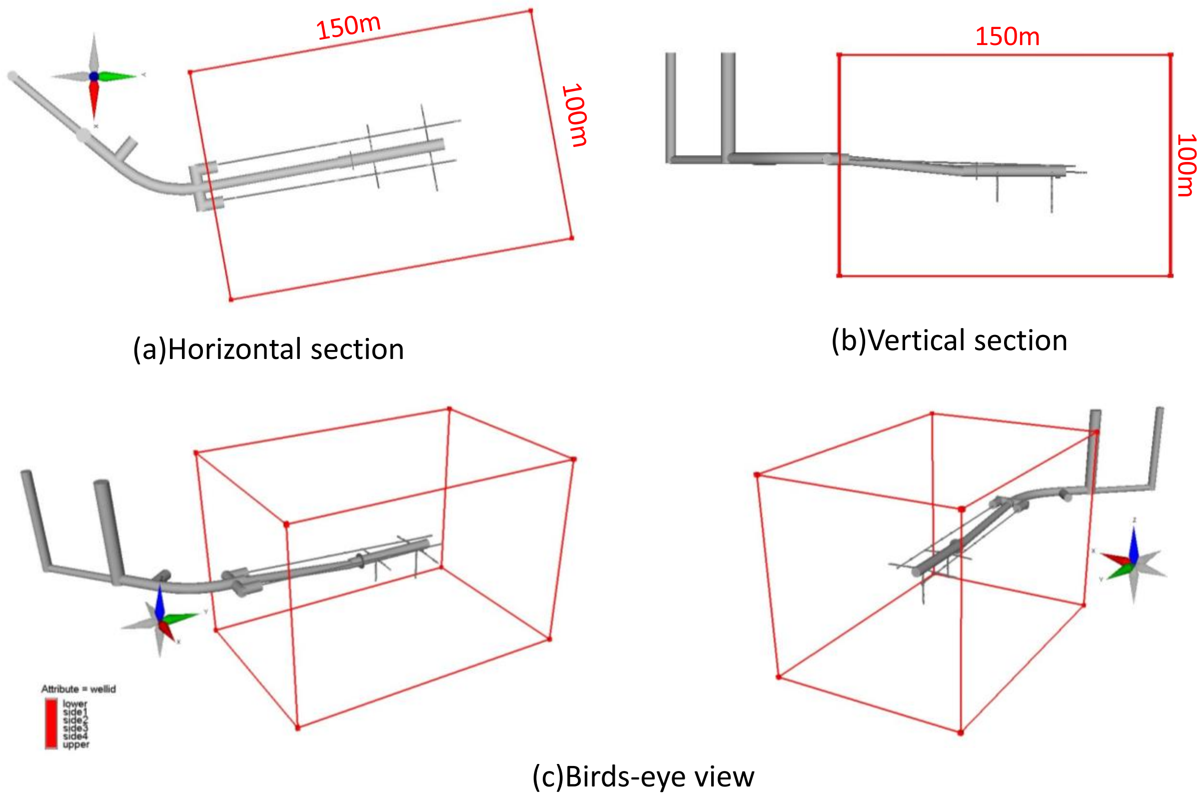

Figure 2.4 The visualization area of numerical results in task C

Table 2.1 The coordinate information of the visualization area

E-W(m)	N-S(m)	E.L.(m)	
6522.7	-68943.5	-250	Upper boundary
6496.1	-68795.9	-250	Upper boundary
6397.7	-68813.7	-250	Upper boundary
6424.3	-68961.3	-250	Upper boundary
6522.7	-68943.5	-350	Lower boundary
6496.1	-68795.9	-350	Lower boundary
6397.7	-68813.7	-350	Lower boundary
6424.3	-68961.3	-350	Lower boundary

3. Working plan of Japan Atomic Energy Agency (JAEA) team in Step 1

The overview of simulations performed in Step 1 by JAEA is summarized below.

3.1 Modeling strategy and approach

- The main objective of JAEA's modeling is a characterization of spatial heterogeneity of geological environment, depending on the distribution of fractures at drift scale; tens of meters to hundreds of meters square.
- The H-M-C changes during the excavation of the inclined drift and the CTD are simulated as a coupled problem.
- The numerical modeling and simulation are performed with the H-M-C coupled simulator "Couplys", JAEA's in-house software. "Couplys" consists of "Thames", "Dtransu3D" and "PHREEQC" (Figure 3.1).
- "Thames" is a full coupled simulator of the hydro-mechanical problem, "Dtransu3D" solves the advective-dispersive problem by the Eulerian-Lagrangian method and "PHREEQC" addressed hydrochemical problems. These three simulators are executed sequentially.
- A Continuum porous medium (CPM) model is applied as the modeling approach in Step 1. The CPM model will be a base model to evaluate an improved model by introducing heterogeneity representing fracture as step in task proceeds.
- In Step 1, the simulation of groundwater flow is solved as part of the H-M-C problem. The fully coupled problem of groundwater flow and mechanics is solved and interaction between hydraulic pressure and rock stress is considered.
-

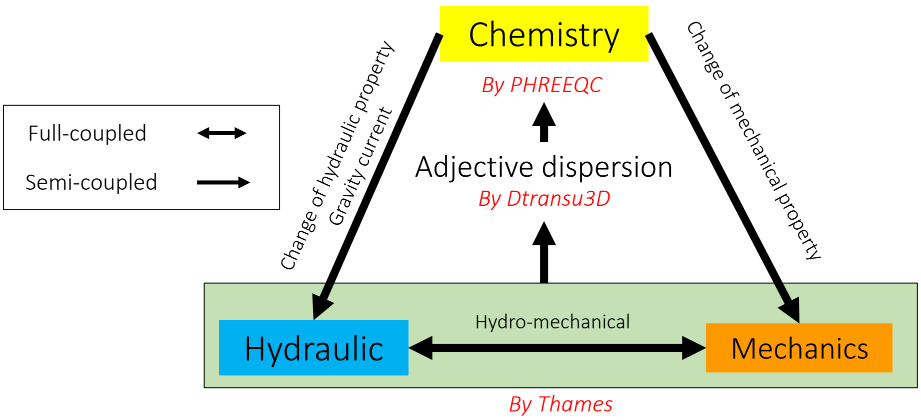

Figure 3.1 Modeling method of Couplys, H-M-C coupled simulator

3.2 Objective of modeling in Step 1

(1) Hydrogeology

The objective of groundwater flow simulation in Step 1 is to construct a reference model of hydrogeology with CPM model and to estimate hydraulic pressure change around the CTD due to drift excavation.

Quantitative understanding the behavior of the groundwater flow with a variety of simulations and model parameterization is also one of the objectives, because this information will be useful for the model calibration in later steps.

(2) Rock mechanics

Some of the objectives of the mechanical simulation are same as ones of groundwater flow simulation, the construction of a reference model of rock mechanical for the later steps, the understanding of behavior with different physical properties and simulation approaches and the development of the initial condition for the next step.

In addition to these objectives, the rock mechanical simulation in Step 1 is aimed at estimating the characteristics of the Excavation Damaged Zone (EDZ). Rock fracturing by stress release following the excavation is one of the key mechanisms of EDZ formation and it is expected that the simulations will provide insight to this process, noting that the EDZ is recognized to have the potential to affect the H-M-C process significantly. Therefore, understanding of the HMC system taking into account the EDZ will be hopefully one of our topics of interest. Many studies show evidence of the existence of EDZ by GPR, electrical resistivity tomography (ERT), etc. Modeling of EDZ and model validation with observed data could give us not only evidence of the existence of the EDZ but also information of wider phenomena in the EDZ. The information could contribute to the evaluation of tunnel stability during post-closure.

(3) Chemistry

The hydrochemical simulation of Step 1 is focused on advection-diffusion phenomena in groundwater due to hydraulic pressure change during drift excavation. Construction of a reference model of hydrochemistry and estimating the change in hydrochemical conditions around the CTD is the main objective of the hydrochemical simulation.

Quantitative understanding of the evolution of hydrochemical conditions with different simulation approaches and parameterization, is also one of the main objectives, because this information will be useful for the model calibration in later steps.

3.3 Simulation condition and model setting

3.3.1 Modeling area

The modeling area is planned to set the same as visualization area (Figure 2.4). A particular focus for the modeling work is on the CTD area.

3.3.2 Theory of numerical simulation

In this study, we use the FEM code Couplys. Couplys consists of three simulators as shown in Figure 3.1. Thames simulates THM components, and transport (advection-diffusion) component is then calculated using Dtransu3D. Thames constitutive model is based on Biot's theory for coupling of hydro-mechanical behavior and Duhamel-Neuman's theory for the effect of thermal on deformation. Then, energy balance equation is solved for thermal transfer [6]. The detail of theory and simulation code is described in Kobayashi and Ohnisi (1986) [7] and Ohnish et al. (1987) [8]. Dtransu [9] solves the advective-diffusive equation according to the flow calculated by Thames. Dtransu employs the Euralian Lagrangian method for numerical accuracy. This simulator in addition to PHREEQC is incorporated for the simulation of THMC process as Couplys.

3.3.3 Geological unit

The distribution of geological units in the modeling area is shown in Figure 3.2. The UHFD, LSFD and the fractured zone along the Main-shaft fault is present in the modeling area. However, the LSFD is the main geological unit in the modeling area and is distributed around the CTD. Therefore, LSFD is only unit considered in JAEA's modeling.

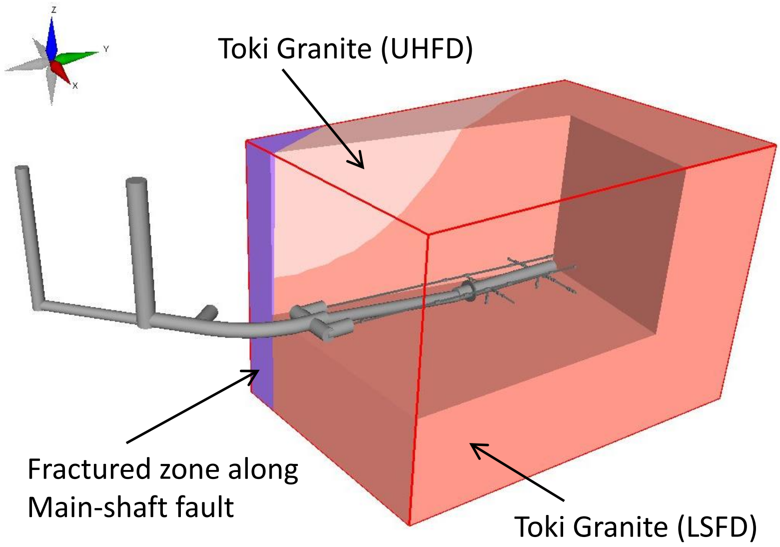

Figure 3.2 Distribution of geological units in the modeling area

3.3.4 Mesh generation

Elements near the tunnel surface were discretized with an appropriately fine mesh. The shortest length of the edge in the fine mesh will be set to about 1 m for evaluating more detail variation of geological environment near the tunnel. The simulation domain was discretized with hexahedral elements. Mesh size will be set to larger as it is far from the surface of the tunnel. The total number of elements is planned to be less than 100,000 elements. These restrictions of model discretization come from limit of simulation code ability.

3.3.5 Parameters

(1) Hydrogeology

Hydraulic parameters for the LSFD for CPM modeling is set based on the previous result of the MIU project (Table 3.1). Average values of the results of hydraulic packer tests in 12MI33 borehole (Table 3.2) are applied as the hydraulic conductivity of LSFD. Another parameter of LSFD is set based on Onoe et al. (2014) [10].

(2) Rock mechanics

Elastic modulus, porosity, Poisson's ratio, etc. measured by core sample tests performed as a part of rock stress measurements were used to define the rock mechanics parameters (Table 3.3).

(3) Chemistry

The advective-dispersive analysis is focused on disturbance of chloride ion concentration in groundwater due to hydraulic pressure change during drift excavation. Input parameters for advective-dispersive analysis are shown in Table 3.1.

Table 3.1 Hydraulic parameters of LSFD

Hydrogeological units	Hydraulic conductivity (ms^{-1})	Specific storage coefficient (m^{-1})	Porosity	Vertical dispersion length (m)	Horizontal dispersion length (m)	Effective diffusion coefficient (m^2/s)	Retardation coefficient	Damping ratio
	logK	logSs						
Toki Granite (LSFD)	-8.0	-6.0	0.001	4.3	0.43	1.0E-12	1.0	0.0

Table 3.2 Result of hydraulic packer test in 12MI33 borehole

Borehole	Test No.	Top of test section (mabh)	Bottom of test section (mabh)	Test length (m)	Inflow rate (L/min)	Hydraulic pressure (MPa)	head (Elm)	T (m^2/s)	k (m/s)
12MI33	No.1	12.10	18.90	6.80	2.50	3.73	81.85	1.78E-07	2.62E-08
	No.2	37.10	42.56	5.46	7.50	4.02	110.20	6.01E-07	1.10E-07
	No.2'	20.10	36.10	16.00	0.10	3.84	92.29	9.78E-08	6.11E-09
	No.3	44.20	54.50	10.30	1.90	3.98	105.99	8.65E-08	8.40E-09
	No.4	53.20	63.50	10.30	0.42	4.00	106.79	4.96E-09	4.82E-10
	No.5	65.20	85.50	20.30	0.50	4.00	106.31	1.93E-08	9.53E-10
	No.6	105.20	107.00	1.80	5.20	4.02	106.30	4.91E-07	2.73E-07

Table 3.3 Result of rock mechanical test in 12MI35 borehole

13MI35									
Borehole information	Direction of borehole	N174.7E 7.8							
	Depth (m)	20.5							
	Number of measurement	6							
Measurement information	Measurement method	CCBO							
	Section name	OC35-1	OC35-2	OC35-3	OC35-4	OC35-5	OC35-6	OC35-7	OC35-8
	Section depth(m)	12.66	14.16	14.16	14.26	15.05	16.03	17.03	18.03
Elastic property	Young's modulus(GPa)	53.6	52.6(OC35-1)	−	−	54.8	−	46.7	−
	Poissons ratio	0.22	0.25(OC35-1)	−	−	0.22	−	0.25	−
Stress tensor(MPa)	σ x	9.01	−	−	13.7	7.94	8.06	6.87	7.7
	σ y	28.85	−	−	5.29	12.26	11.28	12.07	10.59
	σ z	9.82	−	−	6.65	7.6	8.23	6.9	8.15
	τ xy	2.96	−	−	1.72	0.07	1.05	2.51	−4.26
	τ yz	0.16	−	−	0.21	1.92	−1.17	−1.61	−1.09
	τ zx	−0.84	−	−	0.33	1.66	1.42	1.58	0.5
Principle stress	σ 1	29.28	−	−	14.06	13.03	11.77	13.22	13.88
	H (Horizontal direction)	8	−	−	79	8	−170	−161	145
	V (Vertical direction)	0	−	−	3	22	14	9	12
	σ 2	10.25	−	−	6.64	8.98	9.56	8.41	7.92
	H (Horizontal direction)	−82	−	−	−41	112	86	99	−55
	V (Vertical direction)	63	−	−	84	31	45	50	78
	σ 3	8.14	−	−	4.94	5.78	6.24	4.21	4.63
	H (Horizontal direction)	98	−	−	169	−111	−67	−63	54
	V (Vertical direction)	27	−	−	5	51	42	38	4

3.3.6 Initial condition

(1) Hydrogeology

The initial condition of hydraulic head is set based on the monitoring of the boreholes around the CTD.

12MI33 and MIZ-1 boreholes are located in the modeling area, and 09MI21 is located at 300 m below ground level (Figure 3.3).

Hydraulic head of these monitoring boreholes before the drift excavation is almost same value, therefore a uniform distribution of hydraulic head in the modeling area is applied as an initial condition (Table 3.4).

(2) Rock mechanics

The measured rock stress (Table 3.3) is used for the initial stress condition. Uniform initial stress condition linearly changing according to the depth will be tested.

(3) Chemistry

The initial chloride ion concentration in groundwater is based on the monitoring results in the boreholes around the CTD.

The concentration gradient of chloride ion with depth is estimated from these monitoring results (Table 3.5). Therefore, vertical gradient of chloride ion concentration assuming a linear approximation is considered as an initial condition (Table 3.5).

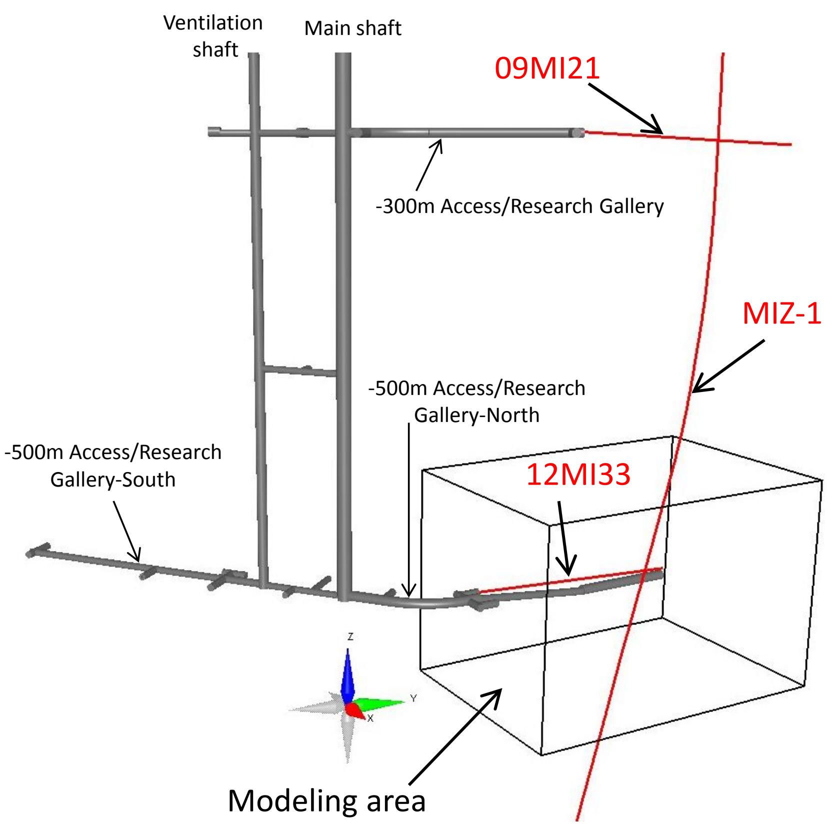

Figure 3.3 Location of monitoring boreholes around the CTD

Table 3.4 Initial condition of hydraulic pressure for numerical simulation

Borehole	Section ID	Top of section	Bottom of section	Hydraulic head (m)	Remarks
12MI33	No.1	12.1 mabh	18.9 mabh	81.8	Hydraulic packer test data
	No.2	37.1 mabh	42.6 mabh	110.2	
	No.2'	20.1 mabh	36.1 mabh	92.3	
	No.3	44.2 mabh	54.5 mabh	106.0	
	No.4	53.2 mabh	63.5 mabh	106.8	
	No.5	65.2 mabh	85.5 mabh	106.3	
	No.6	105.2 mabh	107.0 mabh	106.3	
MIZ-1	No.3	-84.1 E.L.m	-434.1 E.L.m	111.9	Long-term monitoring data (2013/3/31)
09MI21	No.1	0.0 mabh	66.1 mabh	102.8	
	No.2	67.1 mabh	77.1 mabh	111.3	
	No.3	78.1 mabh	88.1 mabh	107.8	
	No.4	89.0 mabh	103.0 mabh	111.0	
Initial condition of hydraulic pressure in the simulation area				110.0	Uniform distribution

Table 3.5 Initial condition of chloride ion concentration for numerical simulation

Borehole	Date	Monitoring point (mabh)			Cl^- (mg/L)	Average of Cl^- (mg/L)	Monitoring depth (E.L.m)
09MI21-1-21	2013/3/11	-0.6	-	66.1	198	189	-100
09MI21-2-21	2013/3/11	67.1	-	77.1	193		
09MI21-3-21	2013/3/11	78.1	-	88.1	150		
09MI21-4-21	2013/3/11	89.0	-	103.0	214		
12MI33_Pumping test _No.1(3)	2013/2/19	12.1	-	18.9	344	380	-300
12MI33_Pumping test _No.2(3)	2013/2/18	37.1	-	42.6	366		
12MI33_Pumping test _No.6(3)	2013/3/8	105.2	-	107.0	409		
12MI33_Zone 1	2013/3/18	105.4	-	107.0	431		
12MI33_Zone 1	2013/6/27	105.4	-	107.0	376		
12MI33_Zone 2	2013/6/27	85.7	-	104.5	413		
12MI33_Zone 3	2013/6/27	64.0	-	84.8	401		
12MI33_Zone 4	2013/3/19	53.8	-	63.1	327		
12MI33_Zone 4	2013/6/27	53.8	-	63.1	329		
12MI33_Zone 5	2013/6/27	44.1	-	52.9	402		
Initial condition of chloride ion concentration in the simulation area					C=-0.9553*Z+93.225 C: Chloride ion concentration (mg/L) Z: Depth (E.L.m)		

3.3.7 Boundary condition

(1) Model boundary: Hydrogeology, Rock mechanics, Chemistry

The boundary condition of the model boundary is set according to the initial condition of modeling area. The boundary condition is shown in Figure 3.4.

(2) Internal boundary of drift wall: Hydrogeology, Rock mechanics, Chemistry

Atmospheric pressure is set at the drift wall as a boundary condition of hydraulic pressure (essentially assuming 100% water relative humidity in the tunnel). The free boundary condition will be used as a boundary condition of chlorine concentration and rock stress. The boundary condition is shown in Figure 3.4.

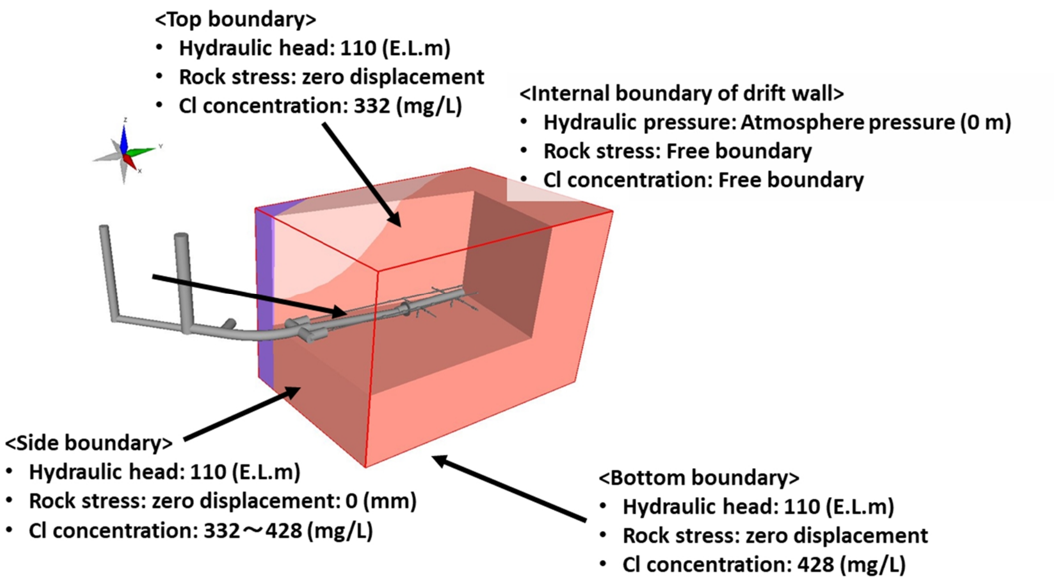

Figure 3.4 Boundary condition for numerical simulation

3.3.8 Drift excavation modeling

The excavation progress of the inclined drift and the CTD is simplified for the purposes of the numerical simulation (Figure 3.5). Drift excavation is modeled by the progressive removal of elements that form the drift according the to the excavation stage.

The total simulation term will be about 1 year; 180 days for simulation of excavation of inclined drift and the CTD, and 180 days for simulation of the post-excavation behavior.

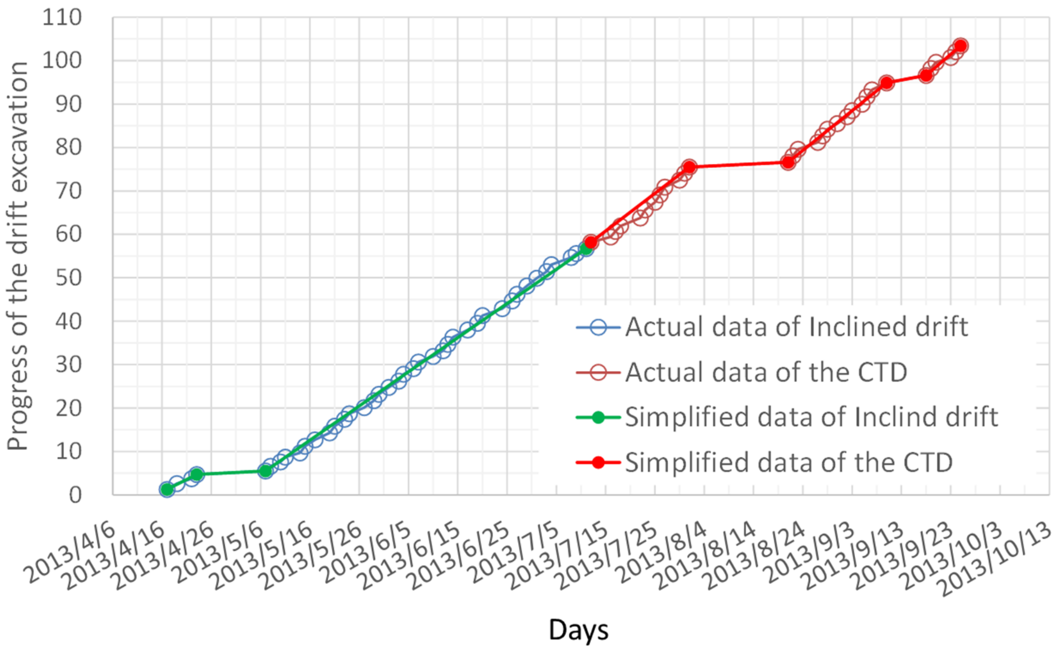

Figure 3.5 Input condition of drift excavation for numerical simulation

3.4 Sensitivity cases

Sensitivity analyses focused on the uncertainty of geological parameters and the boundary condition at Step 1 will be performed in order to understand the influence of key parameters. The results of sensitivity analyses are significantly useful information for model calibration of later steps. Sensitivity parameters are shown in Table 3.5.

3.5 Comparison of the simulation result

- Distribution of hydraulic pressure, rock stress and chloride ion concentration on the horizontal and vertical slices along the CTD will be visualized at several time steps in the numerical simulation of drift excavation.
- Disturbance of hydraulic pressure and chloride ion concentration due to drift excavation at the monitoring section of the borehole, 12MI33 will be shown graphically. The coordinate information of monitoring section in 12MI33 is shown in Table 3.6.
- Total inflow volume of groundwater from the inclined drift and the CTD after drift excavation.

3.6 For the next step

The main objective of Step 1 is to construct a reference model and to estimate disturbance of geological environment around the CTD. Validation of the result of Step 1 modeling will be carried out with a comparison between results of numerical simulation and investigation data in the next step.

Model calibration will be carried out with consideration of heterogeneity such as the distribution of fractures and EDZ around the drift. Concerning the heterogeneity of the fracture distribution in the LSFD, the information from borehole investigation around the CTD will be used. Modeling using a combination of DFN simulation from the fracture density data and representative equivalent volume (REV) method can be one avenue of investigation. In addition, hydraulic interference response during pumping test will be also available to estimate the heterogeneity in the hydrogeological model.

The EDZ area around the drift will be hopefully modeled for simulation according to the geophysical exploration data of electrical resistivity tomography (ERT) and travel time inversion (TTI) provided in Step 2, and the result of numerical simulation of Step 1.

Table 3.5 Sensitivity parameters

Sensitivity parameter		Outline
Paramters	Hydrogeology	-To understand influence of variability of hydraulic conductivity and specific storage coefficient -Several cases
	Rock mechanics	-To understand influence of variability of poisson's ratio and Young's modulus -Several cases
	Chemistry	-To understand influence of variability of porosity -Several cases
Boundary condition	Model boundary (Modeling area)	-To understand influence of boundary condition of modeling area as size of modeling area -3 cases, reference model, twice and five times the size of model
	Internal boundary of drift wall	-To understand influence of internal boundary condition of drift wall as modeling of shotcrete -2 cases: reference model, modeling of shotcrete of drift wall

Table 3.6 The coordinate information of monitoring section in 12MI33 borehole

Section ID	Top			Middle			Bottom		
	E-W(m)	N-S(m)	E.L.(m)	E-W(m)	N-S(m)	E.L.(m)	E-W(m)	N-S(m)	E.L.(m)
12MI33_P1	6445.46	-68845.50	-303.27	6445.30	-68844.80	-303.30	6445.19	-68844.00	-303.36
12MI33_P2	6448.96	-68864.90	-302.24	6447.30	-68855.70	-302.70	6445.63	-68846.50	-303.22
12MI33_P3	6452.81	-68886.20	-301.11	6451.00	-68876.00	-301.60	6449.13	-68865.80	-302.19
12MI33_P4	6454.62	-68896.30	-300.57	6453.80	-68891.80	-300.80	6452.98	-68887.20	-301.06
12MI33_P5	6456.34	-68905.80	-300.07	6455.60	-68901.50	-300.30	6454.78	-68897.20	-300.52
12MI33_P6	6464.16	-68949.20	-297.76	6460.30	-68928.00	-298.90	6456.50	-68906.70	-300.02

4. Working plan of Sandia National Laboratories (SNL) team in Step 1

Through the DECOVALEX-2019 project, the Sandia National Laboratories (SNL) team has obtained a comprehensive set of hydrologic and chemical data from a research tunnel at JAEA MIU. The data were obtained from the experiments in a research tunnel located at 500 m depth, at the MIU as part of Task C, GREET study. In addition, the analyses documented in scientific papers and technical reports will also be used. The main aim of GREET is to understand the hydrological-mechanical-chemical environment in the vicinity of the research laboratory. One of the objectives of Task C, Step 1, is to establish modeling methods and tools for analysis of excavation of the tunnel.

The SNL team will develop a general workflow or methodology to synthesize these data into a flow and transport model. Fracture data analysis and preliminary modeling analysis will be conducted at SNL as part of Task C, Step 1. The fracture data analysis will utilize fracture data collected in the research tunnel and monitoring borehole 12MI33 as well as data from the literature. A discrete fracture model will be developed based on fracture orientation, size and intensity derived from the fracture data analysis. The discrete fracture model will then be upscaled to an effective continuum model to be used in flow and transport simulations. Section 4.1 provides specific details of the fracture model development plan. The flow and non-reactive transport modeling analysis will use project data and the fracture model to construct simulation models to predict inflow into the inclined drift and the Closure Test Drift (CTD) during excavation. The modeling analysis will also predict pressure and chlorine concentration histories at observation points. The plan for the modeling analysis is described in Section 4.2. Geochemical modeling will also be conducted using project geochemical data and the PFLOTRAN code. Reactive transport modeling using thermodynamic databases will be used to predict hydro-chemical behavior in the model area.

A specific plan of activities that SNL will perform for Task C, Step 1 are detailed in Sections 4.1 to 4.3 below.

4.1 Fracture Model Development

The approach to developing DFN considers both, deterministic and stochastic fractures. The deterministic fractures are the conductive fractures observed in the research tunnel and borehole 12MI33. These fractures usually show some flow discharge. The fractures are deterministic with regard to their location defined either by traces or borehole logging data. The fracture radius can be estimated from the trace size analysis. The probability distribution of the fracture radius can be then derived based on the best fit of the data. The size of each fracture will change from realization to realization while the location will remain fixed.

The deterministic fractures will be generated in the Inclined Drift, CTD, and borehole 12MI33. The correlation between the fracture zones in the Research tunnel and borehole 12MI33 will be analyzed.

The tunnel inflow data will be used to estimate mean fracture transmissivity. The relationships will be developed to describe fracture permeability and aperture as a function of fracture radius. The transmissivity of generated fractures should be close to the transmissivity estimated from the packer tests in borehole 12MI33.

The tunnel and borehole fracture data will be used to determine the number of fracture sets and to define the corresponding fracture orientation distributions. Fracture volumetric intensity will be estimated by matching the linear intensity of generated fracture with the linear intensity of the observed fractures.

The stochastic fractures will be generated outside the Research tunnel and borehole 12MI33 using the orientation distributions and volumetric intensity values obtained in the analysis.

The resulting DFN will include deterministic and stochastic fractures. The DFN will be upscaled to an equivalent continuum model using Oda's method [11), 12)]. The anisotropic effective permeability (Kx, Ky, and Kz) and effective porosity fields will be used in the flow and transport simulations.

At first, a few realizations of the upscaled DFN will be considered. The goal of these preliminary simulations will be to match the inflow in the Inclined Drift and CTD. The further development will focus on matching pressure and chlorine concentrations in the monitoring points of 12MI33.

Finally, multiple realizations will be considered and the effects of connectivity and other parameters will be addressed.

4.2 Flow and Non-Reactive Transport Modeling

SNL will develop flow and non-reactive transport models using geometry and hydrology data described in Section 3.

4.2.1 Homogenous Model

Simulations will be conducted assuming a homogenous system using uniform properties. This will allow familiarization with the modeling effort and generate output that can be directly compared with experimental data and the work of other teams. Data for hydraulic parameters given in Table 3.1 will be used for the homogenous model.

Simulations will first start with the CTD-Scale modeling domain which covers the visualization area described in Section 3.3.1 and Figure 2.4. A uniform fine mesh will be used for this case. The boundary of the CTD-Scale domain is close to the inclined drift. A larger domain will then be used to check the boundary. Mesh size for this domain will be progressively increasing away from the tunnel. The simulation domain will include the monitoring sections in Borehole 12MI33 to provide pressure and chlorine concentration history for each modeling case. The coordinates of the monitoring sections given in Table 3.6 will be used.

The boundary and initial conditions used will be as described in Section 3.3.7. Head data will be converted to pressure for ease of use and to compare results with other teams. Hydrostatic pressure conditions will be applied using the domain top and bottom boundary values. A chloride concentration gradient will also be applied to the domain based on domain top and bottom boundary values. For the larger domain, initial and boundary conditions will be extended to fit the increased size.

Simulations will be conducted using PFLOTRAN, an open source, state-of-the-art massively parallel subsurface flow and reactive transport code [13)] in a high-performance computing environment. The simulations will include drift excavation modeling described in Section 3.3.8. The excavation progress data given in Figure 3.5 will be used to set the modeling process. Simulations will be carried out by progressively removing tunnel material. Outputs of pressure and chloride concentration history at observation points and inflow into the inclined drift and the CTD will be reported. The outputs will be compared to measured data. Note that the current modeling work did not include rock mechanics.

4.2.2 Fracture Model

Modeling will also be conducted using the fracture model described in Section 4.1. DFN permeability and porosity data will be upscaled to a continuum model to generate permeability and porosity fields. The CTD-scale domain will be used for this exercise with the same mesh as for the homogenous model. The initial and boundary conditions will be the same as described in Section 4.2.1. Modeling of excavation progress described in Section 4.2.1 will be followed. Outputs of pressure and chloride concentration history at observation points and inflow into the inclined drift and the CTD will be reported. The outputs will be compared to measured data and to that of the homogenous model.

4.3 Geochemical Modeling

SNL has expertise on the use of computational tools in the application of geochemical modeling to interactions of solution and minerals. Clay and cement are ubiquitous materials in Engineered barrier system (EBS) design concepts whose behavior is to long-term repository performance. Clay minerals play key roles in the geologic disposal of nuclear waste as the main host rock mineral in a shale repository but also as a key component in EBS design concepts. Cementitious materials and associated solids are used as backfill/buffer, seals, plugs, and linings in tunnels and disposal galleries. The interaction of cementitious solids with other barrier materials and aqueous fluids in the near-field environment is important to the generation of alkaline solutions that can aggressively react with silica-bearing phases and other EBS materials. The inherent chemical complexities of these phases require robust tools to represent these interactions but also critically assessed thermodynamic data inputs in these models [14), 15)].

The proposed geochemical modeling approach is to:

- Study previous work on the aqueous chemistry trends and other geochemical correlations in the groundwater site data monitoring. An extensive groundwater hydrochemistry characterization studies have been carried out by the JAEA [16), 17)]. These studies will provide the required groundwork in the geochemical assessment of groundwater chemical variability and the effects of perturbations as a result of tunnel/shafts construction operations. One important aspect is the hydrochemical characterization of host-rock source waters and interactions with barrier materials. A subsequent aspect of this collaboration is the geochemical analysis of waters from monitoring of the CTD.
- Evaluate geochemical groundwater data analyses for representative samples and conduct geochemical modeling such as aqueous speciation and overall mineral saturation state consistent with host rock mineralogy. The computer codes EQ3/6, CHNOSZ, and Cantera / Zuzax along with thermodynamic databases will be utilized for this analysis.
- H-C (Reactive-transport) modeling will be explored using the PFLOTRAN massively parallel subsurface flow and reactive transport code along with a thermodynamic database that includes relevant cement and clay phases. An initial 1D / 2D H-C model can be envisioned to scope host-rock/groundwater interactions from sampling boreholes leveraging from the geochemical assessment described in the two previous bullets.
- The mechanical capability in PFLOTRAN can be potentially explored for the H-M-C aspect of this problem. However, that would depend on further analysis of available data and the extent of the coupling, plus acknowledging that geomechanics are at an early stage of implementation within the PFLOTRAN code.

5. Working plan of Technical University of Liberec (TUL) team in Step 1

5.1 Modeling strategy and approach

The H-M-C changes during the construction of inclined and closure tunnel will be simulated as separate processes at the beginning of the project and extended to a coupled form as work progresses. The work will be concentrated on hydraulic and chemical processes, with the possible addition of mechanics in the later stages. For the flow and transport modelling, in-house developed open-source simulation code Flow123d will be used, employing its features of the discrete fracture network and continuum coupling [18] amongst other capabilities.

5.2 Objectives

The objectives follow the described purpose of the task and JAEA plans to understand the observed data related to disturbance of the rock and water by excavation.

5.3 Simulation condition, Model setting

5.3.1 Simulation area

The reference case is the recommended domain in the assignment (Figure 2.4). Besides this, a large-scale model will be used, for a general understanding of the site and to evaluate proper boundary conditions for the reference model.

5.3.2 Geological unit

As given: The whole domain of focused area is located in the lower sparsely fractured domain (LSFD). The level of structural detail will be various, with options specified below (5.5.1).

5.3.3 Parameters

(1) Hydrogeology

Hydraulic conductivity and specific storage measured in a borehole are preferred for defining parameters, considering also more general ranges resulting from all the site boreholes. In case the data for a discrete fracture will not be provided directly, they will be derived from the borehole pressure test considering the intersections of particular borehole interval and fractures.

(2) Rock mechanics

For later use: Elastic modulus, density, porosity, Poisson's ratio, etc. measured from local core samples are preferred for parameters definition.

(3) Chemistry

The thermodynamic database is included in the simulation software. For transport, porosity will be used from experimental data (if available), and dispersivity from the general literature.

5.3.4 Initial conditions

(1) Hydrogeology

The measured hydraulic pressure at the borehole in the vicinity of the experiment drift will be used to specify the initial groundwater pressure condition. Uniform initial pressure or initial pressure linearly changing according to the depth will be tested, or replaced by a hydraulic model of the whole site.

(2) Rock mechanics

The measured rock stress is to be used for the initial condition. Uniform initial pressure or initial pressure linearly changing according to the depth will be tested.

(3) Chemistry

The chemical composition of groundwater as an input is to be defined during the Stage 1, based on the profiles observed in boreholes.

5.3.5 Boundary conditions

(1) Model boundary: Hydrogeology, Rock mechanics, Chemistry

The boundary conditions will be based on a large-scale hydraulic model or simplified to a uniform or linearly changing field derived from the depth and the exploration borehole profile. It will be mostly used to define the prescribed head and groundwater chemical composition.

(2) Drift wall: Hydrogeology, Rock mechanics, Chemistry

The zero pressure will be set on the drift wall as a boundary condition of water head (essentially 100% relative humidity at approximately atmospheric pressure). Zero dispersion flux, i.e. advective only transport, will be prescribed for the chlorine transport during drainage. The prescribed concentration from measurement will be used during flooding. The free boundary condition (zero traction) will be used as a boundary condition of displacement.

5.3.6 Drift excavation modeling

In most cases, the excavation will be represented by a time varying boundary condition (no flow before excavation and zero pressure after excavation, this could be possibly be made in a continuous sense in the software). If necessary, different geometries with coarse steps of changing void size will be applied.

5.4 Output of simulation

The distribution of water head and rock stress on the horizontal and vertical slice along the closure tunnel will be visualized at several time steps in the numerical simulation.

The time variation of change in water head, rock, and chemistry at the location of monitoring borehole will be plotted.

5.5 Details

5.5.1 Hydraulics

In-house developed software Flow123d will be used, which is based on multidimensional conceptual model (combining 3D continuum and 1D/2D fractures) and mixed-hybrid finite element solution, with discretization either in tetrahedrons or triangles. The phenomena are unsteady flow, variably-saturated flow, multicomponent transport, simple reactions (decay, sorption). An interface to geochemical codes is in development.

The initial step will be understanding of the long time borehole pressure evolution: Model of site scale (approx. km) will be prepared, with the simplified geometry of excavation (main shaft, experiment tunnel as straight lines or cylinders), considering gradual excavation in time. In this way, we expect to detect main inhomogeneity, necessary to establish boundary communication of the local model (reference geometry around GREET Figure 2.4). Given hydraulic conductivities related to geological units will be verified through the excavation inflow rates and comparison of the model results and the borehole pressure monitoring.

Next, the reference geometry model will be solved based on the given assignment, i.e. prediction of the GREET excavation effect in term of pressure/head temporal evolution. We will conduct modeling in gradual steps from simpler to more complex models (an introductory part supposed to be made Oct-Nov 2016)

- From uniform (hydrostatic) boundary conditions, through 12MI33 borehole data regression (extrapolation), to general spatial distribution resulting from the large-scale model
- From homogeneous to use of structural data: First, the inhomogeneity will be based on zones used for 12MI33 hydraulic testing. During calibration, discrete fractures based on tunnel wall mapping and borehole logging will be added.

The hydraulic models will be also validated by the tracer and geochemical data (origin of water, flow direction, residence time, mixing).

Before the modeling, there were several preparation steps of data understanding for the first months of the project (Jul-Sep 2016): a conceptual model of pressure monitoring reaction on excavation progress, distribution of pressure along boreholes, the variability of permeability, relation to tracer and geochemical data.

5.5.2 Transport (water origin and residence time)

The available data of natural tracers in the water sample analyses (oxygen and hydrogen stable isotopes, tritium, radiocarbon) will be studied, e.g. plotted to understand the spatial distribution and time evolution. It will be used as a background for the hydraulic and chemical model. Initial investigations of the natural tracers ^{2}H, ^{18}O, ^{3}H and ^{13}C, it seems that the water is a combination of several thousand years old water and some amount of meteoric water, or water from only a few decades old. The hydraulic model, especially any inhomogeneous concept, would be checked to be in accordance with this observation. Also, the mixing interpretation of chemical composition analysis can be compared to the tracer data.

The transport model in the CTD scale will initially use chlorine as a non-reactive tracer, using its natural concentration vertical gradient. If the reactive transport model is to be used for temporal chemical composition changes resulting from excavation, it will constructed based on the chlorine model. It will provide the calibrated transport data like porosity (eventually scale-dependent) and dispersity on a simpler case, before adding the reaction effects.

The simulation will be made in Flow123d together with hydraulics (3D), or as part of detail reactive-transport models (below) in The Geochemist's Workbench (GWB).

5.5.3 Chemistry (reactions, water-rock interaction)

The work is composed of data analysis/understanding and of predictive simulations. Data analysis is expected to be a substantial part of the introductory phase of the project. The commercial software The Geochemist's Workbench (GWB) will be used.

The particular steps are the following

- Understanding site configuration, borehole placement, type of data.
- Processing of geochemical data:
  - definition of basic groundwater types, finding key differences between groundwater types
  - evaluation of temporal and spatial distribution for physicochemical parameters and chemical components concentrations
  - finding differences between original (natural) and disturbed conditions that developed during the building of the MIU
  - finding a relationship between the rock type and the groundwater type (if any exists)
  - comparing results to geochemical conditions in Czech granite sites.
- Identification of the main processes that determine the chemical composition of individual water types.
- Modeling of water-rock equilibrium:
  - the purpose of this stage is to define reference conditions before excavation disturbance as well as a need to check a consistency of data (e.g. charge balance)
  - comparing geochemical model outputs with real conditions developed at MIU site
  - special attention will be paid to the in situ measured redox potential and its relation to the redox sensitive groundwater components.
- Defining the key points (physico-chemical parameters, groundwater chemical composition) which the system of groundwater-rock will pass over the opening, operation, closure and flooding at the MIU site as input parameters for reactive-transport modeling.
- A dynamic model of geochemical change during excavation later in the proposed work. More options depending on quantitative condition are considered: In case of dominant transport, 1D reactive-transport models will be used. In case of dominant reaction (dissolution/precipitation kinetics), it will be approximated as a batch experiment with changing water composition. Additionally, a suitable model of impact of oxygen in the rock will be tested (e.g. some simplification by means of sensitivity study).

6. Results of Step 1 modeling (JAEA)

6.1 Discretization of model domain

Figure 6.1 shows the mesh used for finite element modelling. The total number of nodes and hexahedral elements are 145,440 and 136,560 before the excavation of inclined and CTD tunnel and 145,680 and 137,040 at the end of excavation. We model the tunnel excavation by removing the elements located at tunnel step by step and the number of elements and nodes change during simulation. The number of element is decreased for the modeling of step by step according to the exaction history for the simulation of excavation. The size of whole calculation domain is 317.858 × 213.25 × 208.25 that is larger than focused domain described in section 3 to avoid the boundary effects.

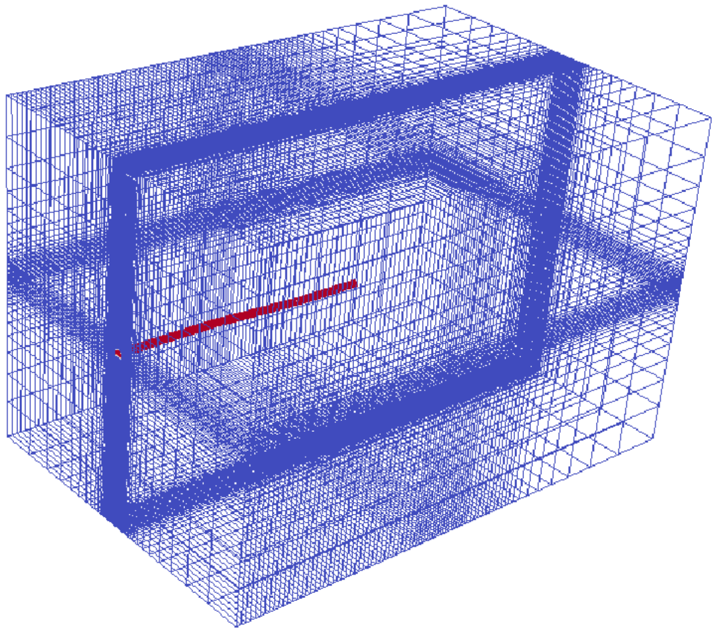

Figure 6.1 Mesh for simulation

6.2 Prediction results of the disturbance during the excavation of CTD using the homogeneous continuum model

In this section, we calculate the time variation of hydraulic pressure, displacement and chlorine concentration for the prediction of disturbance due to the tunnel excavation. The details of parameters, constitutive models and boundary condition are as described in Chapter 3. In addition to the simulation with the basic model, we also perform a sensitivity analysis with the hydrogeological model.

6.2.1 Spatial distribution of hydraulic pressure, displacement and Cl concentration around the CTD

Figure 6.2 shows the spatial distribution of hydraulic head. Simulation results before excavation of research tunnel, the end of excavation of the incline and at end of excavation of closure test drift are shown, respectively. In each column, two horizontal sections and a vertical section including CTD are shown. Hydraulic pressure drops around the tunnel and the area expands according to the length of tunnel excavation concentrically due to the homogeneous hydraulic properties.

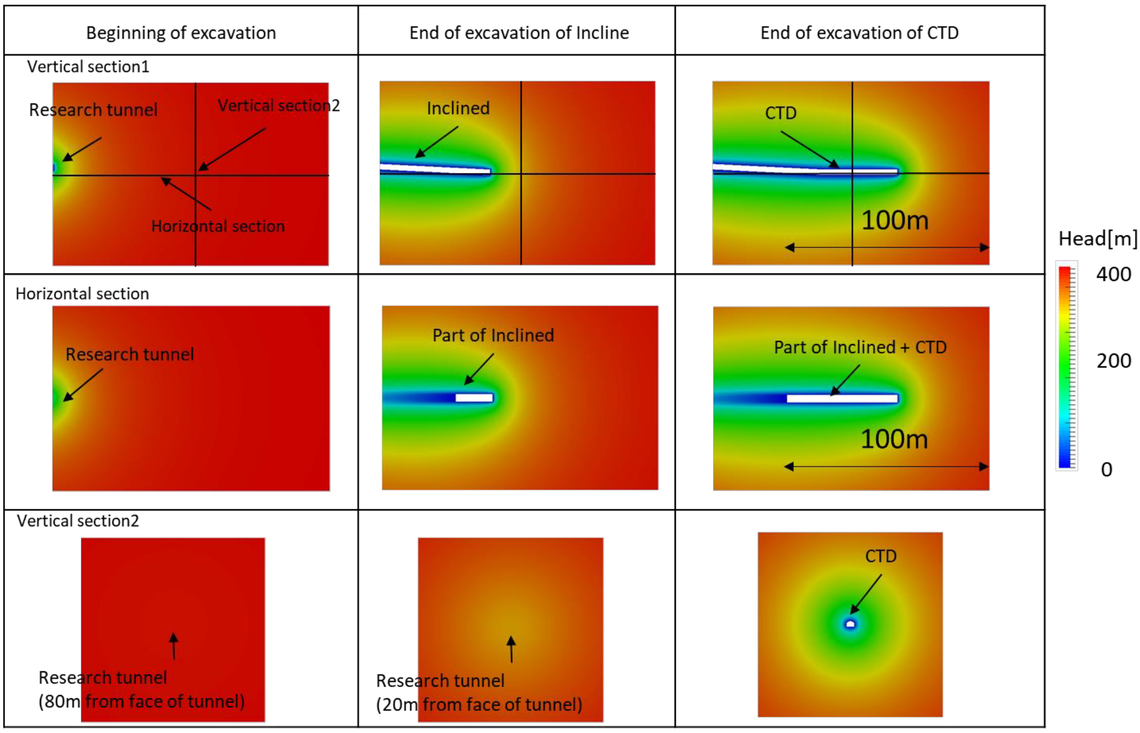

Figure 6.2 Spatial distribution of hydraulic head.

Figure 6.3 shows the spatial distribution of displacement. These results are arranged in the same manner as those of hydraulic pressure. Compressive deformation occurs by excavation of the research tunnel. We perform coupled simulation of the hydro-mechanical problem and these deformations are affected by both effects of the release of stress according to the excavation of tunnel and change of pore pressure. The largest deformation appears at the tip of tunnel face during excavation.

Figure 6.4 shows the spatial distribution of Cl concentration. For this simulation, we do not employ Couplys due to numerical accuracy issues, but use the original Dtransu code that consists of Couplys and open source simulator for the advective-diffusive problem by Eulearian Lagrangian method.

The distribution of concentration around tunnel is slightly affected by excavation of the tunnel. Groundwater flow towards the research tunnel advects the chloride ions. Both low and high concentration zones move to tunnel slightly by this flow. Around the floor of the entrance of the inclined tunnel, a high concentration zone appears. In addition, a low concentration zone also appears at the entrance of CTD. It is estimated that high and low concentrations are influenced by the setting of the time step for simulation. In other words, convergent of simulation could be not sufficient. Shorter time steps would be needed to set for the removal of these overestimates and higher accuracy estimation there.

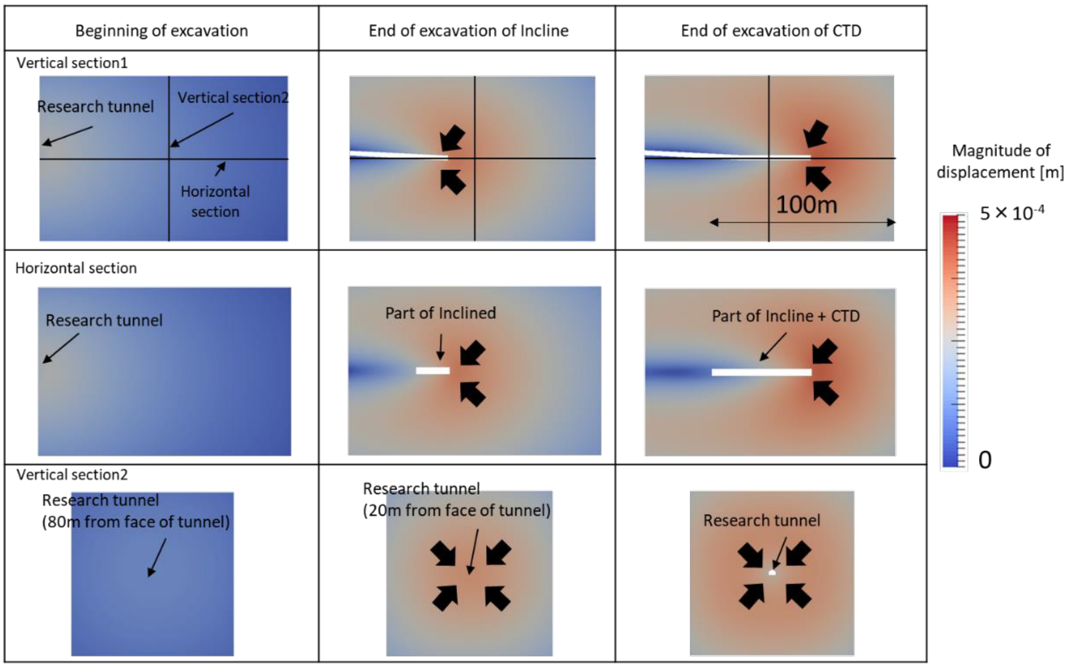

Figure 6.3 Distribution of displacement.

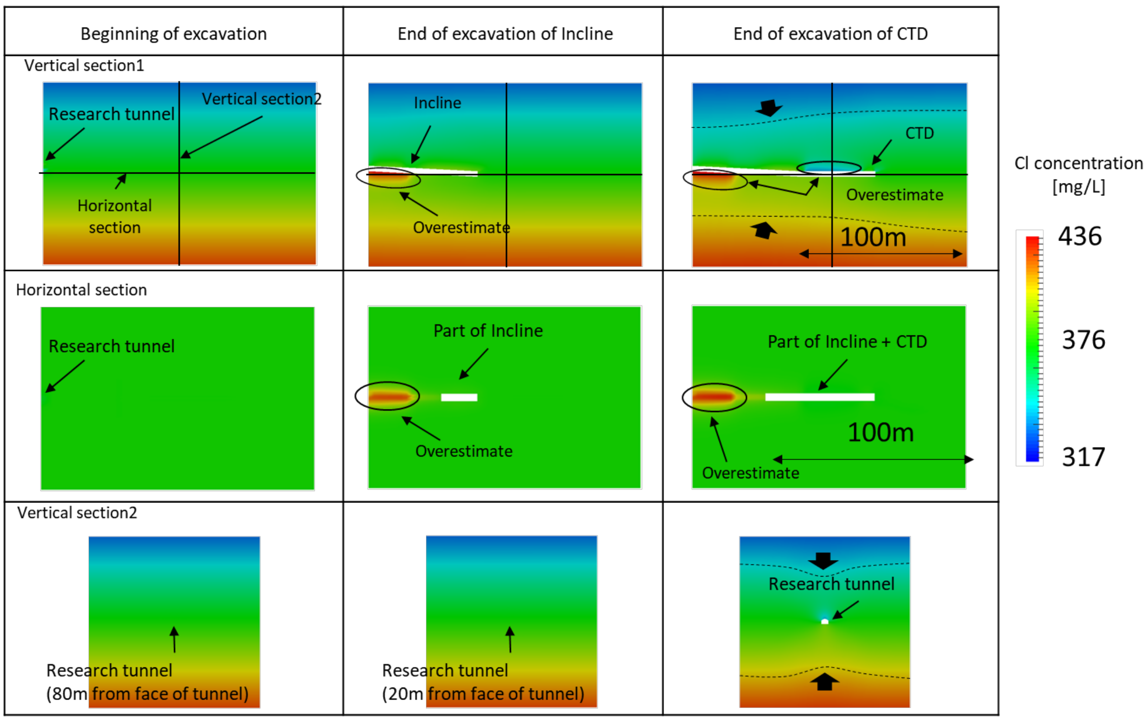

Figure 6.4 Distribution of chlorine concentration.

6.2.2 Time variation of hydraulic pressure and Cl concentration in 12MI33 borehole and its sensitivity to hydraulic properties

Observation data on the drawdown of hydraulic pressure in Borehole 12MI33 during excavation has been recorded. For the comparison of simulated predicted drawdown and observed data, the time variation of predicted hydraulic head is shown in Figure 6.5. Borehole 12MI33 has 6 observation sections separated by packer for monitoring, and each section has a length of several meters. Predictions of hydraulic head at the closest points to the middle points of each section are shown.

The arrows in Figure 6.5 indicate the timing when the tunnel face reaches the horizontal location of each monitoring point. Predicted hydraulic pressure starts to decrease before the tunnel edge reached the horizontal location of monitoring point and continues to decrease until the hydraulic pressure declines to 1.6MPa. The drop of hydraulic pressure at sections 1 and 2 do not decrease to 1.6MPa and the final hydraulic pressure would depend on the distance from the tunnel end in this case.

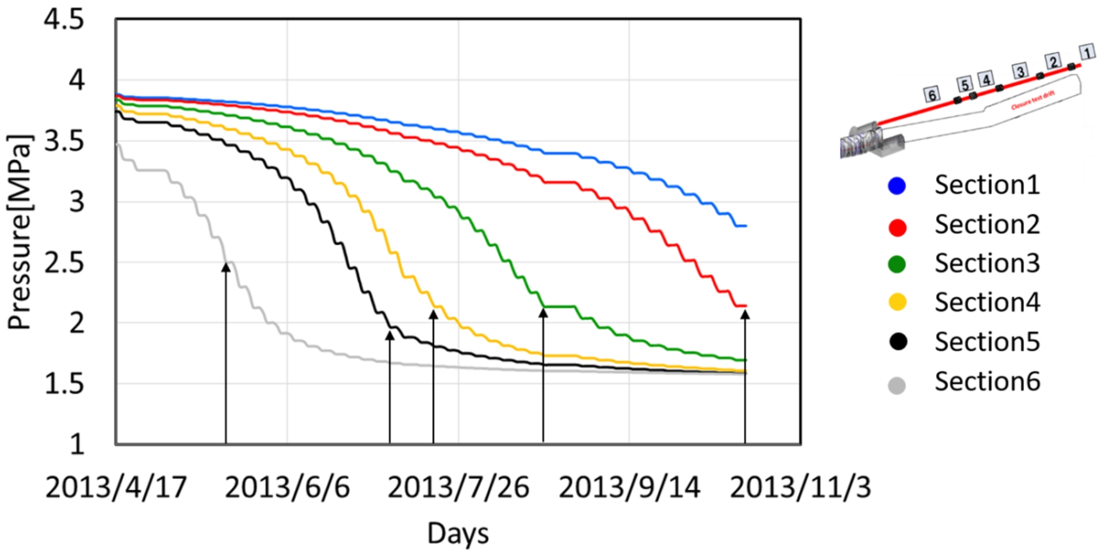

Figure 6.5 Time variation of predicted drawdown in 12MI33.

Figure 6.6 shows the results of the sensitivity of hydraulic pressure in each monitoring point to the value of physical properties. Both sensitivities of hydraulic conductivity and specific storage are evaluated. In addition to the homogeneous model case, a model that consists of rock-mass and shotcrete is evaluated. Shotcrete with the thickness of about 5 to 10 cm was implemented immediately after the drift excavation. This model has two physical properties representing the rock-mass and shotcrete. Elements of 1 layer are set to 100 times lower permeable than rock-mass to consider the skin effect of shotcrete. In the simulation, hydraulic conductivity of elements that corresponds to the shotcrete is extended step by step same speed as the excavation of research tunnel. We assigned just one layer to shotcrete and the thickness is 0.625m~1.75m. The variation of thickness comes from the discretization with different element size. We set the thickness of shotcrete the value due to the computational limit though the actual thickness of shotcrete is several centimeters.

When the subsurface structure is homogeneous where the effect of shotcrete is ignored, all results show the same responses to both hydraulic conductivity and specific storage. Therefore the decrease of hydraulic pressure in the borehole is almost entirely controlled by the boundary condition.

When the skin effect of shotcrete is considered, low permeable layer blocks the decrease of hydraulic pressure and the change of hydraulic pressure is reduced at most about 0.2 MPa. This is because pressure gradient in low permeable shotcrete is much larger than one in surrounding rock to conserve the continuity of Darcy's velocity through the gap of hydraulic conductivity with 100 times contrast. Boundary condition limits the change of pressure between model boundaries and drift boundary to 4 MPa. Nearly 4MPa divergence of hydraulic pressure occurred within the shotcrete layer in this case. As a result, the pressure at monitoring point located outside shotcrete layer remains high. This predicted result suggests that the skin effect of shotcrete significantly affects the hydraulic pressure change in the monitoring sections.

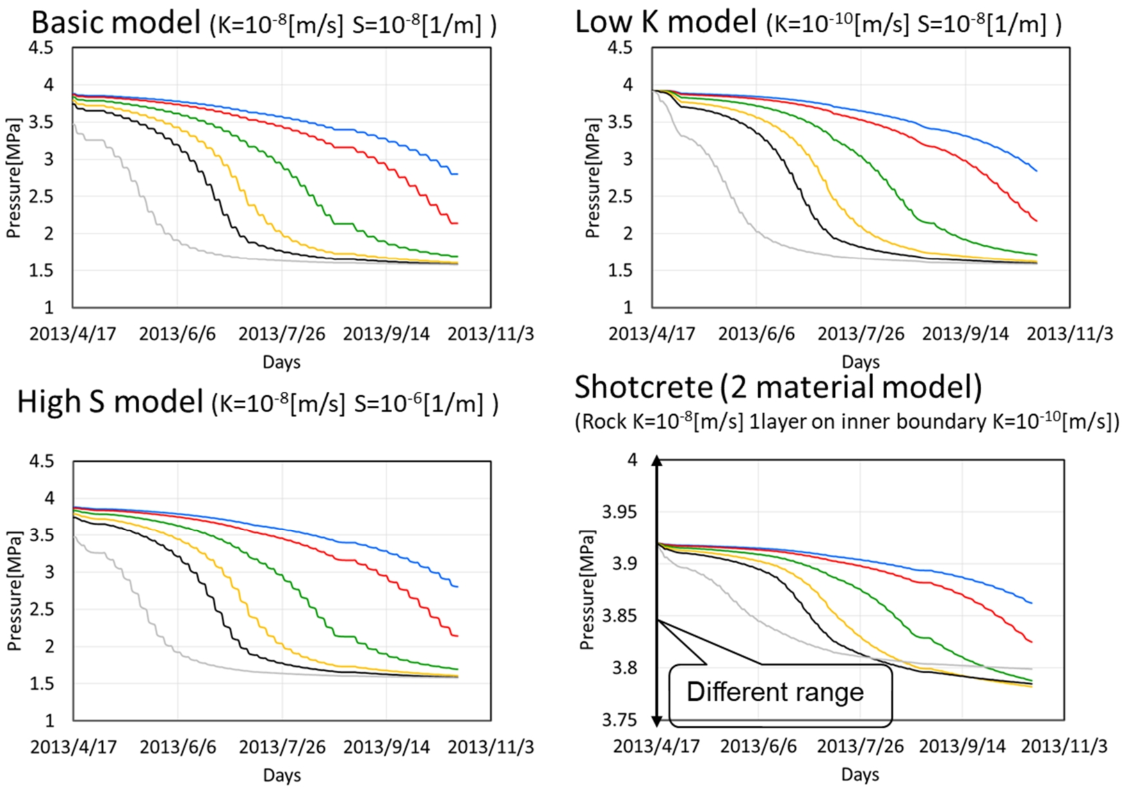

Figure 6.6 Sensitivity of hydraulic properties for the drawdown.

Figure 6.7 shows the predicted time variation of chlorine concentration in 12MI33. The arrows in the graph indicate the timing when the tunnel edge reaches the monitoring point horizontally as with the graph of Figure 6.5. The chlorine concentration starts to change according to the excavation of the tunnel. The fluctuation of Cl concentration is delayed compared to the drawdown of hydraulic pressure in monitoring points. Although the simulated Cl concentration shows the deviation during the tunnel excavation, the change is slight. The groundwater with similar salinity to that around the tunnel moves horizontally from the surrounding rock to the monitoring points located parallel to the tunnel. Therefore, there is no noticeable change in salinity of the groundwater.

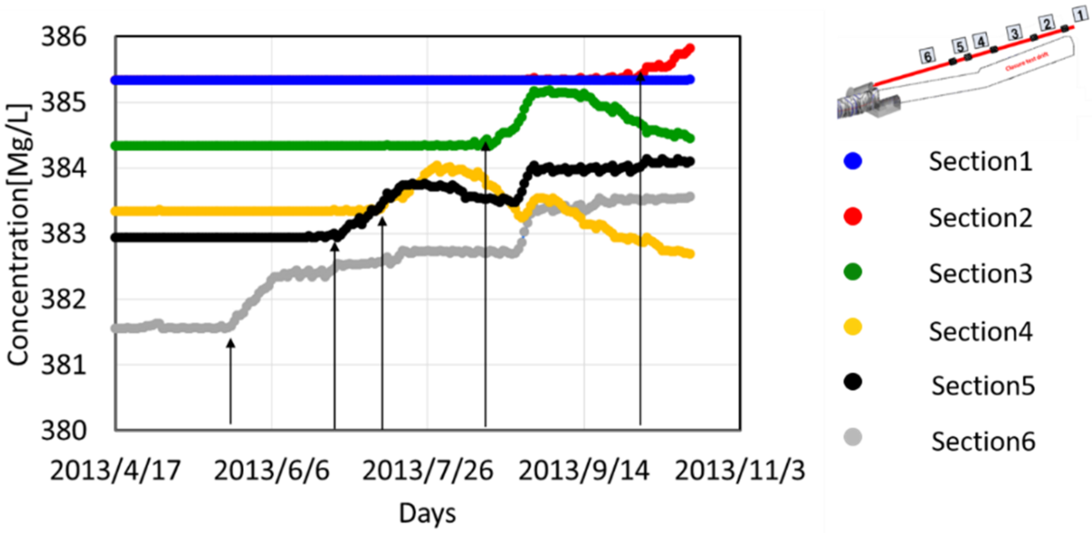

Figure 6.7 Time variation of Cl concentration in 12MI33

6.2.3 Inflow into inclined tunnel and closure test drift

The time variation of inflow rate into these drifts are shown for the comparison with predicted results. Figure 6.8 shows the predicted time variation of inflow during excavation at the inclined drift, CTD and both. The inflow rates increase as the excavation progressed. The inflow rate is proportional to the hydraulic conductivity as shown in the results of the homogeneous model case with a basic model and low hydraulic conductivity model. This is because that the distribution of hydraulic head is controlled by boundary condition as shown in the results of pressure decline and the groundwater flow velocity only reflects the value of hydraulic conductivity according to Darcy's law. When the skin effect is considered, inflow rates decreases compared to the basic case because low permeable layer blocks the flow into the tunnel. Modeling of skin effect influences both drawdown and inflow prediction significantly. The comparison of these simulated results with observed data is compiled at 6.7.

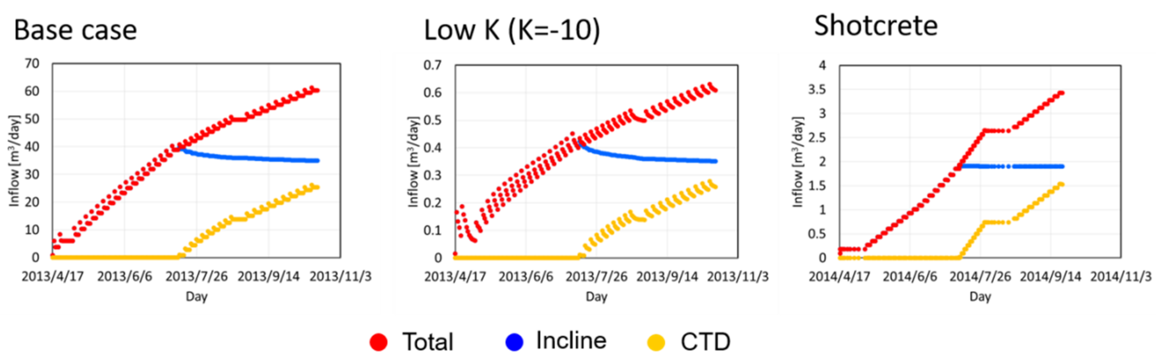

Figure 6.8 Prediction of results inflows into the tunnel.

6.2.4 Summary of prediction results

In this step, we performed a hydro-mechanical and advective-diffusive simulation to predict a disturbance due to the excavation of research tunnel as the first step. For the purposes of prediction, we set the model and simulation conditions from data observed before the tunnel excavation. The summary of our simulation results are as follows:

- The level of drawdown in 12MI33 does not depend on K and is controlled by boundary condition when the structure is homogeneous. The boundary condition limits the range of pressure drop between outer and inner boundaries and pressure gradually change between them. Gradient of hydraulic pressure is also independent on K in this situation. Therefore, K can not be evaluated from pressure distribution but be estimated from the inflow rate into the CTD because inflow rate reflects the Darcy's velocity that is product of K and pressure gradient (Figure 6.6).
- The influence radius of disturbance of hydraulic head due to the excavation of CTD is about 50m from CTD and does not grow according to the extension of CTD. Note that the calculation domain is enough large to avoid the boundary effects (Figure 6.1).
- Variations of Cl concentration do not show a significant change during the excavation of CTD comparing to the range of Cl concentration given as an initial condition. Stronger advection such as channel flow would be necessary to lead the high and low concentration around the model boundary to the monitoring borehole along the tunnel.

6.3 Prediction results of the disturbance during the excavation of CTD using the heterogeneous continuum model

JAEA made heterogeneous continuum (equivalent continuum porous media; ECPM) model based on discrete fracture network (DFN) models. This section describes methodology and result of DFN modeling, conversion of the DFN to ECPM model, and simulation predictions.

6.3.1 Construction of DFN model and ECPM model around the CTD

(1) Estimation of parameter set and DFN modeling

Table 6.1 shows used data for estimating the parameter set needed to make the DFN model. Our simulation aims to know how to predict (or to what extent we can predict) the subsurface phenomenon prior to an actual facility construction phase. For this purpose, we used the data obtained before excavation of the tunnel. Fracture orientation distribution, permeability distribution, and three-dimensional fracture frequency (P_{32}) were estimated based on data from 12MI33 borehole investigations. Fracture radius distribution was estimated by outcrop and lineament data obtained from the surface investigation because this cannot be obtained by borehole investigation. For the estimation of fracture radius, we follow the strategy of the previous study [19] that are different from Sandia's strategy in Section 7. Table 6.2 shows the result of the estimated parameter set. Each estimation methods described below.

Table 6.1 Date for estimating the parameter set

Parameters	Data
Fracture orientation distribution	BTV* of 12MI33
Fracture frequency (P_{32})	BTV* and core logging of 12MI33
Fracture radius distribution	Previous data (Outcrops and lineament at surface)
Transmissivity distribution of fractures	Hydraulic packer test of 12MI33

* BTV means Borehole Television observation.

Table 6.2 Parameter set for simulation

Set	Orientation (Bingham distribution)				P_{32} (m^2/m^3)	Radius (Power-low distribution)	Transmissivity Distribution
	Pole-trend	Pole-plunge	k1	k2			
1	334.39	0.92	-19.50	-7.30	0.08	Dr = 2.7 r_{min} = 1.0	m = -8.4 σ = 1.0 C = 2.3
2	19.14	0.05	-12.00	-4.95	0.22		

a) Fracture orientation distribution

Figure 6.9 shows orientations of each fracture which observed in BTV investigation and core logging of 12MI33. 78 out of 297 fractures are identified as an obvious open fracture. The remaining fractures, which are hair cracks or very thin fractures, are omitted in this analysis because some of those fractures would not be counted in data and bias the stochastic analysis. The fracture orientation distributions were regressed on the Bingham distribution and they were classified into two groups by using ISIS function of FracMan® version7.

b) Three dimensional fracture frequency (P_{32})

P_{32} of each set observed by the 12MI33 investigation was calculated by (6.1) and (6.2).

$$P_{32} = \frac{\sum area}{volume} = \frac{\sum \pi r_1 r_2}{l \pi r_1^2} = \frac{\sum \pi r_1 f_{Terz}}{l \pi r_1^2} = \frac{\sum f_{Terz}}{l} \qquad (6.1)$$

Where r_1 is the minimum length of fracture surface intersected with the borehole, r_2 is the maximum length of fracture surface intersected with borehole, f_{Trez} is the Terzaghi weighting, and l is the borehole length [20), 21)].

$$P_{32[r>r_{min}]} = P_{32[r>r_0]} \left(\frac{r_0}{r_{min}}\right)^{(k_r-2)} \qquad (6.2)$$

Where, $P_{32}[r>r_{min}]$ is the P_{32} of all fractures with r greater than the size r_{min}, $P_{32}[r>r_0]$ is the P_{32} of all fractures with r greater than the size r_0, r_0 is the minimum fracture radius of base data (this study assumes r_0 is the borehole radius of 0.125 m), r_{min} is the minimum fracture radius for DFN model (this study sets r_{min} is 1.0 m), and k_r is the exponent of fracture radius distribution.

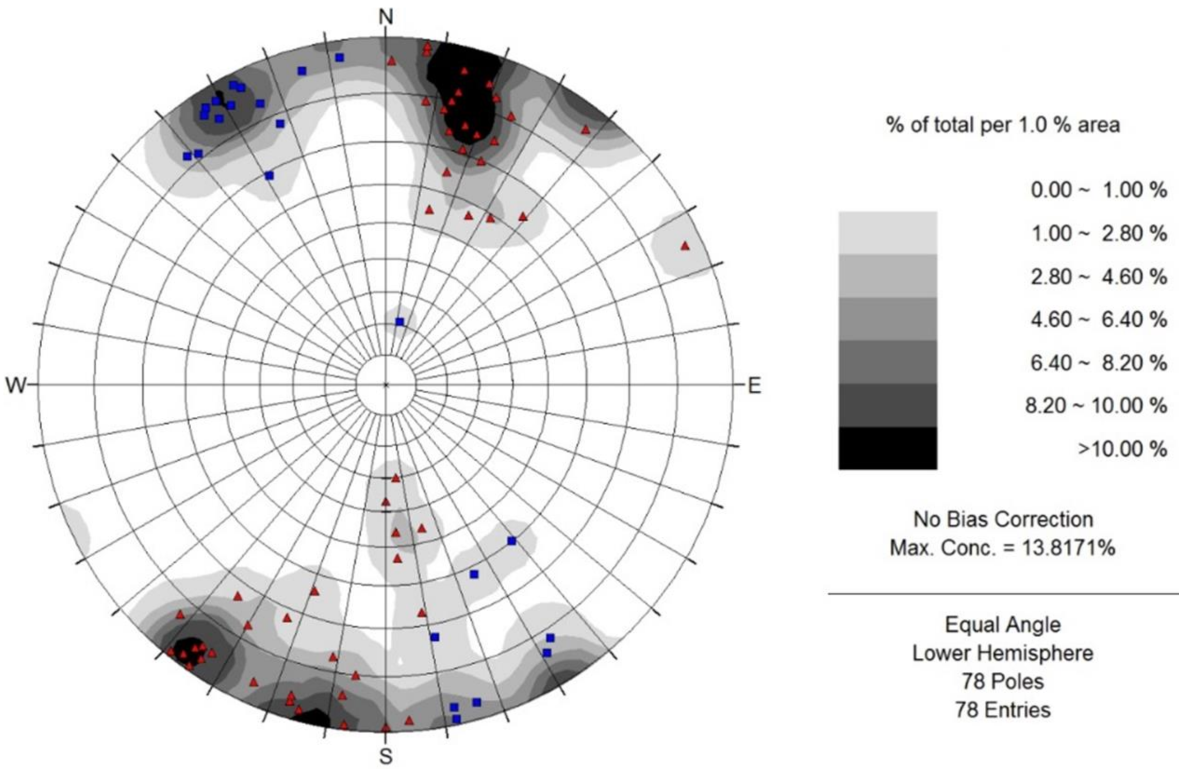

Figure 6.9 Equal angle lower hemisphere stereo net of the 12MI33 fracture poles and fisher concentration plot. Blue quadrangle dot shows Set1 and red triangle dot shows Set 2 for DFN model.

c) Fracture radius distribution

The fracture radius distribution was estimated using previously collected data (outcrops and lineaments based on surface investigations; Figure 6.10). We assumed fracture radius distribution shows a power-low distribution based on the previous study [22]. Scaling exponents of outcrops and lineaments show 1.75 and 1.72 respectively. The equation 6.3 shows the relationship between scaling exponent of fracture radius distribution (Dr) and fracture trace length distribution (Dt). Thus, a scaling exponent of fracture radius distribution was set to 2.75. In the relationship between trace length and CDF (Figure 6.10), all data fit the linear regression curve (approximated CDF) and dispersion from the line that indicates the independent component from the approximated CDF does not appear. Therefore, we used only one CDF of fracture radios for all fracture set.

$$D_r = D_t + 1 \qquad (6.3)$$

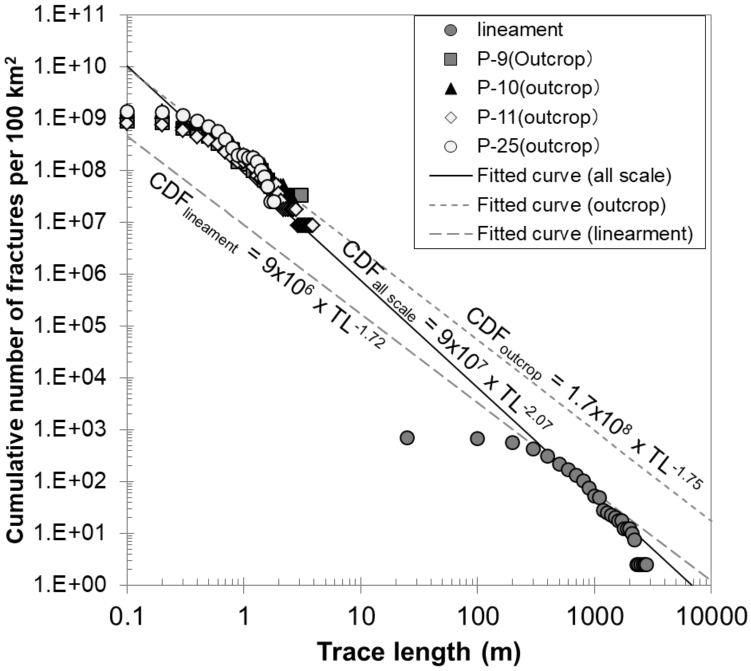

Figure 6.10 Cumulative number of fractures of outcrops and lineaments per 100 km² around MIU site [19]. Note the P-9, P-10, P-11 and P-25 in legend indicates the name of the dataset (Not mean characteristics of DFN such as P32).

d) Transmissivity distribution of fractures

The transmissivity of fractures was estimated by regression analysis of cumulative distribution function (CDF) in hydraulic conductivity. The results of hydraulic packer test of 12MI33 are compiled as a CDF that consists of six points (shown by red dots in right picture of Figure 6.12) and then the CDF is approximated by the CDF derived from the virtual well test with DFN models.

We assume fracture radius and its hydraulic transmissivity correlate with variability (6.4), then decide the unknown parameter, μ and C, in (6.4) to relate fracture radius to transmissivity,

$$T = lognorm(\mu,\, \sigma) \times r^C \qquad (6.4)$$

where T is transmissivity, μ is mean in the natural logarithm distribution, σ is a standard deviation in the natural logarithm distribution (this study assumed σlog10 = 1.0), r is the fracture radius, C is exponent value. The virtual well test was conducted as steady flow simulation, outside boundary condition is the constant head (0.0 m), and test section boundary condition (virtual borehole which length (13.3m) is the average length of monitoring section in12MI33) is the constant head (1.0 m; Figure 6.11). We calculated the transmissivity or hydraulic conductivity in the virtual test according to the Thiem's theory (Eqs. 6.5 and 6.6) and simulated inflow,

$$T = \frac{Q\, ln\left(R/r_w\right)}{2\pi\, \Delta h} \qquad (6.5)$$

$$K = T/L \qquad (6.6)$$

where T is transmissivity, Q is flow rate, R is the radius of influence, r is the radius of the borehole, Δh is a drawdown, K is hydraulic conductivity and L is the length of simulated inflow width. At each set of μ and C, 100 realization models was simulated for the derivation of CDF and then the error between two CDFs, one is from the packer test and the other is from virtual tests, are calculated. The error map is shown in the left picture in Figure 6.12. The parameters that connect fractures to transmissivity distribution (μlog10 = -8.4, σlog10 = 1.0, and C = 2.3) are decided by minimization of the error.

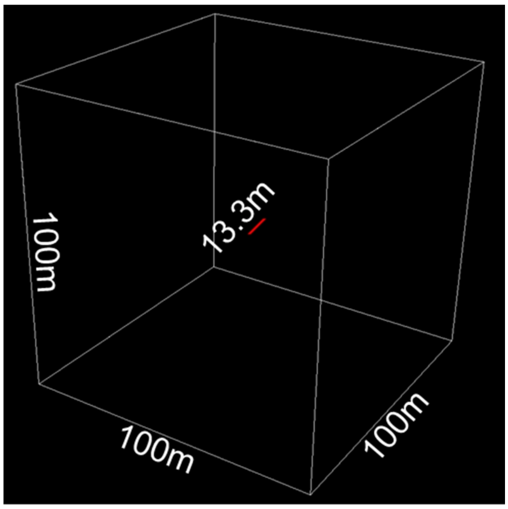

Figure 6.11 Analytical region of virtual well test

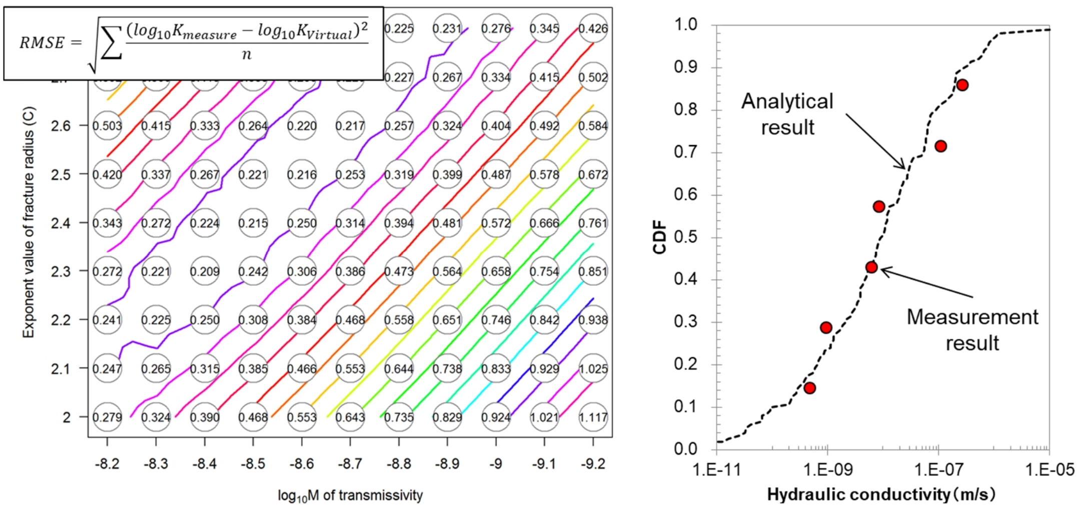

Figure 6.12 RMSE map and relationship between measurement values and analytical values of K

(2) Construction of the ECPM model

Equivalent conductivity values (Oda K) in each 2 m, 5 m, 10 m, and 20 m grids are calculated based on the DFN model (1 realization which shows 50% value of K, hereinafter refer Mod50; Figure 6.13) for construction of the ECPM model. In our simulation, we consider the heterogeneity only in the hydraulic conductivity structure and set other parameters are to be homogeneous for simplicity.

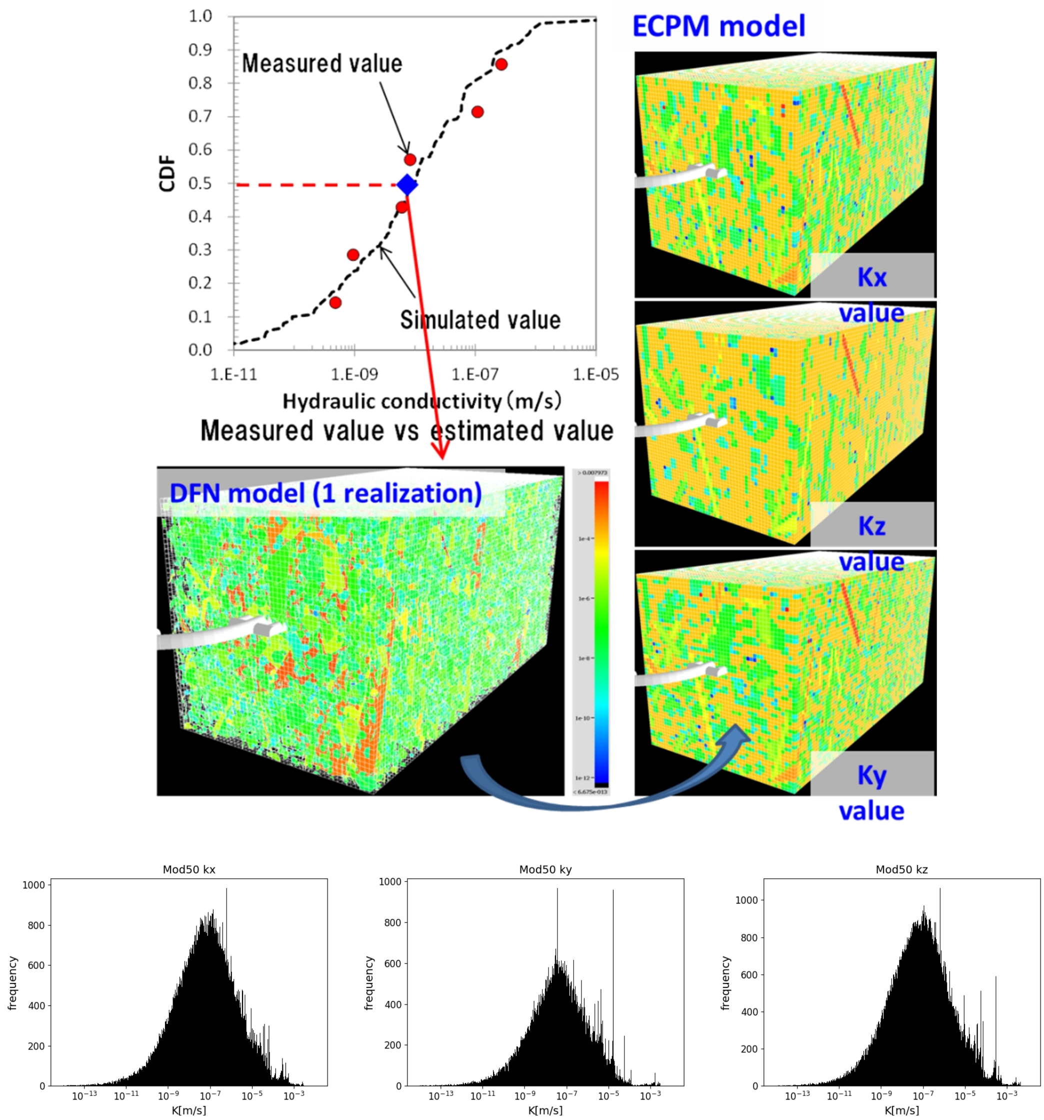

Figure 6.13 DFN model for ECPM modeling. Spatial distribution of anisotropic hydraulic conductivity (upper right) and its frequency (lower)

6.3.2 Simulation with ECPM model

FracMan® generates an anisotropic hydraulic conductivity structure from the realized fracture field. In this study, we averaged hydraulic conductivity of each direction calculated by FracMan® and input the isotropic structure into the H-M simulator. Hydraulic conductivity of

0 m/s is returned from FracMan® at the elements where any fractures do not exist; a hydraulic conductivity of 1.e-12 m / s is assigned there. Hydraulic conductivity higher than 1.e-4 m / s was also limited to 1.e-4 m / s for the stability of numerical calculation. The skin effect of shotcrete is considered by setting the hydraulic conductivity of elements in 1 layer of the tunnel boundary to 1.e-8 m / s.

Thames, a part of Couplys used for our simulation employs the Block Gauss Seidel scheme (e.g., Whiteley et al., 2011 [23)]) that solves different coupled physical problems separately and iterates the calculation until the error related to the coupled effect gets convergence. When we simulate the H-M problem with the heterogeneous model, Block Gauss Seidel iteration for fully coupled simulation does not converge. Therefore, the results of Step1b are the results considering only the weakly coupled effects. The convergence rate of this scheme becomes slow or is not satisfied when the solver is applied to the problem including the matrices with small diagonal value due to heterogeneous model [24)]. SA-AMG (smoothed aggregated algebraic multigrid method [25)]) is employed to solve each physical problem for the convergence of numerical calculation with the ECPM model that has highly heterogeneous structure.

6.3.3 Spatial distribution of hydraulic head, Cl concentration and displacement calculated from a realized sample model

Figure 6.14 shows the distribution of hydraulic conductivity, hydraulic head, displacement and Cl concentration in two vertical and one horizontal slice after the excavation of CTD. The results from one of the realizations of the model are shown.

Due to the heterogeneous feature of hydraulic conductivity structure, the calculated hydraulic head is totally different from the distribution in the case of the homogeneous model shown in Figure 6.2. The areas where the hydraulic head drops do not correspond to the fractures that have a continuous high conductive zone in the model. For example, hydraulic head decreases along a fracture is distributed on bottom of CTD, while the hydraulic head remains about 4MPa around two vertical fracture zones in the inclined tunnel. The change of hydraulic head is not affected by locally distributed high conductivity zone but seems to relate to the connectivity of high hydraulic conductive zone there. In this case, the hydraulic pressure seems to remain high due to the water supply from boundary along continuous high conductive zone. This indicates the difficulty of estimation of change in the hydraulic head during excavation by using model derived from limited fracture data.

The distribution of Cl concentration is highly affected by the advection. The high and low Cl concentration water are conveyed along the continuous high conductive zones, and high and low Cl concentration zones are formed there below and above the tunnel, respectively. These Cl concentrations reflect the distribution of fractures (hydraulic conductivity structure) in the model rather than the distribution of hydraulic pressure. This indicates that the fast flow toward drift is occurred due to the continuous high conductive zone although the pressure drop along the conductive zone is slight. On the horizontal slice including the CTD, distribution of Cl concentration does not change compared to the distribution in other vertical slices and is almost the same as the initial distribution before the inclined tunnel excavation. This is because that the vertical flow conveying Cl ions stagnates on the boundary where the upper flow changes to downward flow due to the flow into the tunnel.

The compressive deformation appears according to the pressure release by excavation of the tunnel. Due to the hydro-mechanical coupling effect, the magnitude of displacement becomes large around the area where hydraulic pressure decreases. We do not use the heterogeneous property model for the mechanical simulation, but instead assume uniform properties. However, the estimated deformation in rock mass clearly appears around the location where hydraulic head decreases, illustrating the H-M coupling.

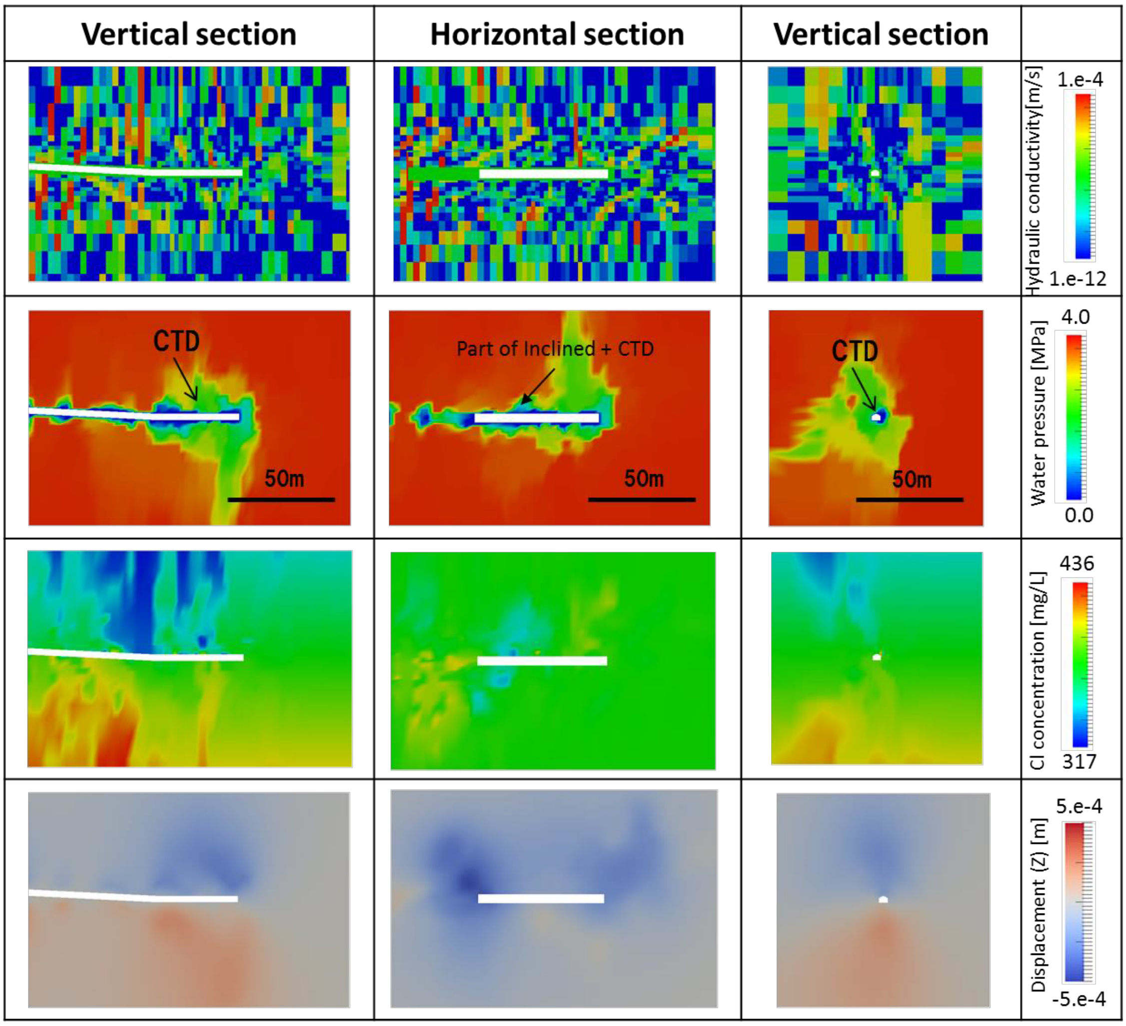

Figure 6.14 The simulation results from a realized model after excavation of CTD. Hydraulic conductivity, pressure, Cl concentration and displacement in Z direction are shown from top to bottom. Distribution in two vertical and horizontal sections are shown from left to right.

6.3.4 Time variation of hydraulic head and Cl concentration in 12MI33

Figure 6.15 shows the predicted time variation of drawdown in 12MI33 during excavation. The hydraulic pressure at sections 2, 3 and 4 are decreased following the excavation. On the other hand, hydraulic pressure at section 1, 5 and 6 remains higher than 3.8 MPa. The hydraulic pressure at steady state does not show the correlation with hydraulic pressure at another monitoring point. Due to several high conductive flow paths in the structure of hydraulic conductivity, the drawdown of hydraulic pressure is independent on the distance from tunnel face to monitoring point as shown Figure 6.5.

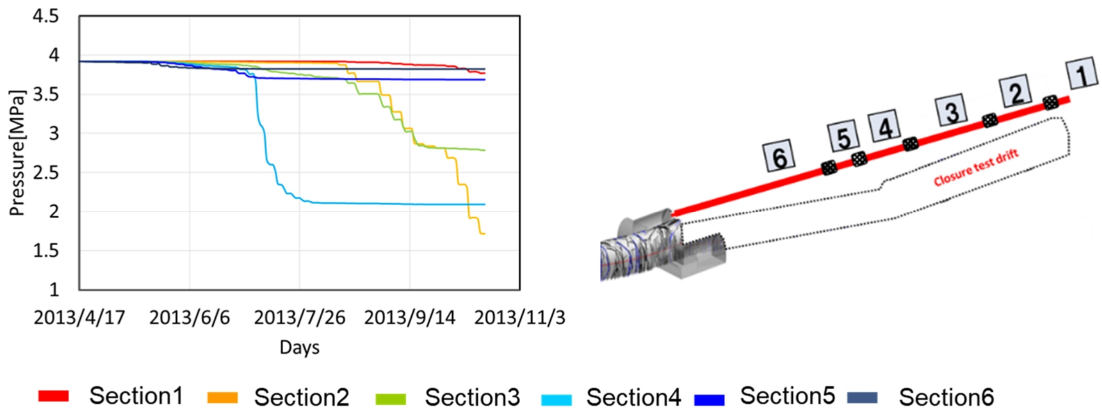

Figure 6.15 Time variation of hydraulic head in 12MI33

Figure 6.16 shows the time variation of Cl concentration in 12MI33 during and about 1 year after excavation. Though the concentration at other monitoring points does not change, Cl concentration estimated in section 4 and 5 deviate. The deviation of Cl concentration is slightly less than 10% of initial concentration.

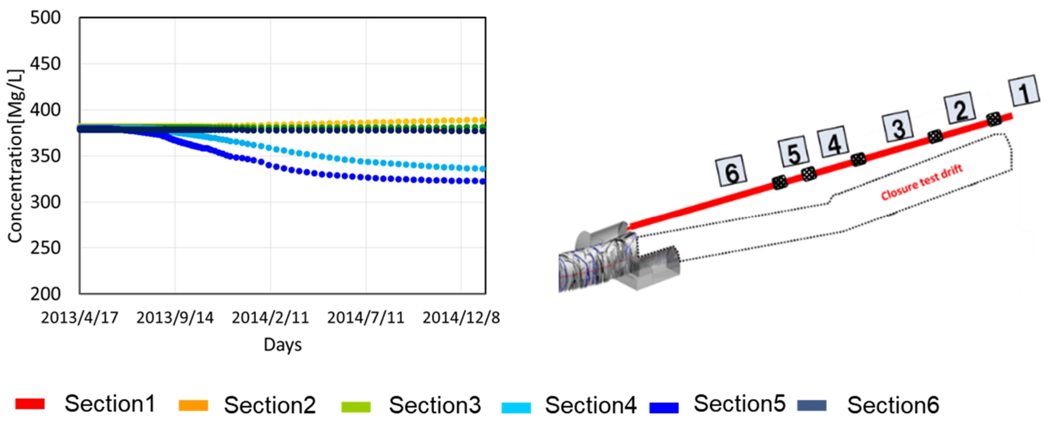

Figure 6.16. Time variation of Cl concentration in 12MI33

6.3.5 Inflow into inclined drift and the CTD

Figure 6.17 shows the time variation of inflow into the inclined tunnel and CTD during and after excavation. The order of total inflow is almost same as the homogeneous model case. However, a fraction of inflow into inclined tunnel or research tunnel differs from the homogeneous model case. In the fractured model, almost all of flux into tunnel part occur around inclined tunnel though the fraction of inflow into inclined and CTD is proportional to the tunnel length of the homogeneous model case. We summarize the comparison of these predicted results with observed data at section 6.7.

To confirm the distribution of inflow into the tunnel, a spatial distribution of magnitude of Darcy velocity in horizontal and vertical slice along tunnel are displayed in Figure 6.18. Fracture parts in the model are clearly highlighted as a large magnitude of Darcy velocity zone and correlate with high or low concentration zone in Figure 6.4. Several path lines with high Darcy velocity about 10^{-5} m/s reaches the inclined tunnel, while only a few flow paths of 10^{-6} m/s crosses the CTD. The inflow rate into each part of research tunnel reflects this distribution of Darcy velocity and the different fracture density between inclined drift and CTD.

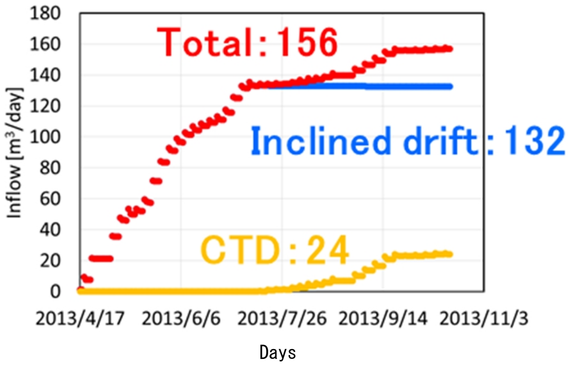

Figure 6.17 Time variation of inflow into research tunnel.

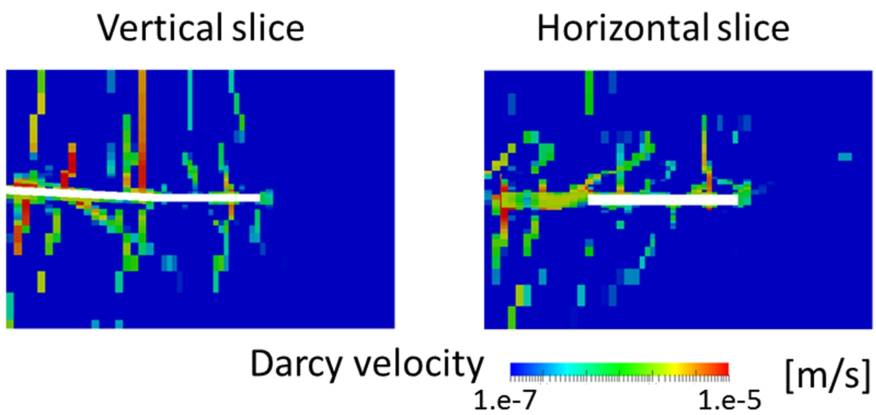

Figure 6.18 special distribution of Darcy velocity

6.4 Model update and calibration based on the data of Step 1

6.4.1 Theory and method of model update

Hydraulic heads after drift construction in each monitoring section were calculated using the DFN models which were constructed by parameter set in Table 6.1 (Figure 6.19). The calculation with 100 models was conducted for steady state. The result shows that the pressure at section No.1 is almost deterministic while the pressure at other points could take a variable value between 0 and 4 MPa.

Among 100 realizations, the model that shows the 69% value of hydraulic conductivity in CDF reproduce the observed pressure the best (Figure 6.20). Therefore, we choose the model (hereinafter refer Opt69) as a calibrated model.

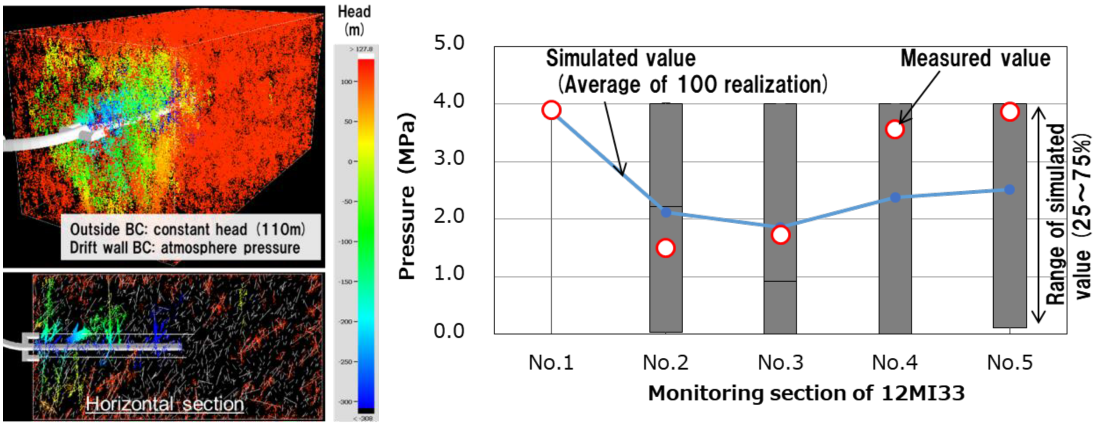

Figure 6.19 Example of head distribution (left) and prediction result of each section (right)

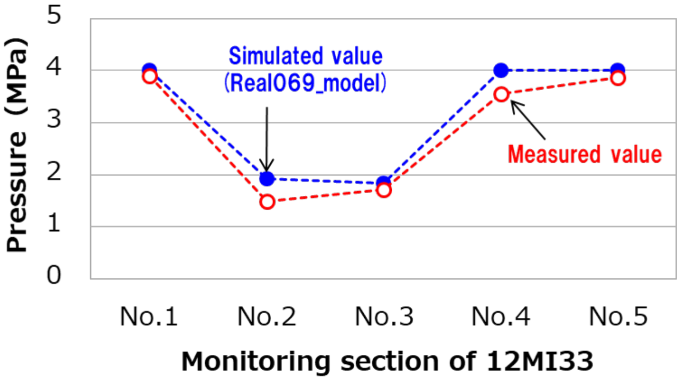

Figure 6.20 Hydraulic head distribution of extracted DFN model (Opt69) and measured value

6.4.2 ECPM modeling based on the fracture data

Equivalent conductivity value (Oda K) in each 2 m, 5 m, 10 m, and 20 m grid size are calculated based on DFN model (Opt69) for construction of ECPM model (Figure 6.21).

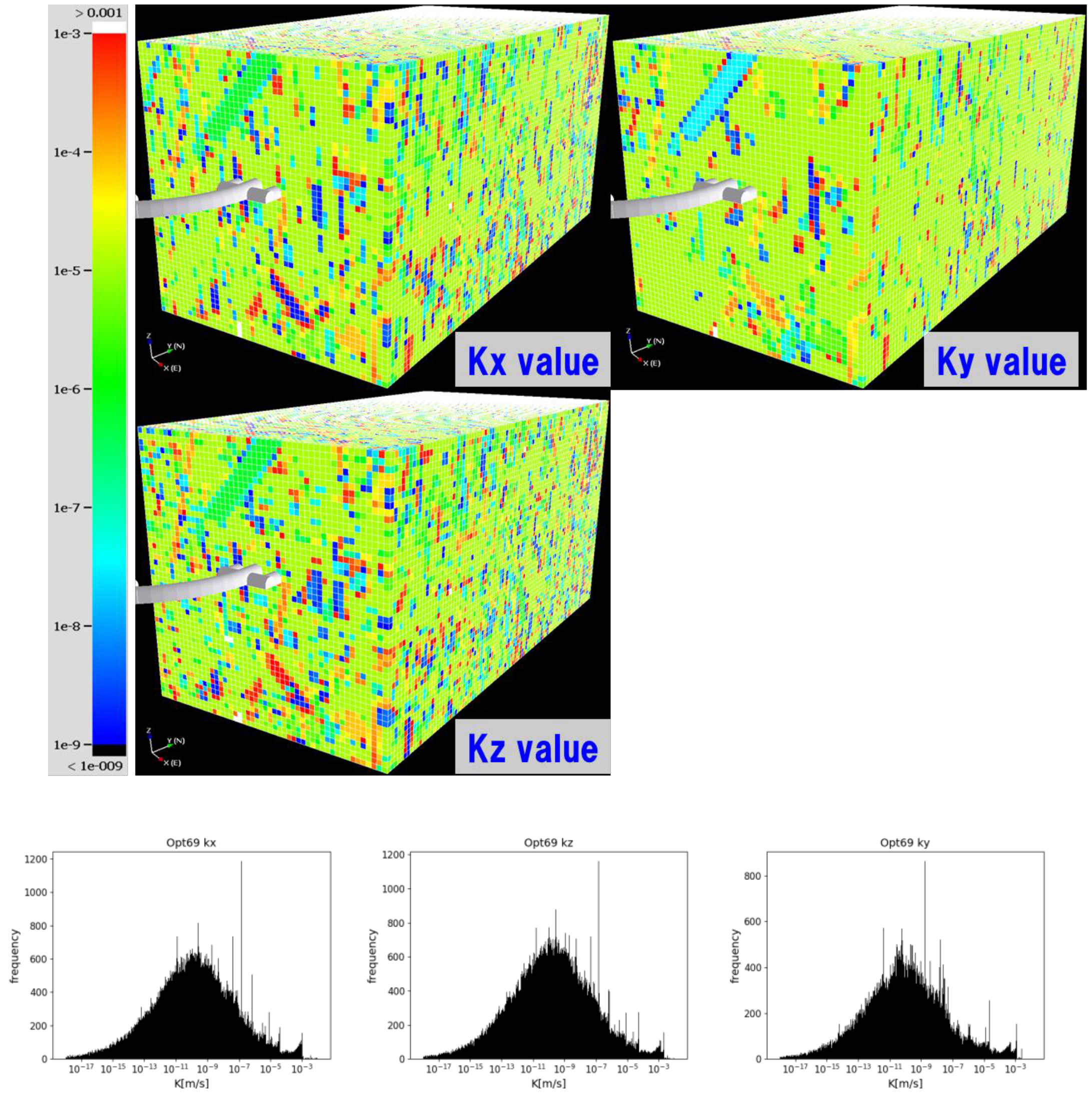

Figure 6.21 DFN model for ECPM modeling. Spatial distribution of anisotropic hydraulic conductivity (upper right) and its frequency (lower)

6.4.3 Result of spatial distribution of hydraulic pressure, Cl concentration and deformation from Opt69

Figure 6.22 shows the simulation results of the spatial distribution of hydraulic conductivity, hydraulic pressure, Cl concentration and displacement in the vertical direction. These results are arranged in the same manner as Figure 6.14. In this simulation, we set the hydraulic conductivity of shotcrete to 2.0×10^{-8} m / s for calibration purposes.

In this model, average hydraulic conductivity is lower than that in the Mod50. The sequential high conductive zones representing the fracture zone are clearly seen compared with Figure 6.14. The relationship between pressure decrease and fracture distribution is clearer than the case with Mod50, especially on the horizontal slice. In the results of Cl concentration, almost whole domain do not change compared to the initial state except for low concentration zone along the fracture around the entrance of CTD. Note that the high and low Cl concentration zones along the upper CTD is an artifact from the lack of numerical accuracy due to the time step size and should be ignored. This distribution of Cl concentration indicates that the almost all of inflow into drift occurs at the entrance of CTD. The rock mass deforms in a compressive way and shows the strong relation with the decrease of hydraulic pressure.

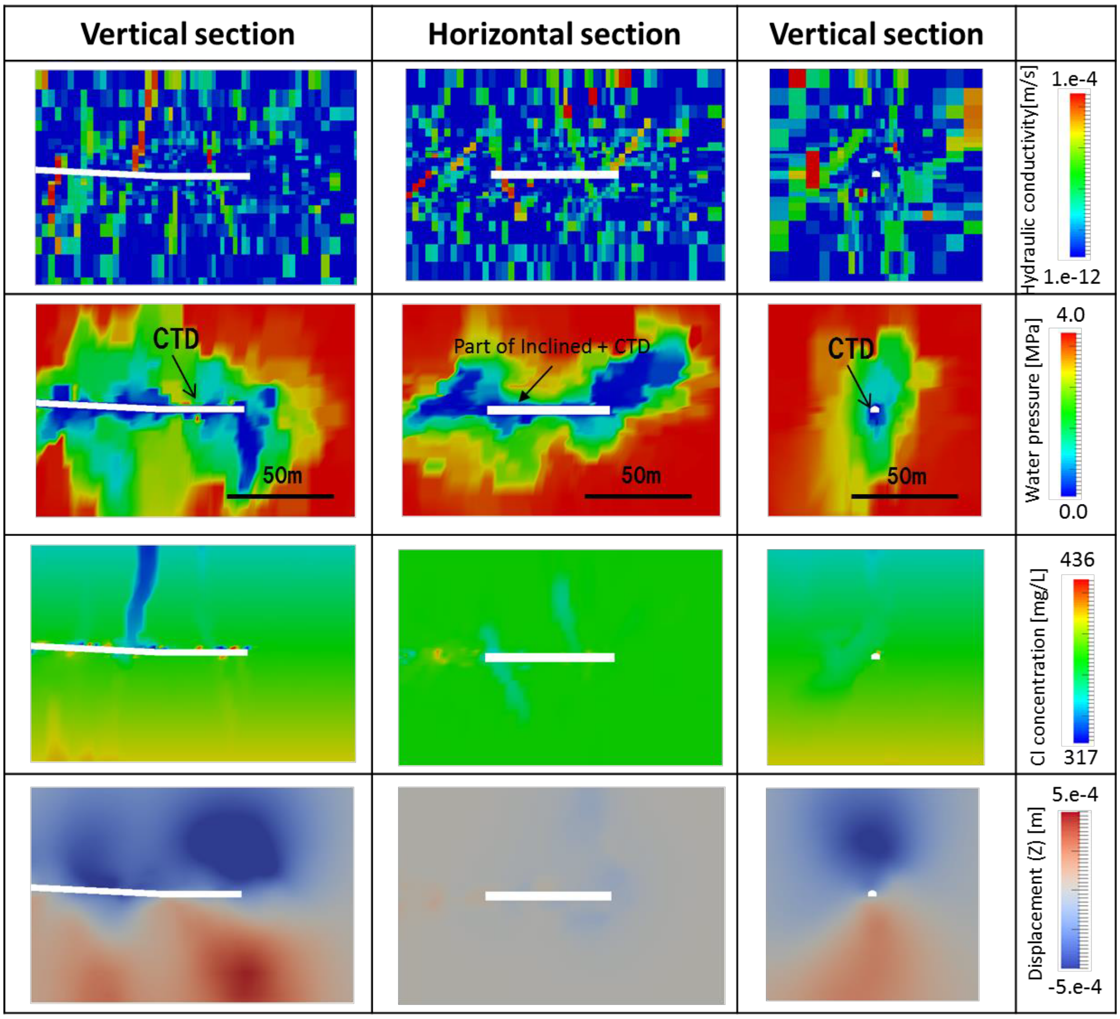

Figure 6.22 The simulation results from Opt69 after excavation of CTD. Hydraulic conductivity, pressure, Cl concentration and displacement in Z direction are shown from top to bottom. Distribution in two vertical and horizontal sections are shown from left to right.

6.4.4 Time variation of hydraulic head and Cl concentration in 12MI33 (Opt69)

Figure 6.23 shows the change in hydraulic pressure in 12MI33. In this model, the hydraulic pressure in all monitoring points decreases as the excavation proceeds. Hydraulic pressure in sections 1, 2 and 6 reaches almost 0 MPa due to fracture across the research tunnel. The hydraulic pressure after excavation differs from the predicted by DFN modelling as shown in Figure 6.20. We use the cell with the size of 2m to generate the equivalent continuous porous medium model. Modelling with this size cells make different monitoring sections in the borehole share the same cell and communicate the hydraulic pressure response to different monitoring sections. To avoid this inconsistency between DFN and ECPM, we would need to use a finer mesh. The behavior or hydraulic pressure at section 1 and 2 is almost same. The high conductive fracture is located at the tip of research tunnel. Elements consisting of this conductive zone are shared by each element including monitoring point and strongly affects the simulated data at the monitoring point.

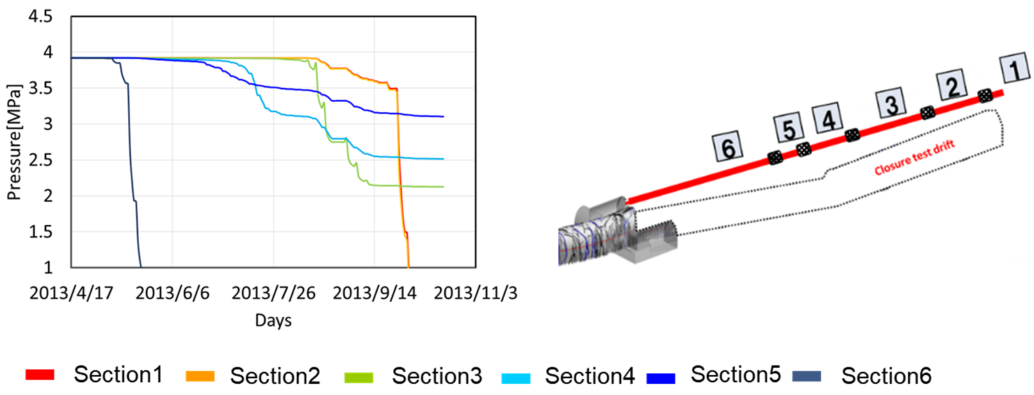

Figure 6.23 Time variation of hydraulic head in 12MI33 (Opt69)

Figure 6.24 shows the time variation of Cl concentration in 12MI33 during excavation and one year after excavation. Cl concentration in these monitoring points does not fluctuate at all as shown in Figure 6.16, while the decrease of hydraulic pressure more intensive than the variation in Figure 6.15. The change in Cl concentration is not necessarily related to the change in hydraulic pressure.

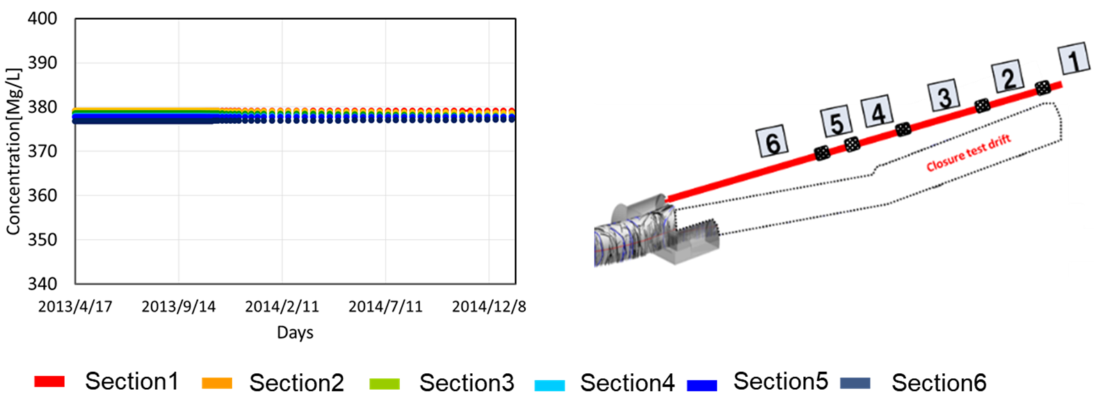

Figure 6.24 Time variation of Cl concentration in 12MI33 (Opt69)

6.4.5 Inflow into inclined drift and CTD (Opt69)

Figure 6.25 shows the time variation of inflow into the research tunnel. The inflow rate around inclined tunnel occupies more than 95% of total inflow rate. The bias of the fraction of inflow rate between the inclined tunnel and the CTD is bigger than that in Figure 6.17. The high Darcy velocity area appears only along three fracture zones as shown in Figure 6.26, two in the inclined tunnel and one in CTD. These two fractures in inclined tunnel connect to the outside of focused domain as shown in Figure 6.26 and much water would be channeled through these fracture zones. On the other hand, the high-velocity zone across the CTD is included within the domain and the velocity is slower than that in other fractures. Less connectivity of fractures across the CTD than that across inclined tunnel would cause the smaller inflow rate.

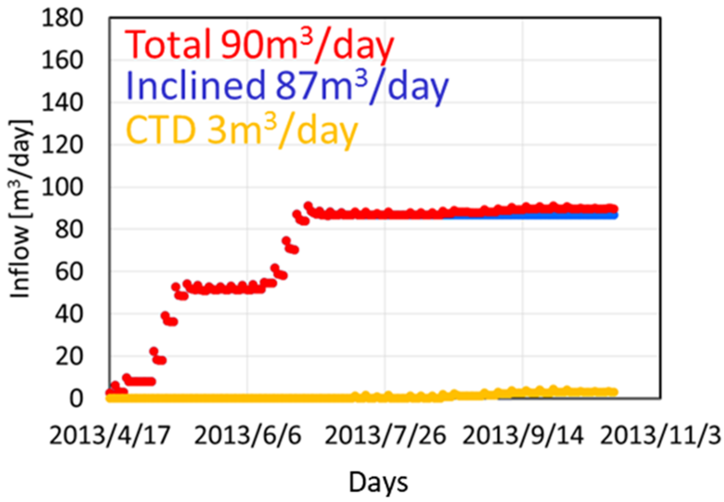

Figure 6.25 Inflow rate into research tunnel.

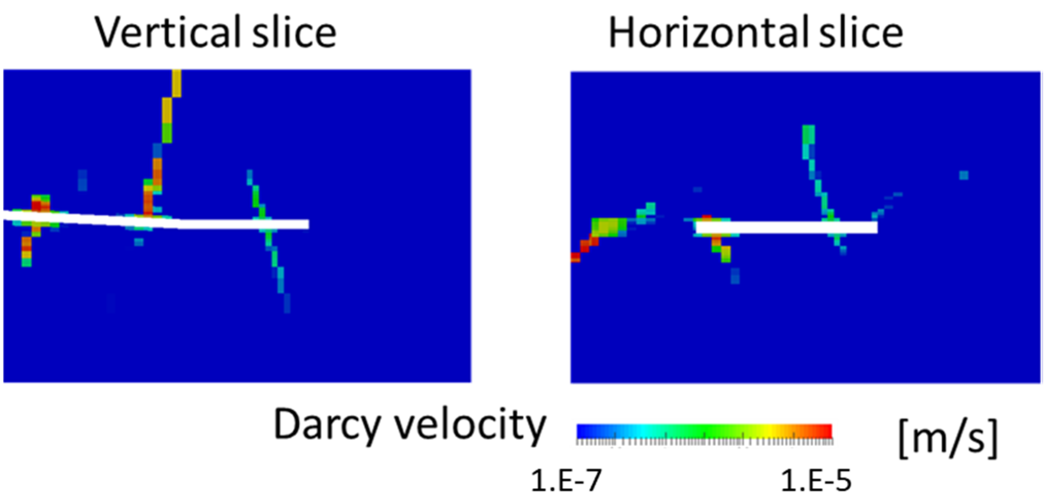

Figure 6.26 Darcy velocity in vertical and horizontal section along research tunnel.

6.5 Effect of length of monitoring point

In this study, we define the mid-points of each monitoring section in 12MI33 as monitoring points to compare the simulated results with observed data. However, our models include several nodes in the monitoring sections which allows the variation in hydraulic pressure along the borehole to be seen.

Figure 6.27 shows the hydraulic pressure at steady state along the 12MI33 borehole. The width and height of the colored bars indicate the length of monitoring section and observed hydraulic pressure, respectively. The monitoring sections except for section 1 include more than two nodes and several of the monitoring zones show very large changes in pressure within the that zone. In such case that the monitoring sections locates within highly heterogeneous structure, the value picked up at a points do not become a representative value at a measurement point. The modeling of monitoring borehole or some averaging technique is needed to be applied for the appropriate comparison in such case.

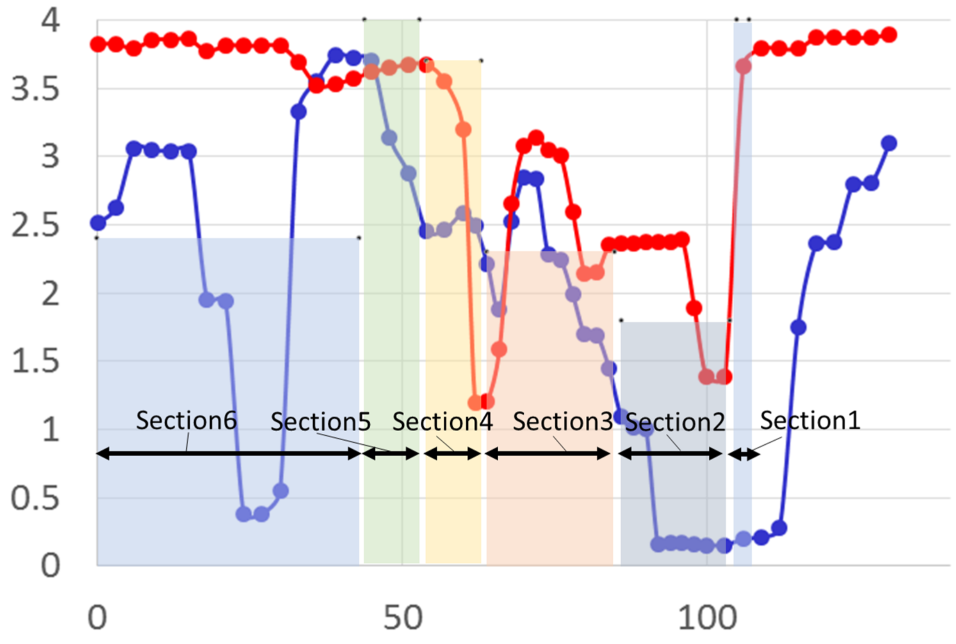

Figure 6.27 Length of each monitoring section and simulation results on nodes along 12MI33.

6.6 Summary of ECPM model and simulation results

In this Step, we performed a hydro-mechanical and advective-diffusive simulation to predict a disturbance due to the excavation of research tunnel within a heterogeneous model. Several fracture models are constructed using a stochastic method according to the probability function derived from geological data. Two of them are chosen for coupled simulation, one is a realization that shows the 50% value of the observed hydraulic conductivity CDF generated through a virtual hydraulic packer test (Mod50) and the other is the model that the hydraulic pressure in 12MI33 after excavation best matches the observations (Opt69). Then, they are converted to equivalent continuous porous medium for finite element modeling. We estimate the pressure field, deformation and Cl concentration by this method. The summary of simulation results are as follows:

- The hydraulic pressure in the monitoring sections in Borehole 12MI33 does not correlate with the hydraulic conductivity structure but would be affected by the connectivity of high conductive zone representing fracture zone.
- Cl concentration along the 12MI33 borehole does not show the significant change

although the complex hydraulic pressure change and high Darcy velocity along fracture zones are present.

- Deformation of around the tunnel shows the good correlation with the decrease of hydraulic pressure due to the coupled effect.

6.7 Comparison of each simulation result with the observed data

In this Step, we constructed three models, a homogeneous model and two heterogeneous models. To evaluate the ability to predict a disturbance due to the excavation, we compared the simulated results to the observed data. In this step, the data of time variation of hydraulic pressure and Cl concentration in 12MI33 hydraulic pressure and inflow into research tunnel are available. We compared these results.

Figure 6.28 shows the comparison of time variation of hydraulic pressure in 12MI33. Observed data, simulation results from a homogeneous model and two heterogeneous models are shown respectively. In case of the homogeneous model, the drawdown of hydraulic pressure smoothly occurs compared to the observed data. All data in six monitoring points are predicted to decrease during the excavation, though the data for sections 1, 5 do not decrease at all in observed data. Hydraulic pressure at section 2, 3 and 6 shows a reasonable fit, less than 1 MPa difference, to the observed data at steady state. When the Mod50 is used, the hydraulic pressure at section 2 shows good agreement and that of section 6 shows a reasonable fit compared to the observed data. In addition, the pressure at sections 1 and 5 also shows good agreement with the observed data. In this case, both rapid decrease and stable state of hydraulic pressure can be reproduced. When Opt69 is used, the hydraulic pressure at section 1, 2 and 6 reaches almost 0 MPa as soon as the hydraulic pressure started to decrease. In this case, the hydraulic pressure in section 3 shows good agreement with the observed data, though the hydraulic pressure in other points is too low.

Figure 6.29 shows the comparison of time variation of Cl concentration in 12MI33 during and 1 year after excavation. The results are arranged in the same manner as Figure 6.29. All of the simulated results show a slight change or almost no change when compared with the observed data.

Figure 6.30 shows the comparison of inflow rate into inclined tunnel and CTD. Only the inflow rate after excavation is available as shown in Figure 6.30. The total inflow rates of all results show good agreement with observed data. However, the fraction of inflow rate between the inclined tunnel and CTD in simulated results are largely different from the measurements. This is due to the random generation of highly conductive zones in the model. Two models, we used include, as Figures 6.14 and 6.22 show, fewer fractures in CTD than inclined zone. Conditioning the randomly generated model with the observed geological data would improve the fraction of inflow rate in each tunnel section. From these results, total inflow rate into the tunnel would be more predictive than with the variation of hydraulic pressure or Cl concentration.

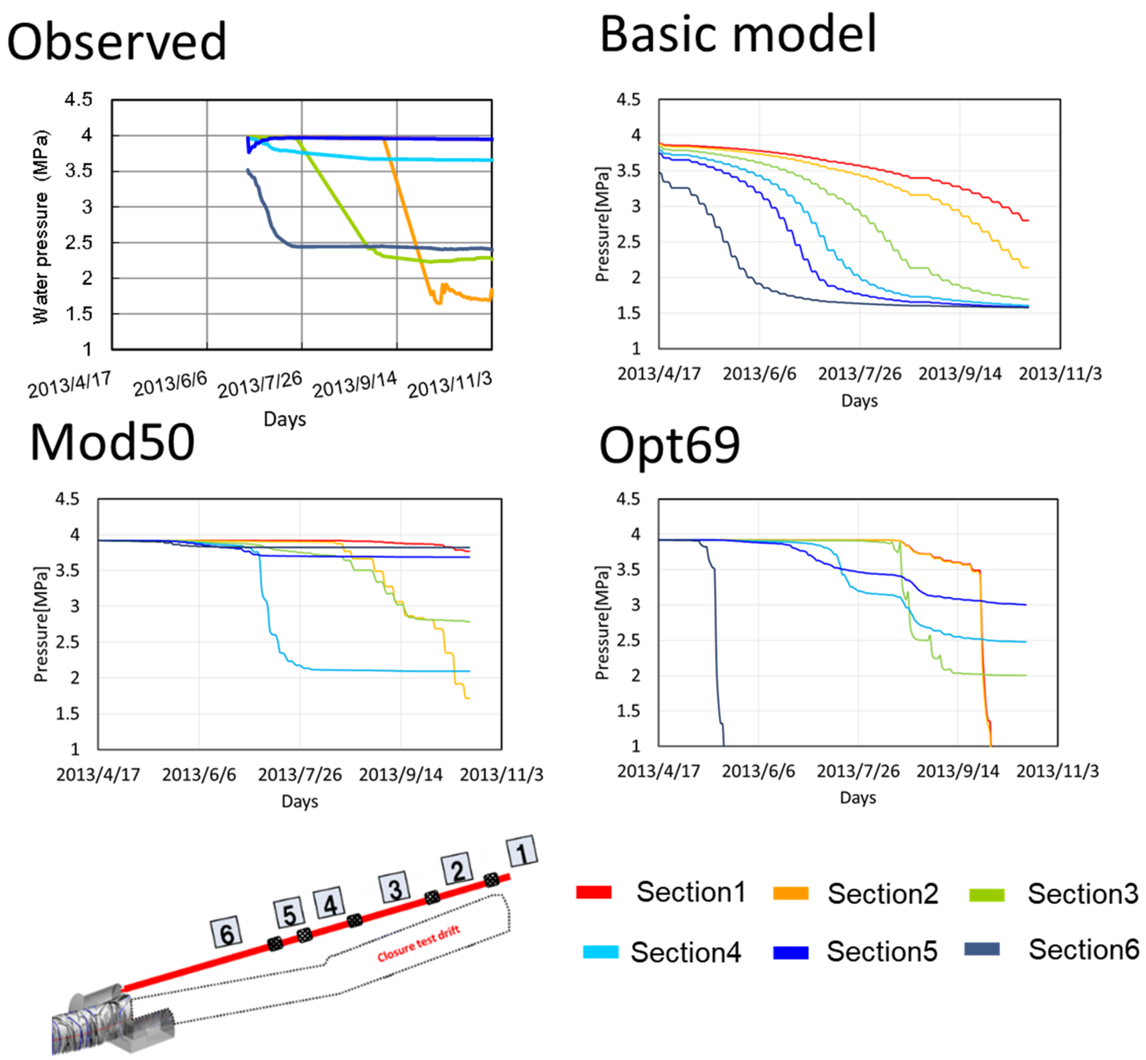

Figure 6.28 Comparison of time variation of hydraulic pressure in 12MI33.

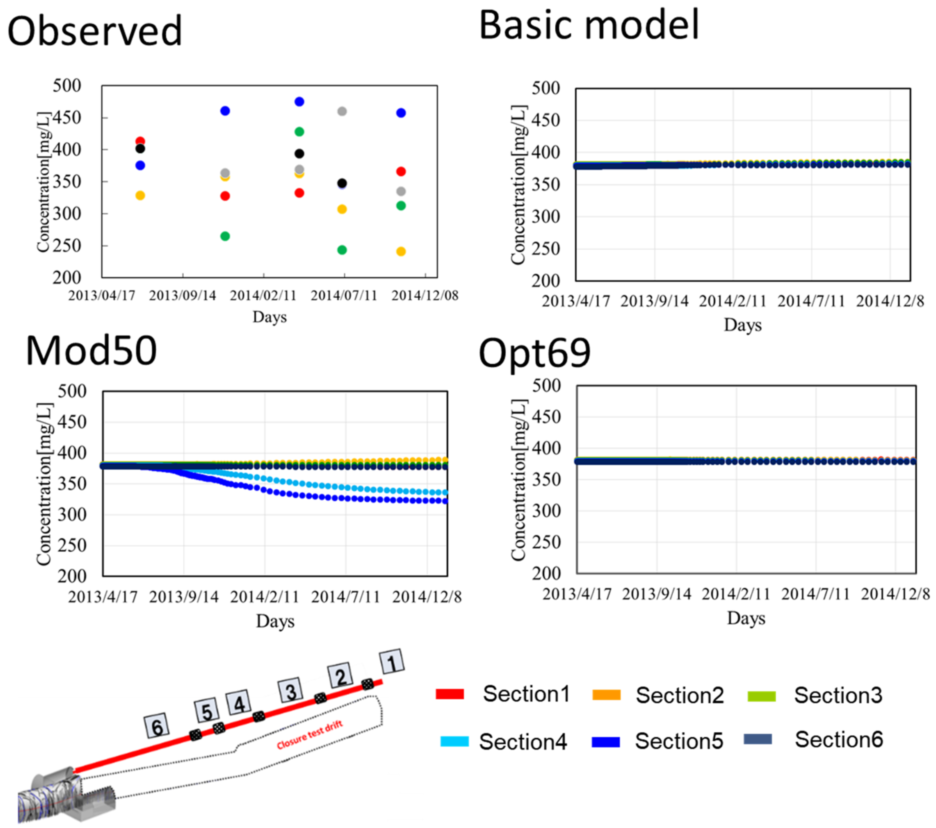

Figure 6.29 Comparison of time variation of Cl concentration in 12MI33.

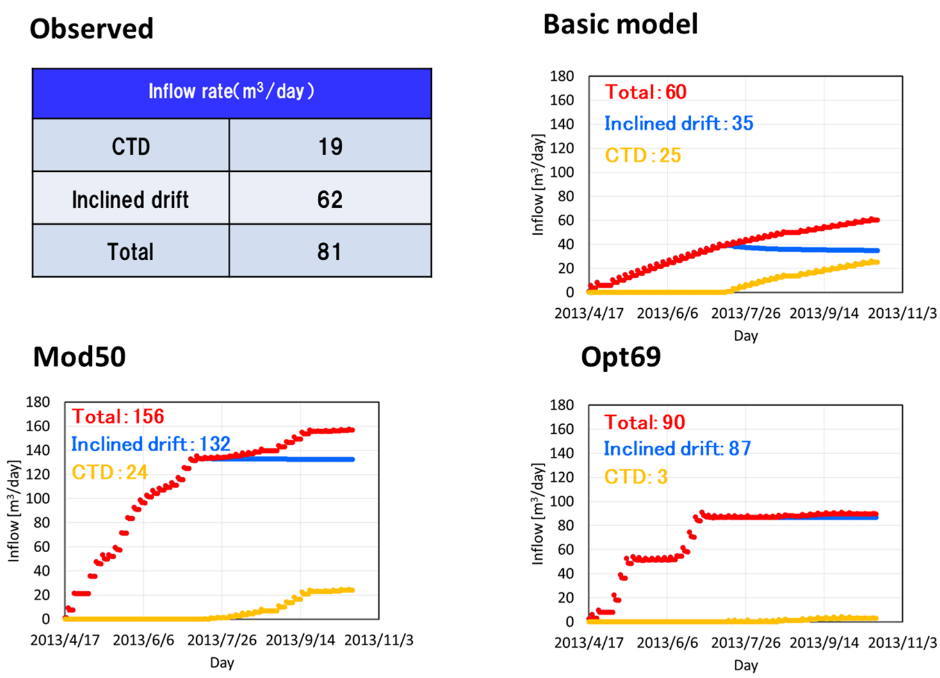

Figure 6.30 Comparison of time variation of Cl concentration in 12MI33.

6.8 Conclusions of Step1

In this step, we try to predict a disturbance during the excavation of the research tunnel. We use the datasets observed before excavation of inclined tunnel and CTD to define the simulation for prediction purposes. We consider the fractures stochastically using a DFN model and convert the fracture model to an equivalent continuous porous media (ECPM) by Oda's model. The prediction simulation is performed using the converted model. The data on hydraulic pressure, Cl concentration and inflow are available for the comparison of simulated results with the observed data. In addition to these parameters, we simulated the mechanical behavior affected by hydraulic pressure, though there is no mechanical data for comparison. From the simulated results and their comparison with the observed data, we summarize the conclusions of Step1 as:

- The simulation with models considering the fractures could reproduce the time variation of hydraulic pressure independent of the location of monitoring points. However, the prediction of hydraulic pressure to fit all observed data is difficult by using the model that randomly generates high conductive zone.
- The predicted Cl concentrations along the 12MI33 borehole do not show the significant change even though the flow paths corresponding to the fracture zones are considered. Comparison of simulated results with observed data suggests that the drainage by drift gathers water from deeper or shallower parts than our model domain.
- The total predicted inflow into the research tunnel from both homogeneous and heterogeneous models, show good agreement with the observed data. The prediction of inflow at the tunnel scale would be possible.

7. Results of Step 1 modeling (SNL)

7.1 Fracture data analysis and fracture model development

7.1.1 Introduction

The major goal of this study was to develop a fracture model of the granite rocks for the area surrounding the MIU Research tunnel at 500 m depth. The fracture model is needed for simulation of hydrogeologic and geochemical conditions in the various experiments being conducted in the research tunnel as a part of the GREET project.

The modeling domain is 100 × 150 × 100 m with the main experimental part of the tunnel, Closure Test Drift (CTD), located approximately in the center. The majority of the model is within the lower sparsely fractured domain (LSFD) of the Toki granite. Figure 7.1.1 shows the modeling domain, the research tunnel (CTD and Inclined Drift), the horizontal monitoring borehole 12MI33 (with 6 test intervals), and the vertical exploratory borehole MIZ-1 (only 2 test intervals are inside the modeling domain).

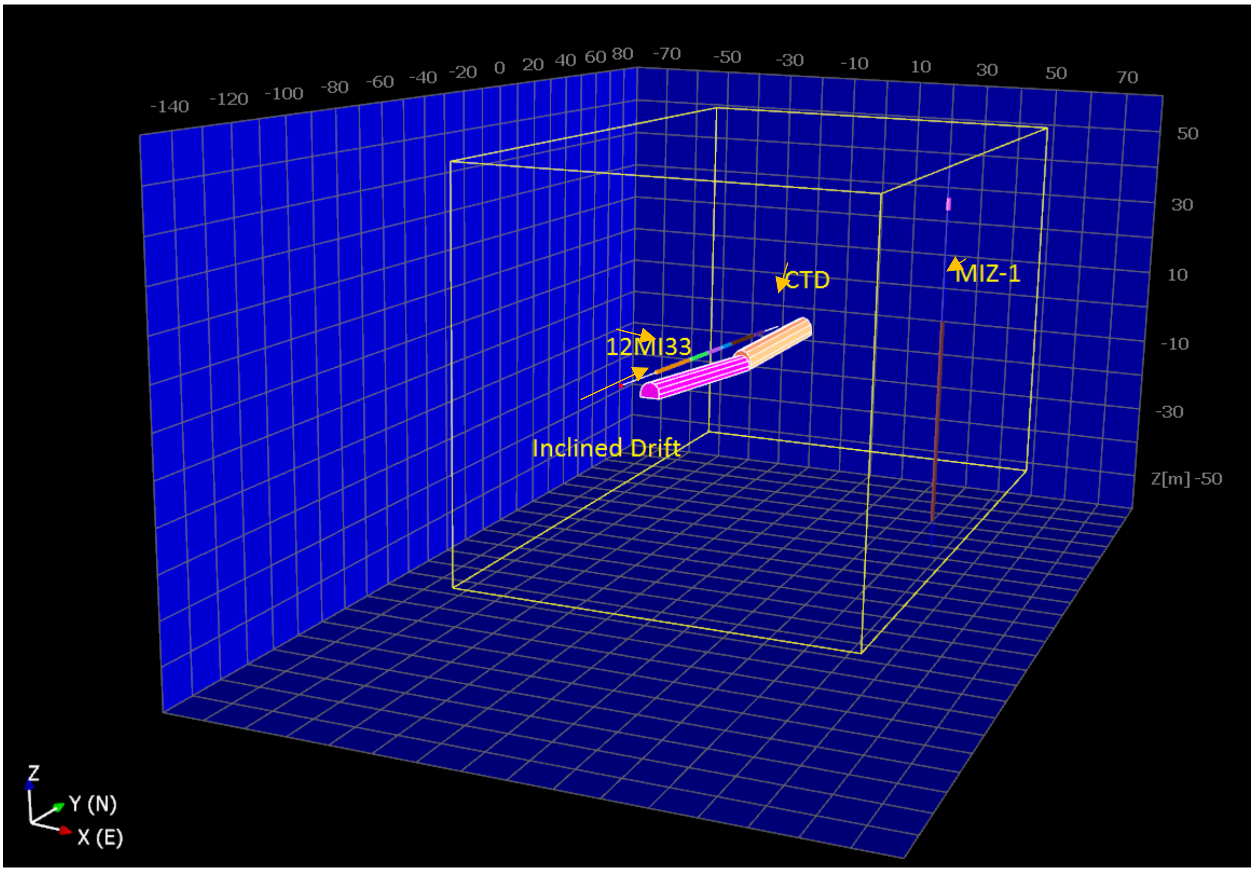

Figure 7.1.1 Modeling domain and location of research tunnel and boreholes.

The following data were used in the fracture analysis:

- Fracture traces on the walls of CTD, Inclined Drift, and Access Drift. Note that Access drift fracture data were used in the initial analysis even though this drift is outside the modeling domain. However, these fractures were not used in the developing of fracture properties because they were found to be different from the fractures in the Inclined Drift and CTD.

- Fractures observed in borehole 12MI33.
- Packer test data in 6 test intervals of 12MI33 and 2 test intervals of borehole MIZ-1.
- Measured inflow into the research drift.

The goal of the fracture analysis was to estimate fracture orientation, size, and intensity and use these estimates to develop the discrete fracture model (DFN). The DFN model is then converted to an equivalent continuum model with the grid cell size 1 × 1 × 1 m (1,500,000 grid blocks) using Oda's method [11]. Multiple realizations of DFN and the corresponding equivalent continuum model will be used to simulate groundwater flow and transport in the vicinity of the research tunnel. The development of a DFN is demonstrated using one realization as an example. FracMan® 7.6 [12] was used to develop the model.

7.1.2 Generating fractures using research tunnel fracture trace data

Two thousand and twenty three fractures were considered on the wall of the research tunnel. Figure 7.1.2 shows the observed fracture traces and location of monitoring points in borehole 12MI33. The fracture trace data include trace segment coordinates, length, dip, strike, alteration (if any), and flow range (if any). If an alteration was observed, the filling was described using the following categories carbonate, chlorite and/or sericite, and unconsolidated clayey filling including smectite.

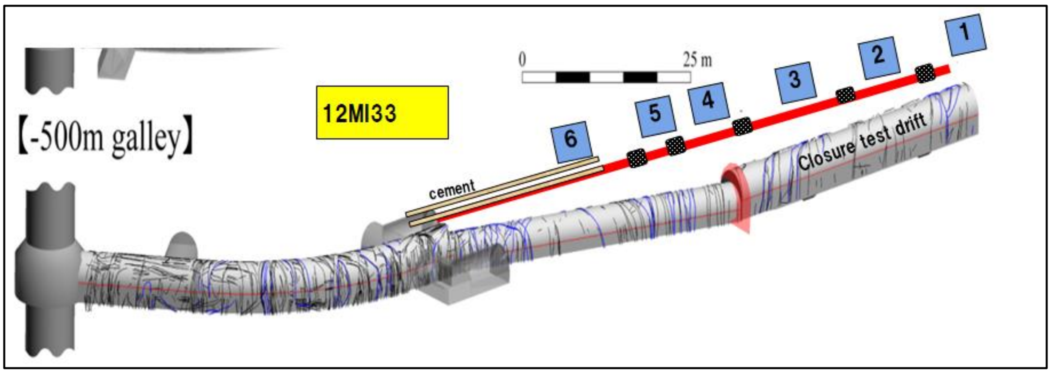

Figure 7.1.2 Observed fracture traces in the research tunnel and location of monitoring points in borehole 12MI33.

It was assumed that the fractures that did not exhibit any flow discharge are either closed fractures or small fractures not connected to the fracture network. There are 146 fractures (7.2 %) with the observed flow discharge. They are characterized in the original data set based on the flow range as "flow" (F) fractures (>1 L / min), "drop" (D) fractures (>0.1 L / min), and "wet" (W) (< 0.1 L / min) fractures. These fractures were selected for the analysis and fracture model development (Table 7.1.1). The trace data were imported into the model and are shown in Figure 7.1.3.

Table 7.1.1 Research tunnel fractures included in the fracture analysis.

Research Tunnel Area	F-Fractures (flow>1.0 L/min)	D-Fractures (flow>0.1 L/min)	W-Fractures (flow<0.1 L/min)	All Fractures with Flow
CTD	4	15	3	22
Inclined Drift	14	42	N/A	56
Access Drift	N/A	65	3	68
Total	18	122	6	146

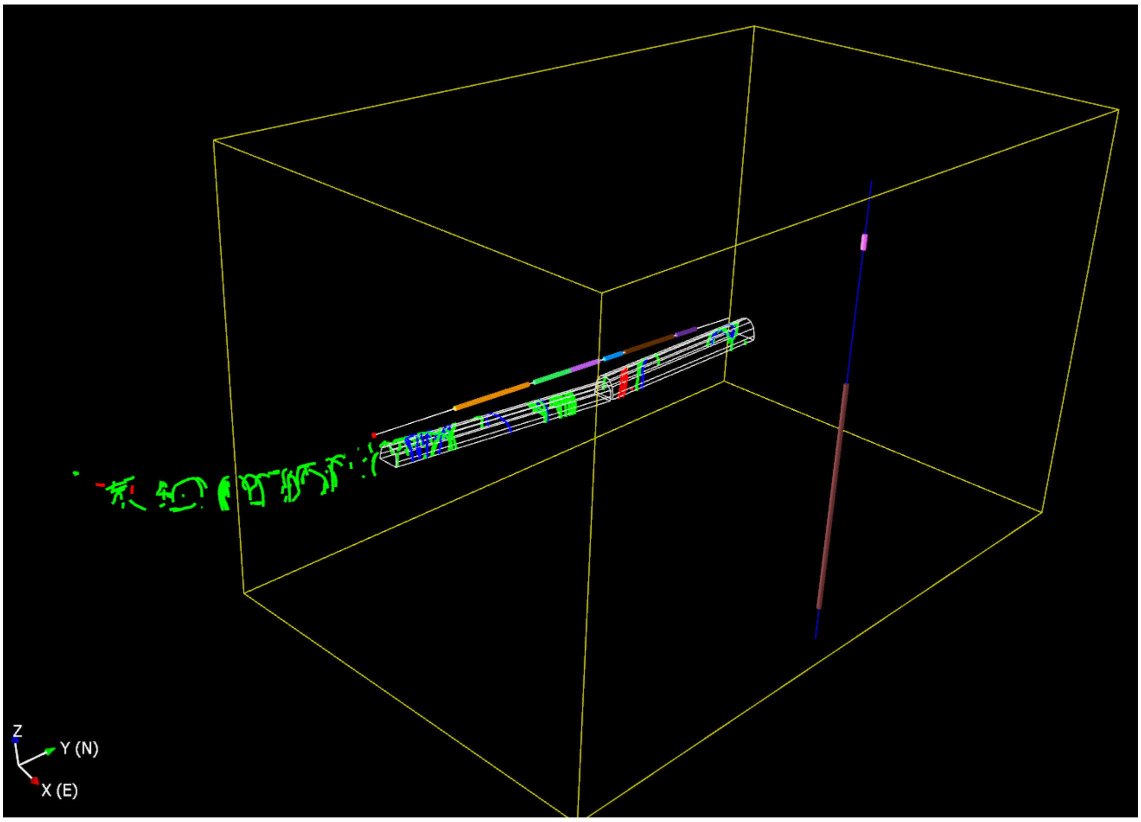

Note: F-fractures are shown in blue, D-fractures are shown in green, and W-fractures are shown in red color.

Figure 7.1.3 Traces of the fractures on the Research tunnel walls included in the analysis.

The observed fracture traces can be used to generate each individual fracture. The dip direction and dip angle of the fracture are derived from the plane containing the fracture traces. Thus, the location of the fracture plane center and its orientation is fixed. However, the fracture size and shape are generally not known and need to be defined. This analysis assumes that the fractures have a circular shape (aspect ratio 1:1), which is a common assumption of DFN models.

The fracture size was derived from the trace length analysis. It was assumed that the fractures with different flow discharges may have different sizes. Consequently, the analysis was conducted separately for F-, D-, and W- fractures. Fracman uses an algorithm described in Zhang (2002) [26] and La Pointe (2002) [27] to estimate fracture size (equivalent radius) from the trace length and offers different probability distributions for fitting the data. The power-law and lognormal distributions were considered in this analysis.

The results of the fracture size analysis are shown in Figure 7.1.4 for the power-law and in Figure 7.1.5 for the lognormal distribution. The distributions of W- and D- fractures are very similar and were combined in one. The F-fracture distribution is different from D- and W- fracture distributions. The trace length distributions of all sets are best described with the lognormal distribution. The power-law distribution, that is often assumed for fracture size, is not a good fit to these data.

The equivalent fracture radius distributions estimated from the trace length data are summarized in Table 7.1.2. The F- fractures with greater flow rates are also the ones with the larger size. This is consistent with the common concept that the fracture parameters affecting the flow (transmissivity and aperture) are positively correlated with the fracture radius.

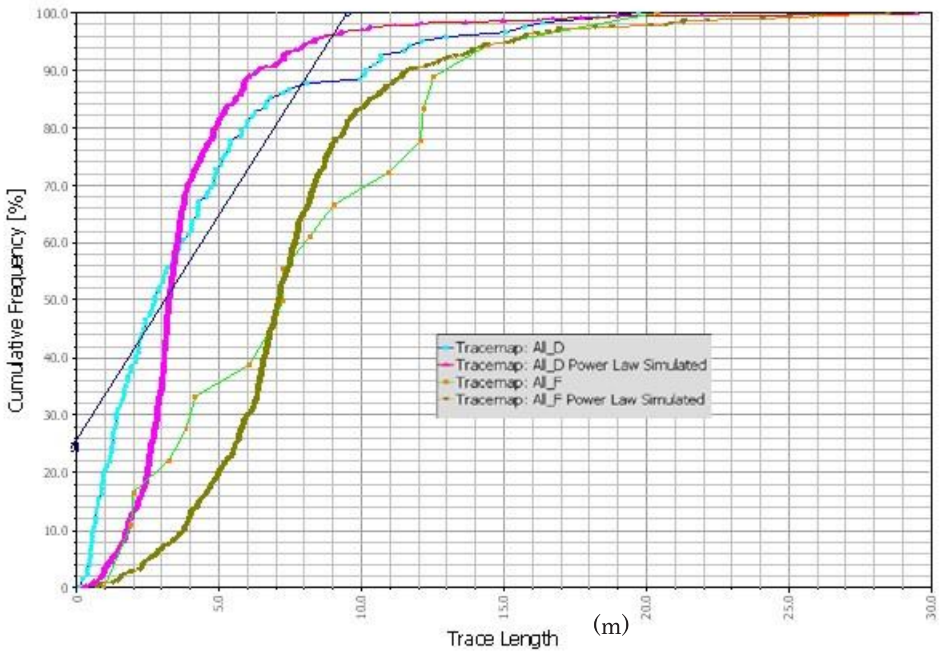

Figure 7.1.4 Power-Law Distribution Fit to the Fracture Trace Data.

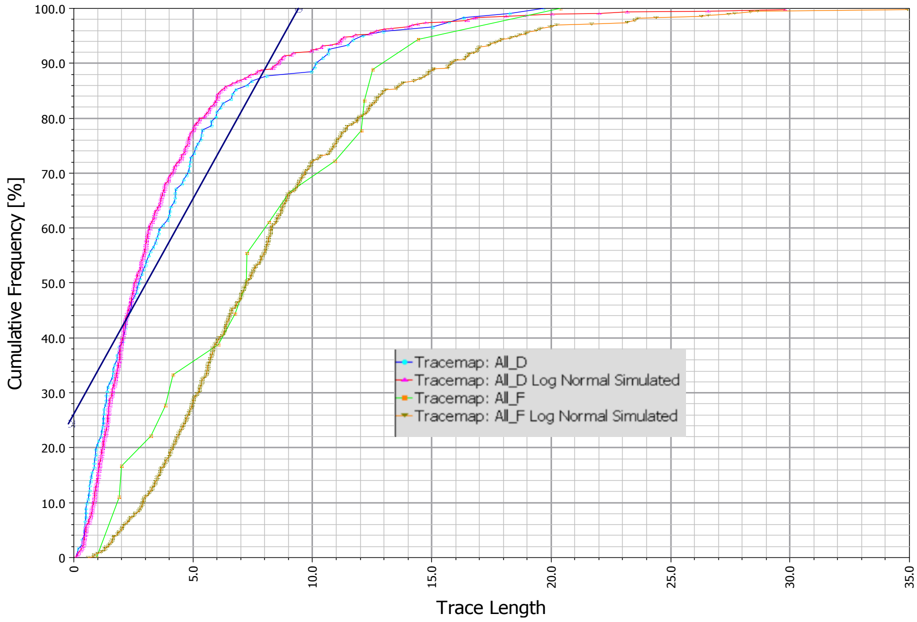

Figure7.1.5 Lognormal distribution fit to the fracture trace data.

Table 7.1.2 Equivalent fracture radius distribution parameters.

Fracture Set	Distribution Type	Mean/Minimum Radius (m)	Standard Deviation/Exponent
D- and W-Fractures	Lognormal	1.42	1.29
F-Fractures	Lognormal	3.88	2.15
D- and W-Fractures	Power-Law	1.5	3.4
F-Fractures	Power-Law	3.3	3.9

One hundred and forty six fractures were generated in the Research Tunnel using the lognormal distributions defined in Table 7.1.2 for the equivalent fracture radius (either F- or W- and D- depending on the fracture type). Note that the size of fractures will vary from realization to realization. Figure 7.1.6 shows the generated fractures for one realization.

The remaining fracture parameters that must be defined for DFN are fracture hydraulic conductivity (or permeability) and fracture aperture. Very few data are available on fracture aperture. Even when fracture aperture is reported, it seems to apply only to the surface of the tunnel or borehole walls. The values are too large (1 mm or greater) to be representative of the conditions within the rock mass. The fracture aperture values typical for granite rocks are in the order of tenths to hundreds of microns, except for the large fractures in fault zones [28].

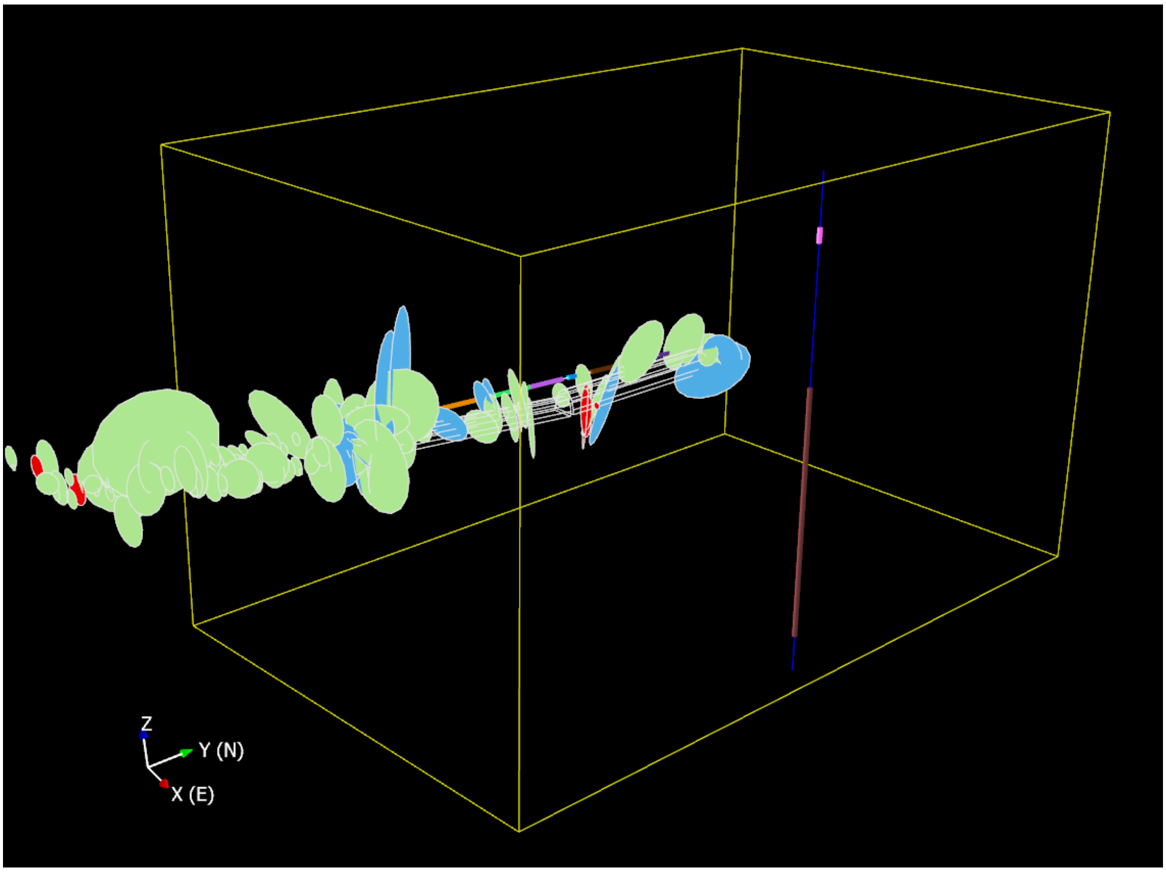

Note: F-fractures are shown in blue; D-fractures are shown in green; and -fractures are shown in red color.

Figure 7.1.6 Fracture generated in the research tunnel.

The hydraulic conductivity k_{int} was derived from the transmissivity evaluated in the packer tests T_{int} as:

$$k_{int} = \frac{T_{int}}{l_{int}} \qquad (7.1.1)$$

where l_{int} is the length of the test interval.

T_{int} measured in these tests represents the transmissivity of the test interval. A test interval may intersect different types of fractures with different connections to the fracture network. These fractures may have different size, hydraulic conductivity, and aperture. Thus, the interval transmissivity and hydraulic conductivity values cannot be easily converted to fracture transmissivity and hydraulic conductivity. The same principle applies to the observed inflow into the tunnel.

This analysis uses all available data in combination with the discrete fractures generated in the tunnel and borehole 12MI33 to evaluate fracture transmissivity. The initial evaluation of fracture transmissivity is based on the observed range of flow through the different types of fracture. The analytical solution for the unit inflow (Q) into a circular tunnel with radius r located at depth h[29] is:

$$Q = \frac{2\pi k(A+H)}{\ln(\frac{h}{r}+\sqrt{\frac{h^2}{r^2}-1}} \quad (7.1.2)$$

$$A = h(1-\alpha^2)/(1+\alpha^2) \text{ and } = \frac{1}{r}(h-\sqrt{h^2-r^2} \ ,$$

where k is the hydraulic conductivity.

The inflow through the fracture (Q_{fr}) with aperture b is:

$$Q_{fr} = Q \cdot b \ = \ \frac{2\pi T(A+H)}{\ln(\frac{h}{r}+\sqrt{\frac{h^2}{r^2}-1}} \quad (7.1.3)$$

$$T = k \cdot b$$

where T is fracture transmissivity.

Fracture transmissivity T was calculated from Eq. 7.1.3 assuming r = 2.5 m, h = 500m, and H = 110 m. The transmissivity of F- fractures (Q_{fr} > 1.0 L / min) is > 2.6 × 10^{-8} m^2 / s, transmissivity of D- fractures (Q_{fr} > 0.1 L / min) is > 2.6 × 10^{-9} m^2 / s, and the transmissivity of W- fractures (Q_{fr} < 0.1 L / min) *is* < 2.6 × 10^{-9} m^2 / s.

It was assumed that the inflow into CTD (Q_{CTD}) and Inclined Drift (Q_{Incl}) can be approximated by the following equations:

$$Q_{CTD} = Q_{CTD\_F} + Q_{CTD\_D} + Q_{CTD\_W} \quad (7.1.4)$$

$$Q_{CTD\_F} = 1.0\frac{L}{min} \cdot N_{F_{CTD}} \cdot c, \qquad Q_{CTD\_D} = 0.1\frac{L}{min} \cdot N_{D_{CTD}} \cdot c, \qquad Q_{CTD\_W} = 0.1\frac{L}{min} \cdot N_{W_{CTD}}$$

$$Q_{Incl} = Q_{Incl\_F} + Q_{Incl\_D} + Q_{Incl\_W} \quad (7.1.5)$$

$$Q_{Incl\_F} = 1.0\frac{L}{min} \cdot N_{F_{Incl}} \cdot c, \qquad Q_{Incl\_D} = 0.1\frac{L}{min} \cdot \mathrm{N}_{D_{Incl}} \cdot c, \qquad Q_{Incl\_W} = 0.1\frac{L}{min} \cdot N_{W_{Incl}}$$

where N_{F_CTD} and N_{F_Incl} is the number of F-fractures in CTD and Inclined Drift respectively, N_{D_CTD} and N_{D_Incl} is the number of D-fractures, N_{W_CTD} and N_{W_Incl} is the number of W-fractures, and c is a constant. Introducing c accounts for the fact that the flow through a fracture was express in terms of a value greater or smaller than a specific limit. The value of c = 2.3 was derived by matching the observed inflow into CTD and Inclined Drift with the inflow values calculated with Eqs. 7.1.4 and 7.1.5.

The Access Drift was not considered because of two reasons: it is outside the modeling domain and it is affected by the proximity to the Main Shaft fault and UHFD.

The observed and calculated values are summarized in Table 7.1.3. The fracture transmissivity values that correspond to the calculated inflow values are: 6.0 × 10^{-8} m^2 / s (F-fractures), 6.0 × 10^{-9} m^2 / s (D- fractures), and 2.6 × 10^{-9} m^2 / s (W- fractures).

Table 7.1.3 Comparison of measured and calculated inflow into the Research tunnel.

Research Tunnel Area	Measured Tunnel Inflow (L/min)	Number of Fractures			Calculated Inflow (L/min)			
		F	D	W	F	D	W	Total
CTD	13	4	15	3	9.2	3.45	0.3	12.95
Inclined Drift	43	14	42	N/A	32.2	9.66	0	41.86

The fracture aperture can be estimated from the cubic law relationship [30] between the transmissivity and aperture:

$$T = \frac{b^3}{12}\frac{\rho g}{\mu} \qquad (7.1.6)$$

where ρ is the water density, g is the gravity acceleration and μ is the water viscosity.

Assuming ρ=998 kg / m^3 and μ=0.001 N s / m^2 the calculated aperture values are: 42 micron (F-fractures), 20 micron (D-fractures), and 15 micron (W-fractures).

The fracture permeability (k) can be calculated as:

$$k = \frac{b^2}{12}\frac{\rho g}{\mu} \qquad (7.1.7)$$

The calculated fracture permeability values (approximation of mean) are: 1.5 × 10^{-10} m^2 (F-fractures), 3.2 × 10^{-11} m^2 (D-fractures) and 1.8 × 10^{-11} m^2 (W-fractures).

The following ranges were derived for the fracture parameters:

Fracture transmissivity: 2.6 × 10^{-9} - 6.0 × 10^{-8} m^2/s

Fracture permeability: 1.8 × 10^{-11} - 1.5 × 10^{-10} m^2

Fracture aperture: 15 - 42 micron

Note that these ranges apply to the average parameter values.

There is no enough data to develop probability distributions for permeability and aperture. Instead, this analysis assumes correlations between the lognormally distributed fracture equivalent radius (R) and fracture permeability (k) and aperture (b) in the following form:

$$k = \gamma_1 \cdot R^{\omega} \qquad (7.1.8)$$

$$b = \gamma_2 \cdot R \qquad (7.1.9)$$

where γ_1, γ_2, and ω are coefficients.

The coefficients were adjusted to match the calculated inflow into the tunnel with the observed inflow. Eq. 7.1.3 was used to calculate the inflow through each fracture shown in Figure 7.1.6. Each fracture has a different radius and, thus, different permeability and aperture (Eqs. 7.1.8 and 7.1.9) and different transmissivity (Eq. 7.1.6). A good match was obtained with the following coefficient values:

- $\gamma_1 = 1.55 \times 10^{-12}$
- $\gamma_2 = 1.16 \times 10^{-5}$
- $\omega = 2.3$

The results of the calculations with these coefficients are summarized in Table 7.1.4. The average transmissivity of fracture is 2.5×10^{-8} m^2/s. This falls into the estimated transmissivity range 2.6×10^{-9} - 6.0×10^{-8} m^2/s.

Table 7.1.4 Comparison of calculated inflow from generated fractures and observed inflow into Research tunnel.

Generated Fractures		
Type	∑ **Transmissivity** (m^2/s)	∑ **Inflow** (L/min)
D	1.94E-06	61.03
F	1.58E-06	49.78
W	9.71E-08	3.06
Total	3.62E-06	113.87
Measured Inflow into the Research Tunnel (L/min): 104		

7.1.3 Generating fractures using borehole 12MI33 fracture data

Borehole 12MI33 is a horizontal borehole that is parallel to the Research tunnel (Figure 7.1.1). The packer tests were conducted in 6 test intervals. The test intervals also serve as the monitoring points (Figure 7.1.2) for observation of temporal variations in pressure and geochemistry in the vicinity of the Research tunnel. Two hundred and ninety seven fractures were recorded in the borehole. The fractures were classified as “crack”, “hair crack”, “discontinuity crack”, and “mineral vein”. The fractures described as cracks that had recorded aperture values were assumed to be permeable fractures, such as F-, D-, and W-fractures observed in the Research tunnel. Seventeen such fractures were identified. The fracture data were imported into the model. The fractures were generated in accordance with these data (depth and orientation) using F-fracture lognormal distribution for fracture radius. F-fracture radius distribution produced closer results to the packer test results as shown below.

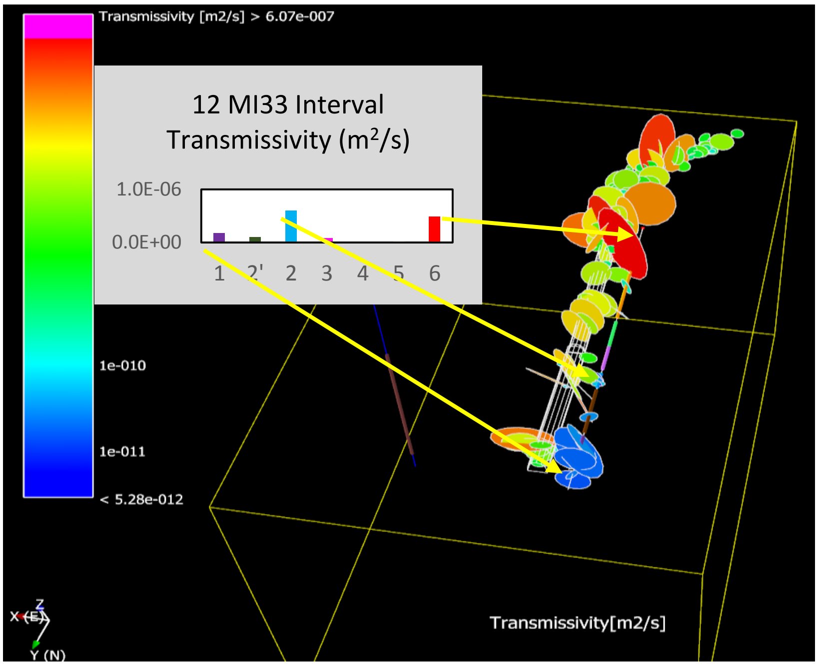

Figure 7.1.7 Transmissivity of fractures in the Research tunnel and borehole 12MI33.

The fractures generated in the borehole are shown in Figure 7.1.7 along with the Research tunnel fractures. Figure 7.1.7 also shows the transmissivity of the test intervals obtained in the packer tests. The high transmissivity intervals 1, 2' and 6 coincide with the zones in which fractures generated in both, Research tunnel and borehole, are present. Intervals 2 and 3 intersect a few fractures and their transmissivity is lower. Intervals 4 and 5 do not intersect any of generated fractures and their transmissivity is significantly lower.

Tables 7.1.5 and 7.1.6 compare the transmissivity of the generated fractures in borehole 12MI33 and the transmissivity of the test intervals from the packer tests in this borehole. The total transmissivity of fractures generated in the borehole (7.6×10^{-7} m^2/s) is close to the total transmissivity of the test intervals (9.9×10^{-7} m^2/s).

The following can be concluded:

- The locations of 17 fractures generated in borehole 12MI33 are consistent with the locations of fractures in the Research tunnel.
- Fracture properties derived from the Research tunnel fracture trace analysis are consistent with the packer test data in borehole 12MI33.

Table 7.1.5 Transmissivity of the generated fractures in borehole 12MI33.

Fracture	Transmissivity (m^2/s)	Fracture	Transmissivity (m^2/s)
1	1.14E-08	10	8.30E-09
2	2.71E-09	11	5.36E-09
3	1.74E-08	12	2.62E-09
4	7.26E-09	13	1.60E-08
5	1.39E-08	14	2.34E-08
6	2.94E-09	15	4.27E-07
7	6.28E-08	16	6.59E-08
8	5.01E-08	17	1.82E-08
9	2.30E-08	Total	7.58E-07

Table 7.1.6 Transmissivity of the test intervals from borehole 12MI33 packer tests.

Interval	Transmissivity (m^2/s)
1	1.78E-07
2'	9.78E-08
2	6.01E-07
3	8.65E-08
4	4.96E-09
5	1.93E-08
6	4.91E-07
Total	9.88E-07

7.1.4 Generating stochastic fractures in the modeling domain

The Research tunnel fracture trace analysis considered in Section 7.1.2 provided estimates of the fracture size, permeability, and aperture. These estimates were corroborated by comparing the packer test results with the transmissivity of fractures generated in borehole 12MI33 in Section 7.1.3. The fractures with the deterministic locations and stochastic properties (radius and correlated with radius permeability and aperture) were generated in the Research tunnel and borehole 12MI33 (Figure 7.1.7).

The size and properties of the fractures outside the Research tunnel and borehole 12MI33 can be assumed in accordance with the above estimates. However, the locations of these fractures are not known. Thus, the stochastic approach is needed. The stochastic generation of fractures requires the following input parameters:

- Number of fracture sets
- Orientation distribution of each set
- Fracture intensity in each set

7.1.4.1 Number of fracture sets and fracture orientation

The number of fracture sets and their orientation was obtained from the analysis of the fractures generated from the tunnel traces using Fracman tool Interactive Set Identification System (ISIS). ISIS [12)] defines fracture sets from field data using an adaptive probabilistic pattern recognition algorithm. ISIS calculates the distribution of orientations for the fractures assigned to each set and then reassigns fractures to sets according to probabilistic weights proportional to their similarity to other fractures in the set. The orientations of the sets are then recalculated and the process is repeated until the set assignment is optimized.

Figure 7.1.8 shows the ISIS set assignment results for the Research tunnel fractures. Even though 3 sets are defined, most of the fractures are in Set 2. The significance levels of the fitted Fischer distributions are low for all sets meaning there is no clear separation into the different sets.

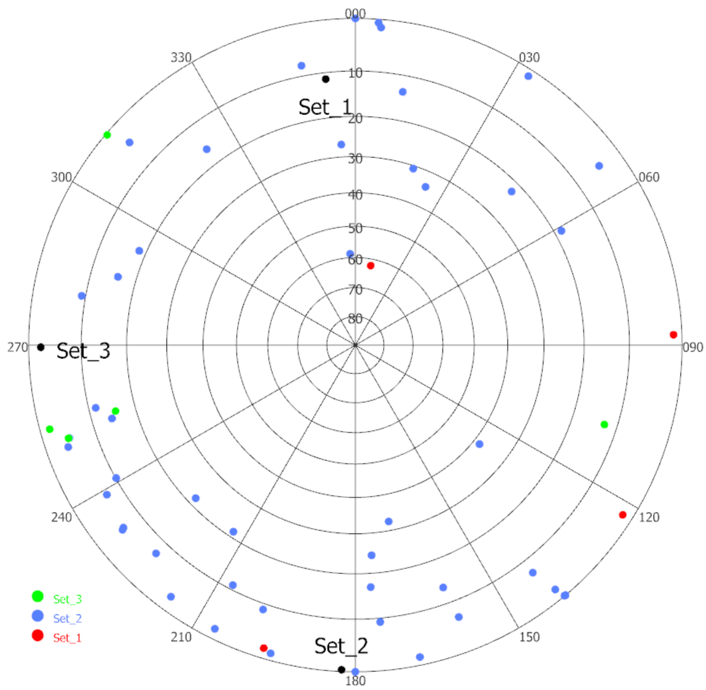

Figure 7.1.8 ISIS set assignment results for the Research tunnel fractures.

In the next step, the fractures in the Access Drift were removed from the analysis because they may be affected by the Main Shaft fault. For example, set 3 in Figure 7.1.8 contains only the Access Drift fractures. The ISIS analysis of fractures in the Inclined Drift and CTD identified only one fracture set. The best distribution (Kolmogorov-Smirnov probability 87%) was Fisher distribution with the flowing parameters:

- mean trend 208^0
- mean plunge 8^0
- concentration parameter k equal to 7

Note that orientation is given in the local coordinate system. The actual coordinate system was rotated 10.2^0 clockwise in the x-y plane to align the tunnel with the y-axis. The calculated Fisher distribution is shown in Figure 7.1.9. The low k signifies a large dispersion or wide range of fracture orientations.

7.1.4.2 Fracture intensity

Fracture intensity has a direct impact on how many fractures will be generated in the modeling domain. Fracture intensity can be specified either as number of fractures in the set (not recommended because it is scale dependent) or as volumetric intensity of fractures in the set, also known as P_{32}. P_{32} [1/m] is scale independent (invariant with respect to the distribution of fracture size) and represents fracture area per unit volume of rock. Neither number of fractures or P_{32} can be directly measured.

This analysis uses the observed linear intensity P_{10} (number of fractures per unit length) of fractures in the Research tunnel (0.19 fractures/m) and in the borehole 12MI33 (0.17 fractures/m) to evaluate P_{32}. The stochastic fractures were generated using Fisher distribution (Section 7.1.4.1), fracture radius (Table 7.1.2), fracture permeability (Eq. 7.1.8), and fracture aperture (Eq. 7.1.9). The fracture P_{32} value is iteratively redefined until the P_{10} values in 2 arbitrary placed imaginary horizontal boreholes matched P_{10} of fractures observed in the Research tunnel and borehole 12MI33.

Figure 7.1.10 shows the stochastic fractures intersected by the two imaginary horizontal boreholes with P_{32}=0.22 1/m. P_{10} in both imaginary boreholes (0.19 fractures/m) matches the observed P_{10} in the Research tunnel and is very close to the observed P_{10} in borehole 12MI33.

The significantly lower P_{10} values (0.04) were calculated for two arbitrarily placed vertical boreholes (Figure 7.1.11). This is because the vertical borehole has lower probability of intersecting sub-vertical fractures.

7.1.4.3 Comparison to the Packer Test results in Borehole MIZ-1

Figure 7.1.12 shows the stochastic fractures that intersect upper and lower test intervals of the vertical borehole MIZ-1. The transmissivity of the generated fractures is provided in Table 7.1.7. The packer test results are summarized in Table 7.1.8. The total transmissivity of generated stochastic fractures (2.1×10^{-7} m^2/s) is higher than the total transmissivity obtained in the packer tests (4.2×10^{-8} m^2/s). The horizontal flow to the vertical borehole in the packer tests is affected by the horizontal permeability. The horizontal permeability is lower than vertical because the fractures are sub-vertical. This can explain some of the difference. Also, only one realization was used in this comparison.

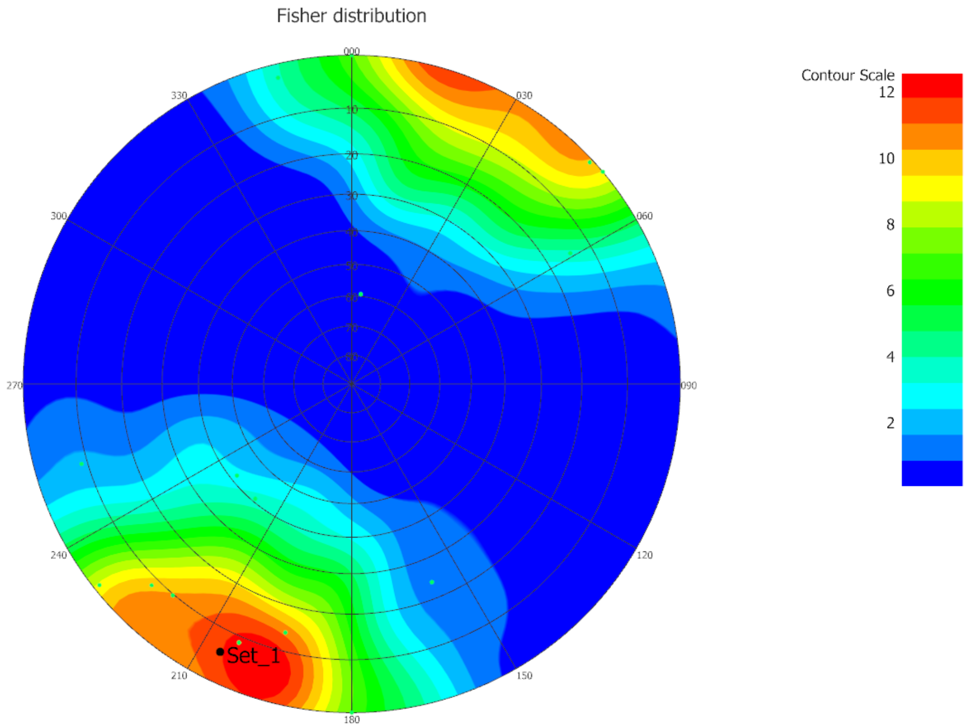

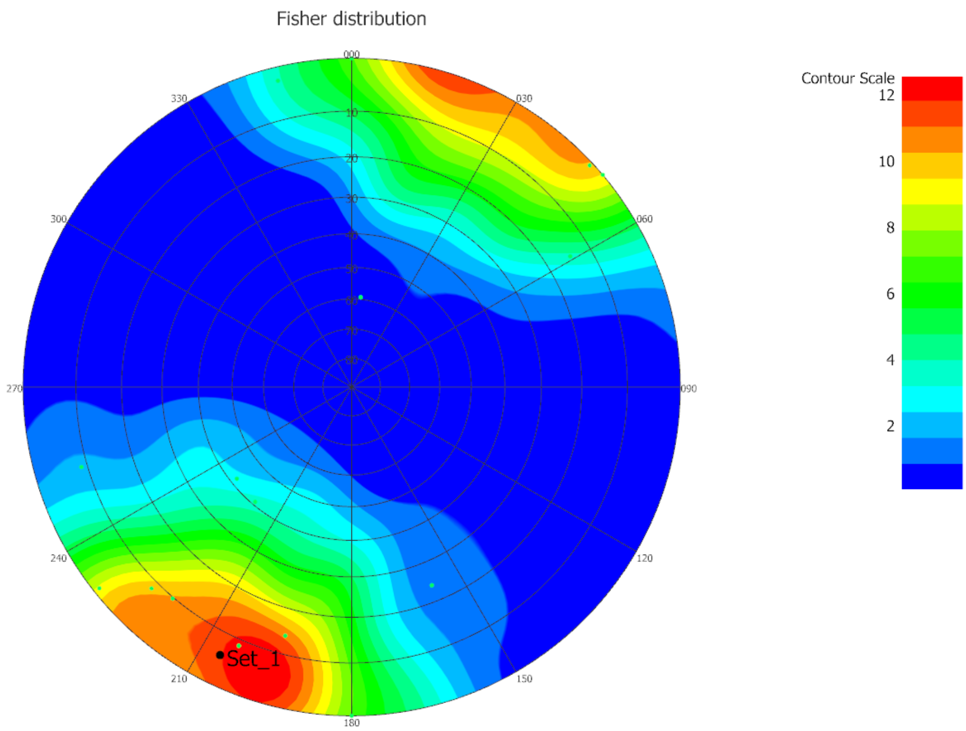

Figure 7.1.9 Calculated Fisher distribution for inclined drift and CTD fractures.

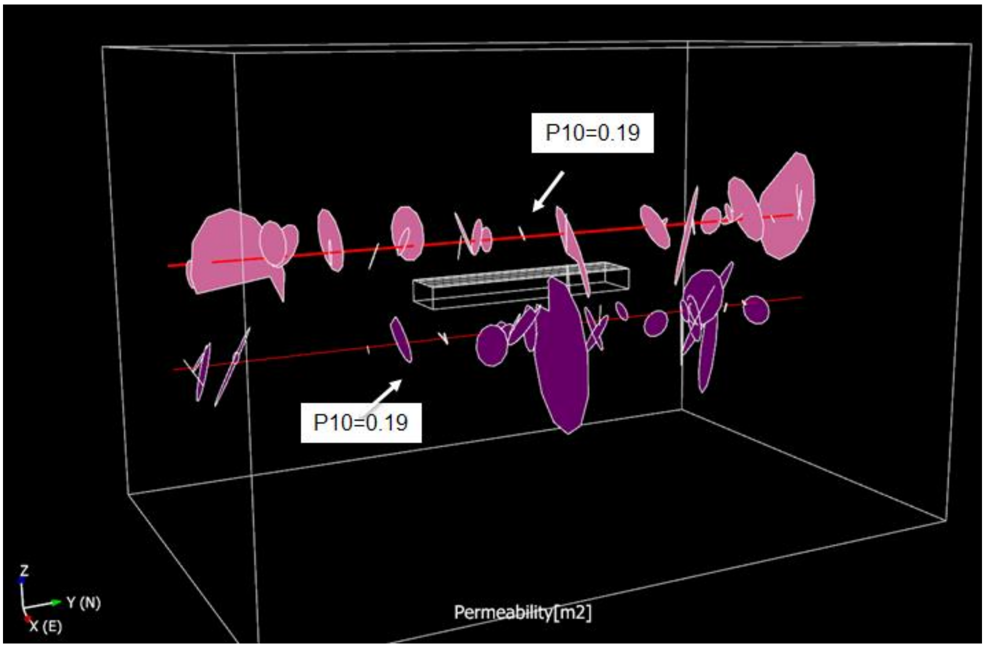

Figure 7.1.10 Stochastic fractures intersecting two imaginary horizontal boreholes.

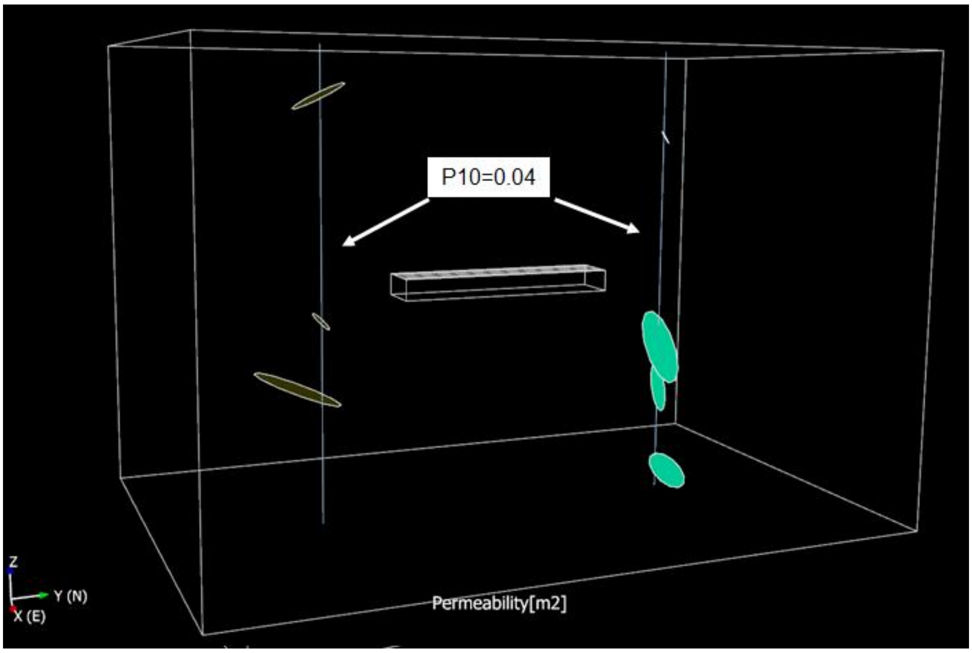

Figure 7.1.11 Stochastic fractures intersecting two imaginary vertical boreholes.

Table 7.1.7 Transmissivity of stochastic fractures intersected by Borehole MIZ-1.

Fracture	Transmissivity (m^2/s)
1	9.54e-08
2	3.54e-08
3	7.34e-09
4	2.52e-08
5	4.38e-08
Total	2.07e-07

Table 7.1.8 Packer Test results in Borehole MIZ-1.

Interval		Transmissivity (m^2/s)
Top (m)	Bottom (m)	
-260.4	-263.3	3.69e-08
-290.9	-342.4	5.16e-09
Total		4.20e-08

NOTE: Only the test intervals within the modeling domain are considered.

7.1.4.4 Stochastic fracture generation

The stochastic fractures were generated assuming one fracture set with the orientation defined in Section 7.1.4.1 and P_{32} = 0.22 calculated in Section 7.1.4.2. The Enhanced Baecher model in Fracman was used. In the original Baecher model [31)] the fracture centers are located uniformly in space, and, using a Poisson process, the fractures are generated as disks with a given radius and orientation. The Enhanced Baecher model extends the Baecher model by providing a provision for fracture terminations and more general fracture shapes.

Figure 7.1.13 shows one realization of the stochastic fractures generated in the modeling domain. The color scale is used to show fracture transmissivity. One realization of the fractures in the Research tunnel and borehole 12MI33 (Figure 7.1.7) is also included.

Figure 7.1.14 shows the stereonet of the generated stochastic fractures. Figures 7.1.15 and 7.1.16 show the sampled distribution of fracture permeability and aperture respectively. The median permeability is 2.3×10^{-11} m^2 and the median aperture is 27 micron.

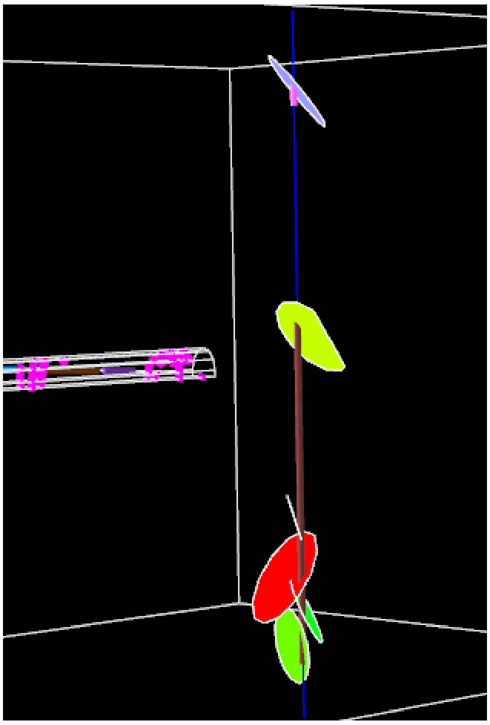

Figure 7.1.12 Stochastic fractures intersected by Borehole MIZ-1.

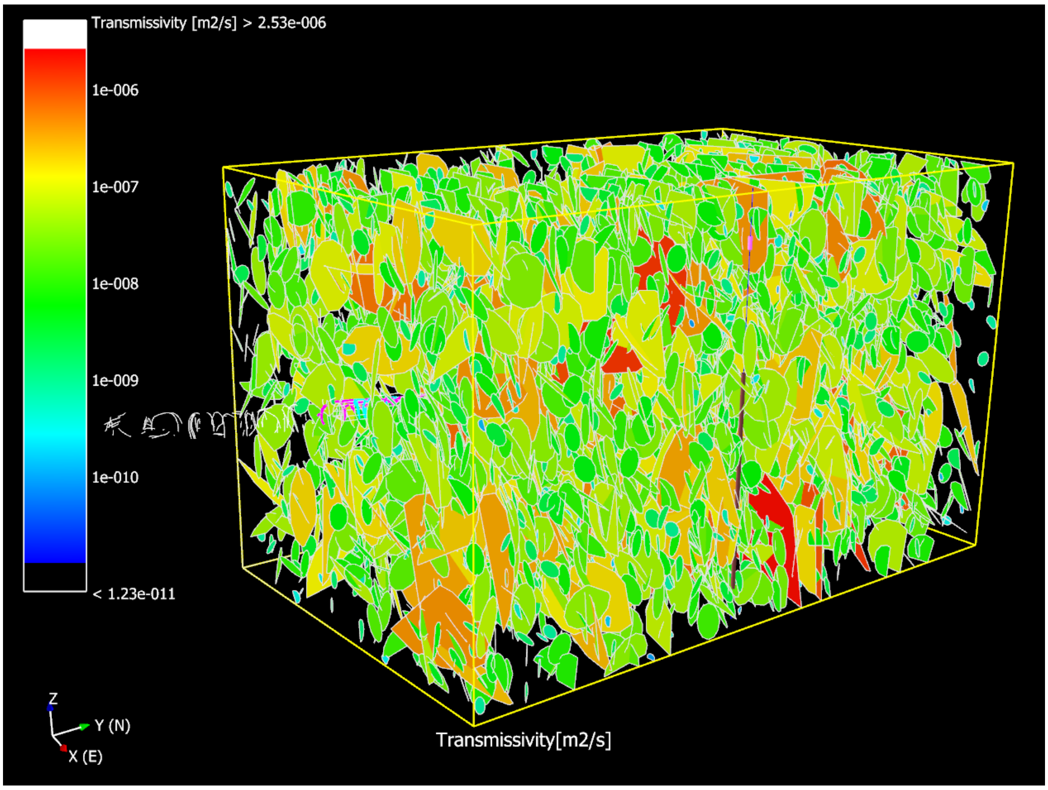

Figure 7.1.13 One realization of stochastic fractures generated in the modeling domain.

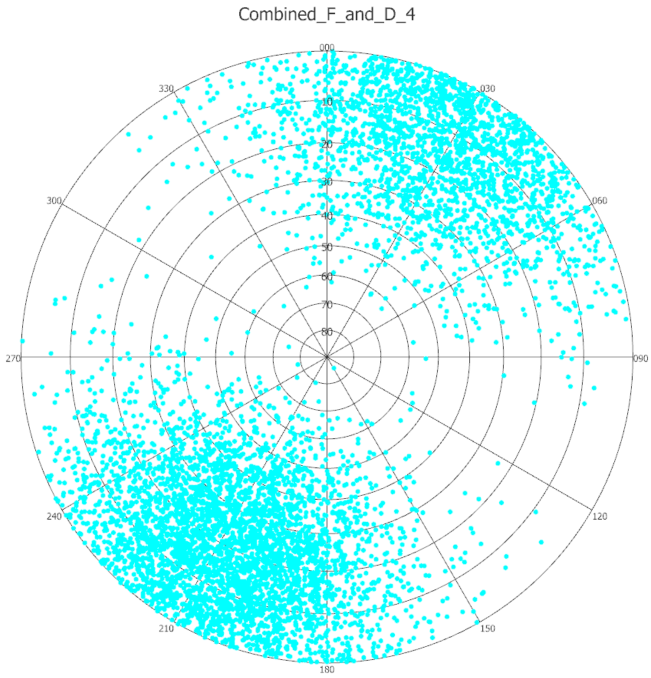

Figure 7.1.14 Sampled stochastic fracture stereonet.

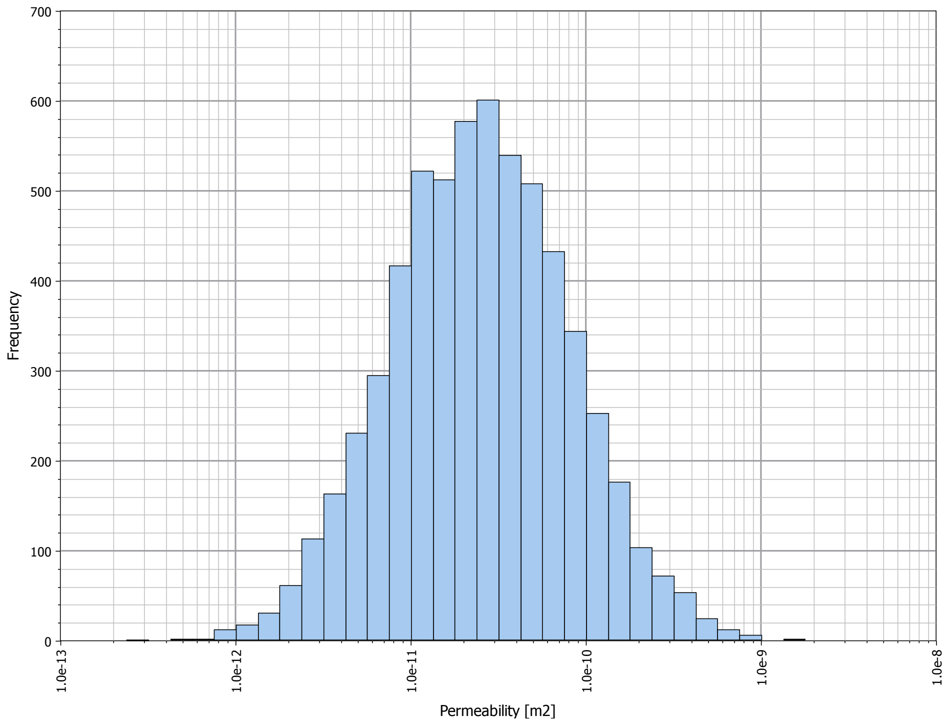

Figure 7.1.15 Sampled stochastic fracture permeability.

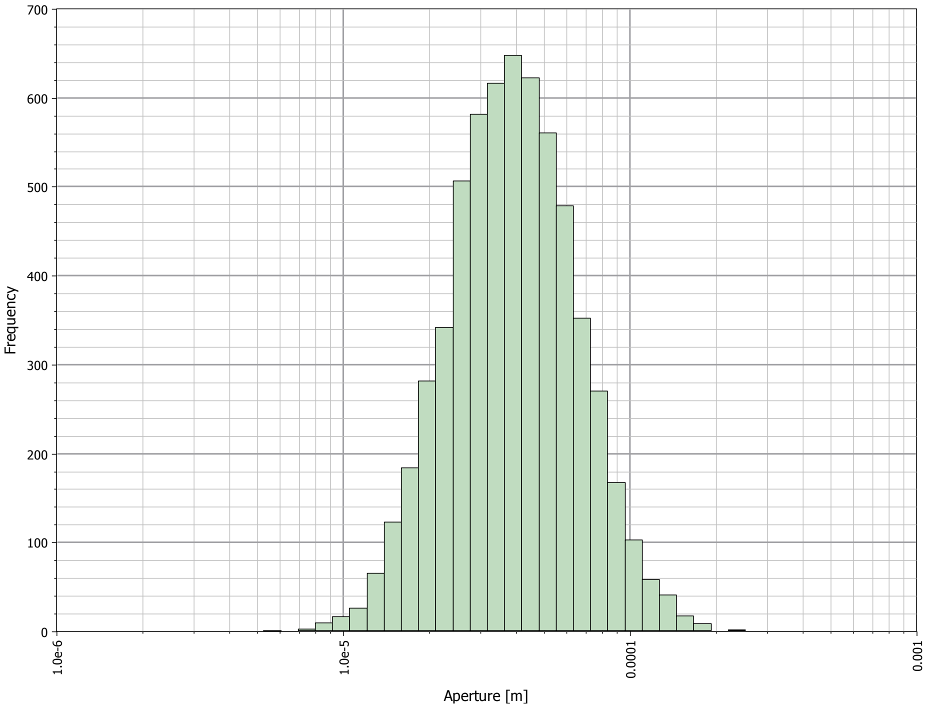

Figure 7.1.16 Sampled stochastic fracture aperture.

7.1.5 Upscaling DFN to the equivalent continuum model

After DFN is generated, it can be upscaled to an equivalent continuum model using Oda's method. Oda's method calculates permeability tensors in 3 dimensions for each cell. Oda tensor is a simplification of Darcy's Law for flow through anisotropic porous medium. The fracture permeability (k) is projected onto the plane of the fracture and scaled by the ratio between the fracture volume (porosity) and the volume of the grid cell. The method is implemented in Fracman in accordance with the following equation:

$$K_{i,j} = \frac{1}{12}(F_{k,k}\delta_{i,j} - F_{i,j}) \qquad (7.1.10)$$

$$F_{i,j} = \frac{1}{V}\sum_{k=1}^{N} A_k T_k n_{i,k} n_{j,k}$$

where $K_{i,j}$ is permeability tensor; $\delta_{i,j}$ is Kronecker's delta; $F_{i,j}$ is fracture tensor; V is grid cell volume; N is total number of fractures in grid cell; A_k is area of fracture k; T_k is transmissivity of fracture k; and $n_{i,k}$, $n_{j,k}$ are the components of a unit normal to the fracture k. Note that only principal components of the permeability tensor (K_{xx}, K_{yy}, and K_{zz}) are the inputs into the flow and transport model.

Fracture porosity (ϵ) of the grid cell is calculated as:

$$\in = \frac{1}{V}\sum_{k=1}^{N} A_k b_k \qquad (7.1.11)$$

where b_k is the aperture of fracture k.

The permeability and porosity of the grid cells without fractures can be defined in accordance with the matrix permeability and porosity. Figure 7.1.17 shows the grid cell permeability (K_{xx}) of the DFN realization shown in Figure 7.1.13. Figure 7.1.18 shows the vertical slices through CTD and Inclined drift.

Table 7.1.9 summarizes the mean properties of the grid cells in the modeling domain. The calculated mean permeability values are close to suggested reference permeability (1E-15 m^2). However, the permeability is anisotropic and changes over a few orders of magnitudes.

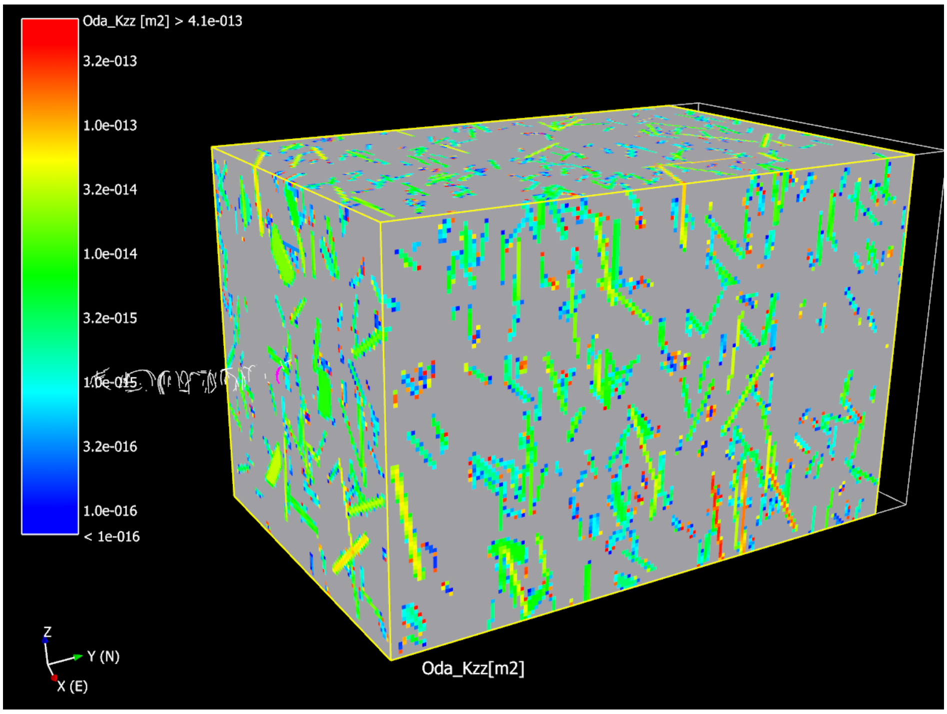

Figure 7.1.17 Vertical grid cell permeability for DFN realization shown in Figure 7.1.13.

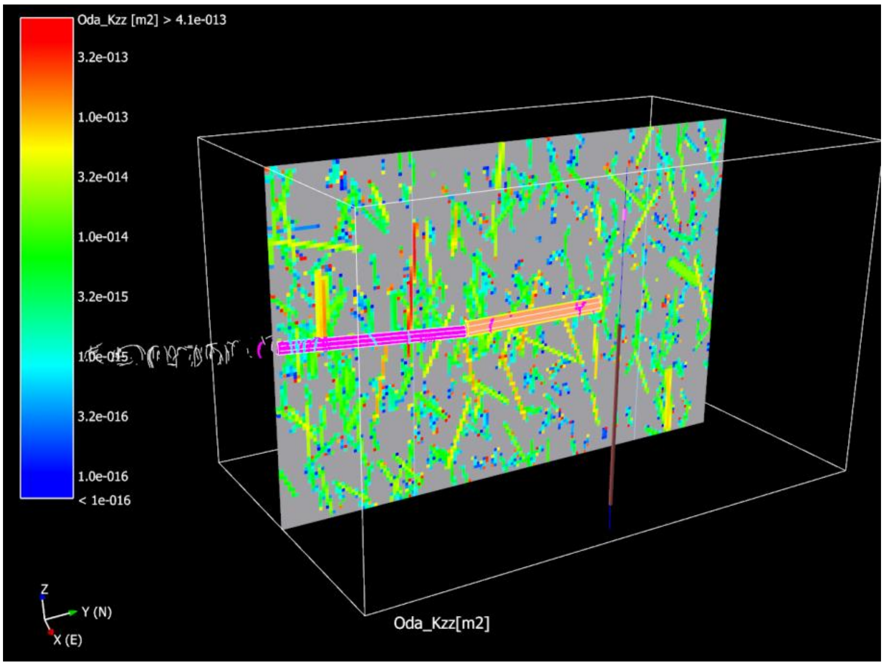

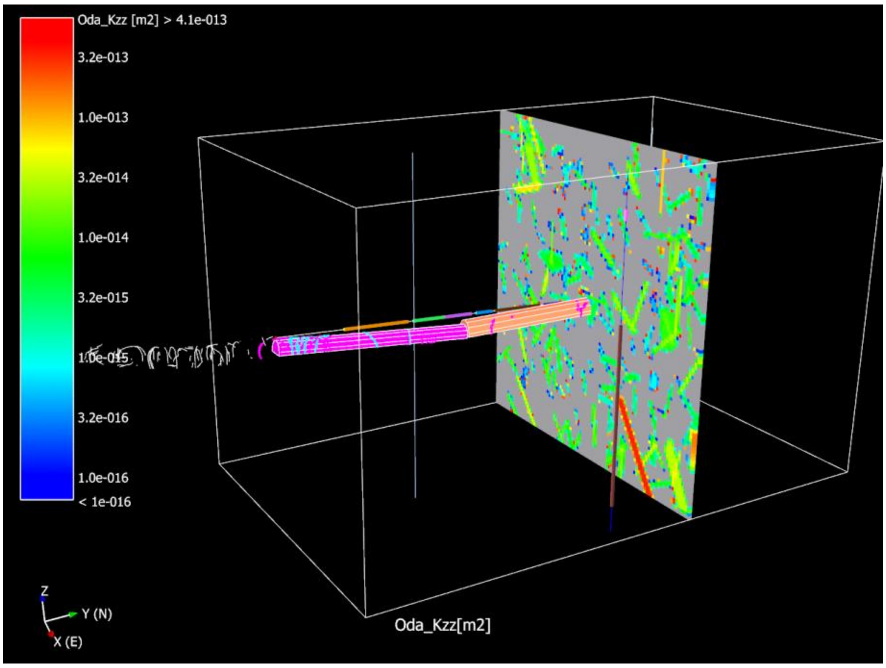

Figure 7.1.18 Vertical slices of vertical grid cell permeability for DFN realization shown in Figure 7.1.13.

Table 7.1.9 Effective continuum model mean grid cell properties.

Parameter	Notation	Mean Value
Permeability (m^2)	K_{xx}	3.04e-15
	K_{yy}	1.31e-15
	K_{zz}	3.5e-15
Anisotropy	K_{xx}/K_{zz}	0.87
	K_{yy}/K_{zz}	0.37
	K_{yy}/K_{xx}	0.43
Fracture Porosity	€	1.64e-05
Number of cells with fractures		40%

Note that the permeability and porosity values calculated with Eqs. 7.1.10 and 7.1.11 will be very low if the total area of the fractures ($\sum A_k$) is very small. The proposed cutoffs for permeability and porosity values are 1×10^{-19} m^2 and 1×10^{-8}. The cells with the permeability lower than 1×10^{-19} m^2 or / and porosity lower than 1×10^{-8} were matrix cells. The number of cells that were below the cutoff values is 1.1% of the total number of cells with fractures in the considered example.

7.1.6 Corroboration with the other studies of the Tono Area

A large amount of fracture data was collected in the Tono area. The fracture data analysis and development of the fracture models at the different scales is an ongoing effort. Bruines (2014) [22] describes the development of the discrete fracture network models for 2 scales – local (9 km × 9 km) and site-scale (2 km × 2 km). Both models extend from the surface to the depth of 2 km and are based on the data from MIU Project Phase I and II investigations.

The characterization of the fractured crystalline rock at the depth of the MIU is based on the data from the boreholes DH-2, DH-15, and MIZ-1 (Phase I data) and 33 boreholes drilled from galleries (Phase II data). The data includes well log data and hydraulic test data. Hydraulic tests were conducted in different sections of the boreholes on the different scales. The models consider both, UHFD and LSFD. The DFN models were upscaled to the equivalent continuum models for transport simulations. Bruines (2014) [22] provided a discussion of the methodology used to develop DFN and equivalent continuum models. However, the results of the analysis were provided only for UHFD. The authors noted that significantly less data is available for the LSFD. The fracture data for LSFD data can be found in JAEA report for boreholes DH-2, DH-15 and MIZ-1.

The modeling domain considered in this study is within the LSFD. It occupies a very small volume of the site-scale model [22]. The data used to develop the fracture model are primarily based on the Research tunnel fracture traces and fracture observations in borehole 12MI33. A portion of borehole MIZ-1 is within the modeling domain. The other boreholes are outside the modeling domain. The major goal of this section is to compare the parameters derived for the small-scale model to the parameters developed for the large-scale models.

The large-scale models use the following conceptual assumptions:

- The fractures are square shaped.

- The fracture size follows a power-law distribution.
- The fracture transmissivity is lognormally distributed and independent of fracture size.

The large-scale DFN was upscaled to the equivalent continuum model using three different grid block sizes: 30 m, 70 m, and 100 m.

As it was previously discussed, the small-scale model assumes the circular shape of fracture. The fracture size follows lognormal distribution (Section 7.1.2, Figures 7.1.4 and 7.1.5). The fracture permeability and aperture are correlated with fracture radius (the larger fractures have larger transmissivity). The small-scale DFN is upscaled to the equivalent continuum model with the grid block size of 1 m.

Both, large-scale and small-scale models assume that not all the fractures conduct flow. As it was shown in Ishibashi and Sasao (2015) [32], only a small portion of all observed fractures are open fractures. The large-scale model further assumes that only open fractures connected to the network conduct flow. These fractures are called the water-conducting features (WCFs). The fractures used in developing the small-scale model are the fractures in the Research tunnel that showed water discharge and the fracture in 12MI33 borehole with the recorded apertures (~10% of observed fractures).

7.1.6.1 Fracture size

The fracture size defined in Ando et al. (2012) for LSFD follows a power-law distribution with minimum 2.5 m, maximum 3,000 m and slope 4.1 (Table 5.3.3-1 in Ando et al., 2012 [33]). The fracture size in the small-scale model is based on the analysis of the fracture traces in the tunnel. The power-law distributions derived from this analysis (Table 7.1.2) have minimum size of 1.5 m and 3.3 m and slopes 3.4 and 3.9. These values are close to the large-scale model size distribution. However, as it was shown in Section 7.1.2, the lognormal distributions provided better fit to the data. The comparison between the large-scale and small-scale models is shown in Figure 7.1.19. While there are some differences, the distributions are similar.

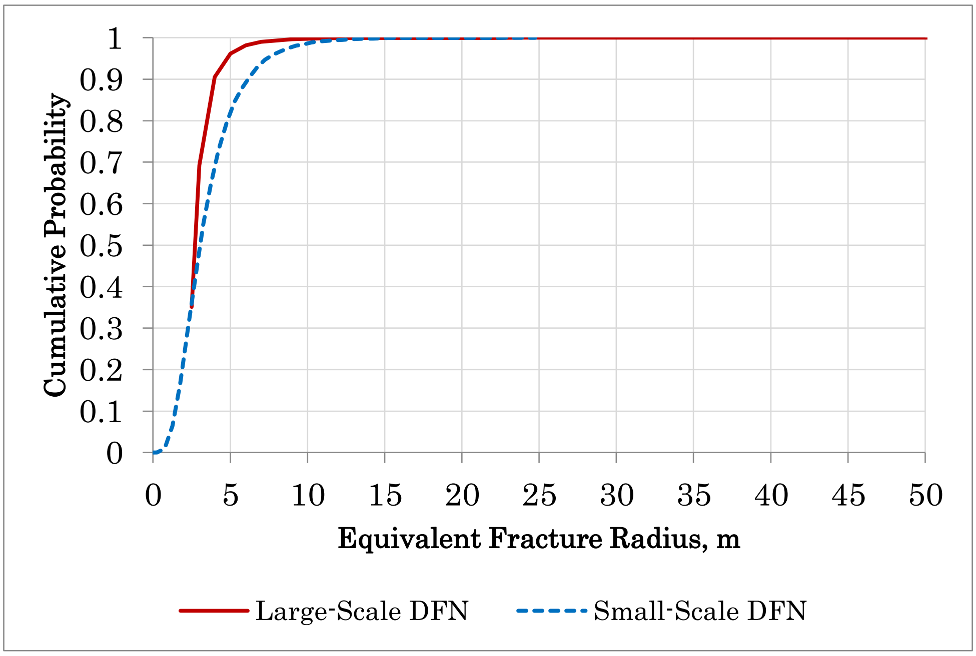

Figure 7.19 Equivalent fracture radius distributions in large-scale and small-scale models.

7.1.6.2 Fracture orientation and intensity

Ando et al. (2012) [33] described 4 sets of fractures in borehole MIZ-1 (Table 5.3.1.6). Three of these sets consist of north-trending sub-vertical fractures (total number of fractures in these sets is 12). The small number of fractures in each set and high values of Fisher dispersion coefficient (κ is 80-147) suggests that 3 sets could, in fact, be one set with lower κ (higher dispersion). Note that Golder (2017) [12] recommends using κ in the range from 20 to 50 for the low orientation variability. The average plunge in 3 sub-vertical fracture sets is 8^0, which is the same as the plunge defined for the stochastic fractures in the small-scale model. The fractures in the small-scale model are north-south trending as well. The additional set of sub-horizontal fractures could have been in the depth interval that is outside the small-scale model domain. The total liner intensity of the 3 sets of sub-vertical fractures in borehole MIZ-1 is 0.045 fractures/m (Table 5.3.1-6). This is consistent with P_{10} = 0.04 calculated for two arbitrarily placed imaginary vertical boreholes intersecting one realization of stochastic fractures (Figure 7.1.11).

The range in calculated (3 sets total) volumetric intensity (P_{32}) is from 0.01 to 0.28 m^2 / m^3 (Figure 5.3.1-20). The calculated P_{32} of the stochastic fractures (0.22) is within this range.

7.1.6.3 Equivalent continuum model hydraulic conductivity

The hydraulic conductivity of the large-scale equivalent continuum model was calculated using dynamic upscaling of large-scale DFN. Figure 7.1.20 shows the cumulative probability distribution of the effective hydraulic conductivity (borehole MIZ-1) for 100-m, 70-m, and 30-m grid block resolution cases (Figure 6.2.2-1). The effective value represents the mean of the hydraulic conductivity in 3 principal directions. The effective hydraulic conductivity of the small-scale equivalent continuum model (1-m grid block) was added to this figure for comparison.

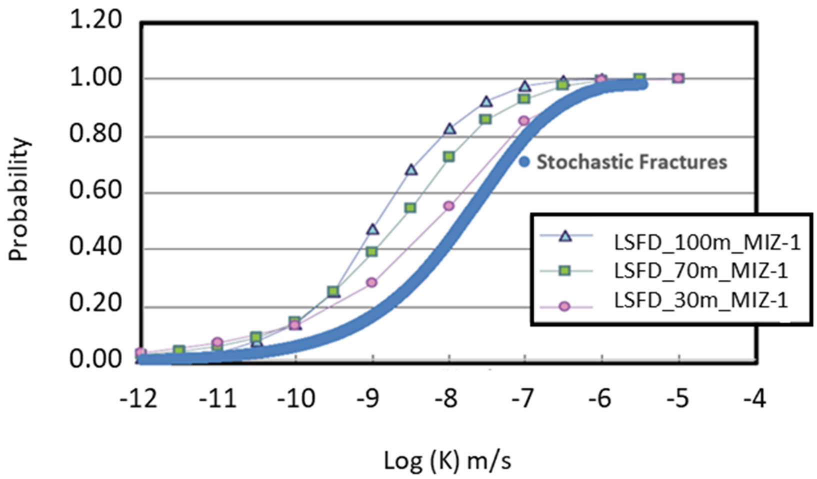

NOTE: This figure was copied from Figure 6.2.2-1 (a) in Ando, 2012[33]. The distribution obtained from the small-scale equivalent continuum model (stochastic fractures) was added to this figure for comparison.

Figure 7.1.20 Cumulative probability distribution of effective hydraulic conductivity in LSFD.

The hydraulic conductivity distribution of the small-scale equivalent continuum model is very similar to the hydraulic conductivity in the 30-m grid block large-scale model. Note that the distributions shift to the right when the grid block size decreases. Consequently, the additional shift can be expected when the grid block size change to 1 m (small-scale model).

The large-scale equivalent continuum model cumulative probabilities of the hydraulic conductivity in 3 principal directions (borehole MIZ-1) are shown in Figure 7.1.21 for 30-m grid block case (Figure 6.2.2-1 b) in Ando et al., 2012 [33]). The up-scaled permeability tensor has evident anisotropy consistent with the fracture orientation – the vertical hydraulic conductivity (K_{11}) is higher than horizontal (K_{22}) and the horizontal hydraulic conductivity is higher along the predominant fracture plane (K_{33}). The hydraulic conductivity in 3 principal directions of the small-scale equivalent continuum model was added to this figure for comparison. The anisotropy in hydraulic conductivity in the small-scale equivalent continuum model is similar to the one in the large-scale model - $K_{zz} > K_{xx} > K_{yy}$.

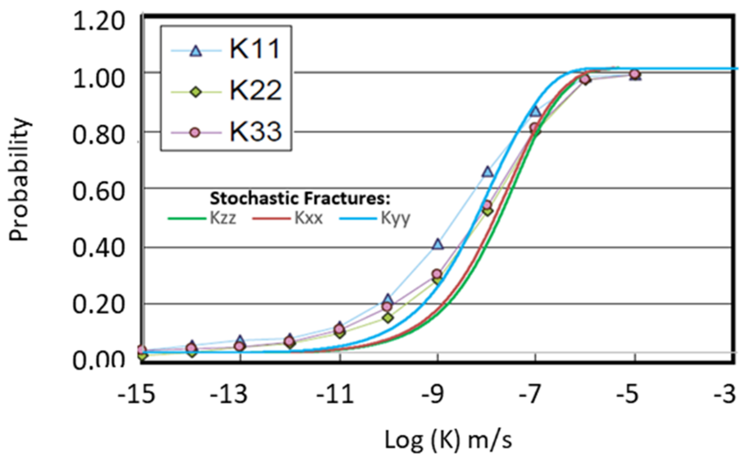

NOTE: This figure was copied from Figure 6.2.2-1 (b) in Ando, 2012 [33]. The distributions obtained from the small-scale equivalent continuum model (K_{xx}, K_{yy}, and K_{zz}) were added to this figure for comparison.

Figure 7.1.21 Cumulative probability distribution of hydraulic conductivity in 3 principal directions in LSFD in large-scale and small-scale models.

7.1.7 Stochastic fractures with two fracture sets

The stochastic fractures were also generated assuming two fracture sets. The first fracture set is the set described in Section 7.1.4.3. The second set is the north-west trending set in Figure 7.1.8. The Fisher distribution parameters for this set are:

- mean trend 303.50^0
- mean plunge 1.30^0
- concentration parameter κ equal to 3.6

The set fracture intensity was calculated the same way as described in Section 7.1.4.2. The set P_{10} was estimated to be 0.06 fractures/m. The calculated set P_{32} was 0.086 1/m.

The DFN with two fracture sets was upscaled to the ECM using the method described in Section 7.1.5. Table 7.1.10 summarizes the mean properties of the grid cells in the modeling domain with two fracture sets. Note that the anisotropy in permeability is similar to the anisotropy obtained with one fracture set. The mean effective permeability is 1.2 - 1.4 times higher in the case with two fracture sets.

Table 7.1.10 Two Fracture Sets Effective Continuum Model Mean Grid Cell Properties.

Parameter	Notation	Mean Value
Permeability (m²)	K_{xx}	3.50e-15
	K_{yy}	1.84e-15
	K_{zz}	4.15e-15
Anisotropy	K_{xx}/K_{zz}	0.84
	K_{yy}/K_{zz}	0.44
	K_{yy}/K_{xx}	0.52
Fracture porosity	€	2.1e-05

7.1.8 Summary

The goal of this analysis was to develop the DFN for the small-scale area surrounding the MIU Research tunnel at 500 m depth. The DFN model was upscaled to an equivalent continuum model with the grid cell size 1 × 1 × 1 m using Oda's method for the flow and transport simulations (Section 7.2).

The DFN model includes:

1) The fractures observed in the Research tunnel and borehole 12MI33. These fractures have deterministic locations and stochastic (radius, permeability, and aperture) properties derived from the fracture analysis.
2) Stochastic fractures (the location changes with each realization) generated based on the fracture size, orientation, intensity, and properties derived from the fracture analysis.

The major results of the fracture analysis are summarized in Table 7.1.11 and described below.

Table 7.1.11 Stochastic Fracture Properties.

Fracture Set	Trend (⁰)	Plunge (⁰)	Fisher Dispersion k	Volumetric Intensity P_{32} (1/m)
Set 1	208	8	7	0.22
Set 2	303	1.3	3.6	0.086

✓ ***Analysis of fractures traces on the walls of CTD, inclined drift, and access drift***

The analysis of the fracture traces in the Research tunnel considered 146 fractures that showed flow discharge. It concluded that the fracture size is best described with the lognormal distributions. The fractures with observed flow >1L/min (F-fractures) have the mean radius of 3.9 m (standard deviation 2.2). The fractures with the observed flow >0.1 L / min (D-fractures) have the mean radius of 1.4 m (standard deviation 1.3).

The analytical solution was used to calculate fracture transmissivity from the observed range of fracture discharge and the total discharge into the Research tunnel. The fracture aperture was calculated from the cubic law relationship between the transmissivity and aperture. The fracture permeability was calculated from transmissivity and aperture. The following ranges were derived for the fracture parameters:

- Fracture transmissivity: $2.6 \times 10^{-9} - 6.0 \times 10^{-8}$ m²/s.
- Fracture permeability: $1.8 \times 10^{-11} - 1.5 \times 10^{-10}$ m²
- Fracture aperture: 15 – 42 micron

It was assumed that fracture permeability (k) and aperture (b) are correlated with the equivalent radius (R). The following relationships were proposed:

$$k = 1.55 \cdot 10^{-12} \cdot R^{2.3} \quad \text{and} \quad b = 1.16 \cdot 10^{-5} \cdot R$$

✓ *Analysis of fractures observed in Borehole 12MI33*

Seventeen fractures with the recorded aperture values were assumed to be permeable fractures in borehole 12MI33. These fractures were generated using the same parameters as in the Research tunnel. The following conclusions were made:

- The locations of 17 fractures generated in borehole 12MI33 are consistent with the locations of fractures in the Research tunnel.
- Fracture properties derived from the Research tunnel fracture trace analysis are consistent with the packer test data in borehole 12MI33.

✓ *Analysis of fracture orientation and intensity for stochastic fracture generation*

- Analysis of fracture orientation concluded that there is one fracture set with the following Fisher distribution parameters:
- mean trend 208^0
- mean plunge 8^0
- concentration parameter κ equal to 7

Note that orientation is given in the local coordinate system. The actual coordinate system was rotated 10.2^0 clockwise in x-y plane to align the tunnel with the y-axis.

The observed linear intensity of the fractures in the Research tunnel and borehole 12MI33 P_{10} was used to calculate volumetric intensity P_{32}. The fracture P_{32} value was iteratively redefined until the P_{10} values in selected locations matched the observed P_{10}. The calculated P_{32} is 0.22.

✓ ***Upscaling to equivalent continuum model***

The DFN was upscaled to an equivalent continuum model using Oda's method. The following mean effective parameters were obtained (one realization):

K_{xx}	3.04e-15
K_{yy}	1.31e-15
K_{zz}	3.50e-15
Porosity	1.64e-05

The calculated mean permeability values are close to suggested reference permeability (1e-15 m^2). However, the permeability is anisotropic and changes over a few orders of magnitudes.

✓ ***Corroboration with the other studies of the Tono Area***

The parameters developed for the small-scale model were compared to the parameters incorporated in the large-scale models. The discrete fracture network models were developed for 2 scales – local (9 km × 9 km) and site-scale (2 km × 2 km). Both models extend from the surface to the depth of 2 km and are based on the data from MIU Project Phase I and II investigations.

The comparison was done for fracture size, orientation, intensity, and effective permeability. It was concluded that the parameters of the small-scale model are consistent with the parameters of the large-scale models.

7.2 Preliminary flow and transport modeling analysis

7.2.1 Introduction

A preliminary modeling analysis was developed using the GREET project data to predict inflow into the Inclined Drift and the Closure Test Drift (CTD) during excavation. The analysis is part of the activities of Task C, Step 1. This report summarizes current progress of the modeling work at Sandia National Laboratories.

The main aim of the current work is to predict inflow into the tunnel as excavation progresses, and provide pressure histories at selected monitoring locations. The project provided data of tunnel excavation progress as the Inclined Drift and the CTD were excavated. The original data was in the form of excavation progress in meters along the axis of the tunnel as a function of excavation dates. Figure 7.2.1 shows a modified version of the excavation progress obtained from the project in terms of days since excavation began. Time zero in Figure 7.2.1 refers to 4/6/2013 in the project data. Time 173 days refers to the completion of excavation of the CTD on or around 9/25/2013. The excavation data in Figure 7.2.1 have been used in simulations of inflow into the tunnel.

Simulations were conducted with PFLOTRAN, an open source, state-of-the-art massively parallel subsurface flow and reactive transport code [13] in a high-performance computing environment. For the analysis a computing system with a capacity of 1848 nodes with 29568 cores; and 64 GB RAM per compute node was used. The system has 600 teraFLOPS. The individual machines are 2.6 GHz Intel processors. For our simulations 5 nodes with 80 processors were sufficient.

The excavation progress was modeled by progressively removing material assigned as the host rock. This is equivalent to increasing the grid blocks representing the tunnel. A schematic diagram of the process is shown in Figure 7.2.2. To get a better representation of the excavation progress, a small portion of rock material was removed at a time. Thus, the material removal was in 1 m increments for a total of 103 m (i.e. 57 m of the Inclined Drift and 46 m of the CTD). This resulted in 103 PFLOTRAN runs applying the pressure and chlorine concentration boundary conditions assigned for the excavated area. The modeling was carried out with output of each PFLOTRAN run used as input for the next run until the complete excavation of the tunnel parts was complete. To automate the simulation process, the Sandia National Laboratories-developed optimization code, DAKOTA, Adam, et al. (2017) [34] was used as a driver to PFLOTRAN. A schematic diagram of the process is shown in Figure 7.2.3. DAKOTA also provides statistical analysis of the process, which will be used in future simulations.

Simulations were carried out for a homogenous representation using the Visualization Area domain, which is a CTD-scale domain recommended by the project, and a larger domain to test the boundary conditions. These simulations are detailed in Section 7.2.2. Simulations were also conducted for a fracture system developed based on the fracture analysis described in Section 7.1. The fracture modeling is described in Section 7.2.3. A summary of the simulation exercise is given in Section 7.2.4.

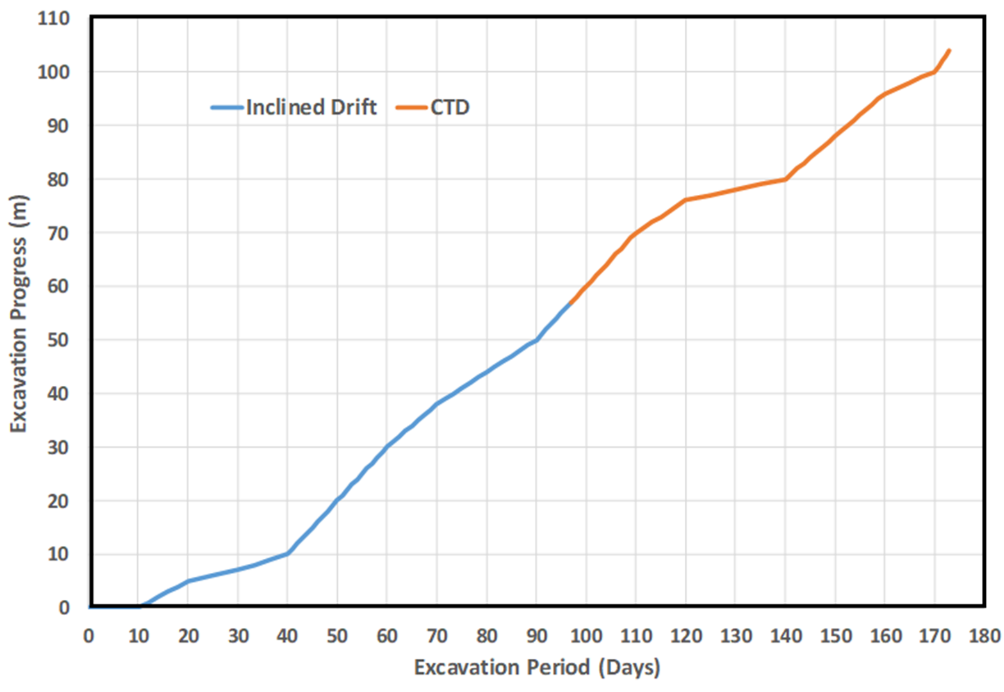

Figure 7.2.1 Data of excavation progress

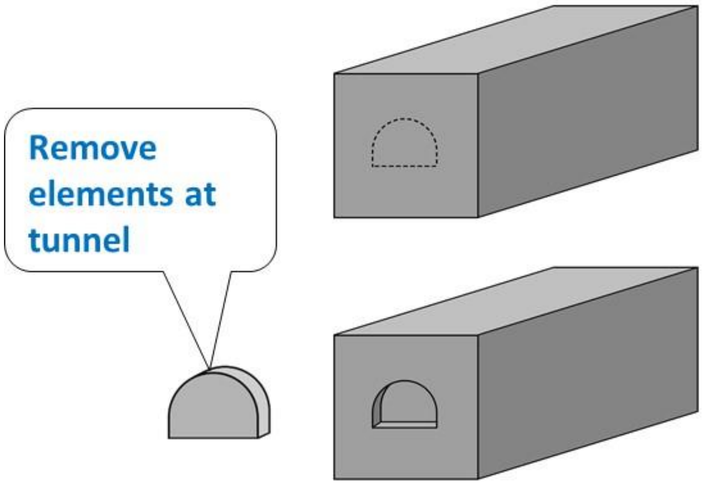

Figure 7.2.2 Schematic diagram showing simulation approach.

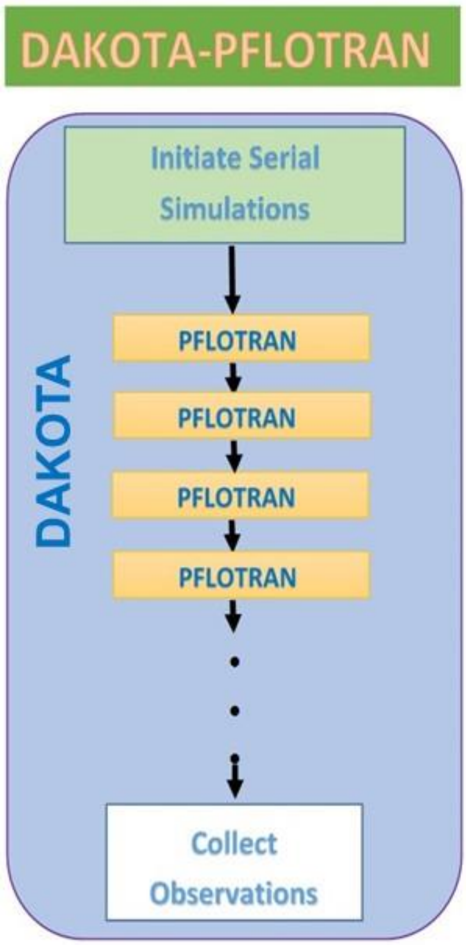

Figure 7.2.3 Schematic diagram for DAKOTA-PFLOTRAN coupling.

7.2.2 Homogenous model

7.2.2.1 Visualization Area Domain

Simulations were conducted for a homogenous model with reference hydraulic conductivity. As outlined by the Task C project, simulations were based on the Visualization Area domain specified by the project. The model has a geometry of 100 m × 150 m × 100 m in the x, y and z directions. The modeling domain is a CTD-scale model and incorporates the Inclined Drift and the CTD. The physical coordinates of the simulation domain are given in Table 7.2.1. The simulation domain also incorporates the monitoring sections in Well 12MI33. The coordinates of the monitoring section are given Table 7.2.2. A schematic representation of the modeled part of the tunnel and the monitoring well is shown in Figure 7.2.4.

For the simulations, a refined Uniform (structured) grid was selected, with grid block size of 1 m × 1m × 1m for a total of 1,500,000 grid blocks. The Inclined Drift is slightly inclined but was modeled as horizontal for ease of meshing. The tunnel was represented using a rectangular shape. The dimensions of these two tunnel parts are given below.

Inclined Drift	***CTD***
Length = 57 m	Length = 46.5 m
Width = 4.5 m	Width = 5.0 m
Height = 3.5 m	Height = 4.5 m

For the simulations, physical properties obtained from the monitoring borehole 12MI33 and other sources were used. The estimated hydraulic conductivity for Toki granite is in the range of log (-8 ± 1) m/s. The homogenous simulations used:

- Reference hydraulic conductivity 10^{-8} m/s (permeability 10^{-15} m^2)
- Porosity 0.001
- Effective diffusion coefficient 10^{-12} m^2/s

Initial and boundary conditions were based on those specified for Task C. Hydrostatic initial pressure conditions are represented by average head measurements of 110 EL m, based on data from monitoring wells. Top, bottom and side boundary conditions were also assigned head of 110 EL m. The excavated area was assigned a constant pressure boundary condition of 1.0 atmosphere. Head data were converted to pressure as shown below. For the conversion, the head of 110 EL m and elevation data in Table 7.2.1 were used.

Pressure at domain top = density × g × (head + elevation) = 3.6 MPa

Pressure at domain bottom = density × g × (head + elevation) = 4.6 MPa

Hydrostatic pressure boundary was assigned on the sides. Top and bottom boundary pressure values shown above were assigned. The initial and boundary conditions also include chlorine concentrations based on data from monitoring wells. For the simulations, the top and bottom boundaries were assigned 332 mg/L and 428 mg/L chlorine concentrations, respectively. The side boundaries were assigned a concentration gradient varying between the top and bottom boundary values. The excavated region was modeled as a free boundary.

Pressure monitoring points were setup using the coordinates in Table 7.2.2. The points were selected to be in the middle of the monitoring section. The chlorine concentration units were converted to molarity (M) for use in PFLOTRAN. The conversion is shown below, using Cl molecular weight of 35.453 g/mol:

Concentration at top = 332 mg/L / (1000 × 35.453 g/mol) = 0.0094 M

Concentration at bottom = 428 mg/L / (1000 × 35.453 g/mol) = 0.012 M

Table 7.2.1 Coordinates of CTD-scale simulation domain

E-W(m)	N-S(m)	E.L.(m)	
6522.7	-68943.5	-250.0	Upper boundary
6496.1	-68795.9	-250.0	Upper boundary
6397.7	-68813.7	-250.0	Upper boundary
6424.3	-68961.3	-250.0	Upper boundary
6522.7	-68943.5	-350.0	Lower boundary
6496.1	-68795.9	-350.0	Lower boundary
6397.7	-68813.7	-350.0	Lower boundary
6424.3	-68961.3	-350.0	Lower boundary

Table 7.2.2 Coordinates of monitoring section in borehole 12MI33

Section ID	Top			Middle			Bottom		
	E-W(m)	N-S(m)	E.L.(m)	E-W(m)	N-S(m)	E.L.(m)	E-W(m)	N-S(m)	E.L.(m)
12MI33_P1	6445.46	-68845.50	-303.27	6445.30	-68844.80	-303.30	6445.19	-68844.00	-303.36
12MI33_P2	6448.96	-68864.90	-302.24	6447.30	-68855.70	-302.70	6445.63	-68846.50	-303.22
12MI33_P3	6452.81	-68886.20	-301.11	6451.00	-68876.00	-301.60	6449.13	-68865.80	-302.19
12MI33_P4	6454.62	-68896.30	-300.57	6453.80	-68891.80	-300.80	6452.98	-68887.20	-301.06
12MI33_P5	6456.34	-68905.80	-300.07	6455.60	-68901.50	-300.30	6454.78	-68897.20	-300.52
12MI33_P6	6464.16	-68949.20	-297.76	6460.30	-68928.00	-298.90	6456.50	-68906.70	-300.02

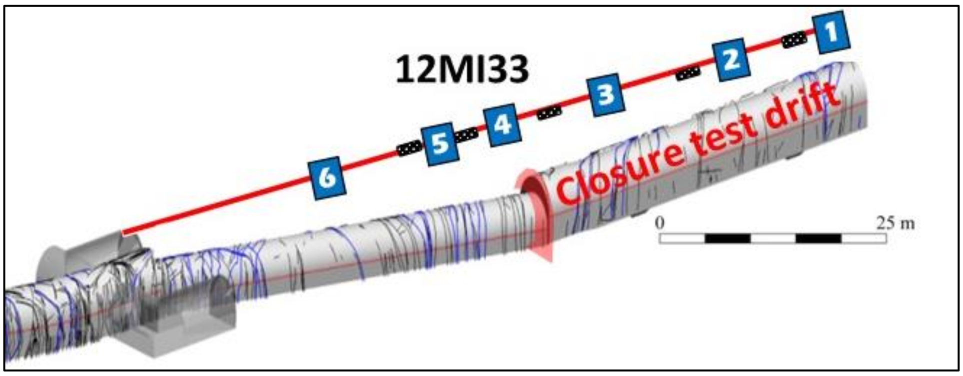

Figure 7.2.4 Schematic diagram showing the modeled part of the tunnel and the monitoring well 12MI33 with the monitoring sections

7.2.2.1 Homogenous model with Visualization Area domain simulation results

A steady state run was made to obtain initial pressure and chlorine concentration conditions before the excavation progress was modeled. Note that the steady state represents the condition before any excavation and is designed to apply the project specified boundary and initial conditions. Representation of the Inclined Drift and the CTD in the model are shown in Figure 7.2.5. Figure 7.2.6 shows distributions of the steady state pressure and chlorine concentration using the initial and boundary conditions described above. The figures show the pressure and concentration gradients as a function of depth.

Simulations of excavation progress were conducted using the steady state pressure distributions and constant pressure boundary conditions inside the tunnel. The DAKOTA-PFLOTRAN system described above was used to separately model excavation progress in the Inclined Drift and the CTD. The outputs were post-processed to evaluate inflow into the tunnel and pressure history at the observation points. Results of pressure and chlorine concentration distributions at 173 simulation time are shown in Figure 7.2.7. The figures represent fluid flow and chlorine transport into the tunnel as a result of the initial and boundary conditions. The left (south) side boundary conditions were set close to the inclined tunnel entrance, and the effect of that is shown in the figures. The left side of the figure in Figure 7.2.7 b) shows high concentrations at the inclined tunnel entrance. Figures 7.2.8 and 7.2.9 show predicted pressure vs. time and chlorine concentration vs. time at the selected monitoring points. Figure 7.2.8 shows higher pressure drawdown in Observation Section 6, which is closer to the Inclined Drift entrance (see Figure 7.2.4 for the relative location of monitoring points). The figure shows the lowest pressure drawdown in Section 1, which is close to the edge of the CTD. This is in line with expectations as the inclined tunnel was open for a longer period of time and thus more inflow compared to the CTD.

The flow of water into the excavated space (Inclined Drift and CTD) was also predicted based on the excavation progress. The output of the simulation was post-processed to determine inflow rate. The resulting inflow into the tunnel (Inclined Drift and CTD) is shown in Figure 7.2.10. Task C project experimental data on inflow into the Inclined Drift and the CTD are given in Table 7.1.3. The recorded inflow into the Inclined Drift is about 43 L/min, or 62.0 m^3 / day. The recorded combined inflow is about 56 L/min, or 80.6 m^3/day. These two data points are shown in Figure 7.2.10. The predicted inflow for the homogenous model with Visualization Area domain matches the data point for the Inclined Drift but over predicts the data point for the combined inflow. The inflow is a function of the boundary and initial conditions as well as material properties selected. Any of these variables could influence the prediction.

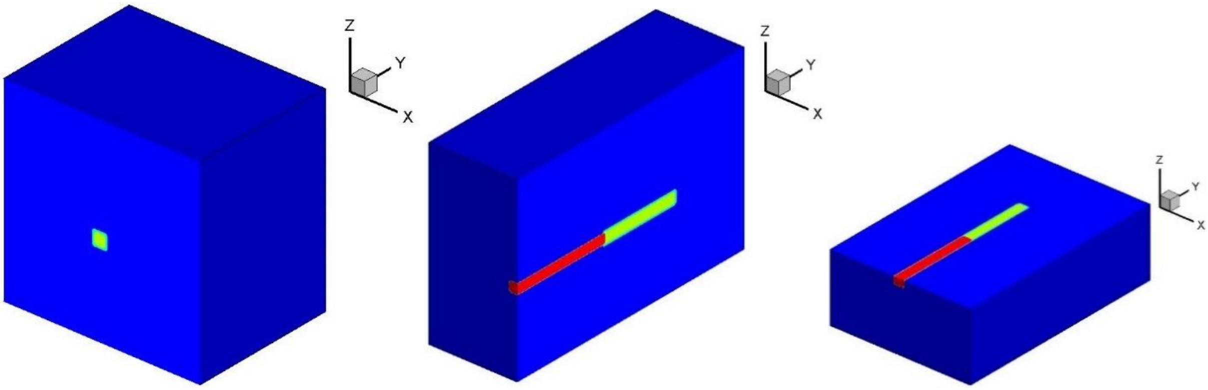

Figure 7.2.5 Placement of tunnel in simulation domain: Inclined Drift and CTD: Cross-section along a) x-axis, b) y-axis and c) z-axis.

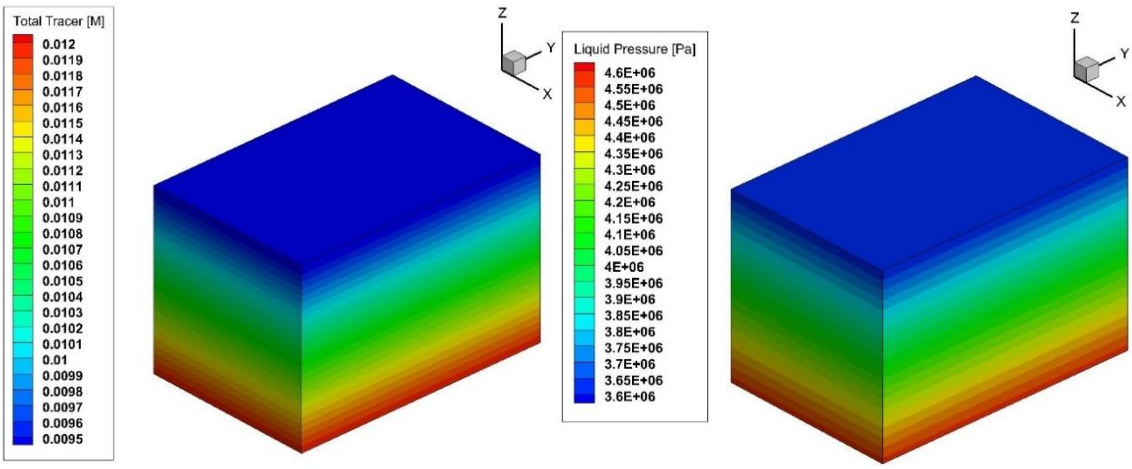

Figure 7.2.6 Steady state pressure and chlorine concentration distribution (molarity units): homogenous system.

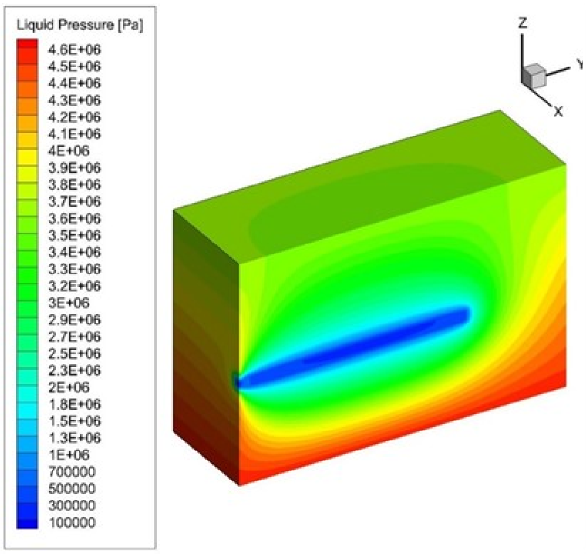

a) Pressure distribution: cross-section along the axis of the tunnel

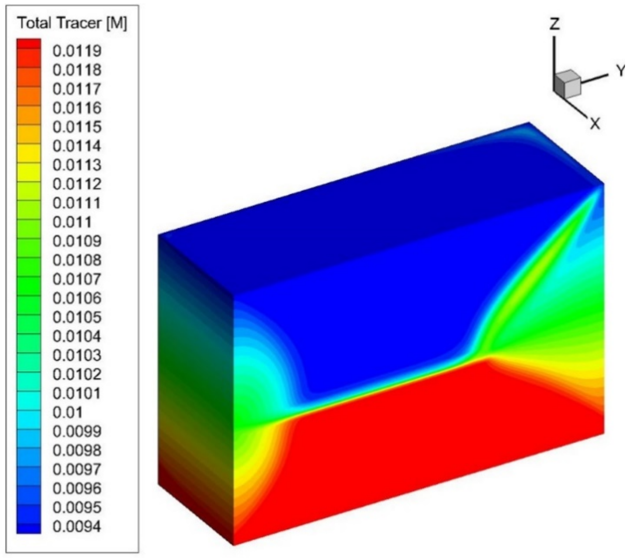

b) Chlorine concentration distribution: cross-section along the axis of the tunnel

Figure 7.2.7 Predicted pressure and chlorine concentration distributions after 173 days simulation time: homogenous system with Visualization Area domain.

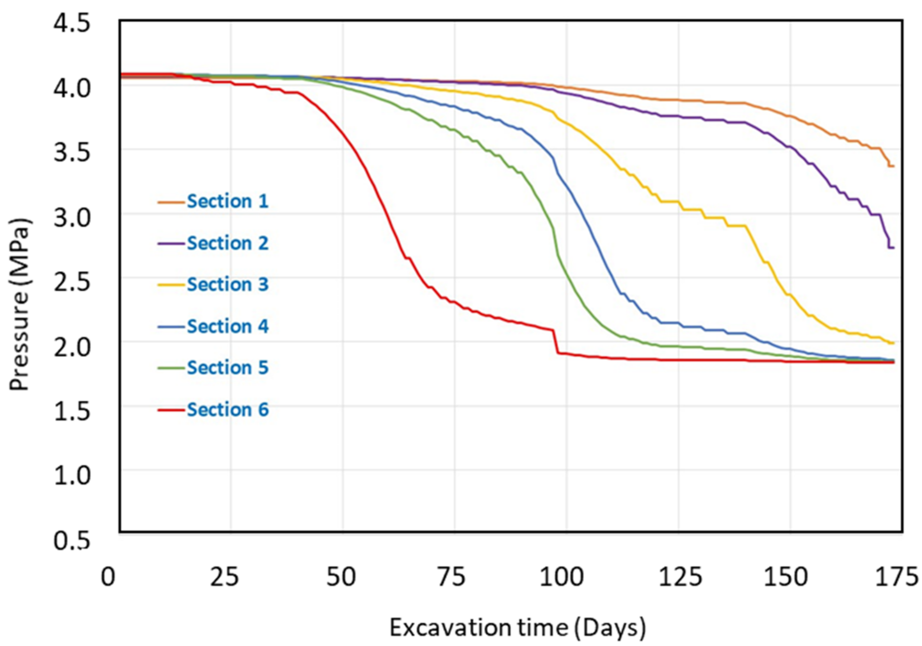

Figure 7.2.8 Predicted pressure history at observation points (in 12MI33) during excavation: homogenous system with Visualization Area domain.

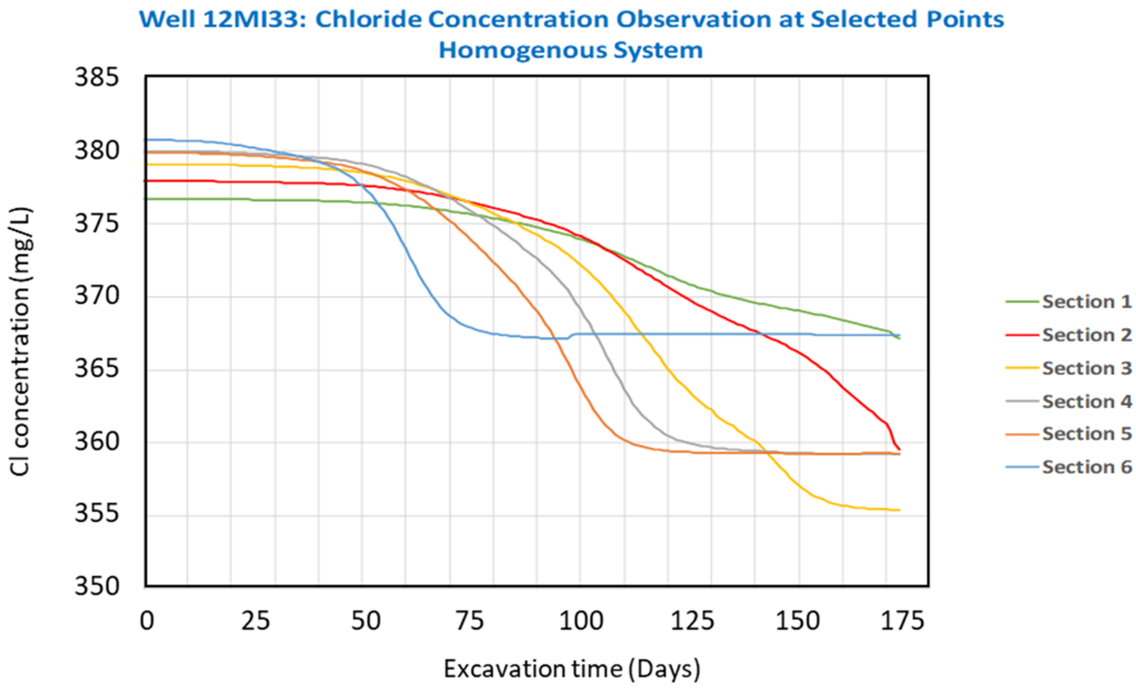

Figure 7.2.9 Predicted chlorine concentration history at observation points (Well 12MI33) during excavation: homogenous system with Visualization Area domain.

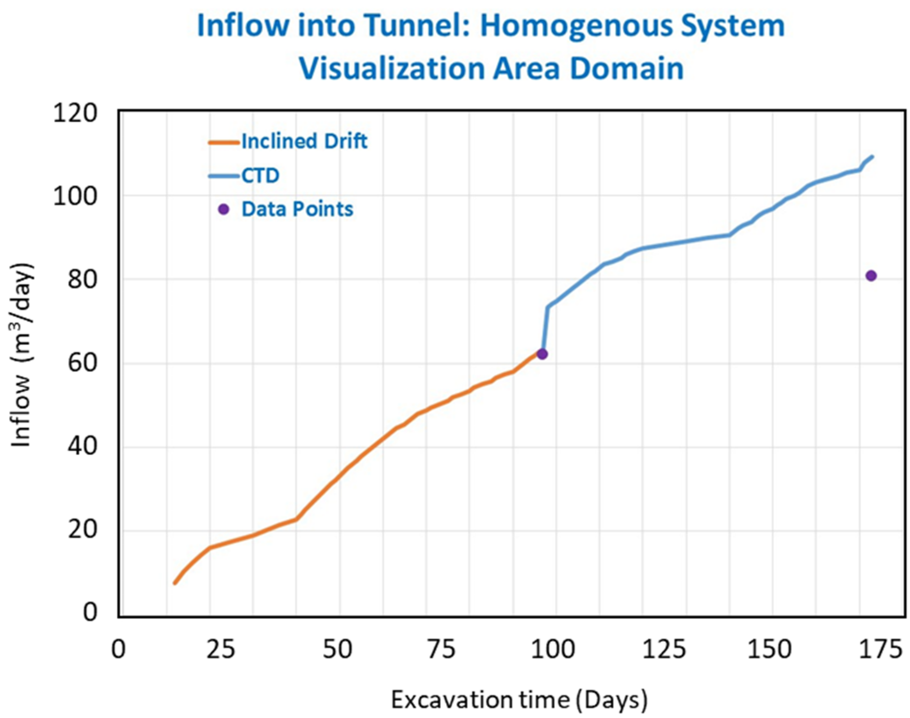

Figure 7.2.10 Predicted inflow into the Inclined Drift and CTD during excavation: homogenous system, Visualization Area domain. Note that the data points represent inflow at inclined drift-only and inclined drift + CTD.

7.2.2.2 Model with large domain

To study the effect of boundary conditions on the predicted output, a larger domain was selected. For the simulations, a grid with 2080 m × 2130 m × 700 m in the x, y, and z directions was used. The same grid block size (i.e. 1 m × 1m × 1m) as the previous model was applied to the Visualization Area. Outside of the Visualization Area, a progressive grid size was used. The new mesh size is 122 × 122 × 117 for a total 1,741,428 grid blocks. The larger domain mesh is shown in Figure 7.2.11. The same pressure and concentration gradient initial and boundary conditions as the previous model were applied. The same material properties were also used.

Simulations described in Section 7.2.1.1 for the Visualization Area domain using the coupled DAKOTA-PFLOTRAN codes were conducted. Simulation results are shown in Figures 7.2.12 to 7.2.16. Figures 7.2.12 and 7.2.13 show pressure and concentration distributions, respectively, at 173-days simulation time. The results do not show effects of boundary conditions as those of Figure 7.2.7 for the Visualization Area domain. The boundary conditions imposed on the left boundary of the Visualization Area domain that is more visible for chlorine concentration (Figure 7.2.7b)), are absent in Figure 7.2.13.

Predictions of pressure and concentration histories at observation points for the large domain case are shown in Figures 7.2.14 and 7.2.15, respectively. The pressure profiles at observation points are similar to those of the Visualization Area domain (Figure 7.2.8) but with larger drawdowns. The same trend is observed when comparing chlorine concentration profiles.

The flow of water into the excavated space (Inclined Drift and CTD) was also evaluated for the large domain homogenous model. The resulting inflow into the tunnel (Inclined Drift and CTD) is shown in Figure 7.2.16 together with the results for the Visualization domain and the data points. The predicted inflow for the homogenous model with large domain under-predicts the data points but is close.

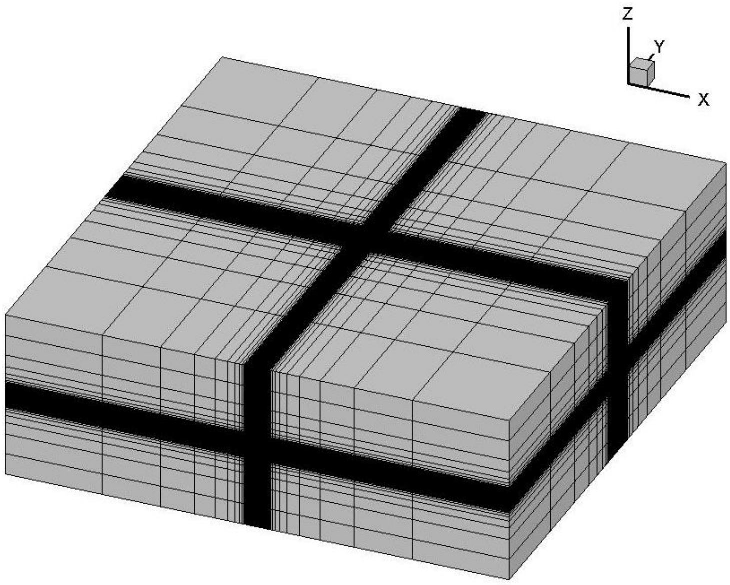

Figure 7.2.11 Grid for large domain

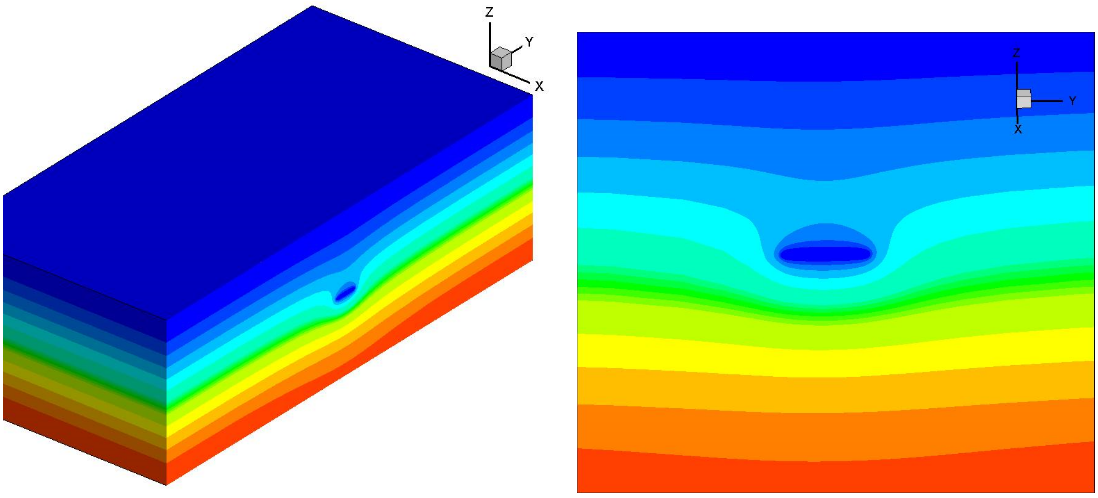

a) Cross-section along the axis of the tunnel

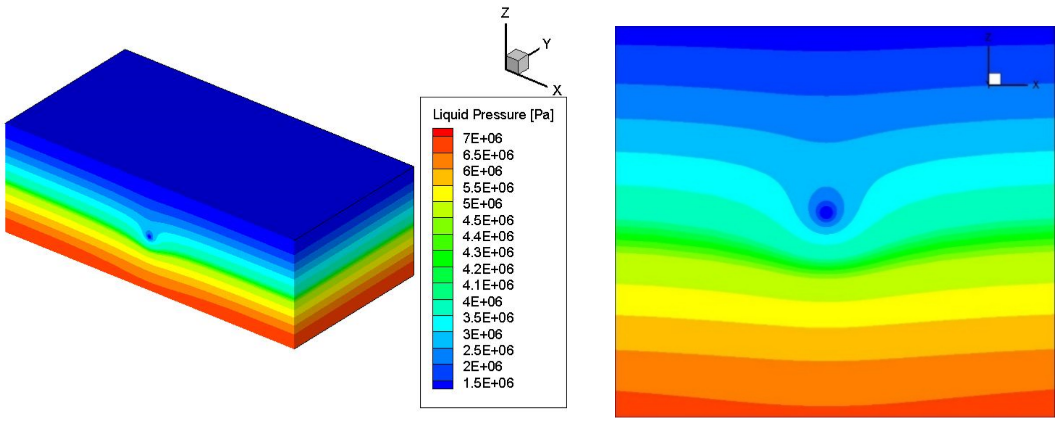

b) Cross-section perpendicular to tunnel axis

Figure 7.2.12 Predicted pressure distribution after 173-days simulation time: homogenous system with large domain.

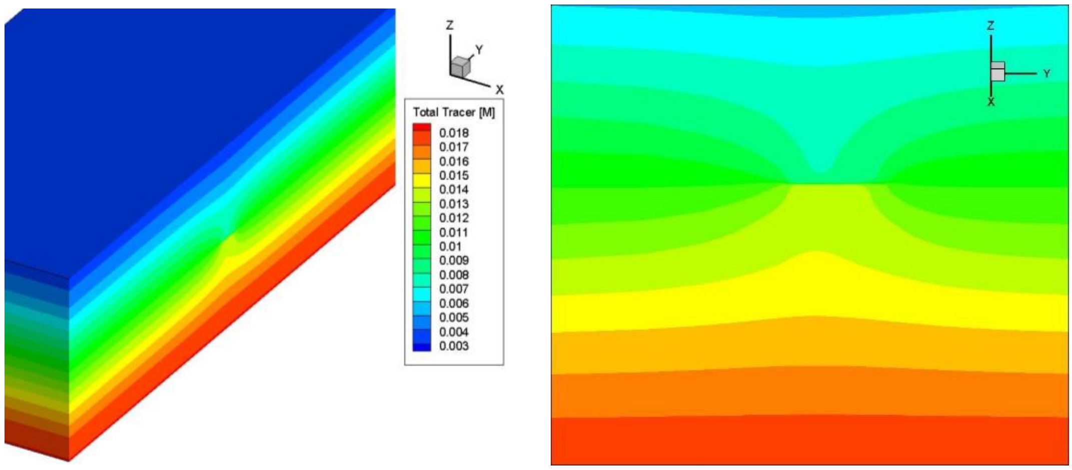

a) Cross-section along the axis of the tunnel

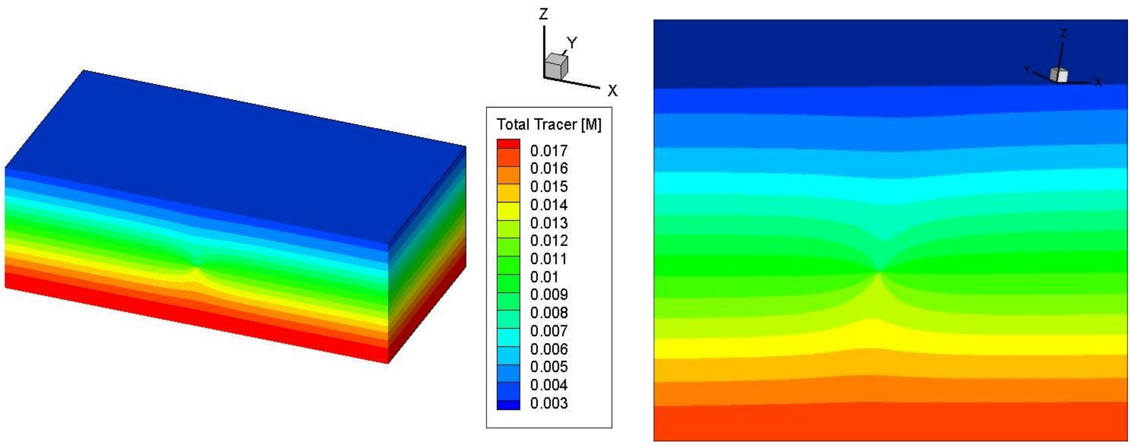

b) Cross-section perpendicular to tunnel axis

Figure 7.2.13 Predicted chlorine concentration distributions after 173-days simulation time: homogenous system with large domain.

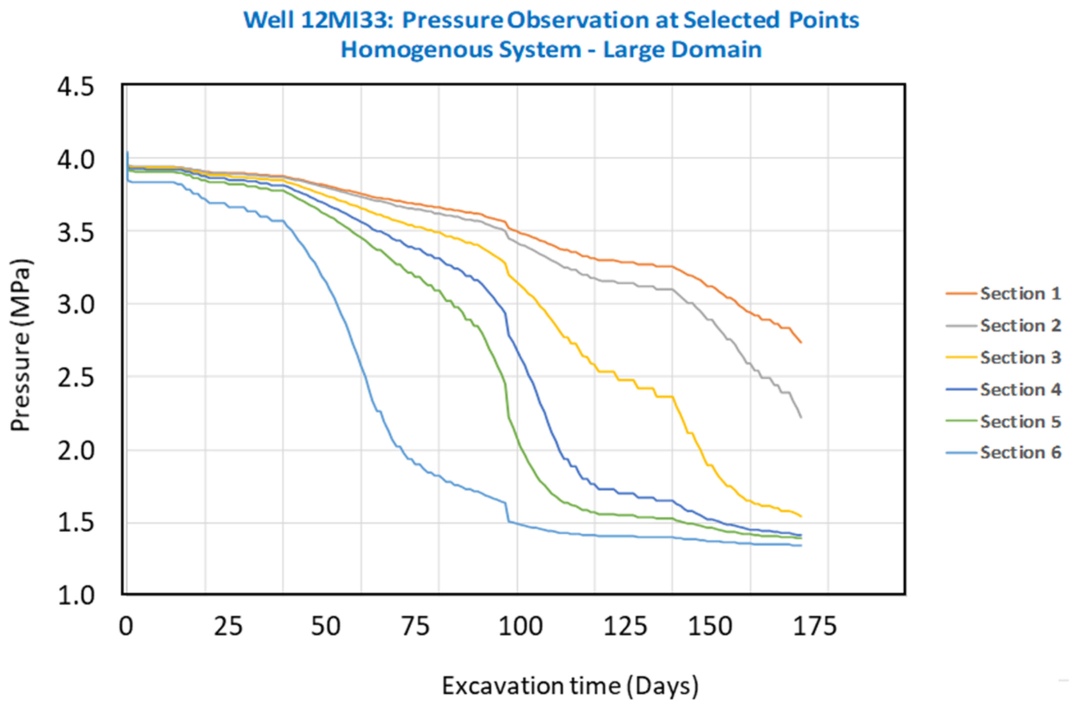

Figure 7.2.14 Predicted pressure history at observation points (in Well 12MI33) during excavation: homogenous system with large domain.

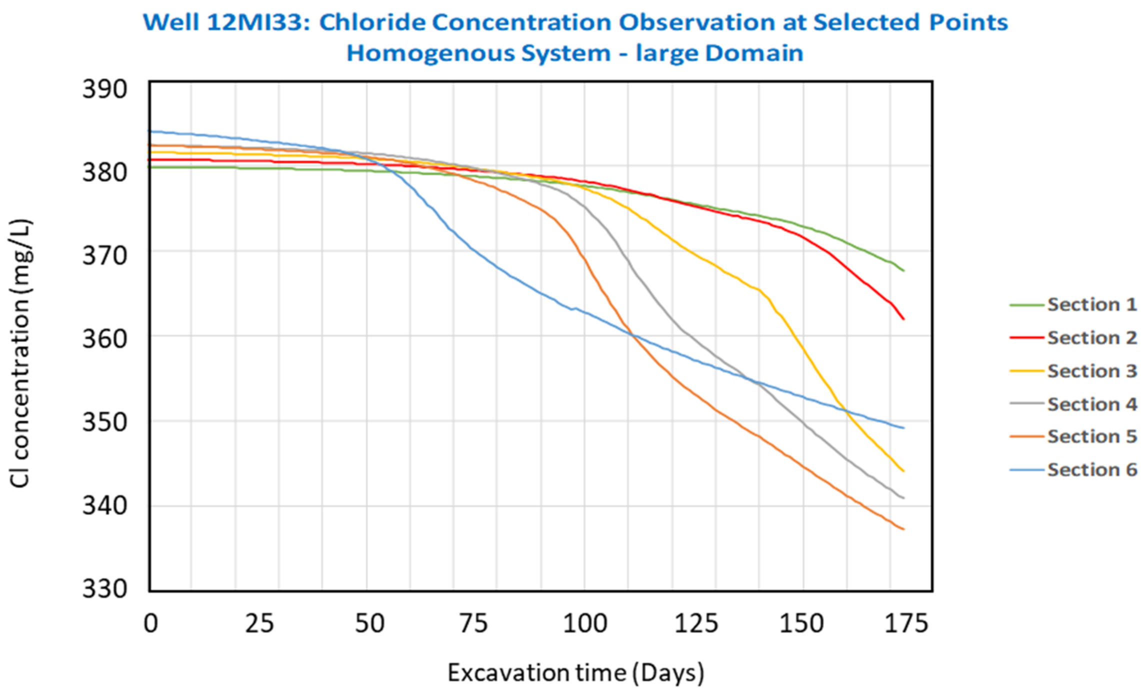

Figure 7.2.15 Predicted chlorine concentration history at observation points (Well 12MI33) during excavation: homogenous system with large domain.

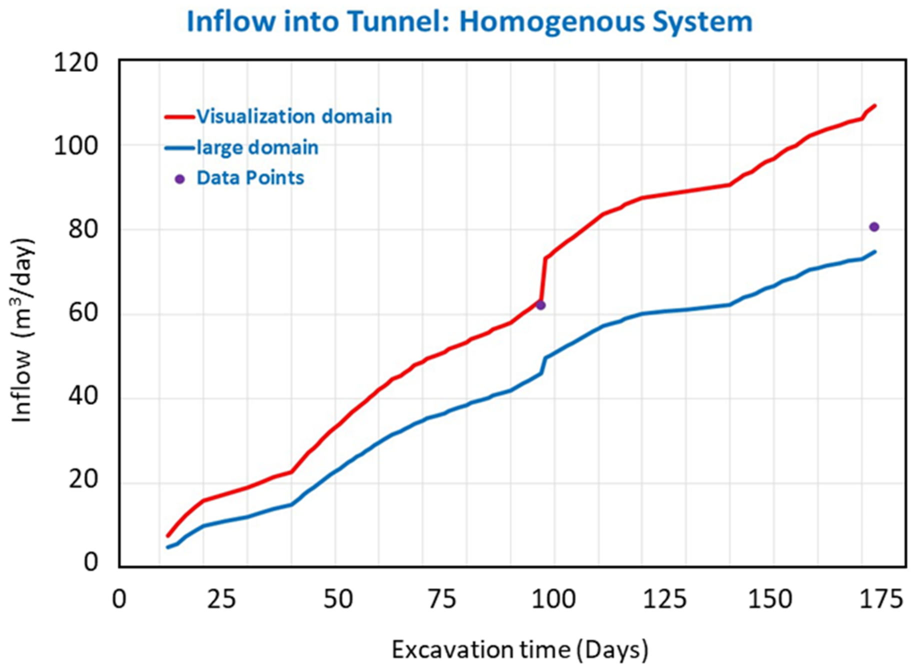

Figure 7.2.16 Predicted inflow into the Inclined Drift and CTD during excavation: homogenous system.

7.2.3 Fractured system model

Section 7.1 describes the fracture model development based on fracture data collected from the excavated areas and boreholes. The analysis produced up-scaled permeability and porosity data for flow and transport modeling of the excavation process. Permeability and porosity fields were obtained for two realizations, for the Visualization Area domain. The first realization is based on a single fracture set while the second realization includes two fracture sets. In generating the permeability and porosity fields the matrix rock was assigned a permeability of 10^{-19} m^2 and a porosity of 0.001. Figure 7.2.17 shows the resulting permeability and porosity fields for the realization with single fracture set. An analysis [35), 36)] was carried out to obtain the effective permeability for both realizations. Flow based effective permeability was calculated using Darcy's law and liquid flux at steady state:

$$q = \frac{-k_{eff}\Delta P}{\mu L} \qquad (7.2.1)$$

where,

q = flux,

k_{eff} = effective permeability,

ΔP = pressure difference between west and east faces (1000 Pa)

μ = dynamic viscosity

L = distance between west and east faces (100 m)

PFLOTRAN flow simulations were carried out using the permeability and porosity fields for the two realizations to estimate flow-based effective permeability. A pressure gradient was imposed between the west and east faces of the Visualization Domain. Equation (7.2.1) was then used to estimate the effective permeability values using flux output on the east face, distance between west and east faces (100 m) and cross-sectional area (1.5×10^4 m^2). The resulting calculated effective permeability along the x-axis (perpendicular to tunnel axis) for the realization with a single fracture set was 1.62×10^{-16} m^2. This value is an order of magnitude lower than the permeability used for the homogenous model. The corresponding effective permeability of the realization with two fracture sets was 3.27×10^{-16} m^2, which is approximately double the value for the realization with single fracture set. Flow-related effective permeability values were also calculated for flow in the other directions. The complete results are shown below. The effective permeability in the vertical direction is higher than the horizontal values indicating more flow in the vertical direction.

Flow-related effective permeability for the realization with two fracture sets.

Horizontal perpendicular to the tunnel axis (x-axis): 3.27×10^{-16} m^2

Horizontal along the tunnel axis (y-axis): 1.95×10^{-16} m^2

Ratio of effective permeability y-axis/x-axis: 0.6

Vertical (z-axis): 5.14×10^{-16} m^2

Ratio of effective permeability z-axis/x-axis: 1.6

The same simulations as described in Section 7.2.1.1 for the Visualization Area domain using the coupled DAKOTA-PFLOTRAN codes were conducted for the fractured system runs. The permeability and porosity fields for the two fracture model realizations were used. Simulation results are shown in Figures 7.2.18 to 7.2.24. Figures 7.2.18 and 7.2.19 show pressure and concentration distributions, respectively, at 173 days simulation time for the realization with a single fracture set. The pressure distributions in Figure 7.2.18 indicate flow into the tunnel in a fractured system. It is evident that use of the Visualization Area domain resulted in boundary effects. The concentration distributions shown in Figure 7.2.19 are not as smooth as results of the homogenous model. The concentration gradient is a function of the porosity field as well as the hydrology of the system.

Predictions of pressure and concentration histories at observation points for the single fracture realization are shown in Figures 7.2.20 and 7.2.21, respectively. The pressure profiles at observation points show larger pressure drawdowns when compared to those of the Visualization Area domain (Figure 7.2.8) and the large domain (Figure 7.2.14) homogenous models. Profiles of chlorine concentration are very different from those of the homogenous model. As also shown in Figure 7.2.19, concentrations are highly affected by the fracture system. Predictions of pressure and concentration histories at observation points for the realization with two fracture sets are shown in Figures 7.2.22 and 7.2.23, respectively. The pressure profiles are similar to the single fracture set. The chlorine concentration profiles are also similar to that of the single fracture set, except for Section 5 which shows a different profile.

The flow of water into the excavated space (Inclined Drift and CTD) was also evaluated for the two fractured system realizations. The resulting inflow into the tunnel (Inclined Drift and CTD) is shown in Figure 7.2.24 together with the results for the homogenous model. Task C project inflow data points (for Inclined Drift and CTD) are also included. The predicted inflow for the single fracture set realization is lower than the other cases and the data points. The predicted inflow for the realization with two fracture sets matches the data points. Note that the results of the fracture system are for two realizations only. Additional realizations would be needed to get better representation of the fractured system.

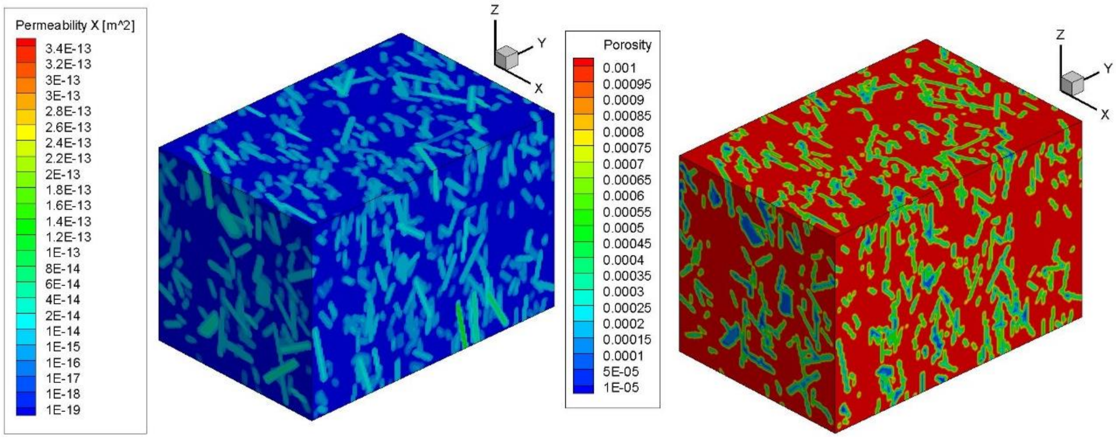

a) XX-permeability tensor b) porosity

Figure 7.2.17 Fracture permeability and porosity for Realization 1: fractured system with Visualization Area Domain.

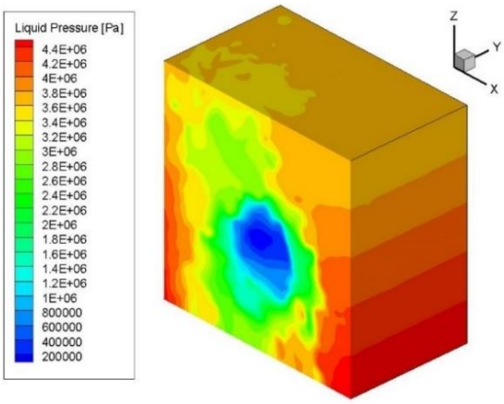

a) Cross-section along the axis of tunnel

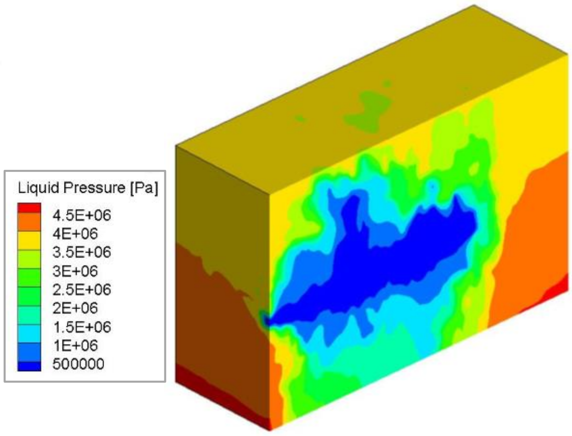

b) Cross-section perpendicular to the axis of tunnel

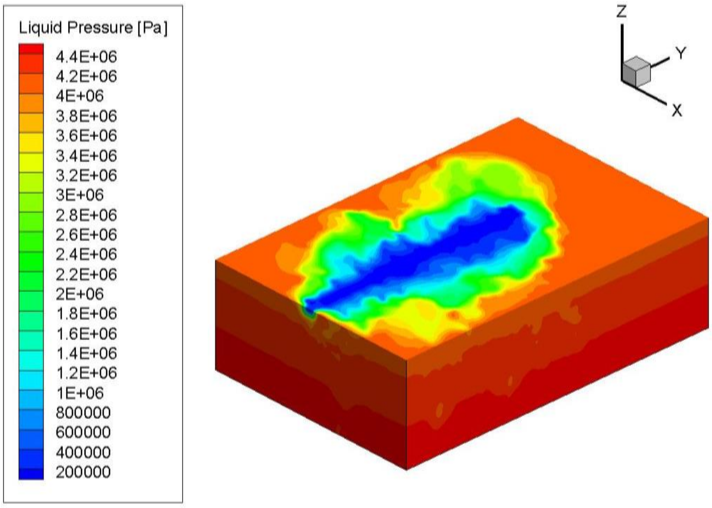

c) Vertical cross-section at location of tunnel

Figure 7.2.18 Predicted pressure distribution after 173-days simulation time: fractured system with Visualization Area domain. Realization 1.

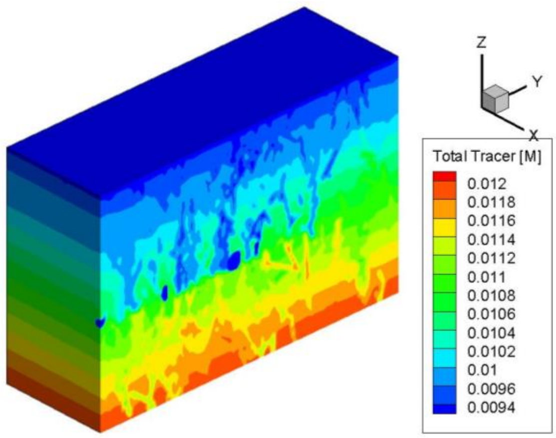

a) Cross-section along the axis of the tunnel

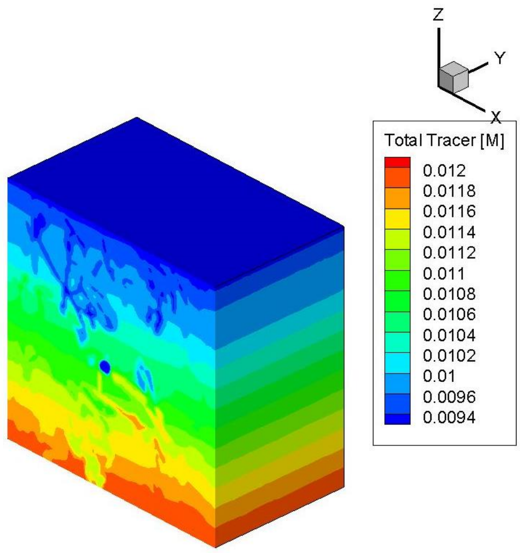

b) Cross-section perpendicular to tunnel axis

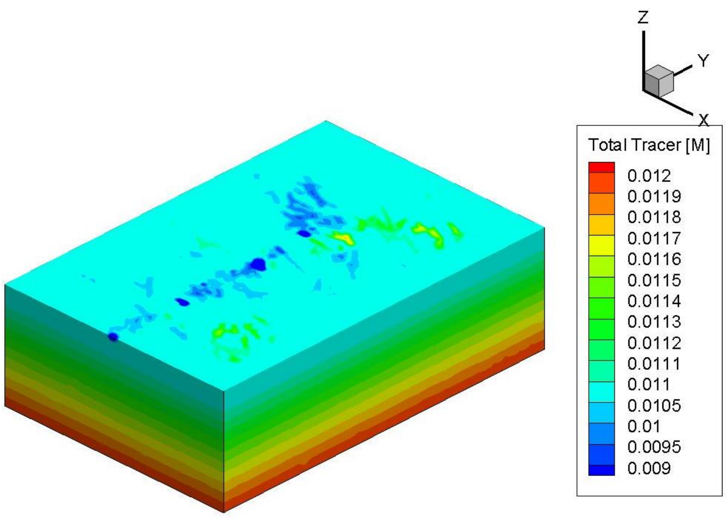

c) Vertical cross-section at location of tunnel

Figure 7.2.19 Predicted chlorine concentration distribution after 173-days simulation time: fractured system with Visualization Area domain. Realization 1. Fracture system with one fracture set.

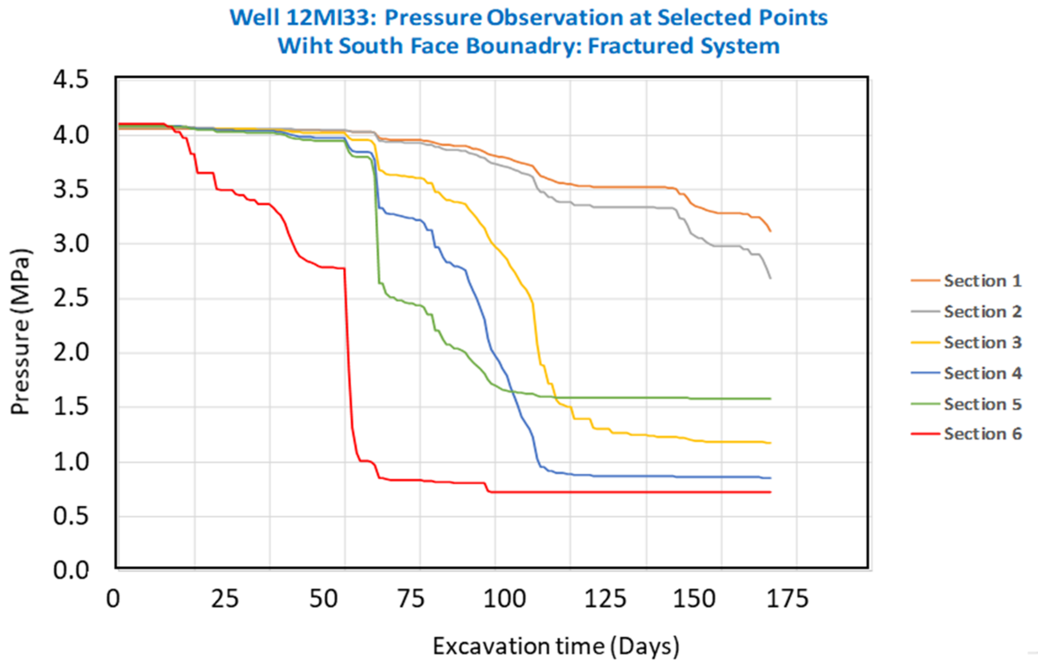

Figure 7.2.20 Predicted pressure history at observation points (in Well 12MI33) during excavation: fractured system with Visualization Area domain. Realization 1. Fracture system with one fracture set.

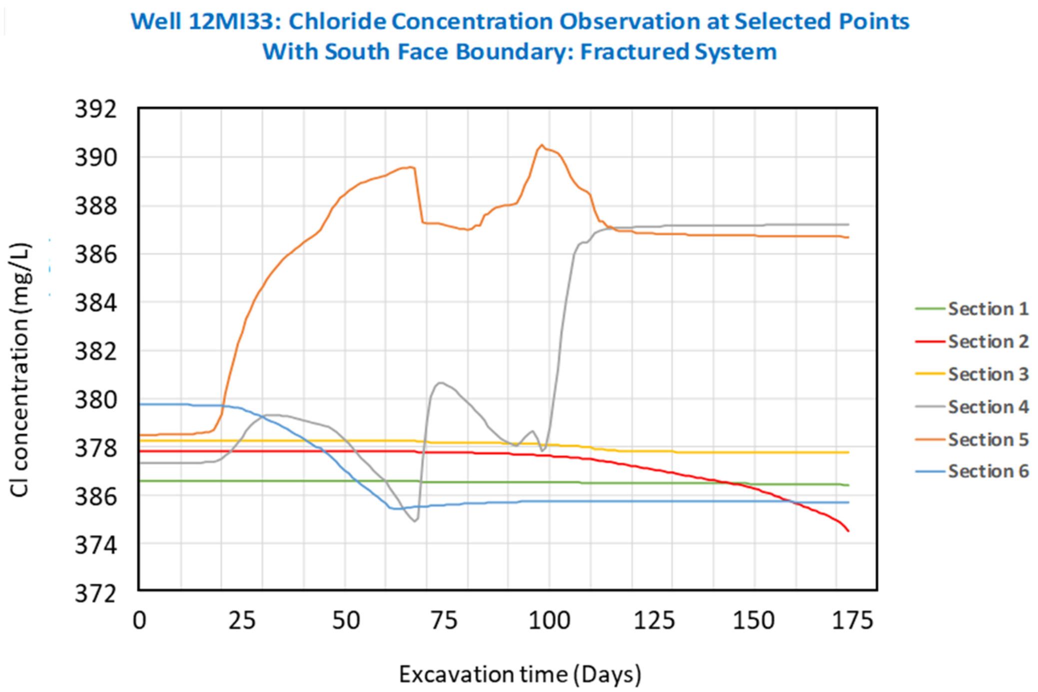

Figure 7.2.21 Predicted chlorine concentration history at observation points (in Well 12MI33) during excavation: fractured system with Visualization Area domain. Realization 1.

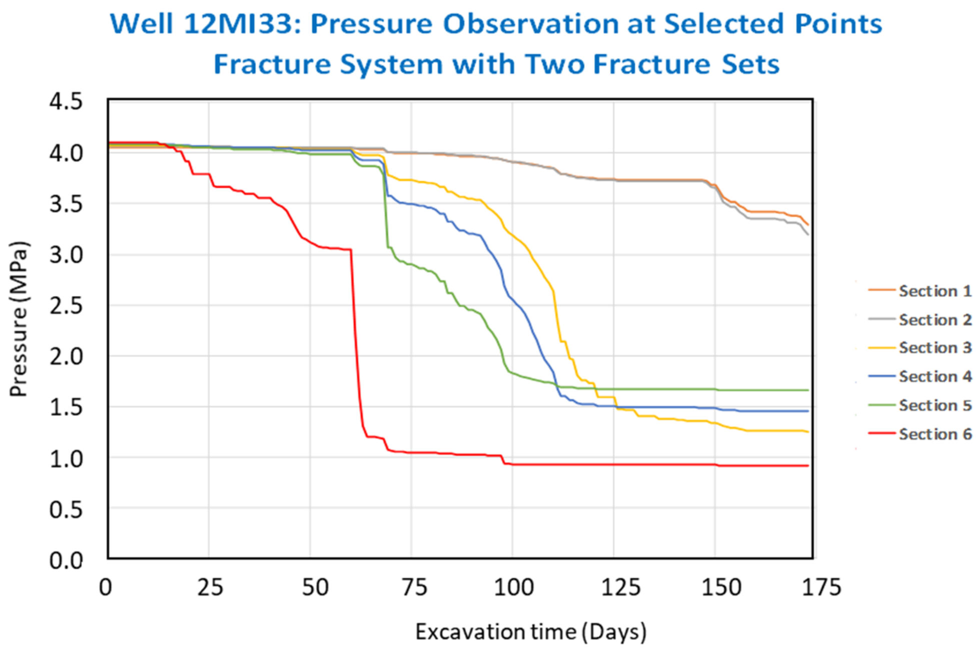

Figure 7.2.22 Predicted pressure history at observation points (in Well 12MI33) during excavation: fractured system with Visualization Area domain. Realization 1. Fracture system with two fracture sets.

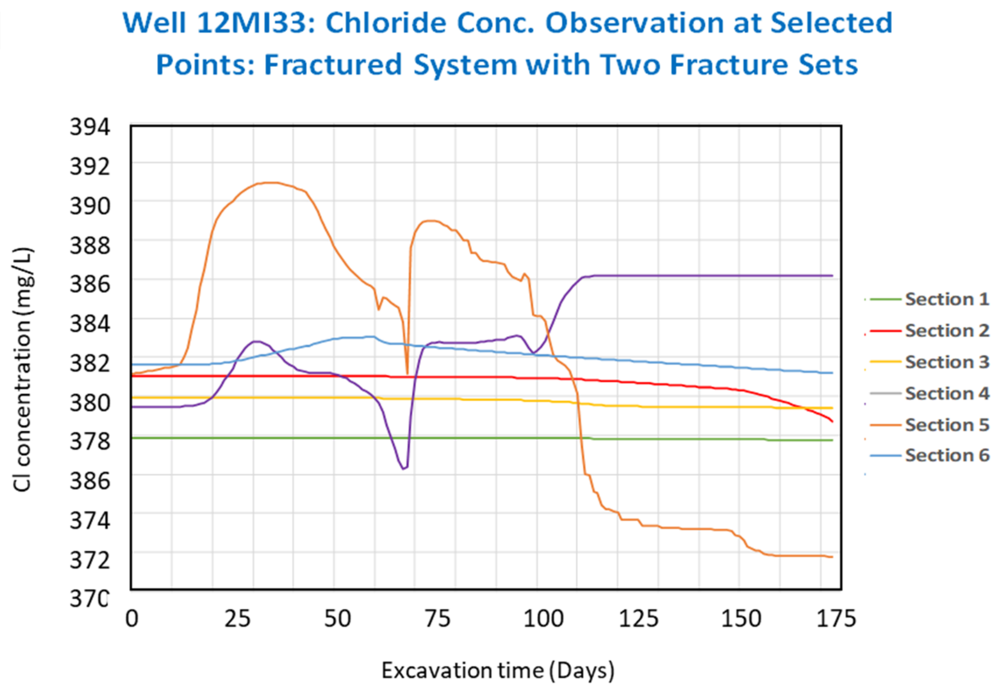

Figure 7.2.23 Predicted chlorine concentration history at observation points (in Well 12MI33) during excavation: fractured system with Visualization Area domain. Realization 1. Fracture system with two fracture sets.

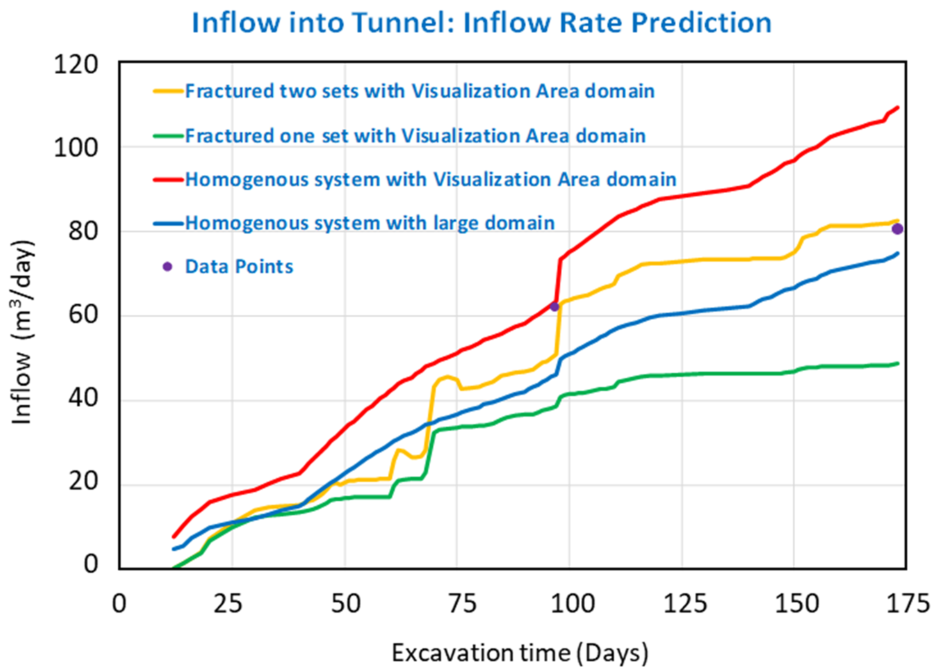

Figure 7.2.24 Predicted inflow into Inclined Drift and CTD: comparison of results of homogenous and fracture systems.

7.2.4 Summary of preliminary modeling work

Preliminary modeling analysis was conducted at Sandia National Laboratories as part of DECOVALEX19, Task C, Step 1. The analysis looked at the use of a homogenous model with reference hydraulic conductivity, and a fracture model developed in Section 7.1, above. For the base case, the CTD-scale Visualization Area domain was used (100 m × 150 m × 100 m). Boundary and initial conditions specified by the project, based on data from wells, were applied to flow and transport. The data include head and chlorine concentration at different parts of the modeling domain. Parameter data also obtained from wells were used. Data of excavation progress for the Inclined Drift and the CTD were also provided. A simulation method was developed to simulate excavation progress by continuously removing material from the excavated area. The DAKOTA statistical analysis and optimization code and the PFLOTRAN numerical flow and transport code were used. Simulations of flow and transport for the homogenous model with the Visualization Area domain indicated boundary effects at the Inclined Drift entrance. The boundary effects were caused by the application of side boundary conditions close to the tunnel entrance. To study the extent of the boundary effects, a new grid was developed with a larger domain (2080 m × 2130 m × 700 m). Simulation results of the larger domain eliminated the boundary effects, which would indicate the need to enlarge the boundaries of the CTD-scale model. The results of the larger domain also showed a predicted inflow rate close to the experimental inflow data.

The modeling analysis also included use of a fracture model developed in Section 7.1. This allowed realistic representation of the system in the excavated region. For the analysis permeability and porosity fields obtained for two realizations were used instead of the constant permeability used in the previous simulations. The same simulation approach as the homogenous model was followed for the CTD-scale Visualization domain. The simulation results provided detailed flow and transport distributions in a fractured system. The inflow predictions with the single set fracture model under-predicted the experimental data, while the predicted inflow of the realization with two fracture sets matched the experimental data. The results are preliminary output for two realizations. More realizations will be needed to obtain average representative output.

8. Results of Step 1 modeling (TUL)

Following the task definition, the modelling was oriented on prediction of the tunnel excavation effects on the hydraulic field and on chlorine transport modelling as a non-reactive tracer. Although the model geometry and boundaries were recommended by the task coordinators for this phase (referred "CTD-scale" below), we made an additional larger URL-scale model besides the one mostly common used by other teams. The purpose was to justify the pressure field on the CTD-scale model boundary. The given concept of the CTD-scale model was also made in several variants, distinguished by the boundary condition and by permeability inhomogeneity. It depends on individual understanding of the term "prediction", what level of the model details could be available: the variants below correspond to the following: (1) only URL-scale averages or variations of parameters, (2) data from the pilot borehole logging (12MI33), (3) limited data from the tunnel itself.

8.1 Large-scale model definition (URL-scale)

The domain is a block with the square base of 5000 m and the height of 1300 m. The URL is modelled as one vertical cylinder representing the two shafts (diameter 5 m) and one horizontal cylinder representing the access drift to CTD simplified to straight and horizontal shape (length 150 m, diameter 5 m).

The geometry and boundary conditions are illustrated in Figure 8.1. We define simplified hydraulic conditions without local topography effects, i.e. the model has a flat top boundary. The lateral sides are impermeable (meaning the symmetry between inside and outside of the model, assuming out of reach of the URL drainage effect), the top and bottom side have a prescribed pressure or head defining the reference conditions. The URL excavation is simulated by switching the no-flow boundary to zero pressure boundary on the shaft/tunnel walls. There are two variants of the top/bottom pressures:

- Higher pressure, considering water table on the top, i.e. p=0 (head of 200 m) on the top and p=11 MPa on the bottom (head of 0 m)
- Lower pressure with higher gradient, water table 40 m below top, p=-0.4 MPa (head 160 m) on the top and p=9.6 MPa (head -140 m) on the bottom (it is 45 m head at the -300 m lab level)

The parameters were set based on the provided data for hydrogeological units (UHFD, LSFD) and individual borehole packer tests: hydraulic conductivity K=10^{-7} m/s (rounded value, little higher than the geometric mean of the packer data) and storage S=10^{-5} m^{-1}.

8.2 CTD-scale model definition

The conceptual model is common for all variants below. The outer dimensions follow the JAEA suggestion and are the same for all variants, i.e. a block 150 m long in the direction of the tunnel, 100 m transversally and 100 m vertically (Figure 8.2). We consider one fixed geometry, where the CTD tunnel is represented as empty space in its maximum extent and the gradual excavation is represented only by time-variable boundary condition described in a special section 8.2.4 below. The model geometry keeps some features of the real tunnel shape: the vertical position of the inclined gallery (approx. 3 m difference) and the CTD is consistent with the documentation. Note that the tunnel is not therefore exactly in the middle of the model vertically (Figure 8.3). The tunnel profile has a horizontal bottom, vertical lower parts of the side walls and semi-circular top, the size is different for the inclined drift and for the CTD. The boundary conditions on the outer walls come from the assumption of no influence by the excavation (inclined + CTD). But there are various approximations of the initial (and unchanged) state around the CTD (section 8.2.3).

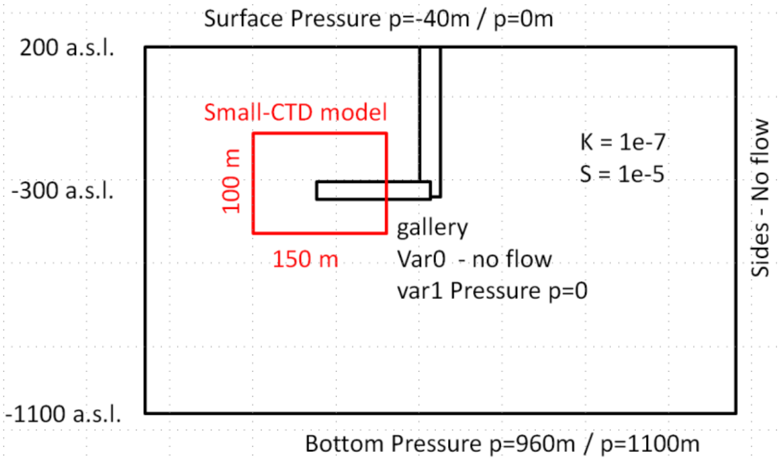

Figure 8.1 Geometry and boundary conditions of the large-scale model (vertical section).

The problem of transient flow and single-component non-reactive transport will be solved (chlorine ions). Considering the other inputs, we need to define:

- Hydraulic conductivity
- Specific storativity
- Porosity
- Molecular diffusion coefficient and longitudinal and transversal dispersivity

While the hydraulic data are well supported by the measurements provided in the data (pressure tests in many of the URL boreholes, including the 12MI33), the transport data were not explicitly measured or not present in the provided data. The porosity 0.01 is used from the provided data of hydrogeological units (possibly obsolete excel file), which differs from Table 3.1 in this report but is consistent with generic literature data of granite. The remaining data are generic, 5 10^{-10} m^2/s pore-water diffusion coefficient and 4.3 m and 0.43 m respectively the dispersivities (less than the typical 1/10 of the model scale for the reason that the studied process scale is actually smaller – around the tunnel). We assume the effect of dispersion is dominant.

The inhomogeneous model variants consider only hydraulic conductivity variations while the other parameters are constant values (due to unavailability of data).

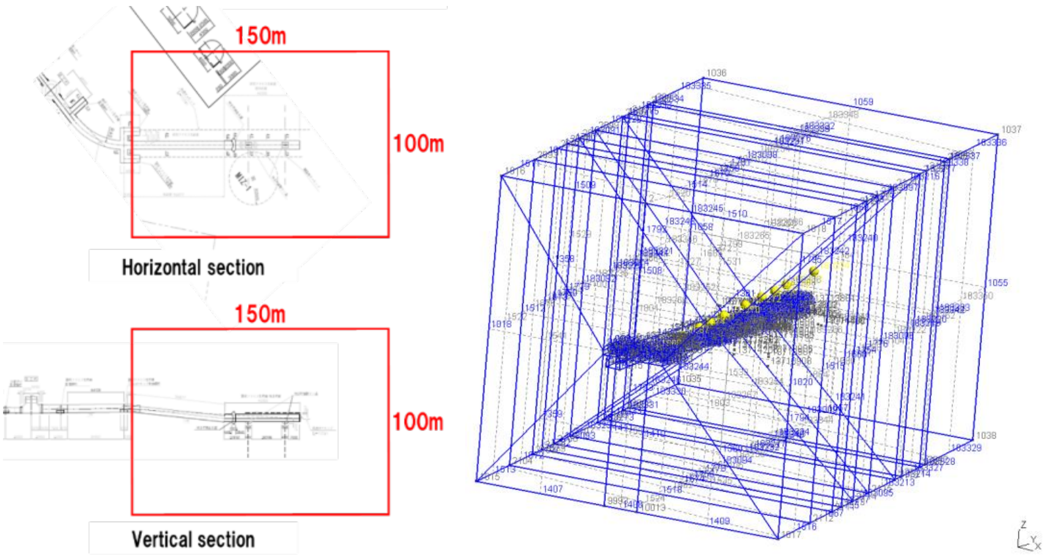

Figure 8.2 Geometry of CTD-scale model – vertical and horizontal view with respect to the real drawing, and the GMSH realization of the model for simulation input.

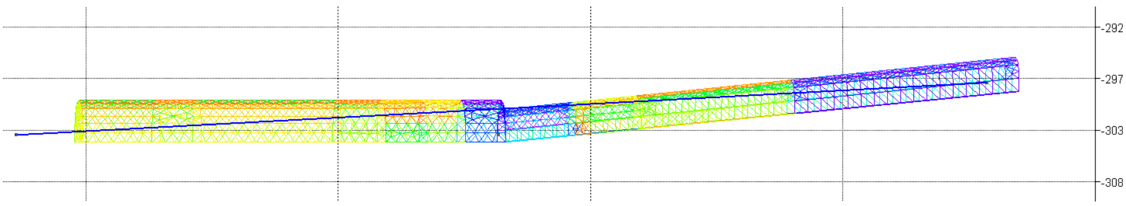

Figure 8.3 Tunnel boundary in the model with meshing – inclined gallery on the right and CTD on the left. The line of 12MI33 is plotted in blue.

8.2.1 Variants of permeability heterogeneity

We consider two models of equivalent continuum

- Homogeneous hydraulic conductivity and storativity as an average from the borehole pressure tests evaluation rounded to an order of magnitude $K=10^{-8}$ m / s, $S=10^{-8}$ m^{-1}.
- Heterogeneous hydraulic conductivity based on the 12MI33 packer intervals.

The latter case considers several significant simplifications but it was suggested as a straightforward use of the only explicit local permeability information before the drift excavation. The model is composed of blocks sorted in the direction of the borehole (i.e. direction of the tunnel) covering the whole perpendicular plane between the boundaries (Figure 8.4). We assume the spatial scale of hydraulic tests is enough to cover the distance between the 12MI33 borehole and the CTD and could predict the permeability near the tunnel wall with possible meter-scale shift in position. The extension to boundaries is only meant as a technical simplification and will be abandoned in the future work.

The packer test intervals do not cover the whole model length. In the places where the packer tests follow each other, there is typically a gap of 1 - 2 meters, so the interface between the two continuum blocks with different hydraulic conductivity is made in the middle of such packer test gap (Figure 8.4, Table 8.1), i.e. a half of the packer own length is accounted to the measured interval. Then the remaining volume is covered by a background value of $K=10^{-9}$ m / s which is a generic estimate on the lower range of the packer tests, as we can expect the larger permeability would be observable on the borehole inflow. The inflow is a part of the logging and is given (almost) continuously, but on the other hand there are also some inconsistency in the data (disappearing water, no full correlation of the inflow and the packer test permeability). In Table 8.1 the model blocks are denoted based on the packer test intervals and the additionally defined blocks are either numbered sequentially, or a symbol is used, similar to the number two packer interval. The interval 86 m to 105 m is not covered by packer tests and the inflow meter data (consistently with other graphic output in the logging protocol) indicate a place at about 90 m with larger permeability. So two different sections No.5' and No.5" are used in the model. The actual K values are order of magnitude estimates within the range of other intervals, not based on any calculation.

To simplify the multiple model variant processing, the geometry and meshing are the same for both homogeneous and heterogeneous model, differing only by the input data – hydraulic conductivities. The mesh has 13637 nodes and 81752 elements (tetrahedra) and is shown in Figure 8.4.

Table 8.1 Parameters of the heterogeneous model – positions of blocks and hydraulic conductivities. The consideration for "own" estimates is given in the text. In the last row shows the monitoring sections in the borehole (see also Figure 8.4).

	No.0	No.1	No.2	No.2'	No.3	No.4	No.5	No.5'	No.5"	No.6	No.6'
Data from	own	Packer test	Packer test	Packer test	Packer test	Packer test	Packer test	own	own	Packer test	own
K [m/s]	1e-9	2.6e-8	1.1e-7	6.1e-9	8.4e-9	4.8e-10	9.5e-10	1e-8	1e-9	2.73e-7	1e-9
Begin [m]	0.0	12.1	37.1	20.1	44.2	53.2	65.2	90.0	95.0	105.2	107.0
End [m]	12.1	18.9	42.6	36.1	54.5	63.5	90.0	95.0	105.0	107.0	end
Monitoring	Sec. 6				Sec.5	Sec.4	Sec.3	Sec.2		Sec.1	

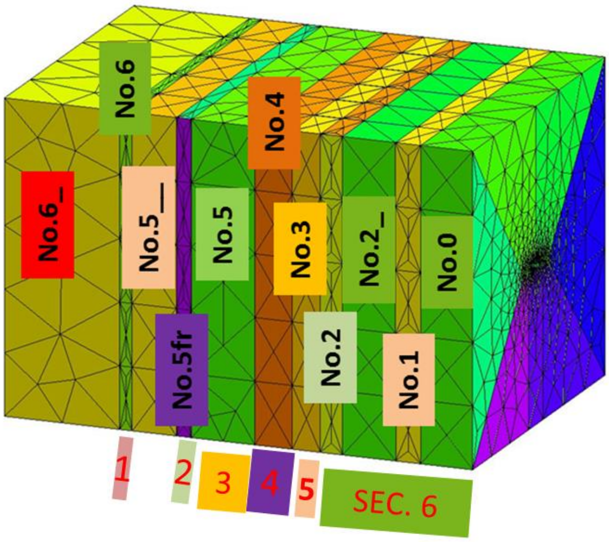

Figure 8.4 Heterogeneous model concept of TUL team – blocks of different permeability aligned with borehole monitoring sections (below the picture).

8.2.2 Fracture model

The fracture model variant could be also understood as a third variant of the permeability spatial distribution; but due to specific data processing, there is a need for a separate discussion. The idea behind this approach is to use the capability of Flow123d code to combine the deterministic discrete fractures and equivalent continuum of the remaining rock blocks among these fractures. The task therefore is mainly how to select the small number of the deterministic fractures which would be representative for the hydraulic properties. Similar to the block heterogeneity construction, the fractures are extended to the model boundary, although such a spatial extent should be understood as not being supported by the data (as the introductory step, it was simpler for processing then to define the outer part of the model e.g. homogeneous).

There are two main groups of the source data: (1) The tunnel wall mapping of the inclined drift and CTD, including a classification by water inflow. (2) The borehole logging and packer pressure tests. These sources are partly complementary, but also they should be ensured to be consistent between each other.

The procedure of data use is the following:

- Take into account only the fractures with some “water attribute”, i.e. either F (flow) or D (drop), assuming these could be highly connected and having impact on the pressure field. It is 78 of 2023 total. The W (wet) fractures were neglected, because they would be too many for the model concept (geometry processing).
- Project them to the vertical direction (within a common line of intersection in the plan view) only to simplify the processing, most of them are close to vertical
- Make a plot (plan view) where the fractures’ intersections with 12MI33 packer intervals are visible (Figure 8.5).
- Select “main” fractures so that especially the higher conductivity packer intervals are covered (intersect with at least one fracture) and F fractures have a priority.

Groups of fractures of similar position and direction can be represented by one (i.e. fracture zone), typically around one or two F fractures with kept position or their average, respectively. There were 14 of such, which were afterwards digitized from the hand-drawing.

- Assign the transmissivities to the individual fractures. This is made using a packer interval transmissivities as constraints, together with one common rock block hydraulic conductivity, explained below in details.

The assignment of the fractures and 12MI33 borehole intervals is shown in Table 8.2, including the evaluated data and additional supporting information of the F and D attributes and aperture. The overall idea is that the set of hydraulic parameters of the model should be able to reproduce the packer test data, simply by summing the contributions of the continuum blocks and individual fractures in each packer interval. So the overall hydraulic effect is emphasized instead of realistic fracture density (anyway, one model fracture plane can represent more "real" fractures). The conductivity of the "rock matrix" (incorporating the fractures not represented explicitly) is estimated so that its contribution for the least permeable packer sections (4 and 5) is balanced with the explicit fractures. The problem is little underdetermined, but most of the relations are unique with one fracture for one borehole interval.

While the result of the above procedure is only the individual fracture description data, i.e. fracture positions, direction and transmissivities, the simulation code input geometry needs a full hierarchy of nodes, lines, areas and volumes, including especially all the fracture intersections among each other and with the boundaries. This task was made in the SALOME software (CAD-like open-source project). The meshing was not yet optimized and resulted in a large mesh of approx. 750000 elements which corresponds to about 3 million degrees of freedom of the flow problem (Figure 8.6). The calculations were limited by memory consumption and time, so only one pilot simulation of the transient hydraulics was made, i.e. without the tracer transport.

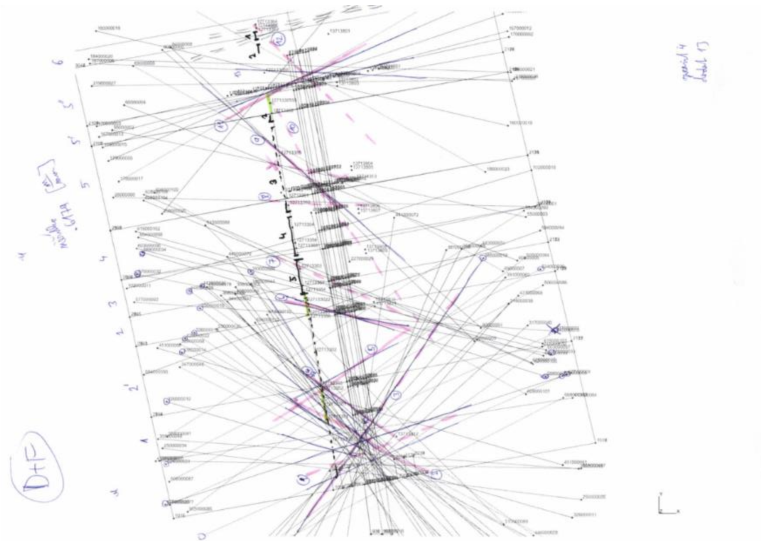

Figure 8.5 Processing of fracture data – traces of the fractures in a horizontal plane in the level of the tunnel and their intersections with the 12MI33 borehole intervals. Selection of 14 model fracture planes as pink hand-drawing. Orientation in the given coordinate system, tunnel entrance on the bottom and CTD end on the top.

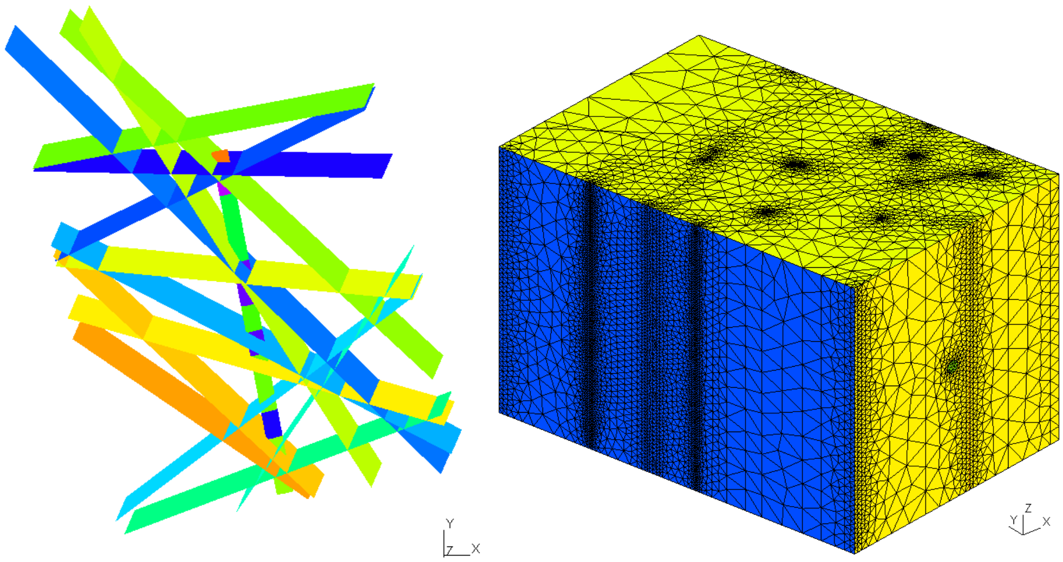

Figure 8.6 Positions of the fractures with respect to the tunnel in few degrees off the top view (left, see the axes), mesh of the coupled fracture-continuum model (right).

Table 8.2 Determination of the fracture transmissivities from the 12MI33 packer test and other reference data (own selection in red). The “x” symbol denotes the existing intersection and a contribution to the measured transmissivity. The blue numbers are manually set such that the calculated sums of intervals in the bottom table block fit their measured or prescribed counterparts.

			packer intervals intersected by model fractures (added own additional - red)											represented items from fracture list		
		No.	0	**1**	**2a**	**2**	**3**	**4**	**5**	5a	5aa	**6**	7	their parameters		
		length	16.6	6.8	16	5.46	10.3	10.3	20.3	5	14.5	1.8	20			
model objects		conductivity														
rock		2.00E-10														
		transmissivity												number	water	aperture
fracture	1	1.00E-08	x											303+427	F (short)	1+3
fracture	2	1.15E-07		x										356+336+426	F	0+0+5
fracture	3	5.00E-09	x											385	F (short)	1
fracture	4	9.50E-08			x									443+446 +393	F	1+0+1
fracture	5	6.00E-08		x										524	F	20
fracture	6	6.00E-07				x								588+576	F	1+0
fracture	7	8.50E-08					x							626+628+etc	D	0+0
fracture	8	3.00E-09						x						28	D	0
fracture	9	1.50E-08							x					90+94	F	5+0
fracture	10	5.00E-09								x				none		
fracture	11	4.50E-08								x				179+170+175	F+D	1+2+0
fracture	12	5.00E-09										x		none		
fracture	13	1.20E-08									x			187	F	1
fracture	14	4.50E-07										x		none (12MI33 based)		
transmissivity total			1.83E-08	1.76E-07	9.82E-08	6.01E-07	8.71E-08	5.06E-09	1.91E-08	5.10E-08	1.49E-08	4.55E-07	4.00E-09			
conductivity total			1.10E-09	2.59E-08	6.14E-09	1.10E-07	8.45E-09	4.91E-10	9.39E-10	1.02E-08	1.03E-09	2.53E-07	2.00E-10			
measured conductivity packer				**2.62E-08**	**6.11E-09**	**1.1E-07**	**8.4E-09**	**4.82E-10**	**9.53E-10**			2.73E-07				
own estimated conductivity			1.00E-09							1.00E-08	1.00E-09		1.00E-09			

Table 8.3 Variants of the TUL model based on various choices of heterogeneity and boundary conditions. Only the filled fields correspond to the evaluated combinations.

Name:	BC from Reference	BC from Large scale
CTD model Homogeneous/Base model/Reference	**REF** BC+IC: Head = 110 m K = 1×10^{-8} m/s Storativity = 1×10^{-8}	X
Heterogeneous/TUL model	**TUL1** BC+IC: Head = 110 m K directly from 12MI33 test	**TUL2** IC from steady state BC from large model + front side is no flow
Fracture	**TUL3 Fracture** BC+IC: Head = 110 m K inversely from 12MI33 (Table 8.2.) Storativity = 1×10^{-8}	X

8.2.3 Outer boundary conditions

The boundary conditions for both the flow and the transport are illustrated in Figure 8.7. Simply, the outer model boundaries have prescribed head and concentrations corresponding to the undisturbed state, based on a simple measurement averaging or regression. The tunnel hydraulic boundary is described in the next section. The transport boundary on the tunnel wall is a usual "free outflow" condition, defined as the total mass flux is equal to the advective flux corresponding to the hydraulic model flux value. There are two kinds of additional variants:

- Choice of "hydraulic undisturbed state"
  - Hydrostatic case with uniform head suggested by JAEA
  - Non-uniform head field resulting from the large-scale model, i.e. including drainage effect of the remaining URL constructions, especially the shaft (other horizontal drifts than CTD are not included). The values from the large-scale mesh are interpolated to different positions of element faces in the CTD-scale mesh.

- Choice of "front" vertical boundary (intersected by the tunnel)
  - In the default case, it is the same as other boundaries, which leads to a discontinuity of pressure/head on the edge of the tunnel/boundary intersection
  - No-flow boundary corresponding to an assumption of the symmetry, i.e. assuming long open tunnel on both sides of the boundary, which is true in the later period of the excavation (except the deviation of the tunnel from the direct line), as well as should be a result of the large-scale model pressure field. The tunnel drainage should dominate the pressure gradient over possible inhomogeneity.

The described variants actually make four total combinations, but only three of them were evaluated (especially there was no more motivation for the non-realistic velocities at the discontinuous edge for the second head value choice). The combinations of model structure concepts and boundary condition choices used for the evaluation below are listed in Table 8.3.

The values of the concentrations both in the initial and the boundary condition are defined as linear increase with depth with the stated top and bottom side values.

The variant with a large-scale model head projection was expected to capture a possible different weighting between the CTD inflow from upwards and downwards. In particular, the resulting head field from the large-scale model contains a significant vertical gradient component (although the horizontal is larger), so that possibly more of the deeper water is drained to the tunnel compared to the shallower water. We note that this consideration was obtained based on the previously measured data presentation, so it is not a true prediction (contrary to intended), but the assumptions and ideas could be in principle obtained also without such knowledge.

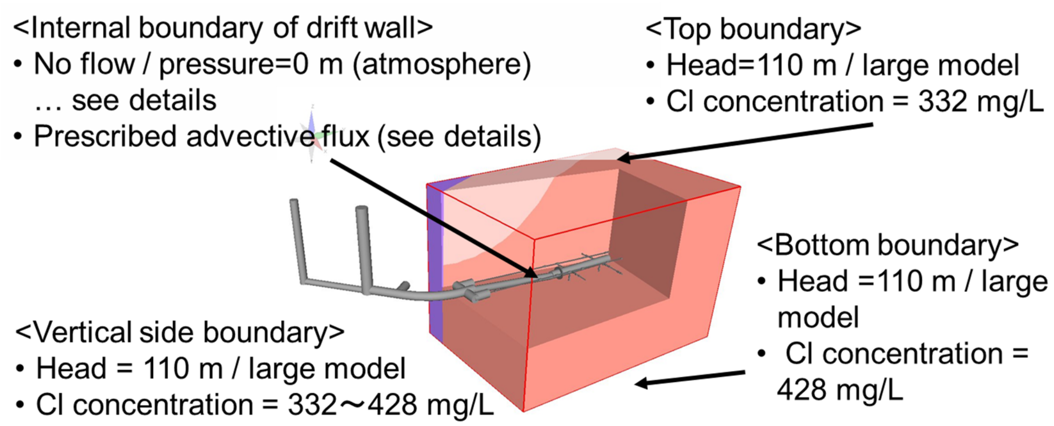

Figure 8.7 Boundary conditions for the flow and the transport problems.

8.2.4 Excavation progress modelling

In principle, the excavation of the drifts means a changing model geometry. To avoid such difficulty, it can be almost equivalently solved by a switch of the boundary condition: if the no-flow condition is prescribed on the tunnel wall, it is equivalent to rock filled tunnel in terms of its hydraulic effect around (assuming no significant gradient across the tunnel is present). Technically, we prescribe zero pressure on the excavated part and no-flow on the remaining part, with the interface between them moving in time. This neglects the flow in the unexcavated rock, but within a relatively short time period. Although the progress of the excavation has a detailed definition in the documentation, including distinguishing the upper and lower parts, we suggested a constant speed of the front movement is enough accurate in current level of modeling. The difference is illustrated in Figure 8.9.

The movement of the two boundaries interface is conveniently achieved by two features of the Flow123d code: the first, quite standard, is the 3rd type (Robin) boundary condition for general flux, which can represent both the 1st type (Dirichlet) and the 2nd type (Neumann) depending on a coefficient

$$-q_d \cdot n = \delta_d \left(q_d^N + \sigma_d^R (h_d^R - h_d) \right)$$

where q^N is the prescribed flux (we use zero), h^R is the prescribed head (we use a z-dependent value appropriate to the zero pressure) and sigma is the Robin coefficient – it leads to dominant flux if close to zero, while to the dominant head difference if close to infinity. We chose 10^{-12} and 10^{12} respectively (units can be disregarded). The second feature, more unique one, is a use of formula parser in the input file, so that any input value can be given as a function of space and time coordinates (predefined symbols x, y, z, t) and includes a "if" construct with the syntax similar to MS Excel. The respective line of the input file is in Figure 8.8, where the numbers mean the space (meters) and time (seconds) values of the excavation front (even if the tunnel is not parallel to y-axis, the position is correct and the little deviation of the front orientation is unimportant).

```
bc_type: total_flux
bc_pressure: 0
bc_robin_sigma: !FieldFormula
value: if((y+68949)<(t-518400)*(106/14342400),1e12,1e-12)
```

Figure 8.8 Input file lines of Flow123d defining the boundary condition on the tunnel wall for temporal progress of the excavation by means of relation between y position and t time in the formula.

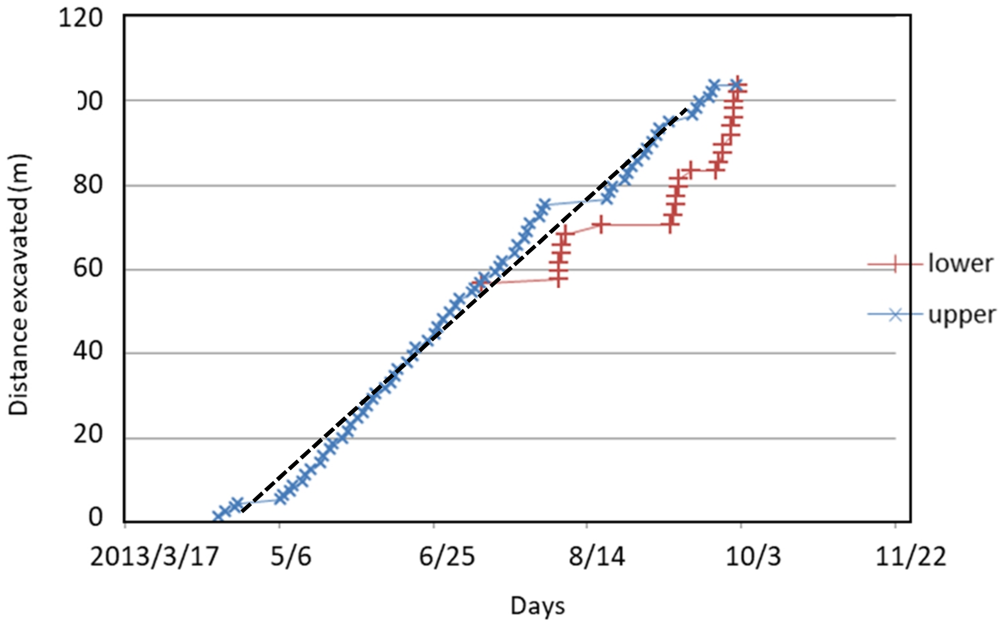

Figure 8.9 Progress of drifts excavation – the documentation data and the linear regression used for the modelling

8.3 Prediction results of the disturbance during the excavation of CTD

The results of prediction are structured to the flow and the transport parts and based on the post-processed values. For the temporal evolution, the evaluated period corresponds to the excavation period, from Apr 2013 until Oct 2013.

8.3.1 Pressure

For compatibility with other teams, the hydraulic conditions are evaluated in the form of pressure (in units of MPa). It is more illustrative than the head (m) values, especially concerning the zero level and relating to the tunnel boundary (zero pressure and -300 m head). The initial (undisturbed) values are 110 m head and 4.1 MPa pressure.

The results for four model variants (or variant combinations) are compared in Figure 8.10. The variants correspond to Table 8.3 concerning the heterogeneity and outer boundary condition source. The REF variant uses the prescribed head on the whole boundary while the other three use the no-flow (symmetry) on the "front" side (intersected by the tunnel).

In all cases, we can clearly observe the drawdown resulting from the excavation drainage. The temporal sequence corresponds to the alignment of the excavation progress position with the monitoring point position. All the heterogeneous models show more steep pressure drops, which correspond to crossing of the interfaces between different permeability or crossing of fractures.

Next, the variants differ by the asymptotic values of the pressures after the excavation. Sections 3-5 always reach the lowest final value between 1.5 and 2 MPa, section 2 stays in the middle of the range and section 1 decreases significantly for homogeneous model but negligibly for the model with blocks (TUL1 and TUL2). As expected, the use of boundary values from the large-scale model (TUL2) has no effect on temporal trends, but determines the overall pressure levels with about 0.1-0.2 MPa difference (10-20 m of head). The different asymptotic value of section 6 for REF model is a result of the front side boundary with a prescribed head. Therefore we find the boundary condition option of TUL1 and TUL2 more suitable, leading to the tunnel drainage controlled pressure similar in section 6 to the sections 3-5 which should be more realistic.

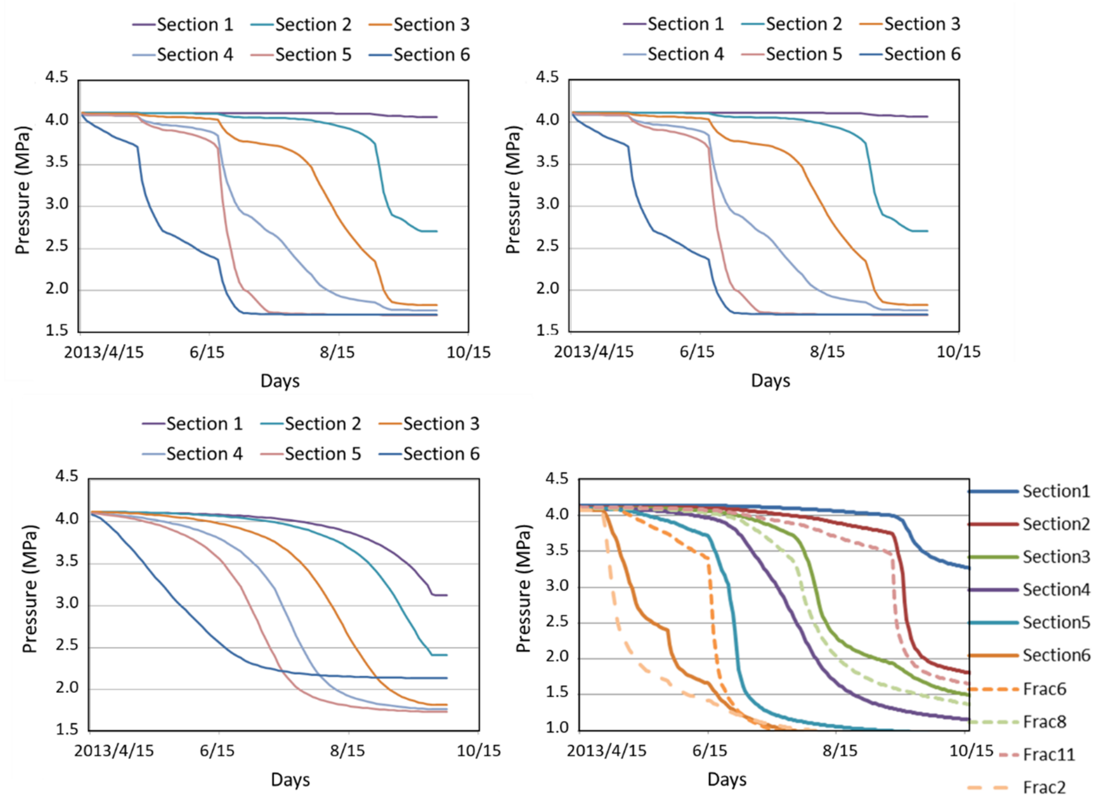

Figure 8.10 Pressure evolution model results in the points corresponding to the monitoring sections – upper left: heterogeneous model (original b.c. – TUL1) ; upper right: heterogeneous model (large-scale b.c. – TUL2); lower left: homogeneous model (with head b.c. on the front – REF); lower right: fracture model (TUL3 Fractures).

Concerning the future comparison of the model prediction and the data, we note that use of the central point of a packer monitoring interval for a respective model output is not necessarily realistic. In principle, the measured packer pressure is dominated by pressure in the most permeable structure intersected by the borehole. On the other hand, it would not be worth evaluating this kind of weighting from the model values along the borehole interval line, given the current coarse prediction level. To demonstrate the possible impact, we have additionally plotted the pressure evolution in the points of the borehole/fracture intersections for the fracture model, as part of the Figure 8.10 graph set. The colors correspond to those of the packed interval intersected and we can see visible effect mainly concerning the time of reaction.

In the remaining figures, the spatial hydraulic field is illustrated. The differences between the two boundary conditions, hydrostatic and large-scale projection, are shown in Figure 8.11. A horizontal gradient directed towards the shafts is visible in the upper part of the model. Figure 8.12 shows the spatial reach of the excavation-induced pressure decrease. The front side (on the right in the picture) is with no-flow boundary in this case. We can also observe a gradient normal to the boundary (top, bottom, lateral) which suggests that the boundary condition can have some effect on the model or, vice-versa, would not be constant in time in reality. Figure 8.13 demonstrates the features of the fracture model.

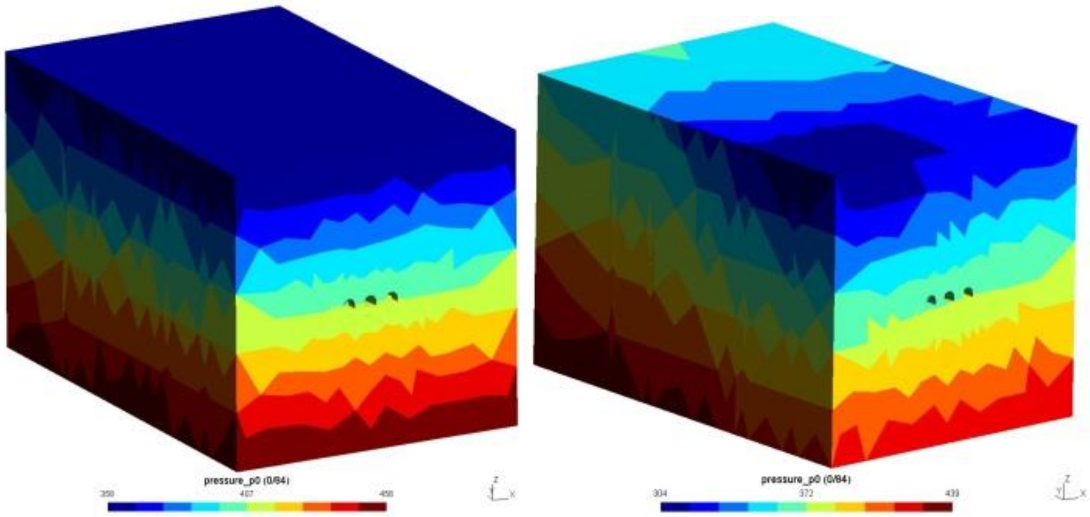

Figure 8.11 Result of field of hydraulic head. Left is the homogeneous model with the hydrostatic boundary and right is the heterogeneous model with the large-scale projection boundary.

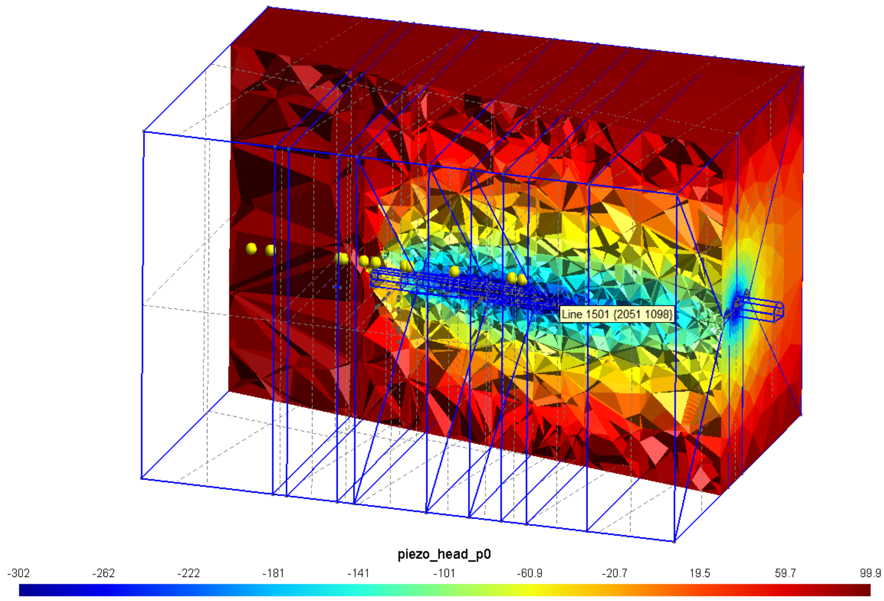

Figure 8.12 Result of field of hydraulic head [m] in the vertical section along the tunnel – effect of the excavation drawdown in the final time.

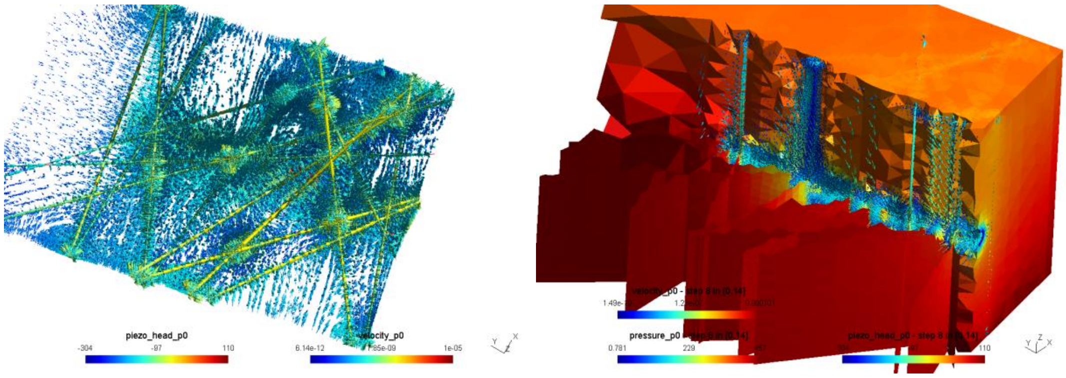

Figure 8.13 Illustrations of the fracture model results – velocity field concentrated to the fracture planes and the hydraulic head field in the middle of the excavation progress (partial section keeping the fracture planes in the front).

8.3.2 Gallery inflow

It was straightforward to evaluate the inflow as a time evolution from the transient hydraulic model, although it was not evaluated with temporal changes. We understand the final model values are those to be compared with the measurement (one value of the gallery inflow and one value of the CTD inflow).

In Figure 8.14, three of the model variants are presented, so that the effects of the heterogeneity can be observed while the boundary condition variants effects are not significant. It is clear that the inflow to the homogeneous model is quite uniform, the same contribution of both inclined gallery and CTD, while for others, the inclined and CTD differ by several factors. It is a direct consequence of the lower permeability in the CTD part than the average permeabilitiy. On the other hand, we could not explain the total inflow difference of about factor of 2 between TUL2 and TUL3 cases, which were defined with the equivalent transmissivity assumption. Also the time trends are more uniform for the homogeneous while with some steps for the heterogeneous cases. Especially for the fracture case, we assume the peaks are results of a sudden intersection with a fracture followed by a flow rate decrease after the pressure gradient decreases.

8.3.3 Results of transport modelling

The advection-diffusion transport was evaluated only for the continuum models (homogeneous and heterogeneous) but not for the fracture model. Again, the post-processing is adapted to the expected monitoring data, i.e. the chemical sampling from the 12MI33 borehole sections. Additionally we evaluated the concentration in the tunnel drainage water, which also can be a value available for measurement and can be considered as some validation of the representativeness of both values for the spatial distribution.

The borehole section values are calculated inside the simulation code as a direct result, only interpolated to the required observation point from the nearest mesh degrees of freedom. The temporal evolutions are plotted in Figure 8.15, for the two representative model variants. The little differences and temporal changes could seem to be numerical error effects (commented below), but there are physical arguments related to model configuration, for some of them:

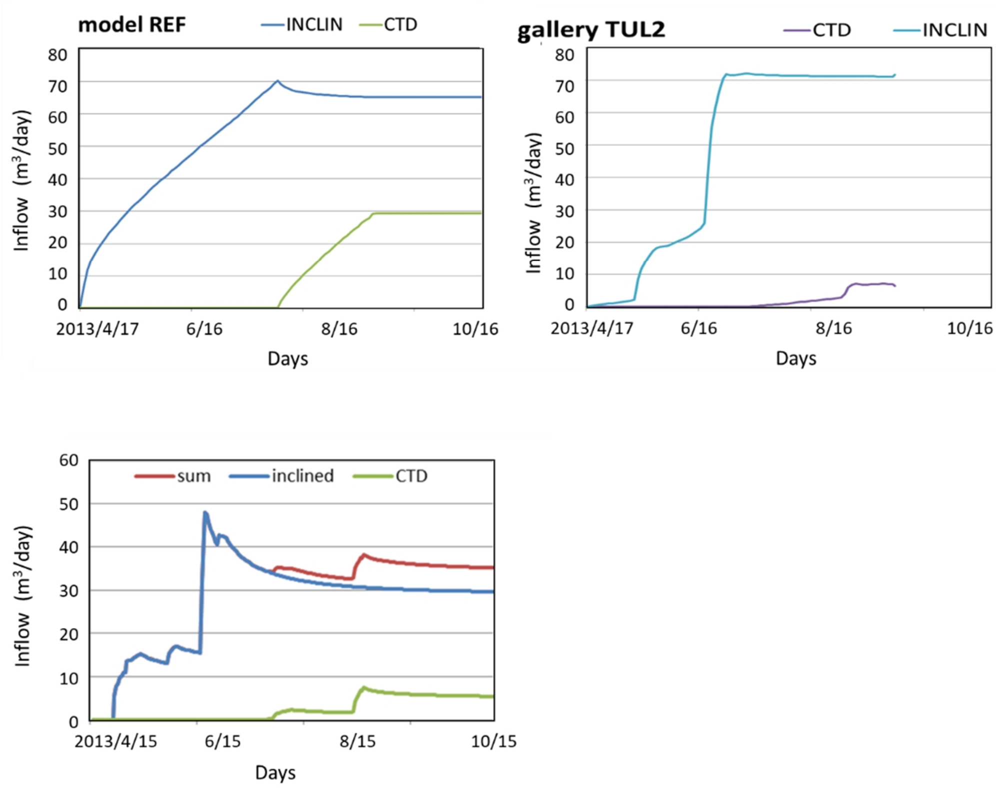

Figure 8.14 Temporal evolution of the inclined gallery and CTD groundwater inflow – upper left: result of the homogeneous model (REF); upper right: result of the heterogeneous model (TUL2); lower left: result of the fracture model (TUL3 Fractures).

First, the borehole is not horizontal (Figure 8.3), so that it crosses the concentration field controlled by the z value in a non-constant profile. Therefore the initial values (visually same for both models) are sorted from the lowest concentration for the highest placed section 6, except the unexplained changed order of section 1 and section 3.

Second, the trend of temporal change should be then controlled by the relative borehole and tunnel position. Assuming the tunnel is draining the water symmetrically around, the water from the lower space is transported to any point below the tunnel axis and vice versa. This is on the other hand more complicated by the non-circular tunnel profile. This consideration is only significant theoretically to understand the model, while the measured data have much less accuracy (the chemical analyses are typically reported with percents to tens of percent uncertainty) than the discussed model variations which are less than one percent.

In principle, the effect of lower concentration flow downwards and higher concentration flow upwards should lead to a sharpened interface between low and high concentration on the level of the tunnel axis (middle height). This is very little visible on the concentration field plot of a vertical section perpendicular to the tunnel, especially through a block of larger permeability (Figure 8.17).

The concentrations in the water seeping into the tunnel are evaluated indirectly from the available software outputs – fluxes through the boundary parts, in particular the volumetric flux from the hydraulic model ("volume per time") and the mass flux from the transport model ("mass per time"). Ratio of these fluxes equals to the concentration in the mix of discharged water, in "mass per volume" units. It is simpler than evaluating a weighted average of concentrations along the boundary elements or nodes. The results are plotted in Figure 8.16. The values are consistent with those of the 12MI33 borehole, with the difference appropriate to the vertical position. There are significant fluctuations which we believe result of the numerical errors in the calculation procedure: first, the volumetric and mass fluxes are calculated from the model discrete unknowns inside the software and second, the concentrations are calculated as the mass flux to volume flux ratio (above) outside the simulation software.

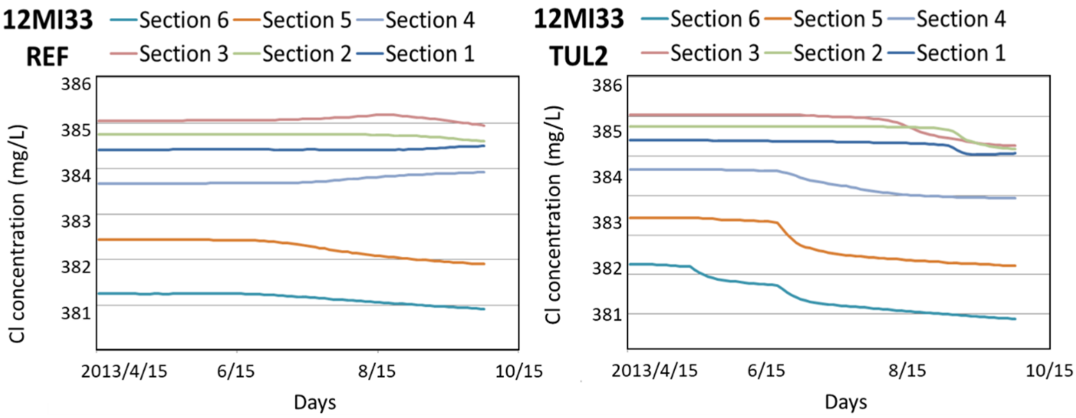

Figure 8.15 Concentration of chlorine during excavation in 12MI33 borehole for two model variants – homogeneous with hydrostatic b.c. and heterogeneous with large-scale pressure field b.c.

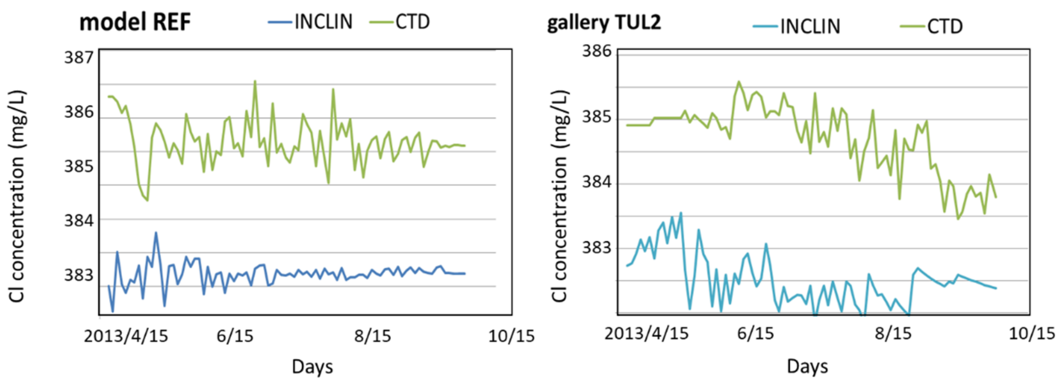

Figure 8.16 Concentration of chlorine in water flux through the tunnel wall, during the time of excavation, for the two model variants (defined in Table 8.3).

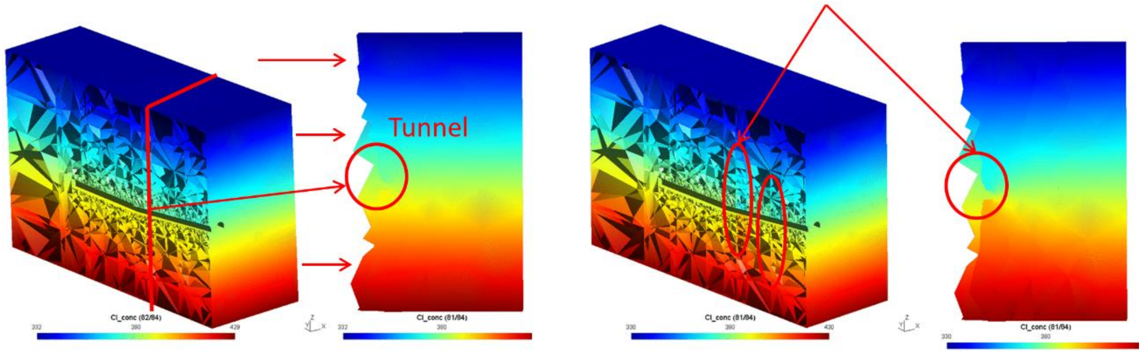

Figure 8.17 Concentration of Chlorine with pointed place, where the concentration makes a little change during excavation.

8.4 Model calibration

This part of work is a transition from Step 1 to Step 2. At the time of this report preparation, the Step 2 solution is in its intermediate phase, so the presented results do not constitute a separate chapter, and should be considered as introductory and incomplete, with possible later improvement and extensions.

The idea of the model calibration for the period of excavation is in using all data available until the end of drainage period, which include the pressure and concentration monitoring in the six sections of the 12MI33 borehole, all the CTD wall structural mapping, and the tunnel inflow rate. Unfortunately, a significant part of the time evolution is not available, due to the reported power switch-off during the excavation.

For the current simulation, the above mentioned data were used; but based on the task definition, other data should be available for this period, such as other borehole pressure tests and monitoring in the boreholes from CTD or parallel to the CTD. These will be used in the continuing work.

8.4.1 Fitted data observations

The main direction how to calibrate the model was in the choice of inhomogeneity structure. As mentioned above, the configuration options used in the predictions, i.e. blocks of different conductivity changing along the CTD or pilot borehole (while constant in the perpendicular direction from the CTD out to the boundary) cannot itself explain the behavior observed in the 12MI33 monitoring sections. From the general complex temporal evolution and mutual relationships of the sections, we can select the following features we will concentrate on in the calibration:

1) The sequence of the pressure drops corresponding to the excavation advance: In the sections with some reaction (i.e. No.2,3,4,6), the order of the reaction corresponds to their position, although some of the relations are not unique, as they can happen with a quite long interval of missing data. In general, any of the model variants are not in contradiction with the data in this behavior.

2) The final value of pressure after the excavation monitoring period, which is different for each section – some fall to the value similar to that predicted while

others keep almost unchanged. This is controlled by outer effect and internal model geometry. To capture this behavior in the model with simple boundary condition, we need to include some inhomogeneity along the path between the tunnel and the boundary – the smaller pressure is the effect of larger conductivity between the tunnel and monitoring section and the larger pressure is the effect of larger conductivity between the boundary and the monitoring section (and smaller conductivity between the tunnel and the section).

3) The slope of the pressure decrease period: This is influenced by the model inhomogeneity, there is a sharp drop in such model (including the fracture model) compared to the gradual decrease in the homogeneous model. On the other hand, the measured data have gaps which do not allow to distinguish fast or gradual decrease for sections No.3 and 2, but the limits suggest rather faster decrease.

Although the chlorine concentration evolution appears to be a good observation of the flow field inhomogeneity, we did not consider the new transport data for the calibration in this stage. The chlorine concentration is evaluated by the models but only for illustration.

8.4.2 Model configuration

The model configuration is based on the previous CTD-scale model geometry and boundary conditions. The difference is in the inhomogeneity concept. The ideas in the background are the following: (1) we need to introduce a varying permeability in the direction perpendicular to the tunnel (Figure 8.19) and (2) the data used as a basis for permeability changes along the tunnel are related to the tunnel and the borehole sections scale, so it should be relevant for such scale in the model (i.e. not for the whole volume as used in prediction). Thus the model geometry is composed of two "nested" parts: the inner one 30 m × 30 m × 100 m using the permeability inhomogeneity and the outer part of homogeneous equivalent continuum with site-scale average permeability. The choice should normally be based on expected spatial scale covered by observation on the tunnel wall and in the borehole, but it is also motivated by more illustrative visualization at this stage.

We work with the variant with the set of deterministic fractures coupled to "matrix" blocks in between (TUL3 in section 8.2.2); the fracture set and geometry is exactly the same (data of the tunnel wall mapping) except the clipping by the inner model block. The views are shown in Figure 8.18.

The parameters to be found by the calibration procedure are the following:

- The permeability and the storativity of each fracture individually
- The permeability and the storativity of the rock blocks between the fractures (homogeneous inner 3D subdomain, as a "matrix")
- The permeability and the storativity of the rock continuum in the outer model subdomain (3D "equivalent continuum")

Practically, we first tested a simpler variant with one common parameter of 3D domains (Rock1) and then the two independent settings as listed above (Rock2). Also, the calibration was done manually, so we did not use all the possible degrees of freedom and tried to get an "optimal" result by changing a few of the fracture parameters with the most necessary impact to the resulting pressure evolution (e.g. making some fractures impermeable, using one common storativity for all).

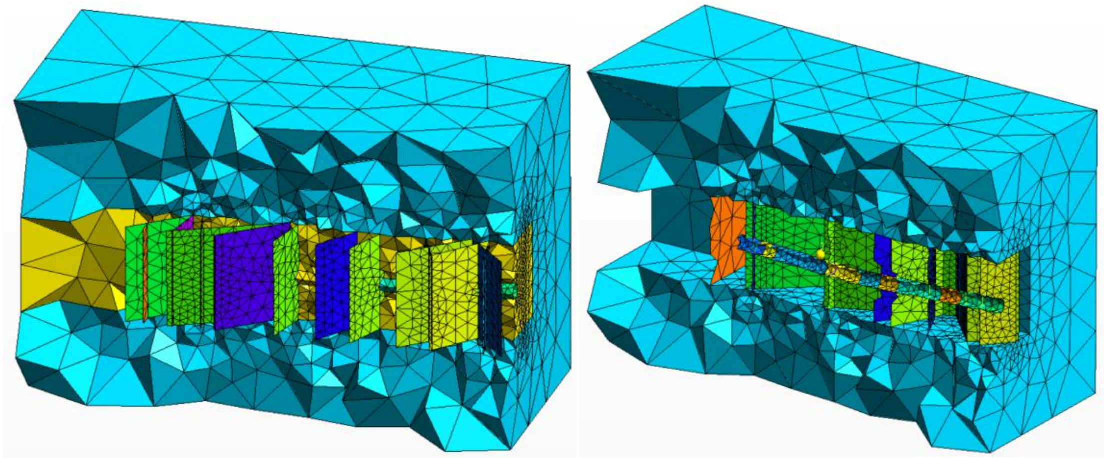

Figure 8.18 Model geometry with domain visibility – left are the whole fractures and half of inner rock, right are half of fractures and no inner rock.

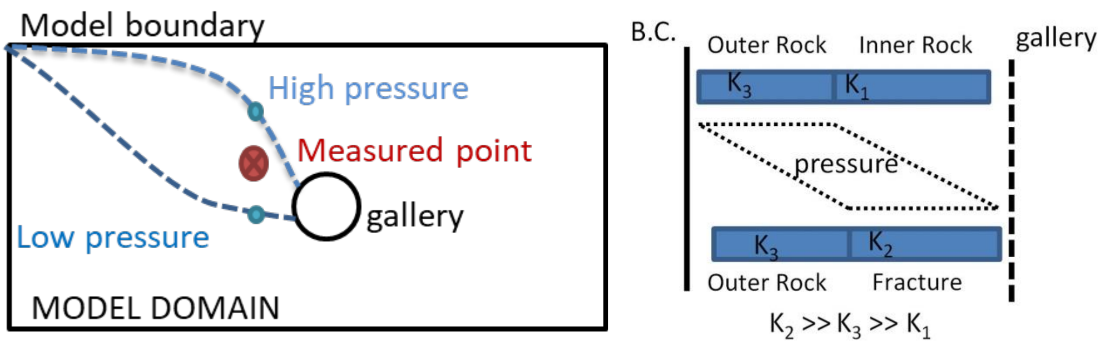

Figure 8.19 Concept explaining different reaction of pressure in a borehole near a tunnel, depending on near/far permeability ratio and a quantitative illustration with data of the Rock3 model variant.

8.4.3 Model Rock3 - coupling fractures and continuum

Due to the principles of the mixed-hybrid FEM in the Flow123d code, the pressure unknowns and fluxes in the fracture subdomain cannot be directly coupled to the discrete unknowns of the 3D domain if the fracture edge touches the surface of the 3D volume. Therefore the hydraulic communication between the inner domain fractures and the outer domain is only possible through the inner domain rock block. It is illustrated in Figure 8.20 left (the 2D-3D communication is "perpendicular" to the 2D plane).

Supposed the inner rock (matrix) is much less permeable, some of the model inhomogeneity choices can result into artificial (non-physical) large hydraulic resistance between the inner and the outer domain. The model Rock3 was created so that the fractures will penetrate a little into the outer 3D continuum domain and the fracture triangular element become a side of at least one 3D domain tetrahedral element to provide the proper communication (Figure 8.20 right). Without this correction, the Rock1 and Rock2 results could only be treated qualitatively with respect to the inner/outer inhomogeneity effects, without relevant relationships between the input permeability and the resulting fluxes and pressure gradients.

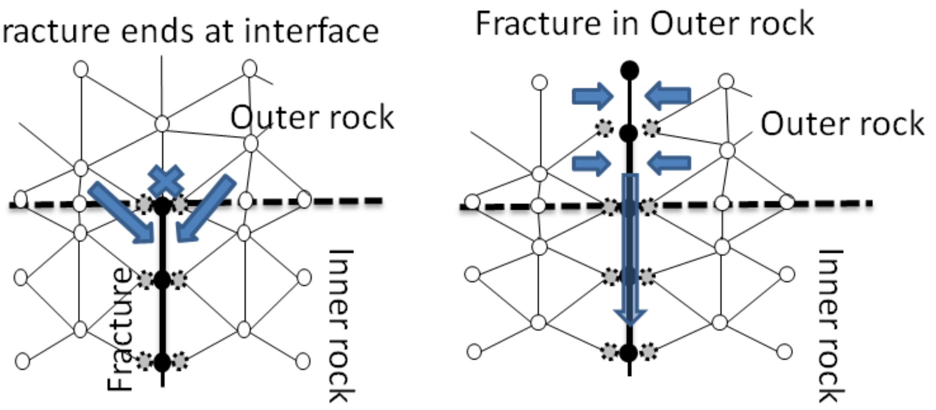

Figure 8.20 2D-3D coupling in the discretisation: Comparison of the Rock 1 and Rock 2 model configuration (left – fractures end at the interface) and the Rock3 model configuration (right – fractures penetrate into the outer rock domain).

8.4.4 Model input data

As mentioned before, this stage was intended to demonstrate the capability to fit the data with various model inputs, but not to perform the full optimization procedure. The settings are demonstrated on two models options Rock1 and Rock2 described above, with either common or independent values of the inner and outer 3D subdomains. The Rock2 variant was later updated to Rock3.

The set of parameters found to fit the measured data with at least some of the quantitative and qualitative features (not all together at the moment) is presented in Table 8.4. The fracture permeability is only changed for one case, where there is clearly very limited communication between the gallery and the respective borehole section, with almost no pressure disturbance during excavation (fracture no.108 in the section No.4). The storativities had very limited effect in some range, but can provide effects on the slope within about two orders of magnitude range. On the other hand, the steady pressure in Section 2 and 5 cannot be seen as “very slow reaction” from very large storativity, which would not have any physical meaning.

So the main values to set are the rock continuum permeabilities. To provide the desired effect, the inner permeability must be significantly smaller than the fractures (in the sense of the total volume transmissivity).

The parameters of Rock3 model and Rock2 model are similar (Table 8.4). The differences between parameters are only in hydraulic conductivity of the outer rock $K = 5 \times 10^{-9}$ and in fracture 108 (where $K = 3 \times 10^{-9}$). The hydraulic conductivity of the inner rock for model Rock3 is the lowest compared to the outer and the fracture hydraulic conductivity. Then the undisturbed pressure can be transferred through the outer rock to the borehole isolated from the tunnel (upper line in Fig.8.19 right) or the drainage effect can be transferred by a fracture against the pressure in the outer rock (lower line in Figure 8.19 right).

Table 8.4 Set of input parameters for the two variants of partially calibrated hydraulic models.

<table>
<tr><td></td><td colspan="2">Model Rock1</td><td>Model Rock2</td><td>Model Rock3</td><td>Model Rock2 and Rock3</td></tr>
<tr><td></td><td>Conductivity m/s</td><td>Storativity 1/m</td><td colspan="2">Conductivity m/s</td><td>Storativity 1/m</td></tr>
<tr><td>Inner rock</td><td rowspan="2">1e-12</td><td rowspan="2">1e-5</td><td>1e-10</td><td>1e-10</td><td>1e-10</td></tr>
<tr><td>Outer rock</td><td>1e-7</td><td>5e-9</td><td>1e-6</td></tr>
<tr><td>Fracture 108</td><td>3e-11</td><td>7e-8</td><td>3e-12</td><td>3e-9</td><td>5e-8</td></tr>
<tr><td>All fractures</td><td>Original various</td><td>5e-10</td><td>Original various</td><td>Original various</td><td>5e-8</td></tr>
</table>

8.4.5 Temporary results – hydraulic

The resulting pressure evolutions are shown in Figure 8.21 for the Rock1 model and Figure 8.22 for the Rock2 model. In the former case, the model is successful in fitting the final pressure values: the lowest for No.2 and No.3 with a continuing decreasing trend, No.6 with slightly higher pressure but the trend not captured (even if we disregard the later pressure rise which cannot be modelled as natural hydraulic-only process), No.4 with very small decrease, and No.1 and No.5 with almost no decrease (still the model has some decreasing trend contrary to the steady measured value). The gradual pressure decrease could be related to relatively large specific storativity value of the rock continuum or wider drainage from the remainder of the facility, the very little pressure decrease of No.1 and 5 to the combination of large storativity and small permeability, which could be seen as unrealistic in the large-scale outer continuum domain.

In the second case (Rock2), the fit was oriented on capturing the pressure decrease trends, in particular on their sharp fall in the relatively narrow times of the data gap. A fragment of No.6 measured pressure evolution shows the slope. We expected a similar slope for No.3 and No.2, where the measurement is not available. . The temporal position of the pressure reaction for No.2, 3, 4 was well-captured, including the slope, but we lost many other representative features of the results. In particular, the No.6 pressure drop is too early and too large, and although the No.1, 4, 5 pressure drops are smaller in the group, it is again too large compared to the measurement. The final pressure is well fitted only in the sections 2 and 3, but with a steady value instead of a slight decrease trend.

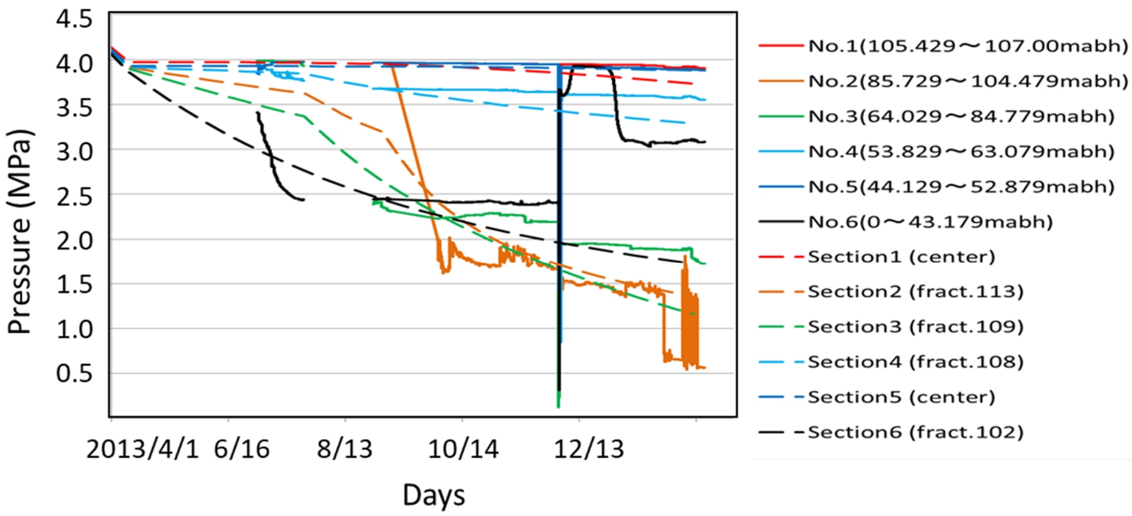

Figure 8.21 Evolution of pressure in Rock1 model, comparison between the measurement (upper legend) and the calculation (lower legend, defining the model observation point).

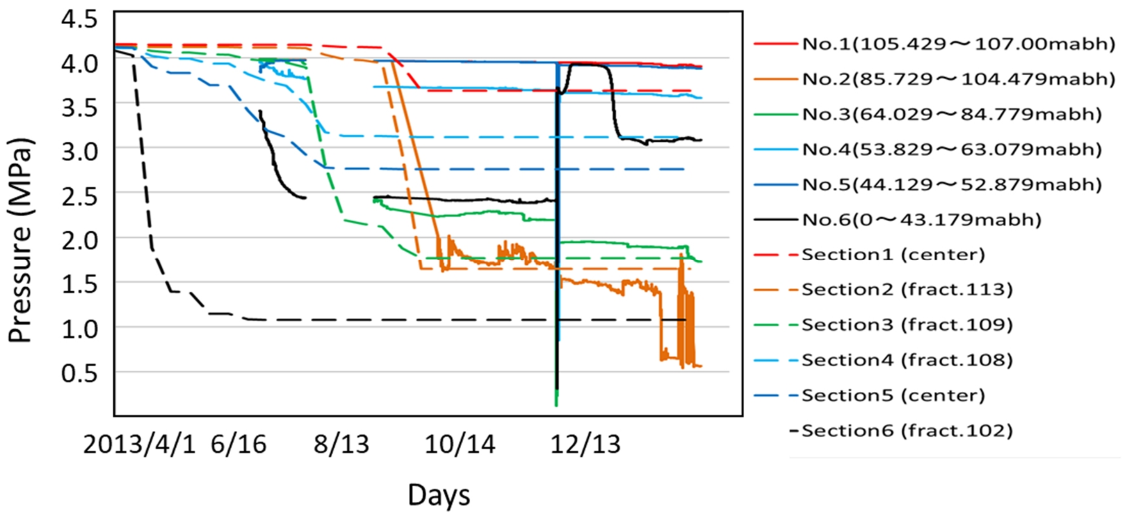

Figure 8.22 Evolution of pressure in Rock2 model, comparison between the measurement (upper legend) and the calculation (lower legend, defining the model observation point).

Next, we can evaluate the tunnel inflow evolution, presented in Figure 8.23 for both Rock1 and Rock2. We did not attempt to calibrate to this data, which would be two single values of the inflow at the time of finished excavation. The reason is that we detected the problem of the limited numerical hydraulic communication between the inner domain fractures and outer domain continuum (described above) – hence the calibrated data would not be representative. The flow is smaller than it should be with a correct coupling of the outer block conductivity and fracture transmissivity. In general, we see the rather small inflow, especially for Rock1 (which is clearly related to small rock continuum permeability) but can be significantly decreased by the "numerical resistance" between the inner and the outer domains (the case of Rock2).

The effect of model inhomogeneity is well seen on the pressure contours in the model sections (Figure 8.24). We can see the intended effect of the fractures with larger drainage side by side with the block of conserved hydraulic pressure. On the other hand, there is the significant effect of the artificial numerical resistance on the inner/outer subdomain interface (large pressure difference through the interface).

8.4.6 Temporary results – transport

At the moment, the transport data were not used for calibration. The purpose of the presenting them here is to help understanding the effects of the updated model structure and of the partly fitted hydraulic parameters, on the chlorine transport behavior. The input parameters the same as those in Section 8.2.1 as well as the initial and boundary concentration distribution (linear increase with depth). The results are shown in Figure 8.25 for the Rock2 variant. We can see the sharpening of the concentration gradient near the tunnel, which is most intensive at the gallery beginning and gradually decreasing further inside, where the time between the local excavation and the model output is smaller. Also, the locations of larger flow along the fractures enlarge the effect.

8.4.7 Results of Rock3 model

The results of pressure evolution are shown in Figure 8.26 for the Rock3 model. Contrary to previous results, the model mostly exhibits a better fit of the measured data trends, and the pressure is not so low overall. For No.6, the model is closer to measurements. For No.2, the model captured the decreasing time precisely but did not capture the final value exactly. Other results of models No.1 and No.3 captured the trend of measurements but the final value of No.3 is worse. No.5 and No.4 models are off the measurements and the final values are farther from measurements than in the previous results of Rock2. We note that the comparison describes the effect of the more physical numerical configuration (a correction of the Rock2 insufficiencies), with the same conceptual consideration and input data.

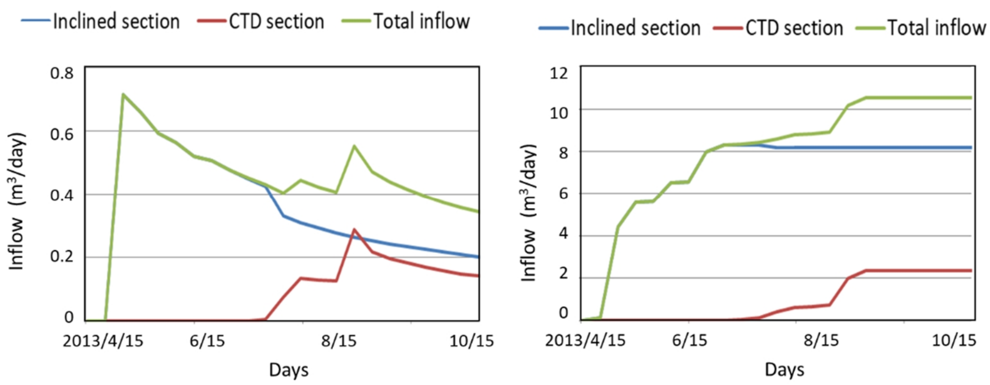

Figure 8.23 Evolution of the tunnel inflow into its two parts, Rock1 variant in the left, Rock2 variant in the right.

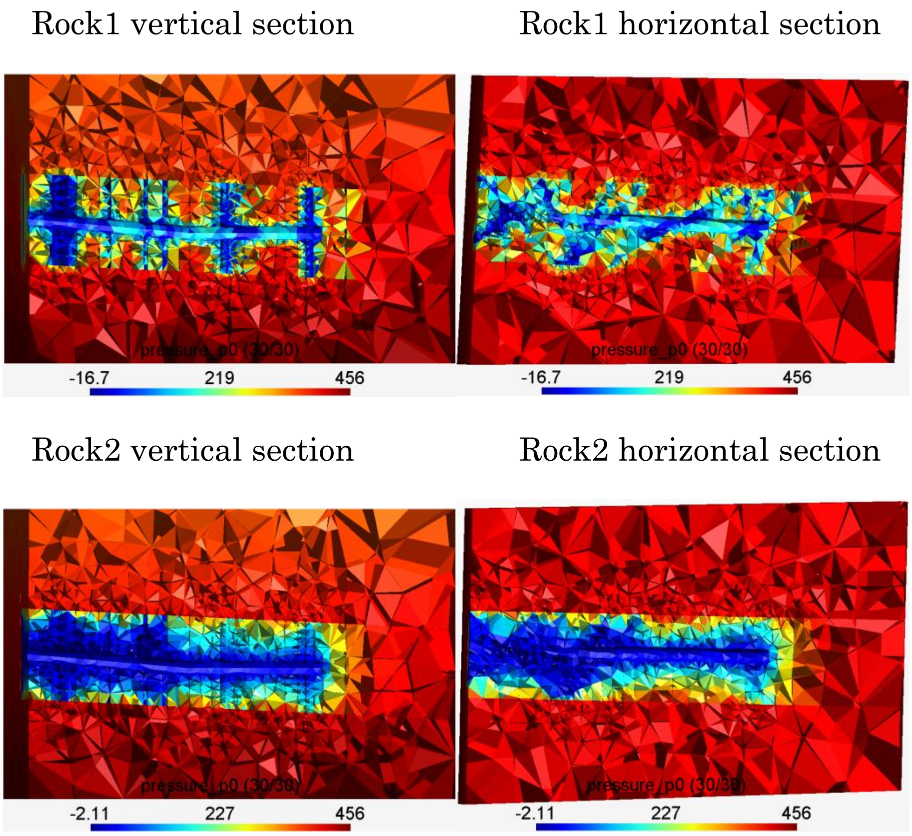

Figure 8.24 Spatial distribution of pressure head [m] in the two calibrated variants and in two sections along the tunnel.

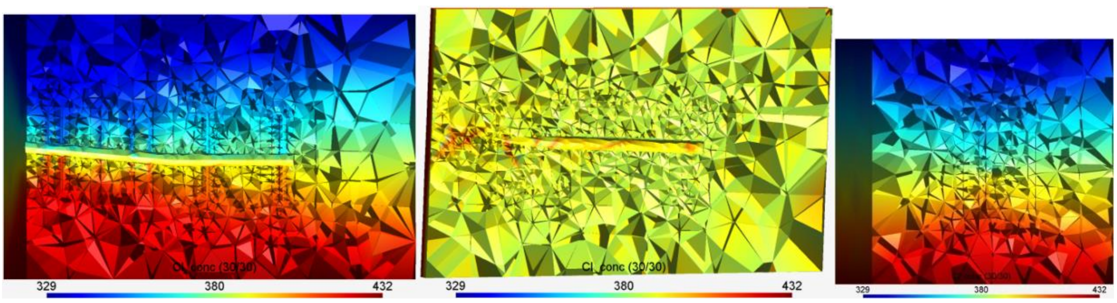

Figure 8.25 Spatial distribution of the chlorine concentration for Rock2, the order of the sections is the vertical along the tunnel, the horizontal and the vertical across the tunnel.

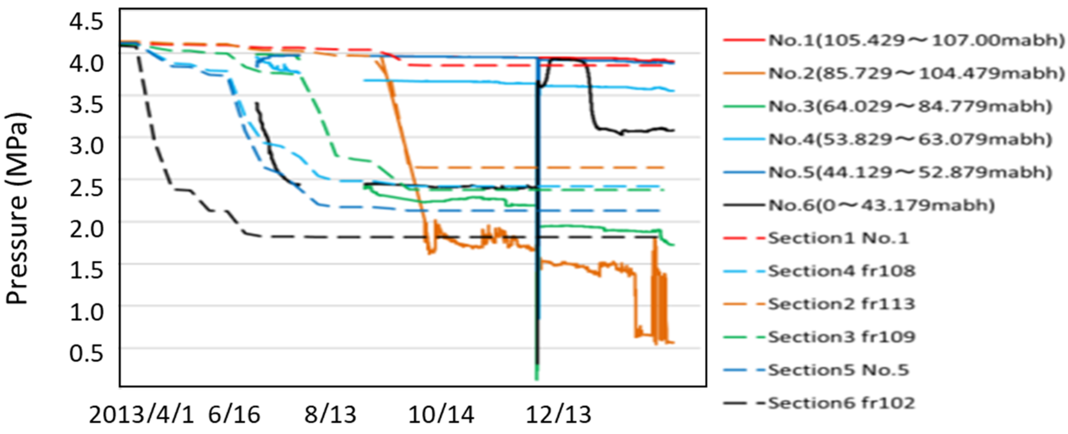

Figure 8.26 Pressure evolutions in Rock3 model, comparison between the measurement (upper legend) and the calculation (lower legend, defining the model observation point).

The spatial distribution of pressure in Figure 8.27 left confirms a realistic hydraulic connection between the fractures and the inner and outer rock. Evidently, the penetrated fractures into the outer rock are very helpful for gradient evolution on the connection between the outer and inner domains. The pressure gradient on fractures is depicted on Figure 8.28. The differences between more conductive fractures and low conductive fractures are shown.

The results of chlorine concentration of Rock3 model are similar to previous results of Rock2 model. The spatial contrast of concentration in and around fractures is more obvious (Figure 8.27 right). Consequently, the effect of establishing high concentration gradient at the tunnel level is more visible than in the other results.

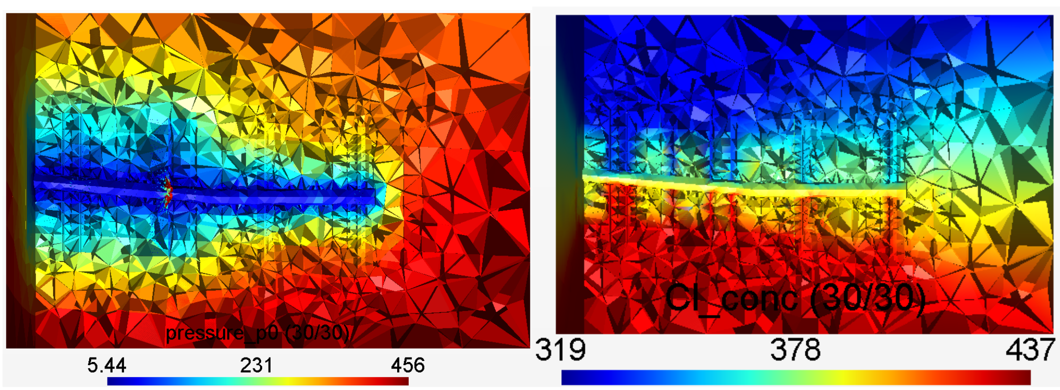

Figure 8.27 Spatial distribution of pressure head [m] (left) and the chlorine concentration [g/L] (right) for Rock3.

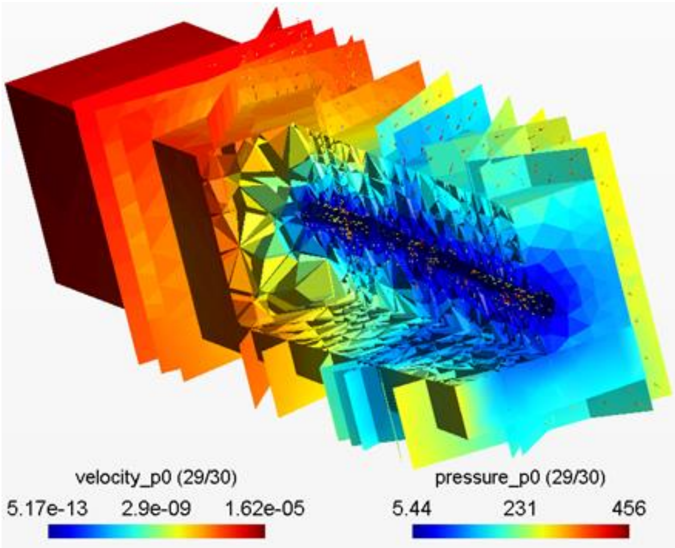

Figure 8.28 Spatial distribution of pressure head and velocity for Rock3 (the outer rock is excluded, the fractures are visible including the penetrating parts, and the inner block is partly cut).

8.5 Evaluation of Step 1

The prediction has been made with several model variants, based on different details selection from the available data. Through this, we get some idea of the impact of conceptual and parameter uncertainty.

The heterogeneity affects the main features of model results partially – the final pressure values are similar, but the rate of change is increased and the inflow rate is strongly controlled by the permeability. For model calibration, a more sophisticated spatial distribution must be considered, to e.g. distinguish the affected and non-affected monitoring sections by the tunnel drainage. This was demonstrated on some examples with different permeability in the near field and the far field of the tunnel. The Rock3 variant appears to be an appropriate start for the Step 2 modelling.

The transport model was expected to show how the concentration changes are affected by the movement of the water of different original depths. Because the heterogeneity models used were symmetric (concerning upper/lower parts), its effect was very small. Possibly, longer a time could be also needed for the arrival of water with more difference in concentration to the monitoring points. Also, we could consider alternative porosity values (i.e. the transport porosity different from the total porosity), an inhomogeneity in the vertical direction as well as an impact of channelization.

8.6 Geochemical data processing

This part has been addressed separately from the main task definition. The specific features of the geochemical study do not readily allow it to be split into the three Steps of subsequent prediction and calibration. One of the reasons is that the necessary introductory step is understanding the processes, i.e. select the components and reactions which control the phenomena observed during the phases of excavation (drainage), re-saturation, and long-term processes. This makes a blind prediction much more difficult that for e.g. the hydraulics and is unlikely to be informative. Therefore the time period of the work on Step 1 is intended to the initial study of geochemical processes in the site scale to get the proper background for studying the CTD scale processes related to the rock and groundwater disturbance. For this reason, the measured chlorine concentrations were not yet used for improvement of the boundary conditions in the hydraulic and transport model, but they will help to define the boundary conditions in Step 2.

Basic hydrochemical characterization of MIU groundwater was already published by Iwatsuki et al. (2015). The aim of this work is to prepare geochemical models of individual groundwater types (to be determined later) that will serve for transport and reactive transport modeling. At the same time, models should make it possible to predict how each type of groundwater will respond to changing conditions (oxidative, anoxic and reductive) and how it will affect the construction materials tested at the MIU Research Laboratory.

8.6.1 Overview of work

Finished work

- prepared internally consistent database in Geochemist's Workbench format including data about redox potential and with unique identification of each sample
  - o 3875 samples in 109 zones from 18 boreholes
  - o time interval: years 2003 - 2016

Work in progress

- basic characterization of groundwater types according to the concentrations of main components (Na^+, K^+, Ca^{2+}, Mg^{2+}, Cl^-, HCO_3^-, SO_4^{2-}) with concentration of total dissolved solids and pH
  - o concentration of dissolved carbonates was calculated from the concentration of total inorganic carbon and checked against measured alkalinity
  - o the accuracy of the analyzes is checked by calculating the charge balance error and comparing to the measured electrical conductivity
- evaluation of the relationship between the concentrations of the main components and the physico-chemical parameters
- assessment of the relationship between the groundwater type and the rock environment
- assessing the development of groundwater chemical composition to the depth
- evaluation of the time development of component concentrations relative to the time bore-hole was drilled

Planned work

- Interpretation of redox potential (where it is possible)
  - ✓ measured ORP

- ✓ redox pairs SO_4^{2-}–(HS^-)–S^{2-}
- ✓ redox pairs NO_3^-–(NO_2^-)–NH_4^+
- ✓ redox pairs Fe^{3+}–Fe^{2+} (Fe^{3+} calculated from T-Fe and Fe^{2+})
- ✓ redox based on DO (dissolved oxygen)
- ✓ redox pair TIC–TOC (total inorganic carbon–total organic carbon)

Remark: Oxidation-reduction processes are much slower compared to other chemical equilibria in the water, and often the oxidative-reduction equilibrium is not achieved. In addition, the oxidation-reduction potential (ORP) depends not only on the total concentration (activity) of the oxidized and reduced forms of the redox pair, but also on their speciation. The speciation of the components is strongly dependent on the pH and the concentration of the other components in water. Therefore, the evaluation and interpretation of ORP will be based on complete geochemical models of individual water types.

- identification of the main processes that determine the chemical composition of individual water types
- preparation of geochemical models for basic groundwater types at MIU site

Partial results from the current stage of the project – what we already know (in examples in the next section):

- there are several types of groundwater
- concentrations of some major components do not change during sampling period, others are increasing or decreasing
- concentrations of physicochemical parameters and some major components change depending on depth or sampling zone for horizontal boreholes
- concentration relationships of the major and minor groundwater components differ for different groundwater types
- the rock environment has a significant effect on the composition of groundwater but it also happens that groundwaters in the same rock type have different composition and vice versa
- MIU deep groundwater differs from ocean water not only by salinity but also by the relative proportion of major cations

8.6.2 Examples of current results

The overall picture of groundwater composition for the main shaft in shown in Figure 8.29. The Piper and Durov diagrams allow to distinguish individual water types and their development in time and space using color coding.

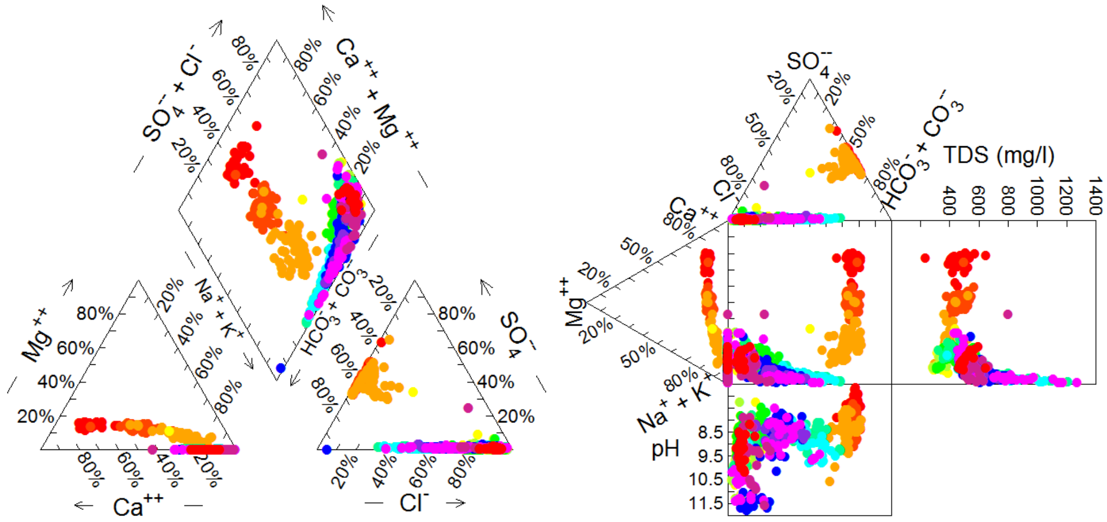

Figure 8.29 Piper and Durov diagrams of water-ring samples from Main shaft (A-WR). The depth of WR in each color is shown in Figure 8.31.

Diagrams in Figure 8.30 allow to track the development of concentrations of individual components and physico-chemical parameters over time. Concentrations of some components do not change from the beginning and are stable, others are increasing or decreasing.

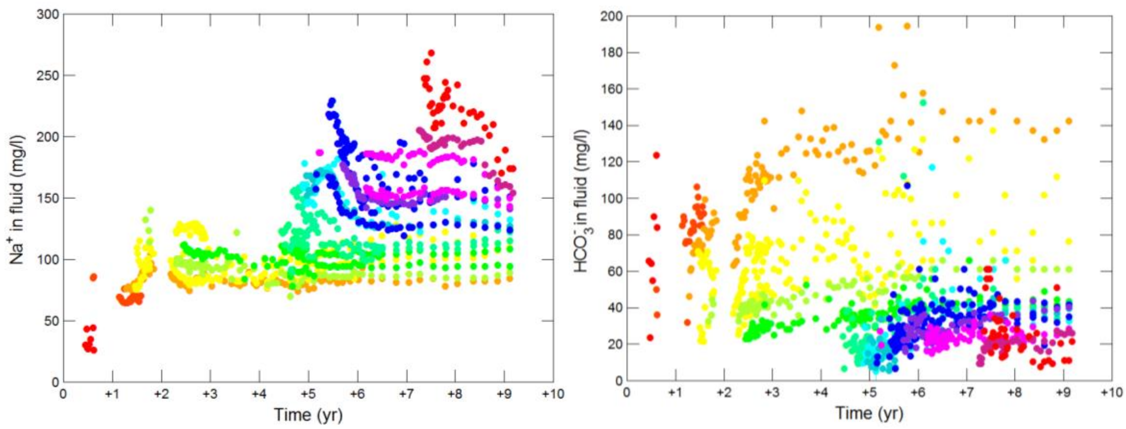

Figure 8.30 Development of Na and HCO3 components in water-ring in Ventilation shaft (B-WR) beginning 1/1/2004. Color coding corresponds to individual sampling zones (depths). The depth of WR in each color is shown in Figure 8.31.

Diagrams in Figure 8.31 allow to track the development of component concentrations depending on depth and with changed color coding also over time.

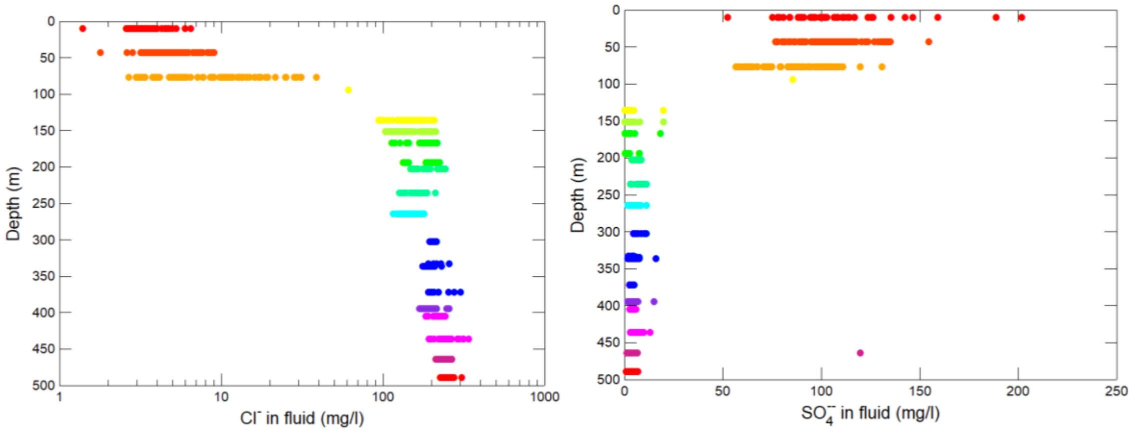

Figure 8.31 Profiles of Cl and SO4 components concentrations in depth in the A-WR.

Concentration relationships of the major and minor groundwater components provide important information for identifying processes that determine their composition. These relationships are different for water types identified so far; an example in shown in Figure 8.32.

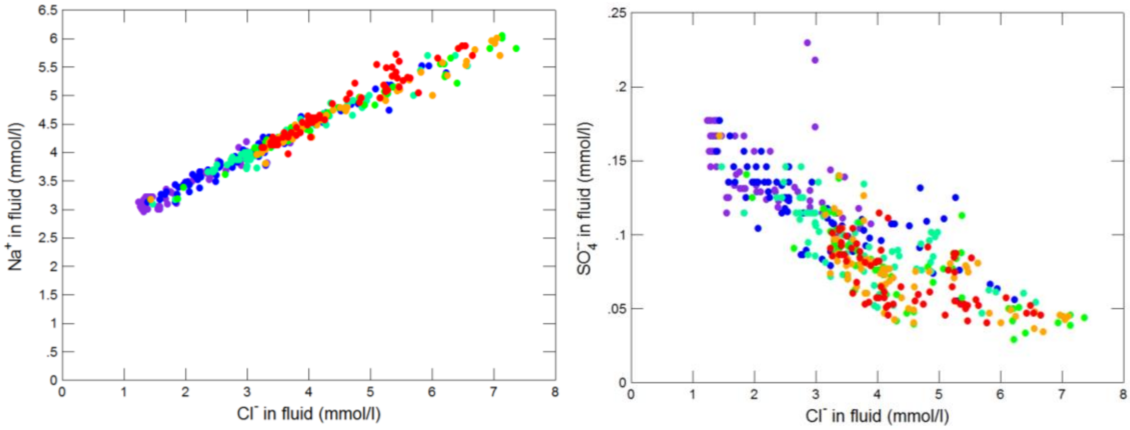

Figure 8.32 Relationships of selected components in 07MI07 borehole samples.

Using the Piper and Durov diagrams, it is possible to determine whether there is a relationship between the groundwater composition (type of groundwater) and the rock type and, if so, what the relationship is. Otherwise, other processes beyond water-rock interaction will be required to interpret the data.

The rock environment has a significant effect on the composition of groundwater, but it also happens that in the same rock the groundwater differs in composition and vice versa, that in different rock types, the groundwater has similar or the same composition (primarily caused by the impact of fractured zones and the direction and rate of water flow). This is shown in a set of diagrams in Figure 8.33.

MIU deep groundwater differs from ocean water not only by salinity but also by the relative proportion of main cations. Data from depth more than 500 m are available only in the MIZ-1 borehole, shown in Figure 8.34.

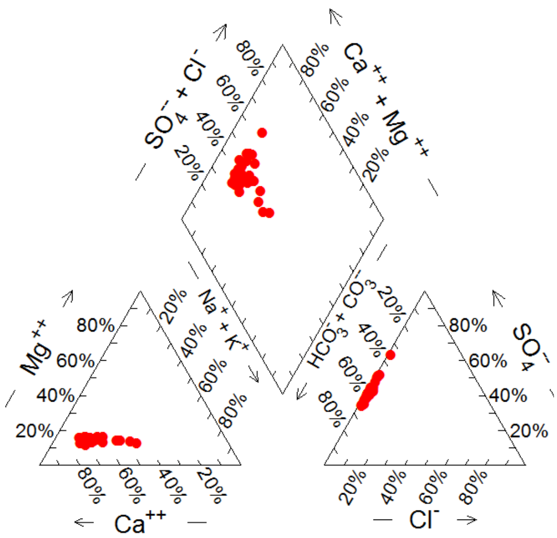

A-WR water collection ring 1 - 10,0 m

Alluvium

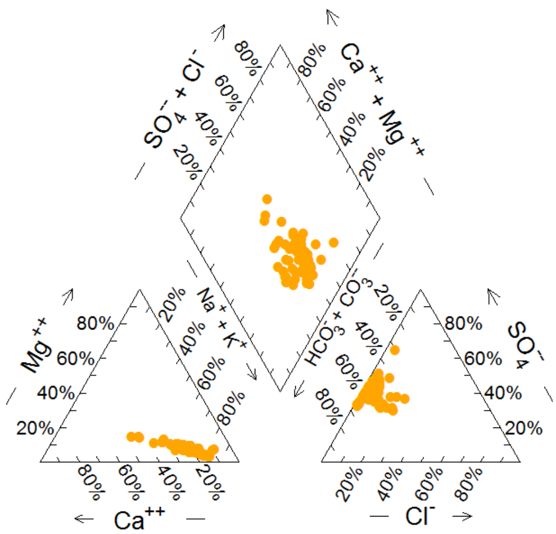

A-WR water collection ring 3 - 77,0 m

Conglomerate

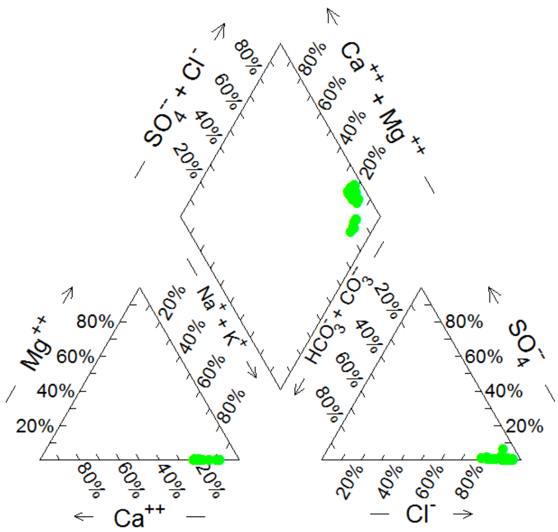

A-WR water collection ring 7 - 167,4 m

Basal conglomerate

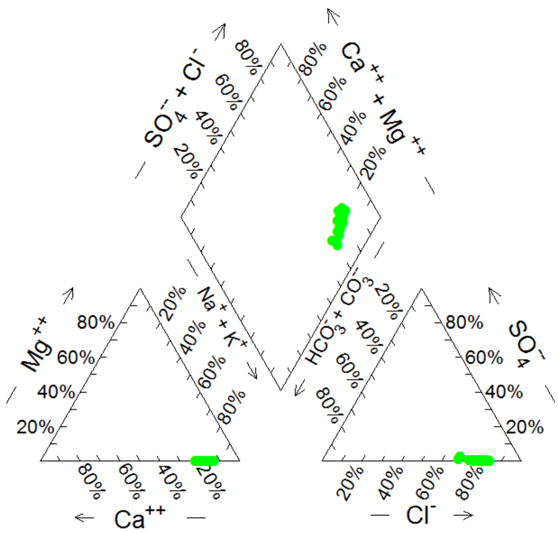

A-WR water collection ring 8 - 194,4 m

Toki granite (UHFD: Upper Highly Fractured Domain)

Figure 8.33 Relationships of groundwater composition to the rock type in A-WR depth zones (ring 1 to ring 18). (1/3)

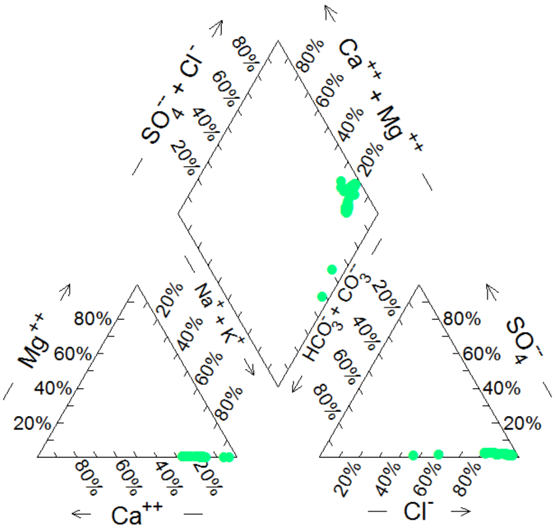

A-WR water collection ring 9 - 202,6 m

Toki granite (LAFZ: Low Angle Fractured Zone)

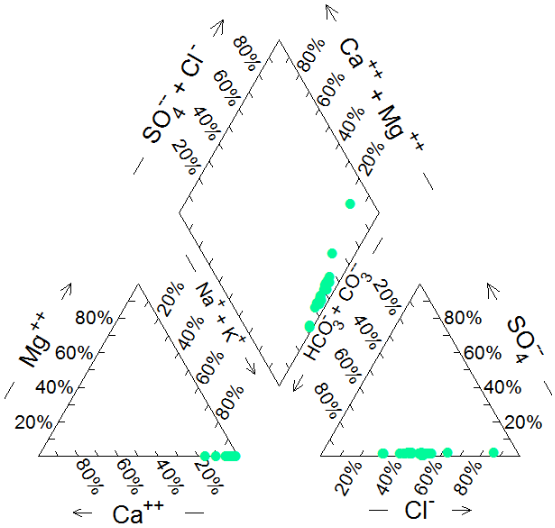

A-WR water collection ring 10 - 236,2 m

Toki granite (LAFZ)

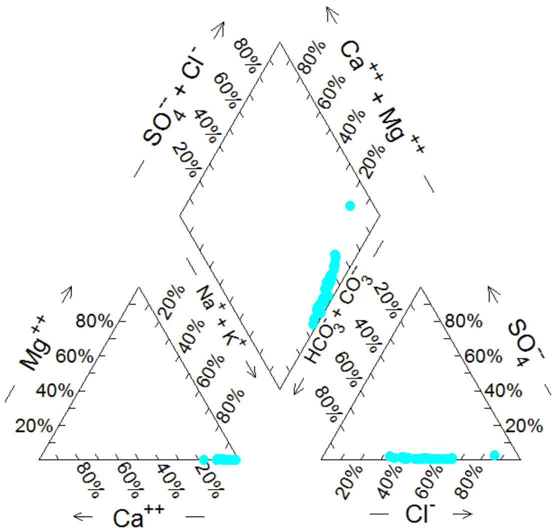

A-WR water collection ring 11 - 264,8 m

Toki granite (UHFD)

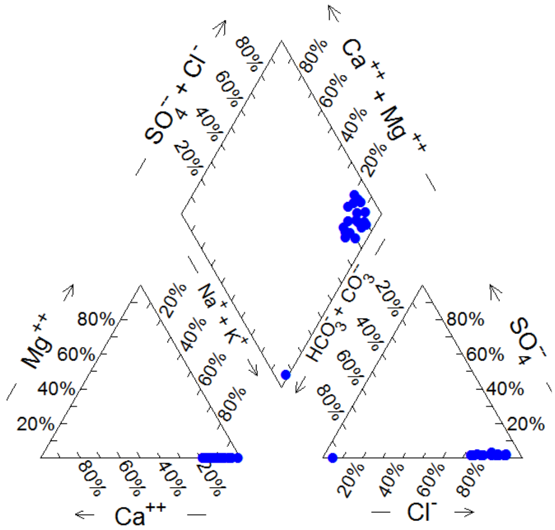

A-WR water collection ring 13 - 302,6 m

Toki granite (UHFD)

Figure 8.33 Relationships of groundwater composition to the rock type in A-WR depth zones (ring 1 to ring 18). (2/3)

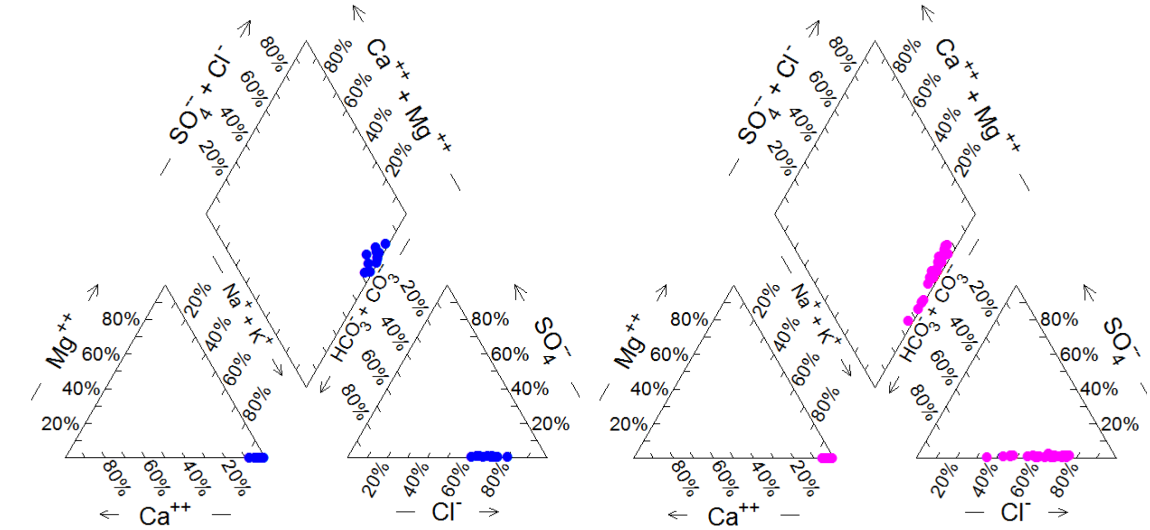

A-WR water collection ring 15 - 372,0 m

Toki granite (UHFD)

A-WR water collection ring 18 - 436,2 m

Toki granite (LSFD: Lower Sparsely Fractured Domain)

Figure 8.33 Relationships of groundwater composition to the rock type in A-WR depth zones (ring 1 to ring 18). (3/3)

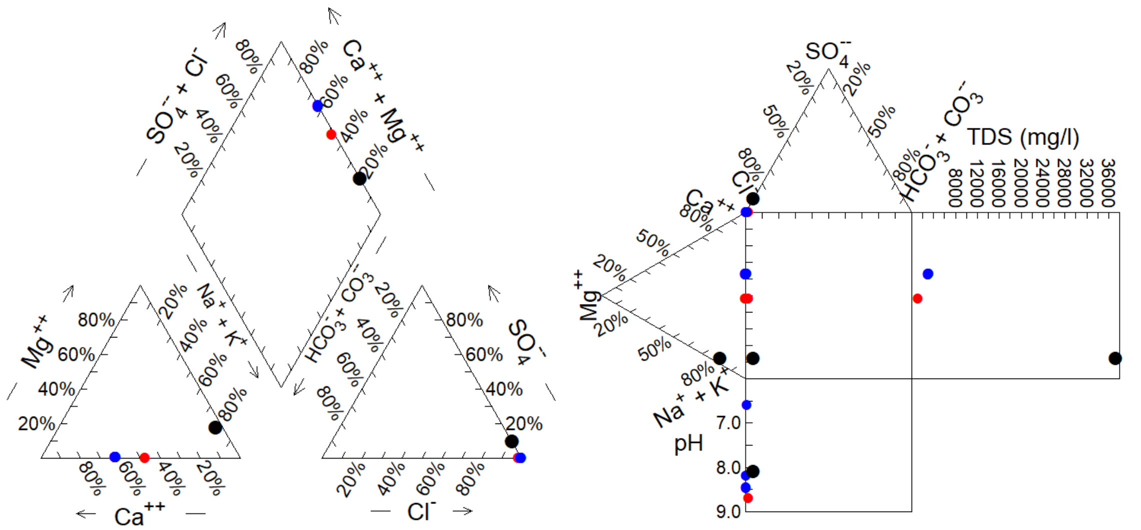

Figure 8.34 Piper and Durov diagrams for deep groundwater from borehole MIZ-1 and their comparison with sea water composition. Red 648.3 m: Na-(Ca)-Cl type, blue 1148.8 - 1169.8 m: Ca-(Na)-Cl type, black Sea water: Na-(Mg)-Cl.

9. Summary of Step 1

In Step 1, the three research teams tested their respective simulation method to estimate the environmental change caused by tunnel excavation based only on preliminary information of granite and pilot borehole investigation. Such a simulation technique would be indispensable for the project administrator of geological disposal to plan the facility layout and risk assessment in facility construction phase.

One of the aims of this Step is to know how to predict, or to what extent we can predict, the subsurface phenomenon prior to an actual facility construction phase. As an index to know the technical ability to predict environmental disturbance, we estimated water inflow rate into the tunnel, the drawdown of hydraulic pressure and change of chlorine concentration during/after the excavation of the tunnel.

The approach, results and key points from the modelling work by each research team are summarized as follows;

<u>JAEA team</u>

1) Steady state flow simulation using DFN model (100 realizations) by FracMan®
2) Extract the DFN model which well reproduces the pressure distribution
3) Convert the DFN model to ECPM model. Estimate transient disturbance of water pressure, chemistry, and rock displacement using Couplys.

The results obtained show that the ECPM model can reproduce the difference of hydraulic pressure changes in each monitoring section by tunnel excavation, but the timing of the drawdown is not well-matched with the observed data. The total inflow rate roughly matches with the observations, but inflow rate in CTD is estimated at a much lower value. The ECPM model at this Step cannot reproduce the large change of Cl concentration seen in the observation data.

The nature of the fracture distribution and hydraulic connectivity between the CTD and monitoring sections could be a key matter for the poor prediction accuracy of Cl concentration.

<u>SNL team</u>

1) Deterministically set the fractures on CTD wall and in borehole (focused on water-conducting features with aperture)
2) Set the permeability of deterministic fractures estimated by inflow rate.
3) Constructed DFN model around the CTD (parameter set are estimated by boreholes [intensity] and CTD [intensity & radius & orientation]) using FracMan. Upscaled from DFN model to ECPM model (Grid size: 1m x 1m x 1m) using Oda's method.
4) Conducted steady state flow and transport simulations using homogenous and fracture (ECPM) models with DAKOTA-PFLOTRAN coupled codes.

ECPM model was able to reproduce the difference of hydraulic pressure values in each section and inflow rates at drifts. However, estimations of the Cl concentration profiles using the ECPM model differed from the experimental data.

The results in Step 1 are preliminary output for only two realizations of the fractured system. More realizations will be needed to obtain average representative output for more detailed comparison with the observed data. Future simulations will also be based on a larger modeling domain to minimize boundary effects.

TUL team

1) Deterministically set the fractures only around drift
2) Set the permeability (K) and storativity (S) of rock matrix two variations; Rock1 (K & S of all rock matrix are same), Rock2 (K & S are different value for around drift and for the remaining part), Rock3 (fractures are penetrated to rock continuum in the far area)
3) Manually calibrated the K and S of rock matrix and fracture using Flow123d

"Rock1" could reproduce the difference of pressure value of each section, while "Rock2" reproduces trend of the drawdown of only section 2 and 3. Both models could not reproduce the inflow values (much lower value). Both models could not reproduce the large disturbance of the observation data. The optimization of K and S in the near area and the far area from the drift is still necessary.

Achievements for the Step1 task by each team are shown in Table 10.1.

Table 9.1 Simulation results of environmental disturbance during tunnel excavation at the end of Step1

Modelling/simulation target	JAEA	SNL	TUL
Code	FracMan, Couplys	FracMan, DAKOTA, PFLOTRAN	Flow123d
GW inflow rate	Total:○ CTD: ×	Total:○ CTD:○	Total: × CTD: ×
Hydraulic pressure	△	○	○
Chlorine concentration	×	×	×

To sum up the simulation techniques in the pre-excavation stage of the facility construction, groundwater inflow rates into the tunnel can be approximately predicted by current modelling procedure. The highest and lowest drawdown of water pressure can be estimated while the rate of the drawdown can't be predicted easily. Moreover, it's difficult to predict the variation of groundwater chemistry. In transport modelling to estimate Cl concentration, it is necessary to reflect the continuity of the fracture network in the model with reference to the spatial distribution of chlorine concentration.

The Main tasks in Step 2 are to develop the modelling and prediction method to estimate environmental recovery during/after the drift closure based on the data of drift and borehole investigations. Such technique would be available for the project administrator to do a safety assessment of the potential for radionuclide transport before the facility closure phase.

References

1) Shibata, K., Ishihara, S., Rb - Sr whole-rock and K-Ar mineral ages of granitic rocks of the Komagane district, Nagano Prefecture, Central Japan. Geochemical Journal, 13, 1979, pp. 133-119.

2) Shikazono, N., Nakata, M., Compositional variation of pyrite, diagenetic alteration and genesis of Tono sandstone-type uranium deposits in Japan. Research Geology Special Issue. 20, 1999, pp. 55-64.

3) Shimono M, Suzuki S, Taguchi Y, Kamemura K, Sato T, Mikake S., Risk assessment approach for underground research laboratory. Proc. ISRM International Symposium: 3rd Asian Rock Mechanics Symposium, 2004, pp. 359-365.

4) Nuclear Waste Management Organization of Japan, Safety of the Geological Disposal Project 2010 - Safe Geological Disposal Based on Reliable Technologies -, NUMO-TR-13-05, 2013, 148 p., (in Japanese).

5) Long, J. C. S., Billaux, D., Hestir, K., Majer, E.L., Peterson, J., Characterization of fracture networks for fluid flow analysis, Lawrence Berkeley Lab., LBL-26868, 1989.

6) Koyama, T., Chijimatsu, M., Shimizu, H., Nakama, S., Fujita T., Kobayashi, A., Ohnishi, Y., Numerical modeling for the coupled thermo-mechanical processes and spalling phenomena in Äspö Pillar Stability Experiment (APSE), Journal of Rock Mechanics and Geotechnical Engineering, 5 (1), 2013, pp. 58-72.

7) Kobayashi, A. and Ohnishi, Y., Effects of non-linearity of material properties on the coupled mechanical-hydraulic-thermal behavior in rock mass. In: Collected Papers of Japan Society of Civil Engineers, Tokyo, Japan Society of Civil Engineers, 1986, pp. 101-110, (in Japanese).

8) Ohnishi, Y., Shibata, H., Kobayashi, A., Development of finite element code for the analysis of coupled thermo-hydro-mechanical behaviors of a saturated-unsaturated medium. In: Tsang CF, editor. Coupled Processes Associated with Nuclear Waste Repositories, Orlando, Academic Press, 1987, p. 551.

9) Nishigaki, M., Hishiya, T., Hashimoto, N., Density dependent groundwater flow with mass transport in saturated-unsaturated porous media, Proceedings of the First Asian-Pacific Congress on Computational Mechanics, 2001, pp. 1375-1380.

10) Onoe, H., Iwatsuki, T., Saegusa, H., Ohnuki, K., Takeuchi, R., Sanada, H., Ishibashi, M., Sato, T., Groundwater recovery experiment using an underground gallery in fractured crystalline rock, Proc. 8th Asian Rock Mechanics Symposium. Int. Soc. Rock Mech., Lisbon, Portugal, ISBN 978-4-907430-03-0, 2014.

11) Oda, M., Permeability tensor for discontinuous rock masses, Geotechnique, 35(4), 1985, pp. 483-495.

12) Golder Associates, Inc., Interactive Discrete Feature Data Analysis, Geometric Modeling and Exploration Simulation, FracMan Manual, April 6, 2017.

13) Hammond, G. E., Lichtner, P. C., and Mills, R. T., Evaluating the Performance of Parallel Subsurface Simulators: An Illustrative Example with PFLOTRAN, Water Resources Research, 50 (1), 2014, pp. 208-228.

14) Jové Colón, C.F., J.A. Greathouse, S. Teich-McGoldrick, R.T. Cygan, T. Hadgu, J.E. Bean, M.J. Martinez, P.L. Hopkins, J.G. Argüello, F.D. Hansen, F.A. Caporuscio, M. Cheshire, Evaluation of Generic EBS Design Concepts and Process Models: Implications to EBS Design Optimization (FCRD-USED-2012-000140), U.S. Department of Energy, 2012, p.250.

15) Jové Colón, C.F., P.F. Weck, D.C. Sassani, L. Zheng, J. Rutqvist, C.I. Steefel, K. Kim, S. Nakagawa, J. Houseworth, J. Birkholzer, F.A. Caporuscio, M. Cheshire, M.S. Rearick, M.K. McCarney, M. Zavarin, A. Benedicto-Cordoba, A.B. Kersting, M. Sutton, J.L. Jerden, K.E. Frey, J.M. Copple, and W.L. Ebert., Evaluation of Used Fuel Disposition in Clay-Bearing Rock (FCRD-UFD-2014-000056), Sandia National Laboratories, SAND2014-18303 R: Albuquerque, NM, 2014, p. 434.

16) Iwatsuki, T., Furue, R., Mie, H., Ioka, S., Mizuno, T., Hydrochemical baseline condition of groundwater at the Mizunami underground research laboratory (MIU). Applied Geochemistry, 20, 2005, pp. 2283-2302.

17) Iwatsuki, T., Hagiwara, H., Ohmori, K., Munemoto, T., Onoe, H., Hydrochemical disturbances measured in groundwater during the construction and operation of a large-scale underground facility in deep crystalline rock in Japan. Environmental Earth Sciences, 74, 2015, pp. 3041-3057.

18) Brezina J., and Hokr, M., Mixed-hybrid formulation of multidimensional fracture flow, In: Numerical methods and applications (Lecture notes in computer science), 6046, 2011, pp. 125-132.

19) Saegusa H. and Matsuoka T., Final report on the surface-based investigation (phase I) at the Mizunami Underground Research Laboratory Project, JAEA-Research 2010-067, 2011, 377p.

20) Wang, X., Stereological interpretation of rock fracture traces on borehole wall and other cylindrical surfaces, Ph. D. dissertation, Virginia Polytechnic Institute and State University, 2005.

21) Follin, S., Levén, J., Hartley, L., Jackson, P., Joyce, S., Roberts, D., Swift, B., Hydrogeological characterization and modelling of deformation zones and fracture domains, Forsmark modeling stage 2.2., SKB R-07-48, 2007.

22) Bruines, P., Tanaka, T., Abumi, K., Hashimoto, S., Saegusa, H., Onoe, H., Ishibashi, M., Development and Application of the GeoDFN and HydroDFN at the Mizunami Underground Research Laboratory, 8th Asian Rock Mechanics Symposium, October 14-16, 2014, Sapporo, Japan.

23) Whiteley, J., P., K. Gillow, S. J. Tavener and A. C. Walter, Error bounds on block Gauss-Seidel solutions of couple Multiphysics problems, International Journal of Numerical methods in Engineering, 88(12), 2011, pp. 1219-1237.

24) Yeckel, A., Lun, L., Derby, J., An approximate block Newton method for coupled iterations of nonlinear solvers: Theory and conjugate heat transfer applications, Journal of Computer Physics, 228 (23), 2009, pp. 8566-8588.

25) Vaněk, P., Mandel, J., Brezina, M., Algebraic multigrid by smoothed aggregation for second and fourth order elliptic problems, Computing, 56 (3), 1996, pp. 179-196.

26) Zhang, H.H. Einstein, Dershowitz, W.S., Stereological relationship between trace

length and size distribution of elliptical discontinuities, Geotechnique, 52 (6), 2002, pp. 419-433.

27) La Pointe, R.P., Derivation of parent fracture population statistics from trace length measurements of fractal fracture populations, International Journal of Rock Mechanics & Mining Sciences, 39 (3), 2002, pp. 381-388.

28) Klint, K. E. S., Gravesen, P., Rosenbom, A., Laroche, C., Trenty, L., Lethiez, P., Sanchez, F., Molinelli, L., Tsakiroglou, C. D., Multi-Scale Characterization of Fractured Rocks Used as a Means for the Realistic Simulation of Pollutant Migration Pathways in Contaminated Sites: A Case Study, Water, Air, and Soil Pollution: Focus 4: 2004, pp. 201-214.

29) Butscher, C., Steady-State Groundwater Inflow into a Circular Tunnel, Tunnelling and Underground Space Technology, 32, 2012, pp. 158-167.

30) Snow, D., Anisotropic Permeability of Fractured Media, Water Resources Research, 5 (6), 1969, pp. 1273-1289.

31) Baecher, G. B., Lanney, N. A., Einstein, H. H., Statistical description of rock properties and sampling, Proceedings, 18th US Symposium on Rock Mechanics, 1-8 (5C1), 1977.

32) Ishibashi, M., Sasao, E., Data on Fractures in the Toki Granite Based on the Deep Borehole Investigations. JAEA-Data/Code 2015-004, 2015, 8 p.

33) Ando, K., Tanaka, T., Hashimoto, S., Saegusa, H., Onoe, H., Study for establishment of the methodology for hydrogeological modeling using hydraulic discrete fracture networks (study on hydrogeology in crystalline fractured rock), JAEA-Research 2012-022, 2012, 60 p.

34) Adams, B. M., Ebeida, M. S., Eldred, M. S., Jakeman, J. D., Swiler, L. P., Dakota, A Multilevel Parallel Object-Oriented Framework for Design Optimization, Parameter Estimation, Uncertainty Quantification, and Sensitivity Analysis: Version 6.6 User's Manual. SAND2014-4633. Updated May 9, 2017.

35) Wang, Y., T. Hadgu, E. A. Kalinina, J. Jerden, J. M. Copple, T. Cruse, W. Ebert, E. Buck, R. Eittman, R. Tinnacher, C. Tournassat, J. Davis, H. Viswanathan, S. Chu, T. Dittrich, F. Hyman, S. Karra, N. Makedonska, P. Reimus, M. Zavarin, C. Joseph, Used Fuel Disposition in Crystalline Rocks: FY16 Progress Report, Fuel Cycle Research and Development, FCRD-UFD-2016-000076, SAND2016-9297 R. September 21, 2016.

36) Wang, Y., T. Hadgu, E. Matteo, J.N. Kruichak, M.M. Mills, J.L. Jerden, J.M. Copple, T. Cruse, W.L. Ebert, R. Tinnacher, J.A. Davis, H. Visnawathan, S. Chu, T. Dittrich, F. Hyman, S. Karra, P. Makedonska, P. Reimus, M. Zavarin, P. Zhao, C. Joseph, J. Begg, Z. Dai, and A.B. Kersting, Used Fuel Disposal in Crystalline Rocks: FY15 Progress Report (FCRD-UFD-2015-000125), Sandia National Laboratories: Albuquerque, NM. USA (SAND2015-10687 R), 2015.

国際単位系（SI）

表１．SI 基本単位

基本量	SI 基本単位	
	名称	記号
長さ	メートル	m
質量	キログラム	kg
時間	秒	s
電流	アンペア	A
熱力学温度	ケルビン	K
物質量	モル	mol
光度	カンデラ	cd

表２．基本単位を用いて表されるSI組立単位の例

組立量	SI 組立単位	
	名称	記号
面積	平方メートル	m^{2}
体積	立方メートル	m^{3}
速さ，速度	メートル毎秒	m/s
加速度	メートル毎秒毎秒	m/s^{2}
波数	毎メートル	m^{-1}
密度，質量密度	キログラム毎立方メートル	kg/m^{3}
面積密度	キログラム毎平方メートル	kg/m^{2}
比体積	立方メートル毎キログラム	m^{3}/kg
電流密度	アンペア毎平方メートル	A/m^{2}
磁界の強さ	アンペア毎メートル	A/m
量濃度 (a)，濃度	モル毎立方メートル	mol/m^{3}
質量濃度	キログラム毎立方メートル	kg/m^{3}
輝度	カンデラ毎平方メートル	cd/m^{2}
屈折率 (b)	（数字の） 1	1
比透磁率 (b)	（数字の） 1	1

(a) 量濃度（amount concentration）は臨床化学の分野では物質濃度（substance concentration）ともよばれる。
(b) これらは無次元量あるいは次元１をもつ量であるが、そのことを表す単位記号である数字の１は通常は表記しない。

表３．固有の名称と記号で表されるSI組立単位

組立量	SI 組立単位			
	名称	記号	他のSI単位による表し方	SI基本単位による表し方
平面角	ラジアン(b)	rad	1 (b)	m/m
立体角	ステラジアン(b)	sr(c)	1 (b)	m^{2}/m^{2}
周波数	ヘルツ (d)	Hz		s^{-1}
力	ニュートン	N		m kg s^{-2}
圧力，応力	パスカル	Pa	N/m^{2}	m^{-1} kg s^{-2}
エネルギー，仕事，熱量	ジュール	J	N m	m^{2} kg s^{-2}
仕事率，工率，放射束	ワット	W	J/s	m^{2} kg s^{-3}
電荷，電気量	クーロン	C		s A
電位差（電圧），起電力	ボルト	V	W/A	m^{2} kg s^{-3} A^{-1}
静電容量	ファラド	F	C/V	m^{-2} kg^{-1} s^{4} A^{2}
電気抵抗	オーム	Ω	V/A	m^{2} kg s^{-3} A^{-2}
コンダクタンス	ジーメンス	S	A/V	m^{-2} kg^{-1} s^{3} A^{2}
磁束	ウエーバ	Wb	Vs	m^{2} kg s^{-2} A^{-1}
磁束密度	テスラ	T	Wb/m^{2}	kg s^{-2} A^{-1}
インダクタンス	ヘンリー	H	Wb/A	m^{2} kg s^{-2} A^{-2}
セルシウス温度	セルシウス度(e)	℃		K
光束	ルーメン	lm	cd sr(c)	cd
照度	ルクス	lx	lm/m^{2}	m^{-2} cd
放射性核種の放射能 (f)	ベクレル (d)	Bq		s^{-1}
吸収線量, 比エネルギー分与, カーマ	グレイ	Gy	J/kg	m^{2} s^{-2}
線量当量, 周辺線量当量, 方向性線量当量, 個人線量当量	シーベルト (g)	Sv	J/kg	m^{2} s^{-2}
酸素活性	カタール	kat		s^{-1} mol

(a)SI接頭語は固有の名称と記号を持つ組立単位と組み合わせても使用できる。しかし接頭語を付した単位はもはやコヒーレントではない。
(b)ラジアンとステラジアンは数字の１に対する単位の特別な名称で、量についての情報をつたえるために使われる。実際には、使用する時には記号rad及びsrが用いられるが、習慣として組立単位としての記号である数字の１は明示されない。
(c)測光学ではステラジアンという名称と記号srを単位の表し方の中に、そのまま維持している。
(d)ヘルツは周期現象についてのみ、ベクレルは放射性核種の統計的過程についてのみ使用される。
(e)セルシウス度はケルビンの特別な名称で、セルシウス温度を表すために使用される。セルシウス度とケルビンの単位の大きさは同一である。したがって、温度差や温度間隔を表す数値はどちらの単位で表しても同じである。
(f)放射性核種の放射能（activity referred to a radionuclide）は、しばしば誤った用語で"radioactivity"と記される。
(g)単位シーベルト（PV,2002,70,205）についてはCIPM勧告2（CI-2002）を参照。

表４．単位の中に固有の名称と記号を含むSI組立単位の例

組立量	SI 組立単位		
	名称	記号	SI 基本単位による表し方
粘度	パスカル秒	Pa s	m^{-1} kg s^{-1}
力のモーメント	ニュートンメートル	N m	m^{2} kg s^{-2}
表面張力	ニュートン毎メートル	N/m	kg s^{-2}
角速度	ラジアン毎秒	rad/s	m m^{-1} s^{-1}=s^{-1}
角加速度	ラジアン毎秒毎秒	rad/s^{2}	m m^{-1} s^{-2}=s^{-2}
熱流密度，放射照度	ワット毎平方メートル	W/m^{2}	kg s^{-3}
熱容量，エントロピー	ジュール毎ケルビン	J/K	m^{2} kg s^{-2} K^{-1}
比熱容量，比エントロピー	ジュール毎キログラム毎ケルビン	J/(kg K)	m^{2} s^{-2} K^{-1}
比エネルギー	ジュール毎キログラム	J/kg	m^{2} s^{-2}
熱伝導率	ワット毎メートル毎ケルビン	W/(m K)	m kg s^{-3} K^{-1}
体積エネルギー	ジュール毎立方メートル	J/m^{3}	m^{-1} kg s^{-2}
電界の強さ	ボルト毎メートル	V/m	m kg s^{-3} A^{-1}
電荷密度	クーロン毎立方メートル	C/m^{3}	m^{-3} s A
表面電荷	クーロン毎平方メートル	C/m^{2}	m^{-2} s A
電束密度，電気変位	クーロン毎平方メートル	C/m^{2}	m^{-2} s A
誘電率	ファラド毎メートル	F/m	m^{-3} kg^{-1} s^{4} A^{2}
透磁率	ヘンリー毎メートル	H/m	m kg s^{-2} A^{-2}
モルエネルギー	ジュール毎モル	J/mol	m^{2} kg s^{-2} mol^{-1}
モルエントロピー, モル熱容量	ジュール毎モル毎ケルビン	J/(mol K)	m^{2} kg s^{-2} K^{-1} mol^{-1}
照射線量（X線及びγ線）	クーロン毎キログラム	C/kg	kg^{-1} s A
吸収線量率	グレイ毎秒	Gy/s	m^{2} s^{-3}
放射強度	ワット毎ステラジアン	W/sr	m^{4} m^{-2} kg s^{-3}=m^{2} kg s^{-3}
放射輝度	ワット毎平方メートル毎ステラジアン	W/(m^{2} sr)	m^{2} m^{-2} kg s^{-3}=kg s^{-3}
酵素活性濃度	カタール毎立方メートル	kat/m^{3}	m^{-3} s^{-1} mol

表５．SI 接頭語

乗数	名称	記号	乗数	名称	記号
10^{24}	ヨタ	Y	10^{-1}	デシ	d
10^{21}	ゼタ	Z	10^{-2}	センチ	c
10^{18}	エクサ	E	10^{-3}	ミリ	m
10^{15}	ペタ	P	10^{-6}	マイクロ	µ
10^{12}	テラ	T	10^{-9}	ナノ	n
10^{9}	ギガ	G	10^{-12}	ピコ	p
10^{6}	メガ	M	10^{-15}	フェムト	f
10^{3}	キロ	k	10^{-18}	アト	a
10^{2}	ヘクト	h	10^{-21}	ゼプト	z
10^{1}	デカ	da	10^{-24}	ヨクト	y

表６．SIに属さないが、SIと併用される単位

名称	記号	SI 単位による値
分	min	1 min=60 s
時	h	1 h =60 min=3600 s
日	d	1 d=24 h=86 400 s
度	°	1°=(π/180) rad
分	’	1’=(1/60)°=(π/10 800) rad
秒	”	1”=(1/60)’=(π/648 000) rad
ヘクタール	ha	1 ha=1 hm^{2}=10^{4}m^{2}
リットル	L，l	1 L=1 l=1 dm^{3}=10^{3}cm^{3}=10^{-3}m^{3}
トン	t	1 t=10^{3} kg

表７．SIに属さないが、SIと併用される単位で、SI単位で表される数値が実験的に得られるもの

名称	記号	SI 単位で表される数値
電子ボルト	eV	1 eV=1.602 176 53(14)×10^{-19}J
ダルトン	Da	1 Da=1.660 538 86(28)×10^{-27}kg
統一原子質量単位	u	1 u=1 Da
天文単位	ua	1 ua=1.495 978 706 91(6)×10^{11}m

表８．SIに属さないが、SIと併用されるその他の単位

名称	記号	SI 単位で表される数値
バール	bar	1 bar=0.1MPa=100 kPa=10^{5}Pa
水銀柱ミリメートル	mmHg	1 mmHg≈133.322Pa
オングストローム	Å	1 Å=0.1nm=100pm=10^{-10}m
海里	M	1 M=1852m
バーン	b	1 b=100fm^{2}=(10^{-12}cm)^{2}=10^{-28}m^{2}
ノット	kn	1 kn=(1852/3600)m/s
ネーパ	Np	SI単位との数値的な関係は、対数量の定義に依存。
ベル	B	
デシベル	dB	

表９．固有の名称をもつCGS組立単位

名称	記号	SI 単位で表される数値
エルグ	erg	1 erg=10^{-7} J
ダイン	dyn	1 dyn=10^{-5}N
ポアズ	P	1 P=1 dyn s cm^{-2}=0.1Pa s
ストークス	St	1 St =1cm^{2} s^{-1}=10^{-4}m^{2} s^{-1}
スチルブ	sb	1 sb =1cd cm^{-2}=10^{4}cd m^{-2}
フォト	ph	1 ph=1cd sr cm^{-2} =10^{4}lx
ガル	Gal	1 Gal =1cm s^{-2}=10^{-2}ms^{-2}
マクスウエル	Mx	1 Mx = 1G cm^{2}=10^{-8}Wb
ガウス	G	1 G =1Mx cm^{-2} =10^{-4}T
エルステッド (a)	Oe	1 Oe ≙ (10^{3}/4π)A m^{-1}

(a) ３元系のCGS単位系とSIでは直接比較できないため、等号「 ≙ 」は対応関係を示すものである。

表10．SIに属さないその他の単位の例

名称	記号	SI 単位で表される数値
キュリー	Ci	1 Ci=3.7×10^{10}Bq
レントゲン	R	1 R = 2.58×10^{-4}C/kg
ラド	rad	1 rad=1cGy=10^{-2}Gy
レム	rem	1 rem=1 cSv=10^{-2}Sv
ガンマ	γ	1 γ=1 nT=10^{-9}T
フェルミ		1 フェルミ=1 fm=10^{-15}m
メートル系カラット		1 メートル系カラット= 0.2 g = 2×10^{-4}kg
トル	Torr	1 Torr = (101 325/760) Pa
標準大気圧	atm	1 atm = 101 325 Pa
カロリー	cal	1 cal=4.1858J（「15℃」カロリー），4.1868J（「IT」カロリー），4.184J（「熱化学」カロリー）
ミクロン	µ	1 µ =1µm=10^{-6}m

（第8版，2006年）